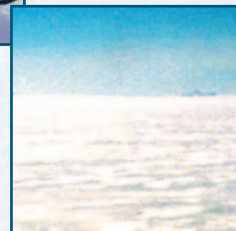


Antarctic Meteorology

A study with Automatic Weather Stations



C.H. Reijmer

Antarctic Meteorology

A study with Automatic Weather Stations

Carleen Reijmer

Cover: Aerial photograph of the Heimefrontfjella and Automatic Weather Stations 5 (photo's by the author) and 4 (photo by Dan Zwartz). Back: drawing courtesy of Pinguinxl, <http://www.pinguinxl.nl/>

Antarctic Meteorology

A study with Automatic Weather Stations

Antarctische Meteorologie

Een studie met automatische weerstations

(met een samenvatting in het Nederlands)

Proefschrift

ter verkrijging van de graad van doctor aan de Universiteit Utrecht op gezag van de Rector Magnificus, Prof. Dr. W. H. Gispen, ingevolge het besluit van het College voor Promoties in het openbaar te verdedigen op maandag 24 september 2001 des middags te 12.45 uur.

door

Catharina Helena Reijmer

geboren op 21 Januari 1974, te Pannerden.

Promotor: Prof. Dr. J. Oerlemans
faculteit Natuur- en Sterrenkunde, Universiteit Utrecht

This thesis is a contribution to the "European Project for Ice Coring in Antarctica" (EPICA), a joint ESF (European Science Foundation) / EC scientific programme, funded by the European Commission under the Environment and Climate Programme (1994-1998) contract ENV4-CT95-0074 and by national contributions from Belgium, Denmark, France, Germany, Italy, the Netherlands, Norway, Sweden, Switzerland and the United Kingdom. Additional support was provided by the Netherlands Antarctic Research Programme (NARP) which is coordinated by Netherlands Earth and Life Sciences Foundation (ALW) of the Netherlands Organization for Scientific Research (NWO).

ISBN: 90-393-2802-1

Contents

Summary	iii
1 Introduction	1
1.1 Background: climate changes	1
1.2 The European Project for Ice Coring in Antarctica	4
1.3 The Automatic Weather Stations	6
1.4 Trajectory studies	11
1.5 Overview	13
2 Surface albedo measurements over snow and blue ice in TM bands 2 and 4 in Dronning Maud Land, Antarctica	15
2.1 Introduction	16
2.2 Experimental setup and meteorological conditions	18
2.3 Narrow and broadband albedo of blue ice and snow	19
2.4 Bidirectional reflectance of blue ice and snow	27
2.5 Concluding remarks	32
3 The annual cycle of meteorological variables and surface energy balance on Berkner Island, Antarctica	35
3.1 Introduction	36
3.2 Location and experimental set-up	36
3.3 Meteorological conditions	38
3.4 The surface energy balance	45
3.5 Summary and concluding remarks	52
4 Meteorological conditions in Dronning Maud Land, East Antarctica	55
4.1 Introduction	56
4.2 Location and experimental set-up	56
4.3 Results	58
4.4 Summary and concluding remarks	75

5	The temporal and spatial variability of the surface energy balance in Dronning Maud Land, East Antarctica	77
5.1	Introduction	78
5.2	Location and experimental set-up	79
5.3	Prevailing meteorological conditions	80
5.4	Model description and validation	83
5.5	Results	87
5.6	Discussion	91
5.7	Concluding remarks	97
6	Moisture sources of precipitation in Western Dronning Maud Land, Antarctica	99
6.1	Introduction	100
6.2	The Automatic Weather Stations	101
6.3	The trajectory model	102
6.4	Model and measurement comparison	103
6.5	Trajectories in 1998	105
6.6	Case study: a major snowfall event in May 1998	111
6.7	Summary and conclusions	115
7	Air parcel trajectories to five deep drilling locations on Antarctica, based on the ERA-15 data set	119
7.1	Introduction	120
7.2	The trajectory model	121
7.3	Precipitation	123
7.4	Results of trajectory calculations	127
7.5	Summary	136
	Bibliography	139
	Samenvatting	149
	Dankwoord	155
	List of publications	157
	Curriculum Vitae	159

Summary

This thesis chiefly addresses a) the use of Automatic Weather Stations (AWS) in determining the near-surface climate and heat budget of Antarctica and, specifically, Dronning Maud Land (DML), and b) the determination of source regions of Antarctic moisture with the aid of a trajectory model and an atmospheric model. The primary motivation behind this interest is the drilling of two ice cores in the Antarctic ice sheet within the framework of the European Project for Ice Coring in Antarctica (EPICA). A thorough knowledge of the meteorological conditions will increase our understanding of the processes that influence the surface mass balance and heat budget.

In Chapter 2, ground-based observations of broadband, narrowband, and bidirectional reflectance are used to study the albedo of blue ice and snow. During summer, surface albedo plays an important role in the amount of heat exchanged between the surface and the atmosphere. The main objective of the study is to improve the methods used to derive surface albedo from satellite measurements and arrive at a better understanding of the processes influencing the magnitude of the albedo.

Chapters 3, 4 and 5 describe the data obtained from ten AWS in Antarctica and how they were used to determine the local surface energy budget. The AWS were placed on two transects perpendicular to the coastline in DML and one on Berkner Island. As expected, mainly the strength of the katabatically forced flow, in combination with the geostrophic flow, determines the near-surface conditions at these locations. The katabatic flow varies in strength depending on the magnitude of surface slope and temperature inversion, and is not active on Berkner Island, a station on a topographic dome. In DML, the strength of the katabatic flow varies, resulting in maximum wind speeds and potential temperatures at the sites with the steepest slopes, at the edge of the Antarctic plateau. The annual mean wind speed varies between 4 m s^{-1} , near the coast and on the plateau, to 7 m s^{-1} , on the edge of the plateau. The annual mean potential temperature varies between -18°C and -1°C . The annual mean temperature ranges from -16°C in the coastal area, where occasional melt occurs, to -46°C on the Antarctic plateau. Owing to the low temperatures, the specific humidity is very low. Accumulation is highest in the coastal regions and decreases with increasing elevation and distance from the coast, from $\sim 400 \text{ mm}$ water equivalent per year (w.e. yr^{-1}) near the coast to $\sim 30 \text{ mm}$ w.e. yr^{-1} on the plateau.

The AWS data, together with a model based on Monin-Obukhov similarity theory, are used to calculate the surface energy budget for the measuring period. The strength of the katabatic flow largely determines not only the near-surface meteorological conditions but also the surface energy budget. The annual average energy gain at the surface from the downward sensible heat flux varies between $\sim 3 \text{ W m}^{-2}$ to 25 W m^{-2} , with the highest values at the sites with the highest wind speeds and potential temperatures. The negative net radiative flux largely balances the sensible heat flux and ranges from $\sim 2 \text{ W m}^{-2}$ to 28 W m^{-2} . The average latent heat flux is generally small and negative ($\sim -1 \text{ W m}^{-2}$), indicating mass loss through sublimation. The annual subsurface fluxes are small ($\sim -0.2 \text{ W m}^{-2}$).

In Chapters 6 and 7, moisture sources of snow falling at five deep-drilling locations in Antarctica (Byrd, DML05, Dome C, Dome F and Vostok) are defined, based on five-day backward air parcel trajectories calculated from data of the European Centre for Medium Range Weather Forecasts. Based on model precipitation, a distinction is made between cases with and without snowfall at the point of arrival. Of the snowfall trajectories ending at DML05 in 1998, 40 - 80 % originate in the Atlantic Ocean between 40 and 60 °S, within four days before arrival. Evaporation along these trajectories is largest during the first half. A case study for May 1998 shows that during snowfall exceptionally high temperatures and wind speeds prevail in the atmospheric boundary layer. The trajectories from the ECMWF Re-analysis Project (ERA-15) cover a 15-year period and show that the oceans closest to the five drilling sites contribute most of the moisture. The latitude band contributing most ($\sim 30\%$) of the total annual precipitation is at 50 - 60 °S, the area just north of the sea ice edge. The calculated trajectories show seasonal dependency, resulting in a seasonal cycle in the moisture sources, which is further enhanced by a seasonal cycle in the amount of precipitation.

Chapter 1

Introduction

1.1 Background: climate changes

In the history of the Earth, the climate has changed considerably numerous times (Dansgaard *et al.*, 1993; Greenland Ice-core Project (GRIP) Members, 1993; Petit *et al.*, 1999). The variability in the Earth's climate system is caused by natural variations in factors such as solar insolation, ocean currents and atmospheric composition due to, for example, volcanic eruptions. During the last century, climate has been additionally influenced by anthropogenic sources, e.g., CO₂ and methane emissions from fossil fuel burning. The sensitivity of the climate system to changes in, e.g., insolation or atmospheric constituents, differs per region. Climate studies have shown that the polar regions are more sensitive to climatic changes than other regions owing to the albedo feedback mechanism (Oerlemans and Bintanja, 1995). Viewed in this light, the Antarctic and Greenland ice sheets are interesting regions to study, also because of their potential contribution to sea level rise. The Greenland ice sheet represents a potential sea level rise of ~7 m and complete melting of the Antarctic ice sheet would raise the sea level by ~60 m. In comparison, the fresh water stored in glaciers and small ice caps represents a potential sea level rise of ~0.5 m (IPCC, 1995).

Not only the (changing) conditions on the surface of the Greenland and Antarctic ice sheets yield valuable information, the ice itself also contains a wealth of historic climate information. Data pertaining to past climate and state of the local atmosphere, such as temperature, chemical composition and atmospheric circulation, are stored in the ice. Owing to the considerable thickness of the ice (3000 to 4000 m) and the low accumulation rate, the length of the records that can be obtained is on the order of 150 to 500 kyr. These records include several glacial-interglacial cycles (Petit *et al.*, 1999). To gain access to these climate records, several deep ice cores have been drilled in the Antarctic and Greenland ice sheet, e.g., Vostok, Byrd, Dome F, Taylor dome (Antarctica), Greenland Ice Core Project (GRIP and North GRIP) and Greenland Ice Sheet Project (GISPII) (see for example Greenland Ice-core Project (GRIP) Members (1993); Dome-F Ice Core Research Group (1998b); Petit *et al.* (1999); Mulvaney *et al.* (2000)). These ice cores have provided insight in the climate at these

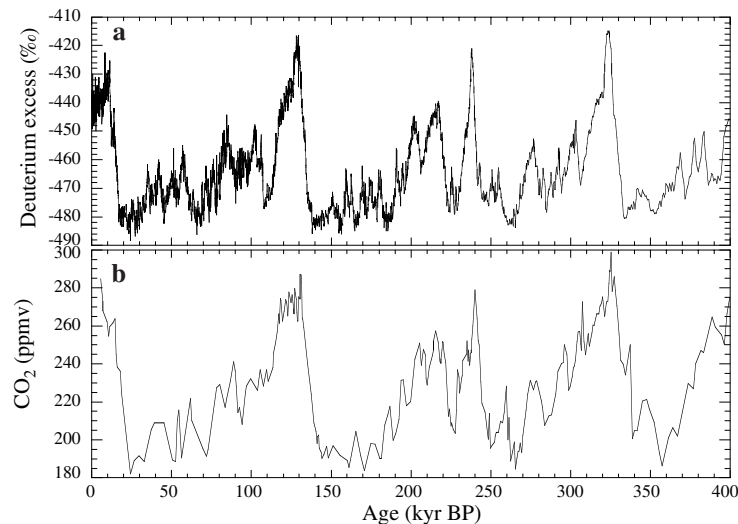


Figure 1.1. Time series of (a) deuterium excess and (b) CO_2 in the Vostok ice core, Antarctica (Petit *et al.*, 1999). CO_2 is presented in parts per million volume (ppmv).

locations over the past 150 to 400 kyr, through the isotope composition of the ice itself, the presence of other elements in the ice, and the composition of air bubbles enclosed in the ice. Figure 1.1 presents an example of records obtained from the Vostok ice core, Antarctica. Deuterium excess is often used as a proxy for air temperature and represents a local signal. CO_2 is stored in the air bubbles and marks global variations in atmospheric composition.

The interpretation of the obtained records is, however, not straightforward. The climatic record is of little value unless the age of the ice is known as a function of depth. Counting annual layers is the most exact method of determining the age of the ice. When the annual layers are too thin and the dates of volcanic ash horizons not well known or no volcanic horizons are present, dating the ice relies on comparison with other dated climate records and ice flow modelling (Patterson, 1994). This introduces additional uncertainties and can result in completely different interpretations of ice core records (Mulvaney *et al.*, 2000). A further problem is how to relate the obtained records of, e.g., isotope content (e.g., hydrogen and oxygen isotopes) and gas composition (such as CO_2 and CH_4) to the state of the atmosphere at a given point in time. The climate recorded in ice cores is mainly determined by the local snowfall conditions and by the origin of the air and moisture. The conditions in which snowfall occurs need not represent the mean conditions at that point (Noone and Simmonds, 1998; Noone *et al.*, 1999). Several factors, such as changes in seasonality of snowfall and changes in moisture source regions (Jouzel *et al.*, 1997; Werner *et al.*, 2000), may bias the ice core record.

The stable-isotope ratios of hydrogen (δD) and oxygen ($\delta^{18}\text{O}$) in the ice are examples of how ice records are related to climate signals and are often used as a proxy for temperature (Petit *et al.*, 1999). In Antarctic ice core records, temperature is of-

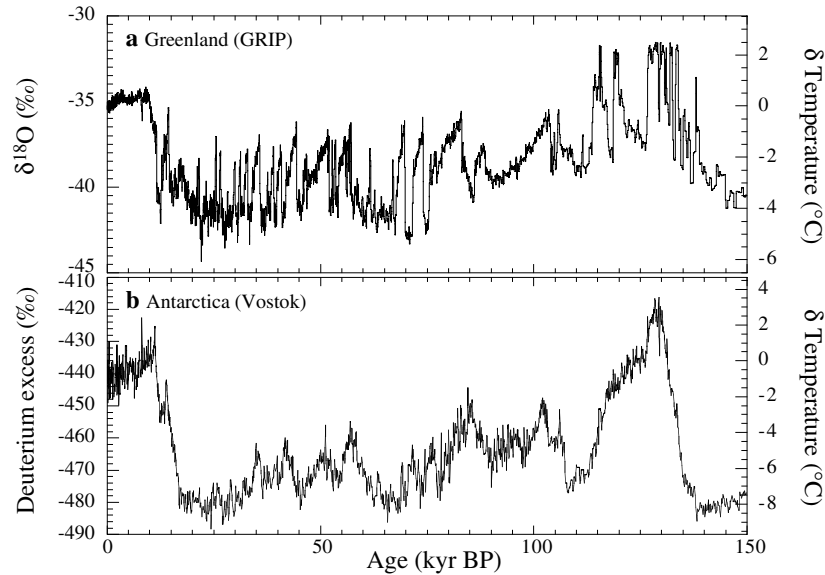


Figure 1.2. (a) Time series of $\delta^{18}\text{O}$ values and derived temperature changes with respect to the present temperature, of the GRIP ice core, Greenland (Dansgaard *et al.*, 1993; Taylor *et al.*, 1993). (b) Time series of deuterium excess values and derived temperature changes with respect to the present temperature, of the Vostok ice core, Antarctica (Petit *et al.*, 1999).

ten related to the deuterium excess d , which is a linear combination of the δD and $\delta^{18}\text{O}$ values (Petit *et al.*, 1991; Jouzel *et al.*, 1997). To obtain a temperature record from d or $\delta^{18}\text{O}$, the relation between annual mean d or $\delta^{18}\text{O}$ and the annual mean temperature needs to be known and is assumed to be linear and constant in time and space. Figure 1.2 presents the time series of $\delta^{18}\text{O}$ for the GRIP ice core, Greenland, and d for the Vostok ice core, Antarctica, with the linearly derived temperature deviation with respect to the present mean temperature for the last glacial-interglacial cycle (~ 150 kyr) (Dansgaard *et al.*, 1993; Taylor *et al.*, 1993; Petit *et al.*, 1999). The figure shows striking similarities between the GRIP and Vostok records. Both records show the sudden increase in temperature at the end of the last glacial maximum (LGM) towards the Holocene (the last $\sim 11,500$ yr). At ~ 130 kyr before present (BP), both records show an interglacial with a decrease in temperature towards the LGM. The Greenland ice core exhibits large temperature variations occurring during the LGM. Not all these variations have corresponding jumps in the Antarctic core.

The assumption of linearity in the above relations is reasonable, as shown by Jouzel *et al.* (1997). However, these relationships are based on present-day conditions and the assumption that the relation remains constant in time is questionable (Jouzel *et al.*, 1997; Jouzel, 1999; Werner *et al.*, 2000). Borehole thermometry and various isotopes in the Greenland ice sheet indicate a temperature difference between the present and the LGM that is about twice as large as the difference estimated by the $\delta^{18}\text{O}$ method (Jouzel, 1999), indicating that the coefficients of the linear relationships

are not constant in time. $\delta^{18}\text{O}$ and d in Antarctic and Greenland snow represent a variety of complex processes. They depend on the surface temperature of the ocean from which the moisture evaporated, the subsequent cycles of condensation and evaporation and the temperature at which the moisture finally condenses before it precipitates. The relationship will therefore depend on moisture source region, seasonality of the snowfall and local conditions. This hampers the interpretation of the $\delta^{18}\text{O}$ and d record (Jouzel *et al.*, 1997; Krinner *et al.*, 1997a; Schlosser, 1999; Werner *et al.*, 2000).

In spite of the problems involved with the interpretation of ice cores, the $\delta^{18}\text{O}$ and d records as well as records of other isotopes and gas content of the ice have provided us with valuable information of the climate over the last 150 to 400 kyr. Besides answering questions, they also left several interesting issues unanswered and raised new ones. How are climate changes coupled between the two hemispheres? Are the rapid climate changes in the LGM, observed in Greenland ice cores, confined to the Northern Hemisphere or are they global phenomena? To answer these and other questions the ice core records of Greenland and Antarctica have to be compared with other records obtained from, e.g., tree rings, lake sediments and deep sea cores. Automatic weather stations (AWS) can provide additional knowledge, giving more insight in the local conditions in which snowfall occurs and the interaction between the atmosphere and snow surface. Furthermore, the use of General Circulation Models (GCMs), climate models and numerical weather prediction models can give information about the state of the atmosphere in present and past climate and the origin of the moisture. This thesis addresses a) the use of AWS in determining the near-surface climate and heat budget of Antarctica, and b) the determination of source regions of Antarctic moisture with the aid of a trajectory model and an atmospheric model. The primary motivation behind this interest is the drilling of two ice cores in the Antarctic ice sheet within the framework of the European Project for Ice Coring in Antarctica.

1.2 The European Project for Ice Coring in Antarctica

The European Project for Ice Coring in Antarctica (EPICA) is a joint ESF (European Science Foundation)/EU scientific programme in which ten European countries¹ cooperate in a joint effort to drill two deep ice cores in Antarctica and analyse the data. The main objective of EPICA is to construct a high-resolution climate record for the Antarctic, and compare the results with other Antarctic and Greenland records to answer questions raised by the existing ice cores. The cores are drilled at Dome C (Wolff *et al.*, 1999) and DML05 (Oerter *et al.*, 2000) (Figure 1.3). The location of Dome C was chosen for its location on a topographic dome, where distortions in the layering due to ice flow is expected to be minimal. Furthermore, the ice thickness at this location is considerable, 3250 ± 25 m (Tabacco *et al.*, 1998), and the accumulation rate is low, ~ 36 mm water equivalent per year (w.e. yr^{-1}) (Petit *et al.*, 1982), which makes

¹Belgium, Denmark, France, Germany, Italy, the Netherlands, Norway, Sweden, Switzerland and the United Kingdom

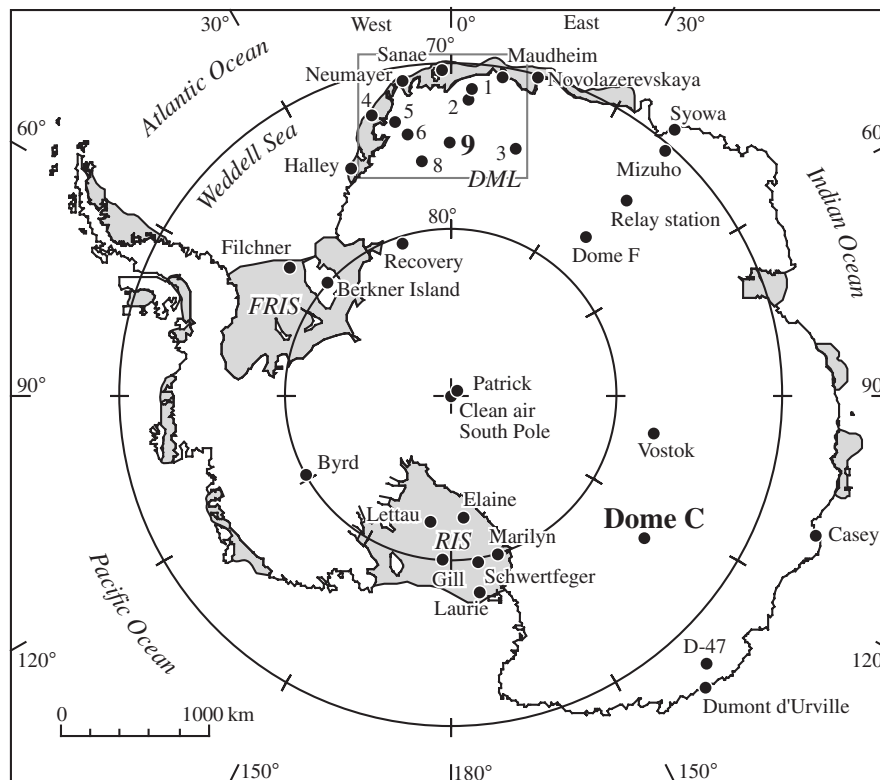


Figure 1.3. Map of Antarctica, showing the locations of the Automatic Weather Stations (AWS, numbers) and other stations mentioned in this thesis. AWS 9 is situated ~ 2 km west of DML05. The box indicates Dronning Maud Land (DML) (Figure 1.4); grey areas are ice shelves; FRIS, Filchner-Ronne Ice Shelf; RIS, Ross Ice Shelf.

it possible to obtain a record covering a time span of ~ 500 kyr, containing several glacial-interglacial cycles. Drilling of the Dome C core started in the austral summer of 1997-98 and first results were reported in, e.g., Wolff *et al.* (1999), Mulvaney *et al.* (2000) and Röthlisberger *et al.* (2000).

The Atlantic Ocean is considered an important link between Antarctic and Greenland climate records (Stocker, 1999). The second EPICA core will therefore be drilled at DML05, in Dronning Maud Land (DML), an area of Antarctica bordering the Atlantic Ocean (Figure 1.3). The relatively high accumulation rate at the selected drilling site, ~ 62 mm w.e. yr^{-1} (Oerter *et al.*, 2000) and the ice thickness of ~ 2000 m (Steinhage *et al.*, 1999) make it possible to obtain a detailed record of the last glacial-interglacial cycle. Drilling at DML05 started in the austral summer of 2000-01. An extensive reconnaissance was made of DML, to identify the optimal site for the deep drilling, preceding the actual drilling at DML05. The EPICA DML pre-site surveys started in the austral summer of 1995-96 and consisted of detailed mapping of the surface and bedrock topography (Steinhage *et al.*, 1999), drilling and analysis of shal-

low and medium deep ice cores and snow pits (Stenberg *et al.*, 1999; Karlöf *et al.*, 2000), study of accumulation patterns (Isaksson *et al.*, 1999; Oerter *et al.*, 2000) and study of the meteorological conditions in DML by means of automatic weather stations and atmospheric modelling (Van den Broeke *et al.*, 1999; Van Lipzig *et al.*, 1999; Holmlund *et al.*, 2000; Bintanja, 2001). The purpose of the AWS and atmospheric models within EPICA is to increase our knowledge about the present mass balance in DML, and to study the energy exchange between atmosphere and snow surface and, therefore, help with the interpretation of ice cores. For example, the AWS provide detailed measurements of meteorological parameters such as accumulation and temperature which give insight into the seasonality of the snowfall and the meteorological conditions in which most snowfall occurs, and are factors that determine the climate recorded in ice cores.

1.3 The Automatic Weather Stations

In the last two decades, about 100 AWS have been deployed and used to study meteorological processes close to the surface and climatological conditions in several regions of Antarctica (Allison *et al.*, 1993; Stearns and Weidner, 1993; Bintanja *et al.*, 1997; Enomoto *et al.*, 1998; Takahashi *et al.*, 1998; Reijmer *et al.*, 1999a). Because of the vastness of the continent, the number of observations was still limited. Moreover, the stations were not evenly distributed over the continent and none of the stations were located in DML. AWS are designed to work for long periods without being serviced and offer the opportunity to measure meteorological variables in remote areas and in harsh weather conditions. This thesis centres on the use of the AWS placed within the framework of EPICA to study the climate of DML. The data will give us insight into the meteorological conditions in DML over a period of several years, following up on the studies of Jonsson (1995), König-Langlo *et al.* (1998), Bintanja and Reijmer (2001) and others. Data could also be used to validate climate and weather prediction models currently used to study the Antarctic climate (Genthon and Braun, 1995; King and Connolley, 1997; Krinner *et al.*, 1997b; Van Lipzig *et al.*, 1999).

1.3.1 Location

The Institute for Marine and Atmospheric Research Utrecht (IMAU) of Utrecht University, The Netherlands, operates the AWS in DML. At present, IMAU operates ten stations in Antarctica, the first of which was positioned on the south dome of Berkner Island in February 1995. In January 1997, three additional stations (AWS 1, 2 and 3) were installed during the Norwegian/Swedish/Dutch ground traverse (Winther *et al.*, 1997). In the austral summer of 1997-98, five additional stations were installed during a Swedish/Norwegian/Dutch ground traverse (Holmlund *et al.*, 2000). Staff of the Alfred Wegener Institute (AWI) in Germany established the tenth station (AWS 9) ~2 km west of the EPICA drilling site in DML, in December 1997. Table 1.1 presents more details of the AWS locations. Figure 1.4 shows the locations of the IMAU AWS in DML.

Table 1.1. Characteristics of the IMAU AWS.

AWS	Latitude	Longitude	Elevation (m a.s.l.)	Slope (m km ⁻¹)	Start date	H_{init} (m)	ρ (g kg ⁻¹)
1 (Site A)	71° 54.0'S	3° 05.0'E	1420	19.5±25.1	31-12-1996	3.19	370±2
2 (Site C)	72° 15.1'S	2° 53.5'E	2400	37.2±15.7	03-01-1997	2.90	325±25
3 (Site M)	75° 00.0'S	15° 00.1'E	3453	0.7±0.3	28-01-1997	2.56	325±8
4 (1090)	72° 45.2'S	15° 29.9'W	34	0.0±0.5	19-12-1997	2.63	390±50
5 (CM)	73° 06.3'S	13° 09.9'W	363	13.5±6.4	02-02-1998	2.73	450±26
6 (Svea cross)	74° 28.9'S	11° 31.0'W	1160	15.0±30.9	14-01-1998	2.83	450±50
7 (SBB01)	74° 34.7'S	11° 03.0'W	1172	-	31-12-1997	0.70	850
8 (CV)	76° 00.0'S	8° 03.0'W	2399	2.2±0.8	12-01-1998	2.64	345±22
9 (DML05)	75° 00.2'S	0° 00.4'E	2892	1.3±0.3	29-12-1997	2.26	335±25
Berkner	79° 34.0'S	45° 46.9'W	886	5.3±1.8	12-02-1995	2.95	368.2

Notes: The surface slope is based on a 10 by 10 km Antarctic Topography (data courtesy of J. Bamber, Bristol University). Slope error estimates are the standard deviations in the mean of 8 points surrounding the AWS. AWS 7 is located in a valley, not resolved in this topography, therefore the calculated slope is faulty and omitted. H_{init} , initial height of the height sensor; ρ , mean snow density based on firn core measurements averaged over the first 0.5 m of firn. Density data AWS 1, 2 and 3 courtesy of M.R. van den Broeke, Utrecht University, 1999; AWS 4, 5 and 8 courtesy of L. Karlöf, Norwegian Polar Institute, Tromsø, 1999; AWS 9 courtesy of H. Oerter, Alfred Wegener Institute, Bremerhaven, 2000.

References: Between brackets the internationally used names for the sites: Site A, C, M, Van den Broeke *et al.* (1999); 1090, CM, Svea cross, SBB01, CV, Holmlund *et al.* (2000); DML05, Oerter *et al.* (2000)

Berkner Island is a large island completely covered by ice and surrounded by the Filchner-Ronne ice shelf, south of the Weddell Sea, Antarctica (Figure 1.3). The AWS measurements were carried out on Thyssen Höhe, the South Dome of Berkner Island. Due to its location on a dome, the station is probably not affected by the predominant katabatic flow found in most other areas of Antarctica. A dome is also a very suitable place for ice coring because distortions due to ice flow are minimal. The British Antarctic Survey (BAS) plans to drill an ice core to the bedrock at this location, within the framework of EPICA. The results of the AWS, especially the temporal variations in the measured mass balance and air temperature, will be useful in the interpretation of the ice core record.

The other nine IMAU AWS were placed in DML, which was one of the least explored regions of Antarctica. Norwegian whalers were the first Europeans to visit the region, in the early 1920s. The first significant scientific expeditions to the area where the German Schwabenland expedition in the austral summer of 1938-39 and the Norwegian-British-Swedish expedition in 1949-52. Permanent occupation and continuous meteorological observations began in the 1950s, preceding the International Geophysical Year, 1957-58, at Halley, a permanently occupied British base on the Brunt Ice Shelf. In the following years, several stations were founded along the coast of DML of which Sanae, a South-African base, in 1962, and Neumayer, a German station on the Ekström ice shelf, in 1981, are the only other wintering stations in the area. There are, however, only a few inland stations that measure meteorological variables in DML on a continuous basis, e.g., Dome F and Relay station (Enomoto *et al.*, 1998; Takahashi *et al.*, 1998). The AWS placed within the framework of EPICA have improved on that significantly.

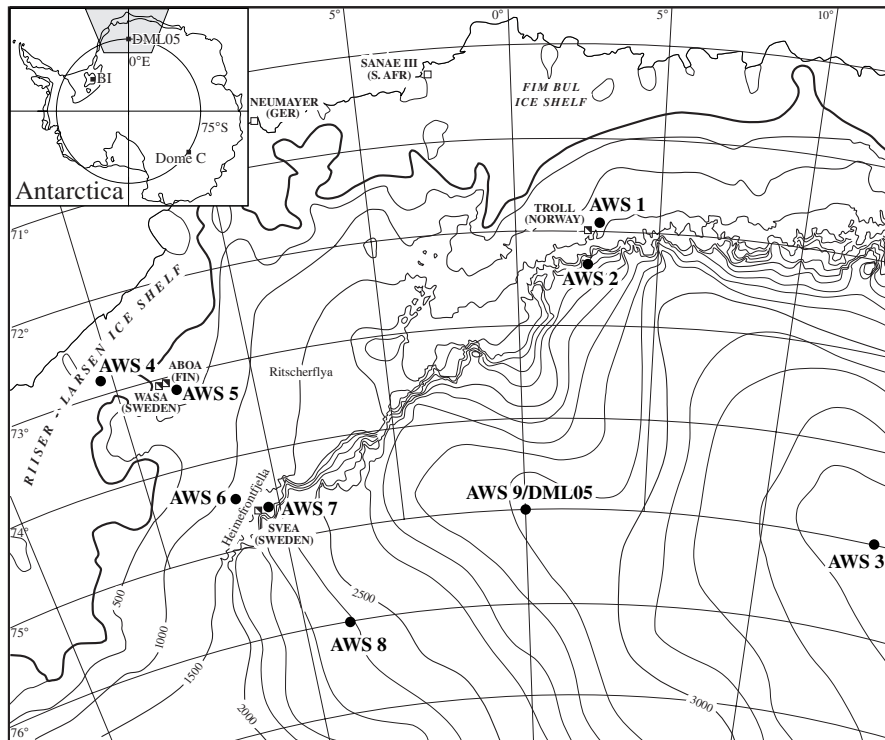


Figure 1.4. Map of Dronning Maud Land (DML), Antarctica, showing the locations of the Automatic Weather Stations (AWS). AWS 9 is situated ~ 2 km west of DML05, the EPICA drilling site. In the inset map of Antarctica the shaded area is DML and Bi denotes Berkner Island.

The locations of the AWS were chosen to cover a substantial part of western DML between an AWS transect south of Halley, operated by the United States Antarctica Research Program (USARP) (Stearns *et al.*, 1997), and a transect of six AWS located on a line from Syowa station to Dome Fuji, operated by the Japanese Antarctic Research Expeditions (JARE) in co-operation with USARP (Enomoto *et al.*, 1998; Takahashi *et al.*, 1998). The DML AWS fill the spatial gap between these two lines of AWS covering an area from 15°W to 15°E and 72°S to 76°S (Figure 1.3). The AWS in DML are placed on two transects perpendicular to the coastline representing different climate regimes; the coastal area, the escarpment region and the Antarctic plateau. AWS 4 is located in the coastal area on an ice shelf where the influence of passing depressions will be considerable and accumulation is largest. AWS 5 is located on the lower part of the ice sheet near the grounding line. AWS 1, 2, 6 and 7 are located close to or on the steep slope towards the Antarctic plateau where the influence of the predominant katabatic flow is expected to be considerable. AWS 3, 8 and 9 are located on the Antarctic plateau, less influenced by the katabatic flow and depressions. Nearly all stations are located on snow; only AWS 7 is located on blue ice. Results from this station are presented in Bintanja and Reijmer (2001).

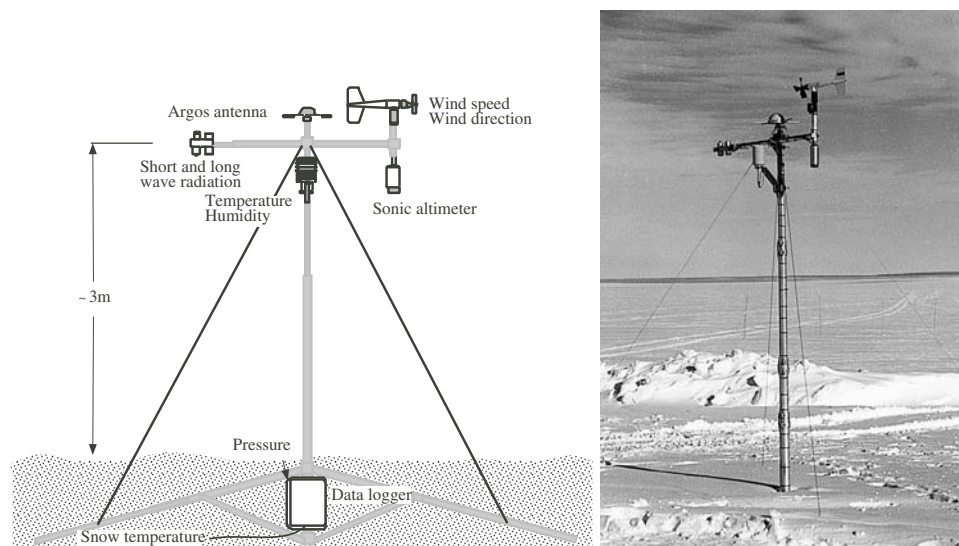


Figure 1.5. (a) Schematic picture of a weather station and (b) a photo of AWS 5. Mounted left on the yard the four radiation sensors, right on the yard the wind speed, wind direction and instrument height sensors, below the yard, the temperature and humidity sensors and at the top of the mast the Argos antenna. Air pressure is measured in the electronics box, which is below the snow.

1.3.2 Experimental set-up

All stations consist of a vertical mast placed on a four-legged frame. They measure air temperature, wind speed, wind direction, instrument height, air pressure and incoming shortwave radiation at one level above the surface (Figure 1.5). Except AWS 2, all stations additionally measure firn temperatures at two (Berkner Island), eight (AWS 1 and 3) or ten (AWS 4 to 9) different depths. AWS 4 to 9 additionally measure relative humidity, reflected shortwave radiation, and incoming and outgoing longwave radiation. Table 1.2 presents the sensor types used on the weather stations and some technical details. The stations sample every six (Berkner Island and AWS 1 to 3) or five (AWS 4 to 9) minutes. Hourly means are calculated for Berkner Island and AWS 1 to 3, and two-hourly means for AWS 4 to 9. The hourly and two-hourly averages are stored locally and transmitted using Argos transmitters. The stations are powered by batteries and are designed to work for two to three years without being serviced. The choice for one measuring level instead of more is based on the desire to operate the stations in a remote area and in harsh weather conditions without the possibility to carry out frequent maintenance. Additional reasons are energy efficiency and more rapid snowing under of lower levels.

The accuracy of the sensors was tested in inter-comparison experiments in the Netherlands in the year prior to placement in Antarctica. The sensors are not ventilated for reasons of energy efficiency, which particularly affects the accuracy of the air temperature and relative humidity sensors. The magnitude of the resulting error depends on the amount of reflected solar radiation, the wind speed and the type of

Table 1.2. *Sensor types with measuring range and accuracy.*

Sensor	AWS	Type	Range	Accuracy
Temperature	I	Aanderaa 2775C	-90 to +30 °C	0.1 °C
	II	Vaisala HMP35AC	-80 to +56 °C	0.3 °C
Humidity	II	Vaisala HMP35AC	0 to 100 %	2 % (<i>RH</i> < 90 %)
				3 % (<i>RH</i> > 90 %)
Wind speed	I	Aanderaa 2740	0.5 to 76 m s ⁻¹	0.5 m s ⁻¹
	II	Young 05103	0 to 60 m s ⁻¹	0.3 m s ⁻¹
Wind direction	I	Aanderaa 2750	0 to 360°	5°
	II	Young 05103	0 to 360°	3°
Pressure	I	Aanderaa 2775C	600 to 1024 hPa	0.5 hPa
	II	Vaisala PTB101B	600 to 1060 hPa	4 hPa
Shortwave radiation	I	Aanderaa 2770	0 to 2000 W m ⁻²	10 W m ⁻²
			300 to 2500 nm	
Longwave radiation	II	Kipp CNR1	305 to 2800 nm	2 %
	II	Kipp CNR1	-250 to 250 W m ⁻²	15 W m ⁻²
Instrument height	I	Aanderaa	1 to 4 m	0.01 m
	II	SR50	0.5 to 10 m	0.01 m or 0.4 %

Notes: The AWS are subdivided into two groups: type I, Berkner Island AWS and AWS 1 to 3, and type II, AWS 4 to 9. In January 2001, the Berkner Island AWS was replaced by a type-II AWS. *RH*, relative humidity.

radiation shield of the sensor. In summer the error can be as large as 10 °C at Berkner Island AWS and AWS 1 to 3. AWS 4 to 9 use different radiation shields and temperature sensors; comparisons with ventilated temperature and humidity sensors show no significant radiation error at these stations.

In below 0 °C temperatures, the maximum relative humidity that can be measured decreases. The measurements are corrected for this effect through the method described by Anderson (1994). After the correction, the uncertainty in the relative humidity becomes ~5 %. The radiation sensors are calibrated before and after operation in Antarctica and show a considerable instrumental drift. Furthermore, the radiation sensors show a temperature dependency. Below ~-20 °C the sensitivity decreases with decreasing temperature. These factors increase the uncertainty in the shortwave radiative fluxes to ~10 % and the uncertainty in the longwave radiative fluxes to ~20 W m⁻².

Another problem is occasional rime on the sensors. This causes the wind speed and wind direction sensors to jam and shields the instrument height and radiation sensors. Especially for the radiation sensors, it is difficult to judge when this happens. Problems with data transmission occasionally result in gaps in the data set. AWS 3, 8 and 9 stop transmitting in winter due to low temperatures. The results presented in this thesis comprise a six-year data set for the Berkner Island AWS, a four-year data set for AWS 1 to 3 and a three-year data set for AWS 4 to 9.

The weather station data of the IMAU AWS will be compared with data from other AWS and permanent stations. Table 1.3 and Figure 1.3 present the location and some other details of these stations. The table also presents references for data and more details about the weather stations.

Table 1.3. Characteristics of weather stations in Antarctica mentioned in this thesis (Figure 1.3).

Station	Latitude	Longitude	Elevation (m a.s.l.)	Slope (m km ⁻¹)
Byrd ^a	80°0.0'S	119°24'W	1530	3.5±1.5
Casey ^a	66°18'S	110°30'E	41	0.0±26.9
Clean Air / South Pole ^b	90°0.0'S	0°0.0'W	2835	0.3±1.3
D-47 ^c	67°24'S	138°42'E	1560	7.0±0.9
Dome C ^d	74°30'S	123°0'E	3280	0.5±0.1
Dome F ^e	77°19.0'S	39°42.2'E	3810	0.0±0.5
Dumontd'Urville ^f	66°42'S	140°0'E	43	10.3±36.4
Elaine ^g	83°6'S	174°12'E	60	0.0±0.0
Filchner ^a	77°42'S	51°13.2'W	20	0.1±0.1
Gill ^g	80°0'S	178°36'W	55	0.2±0.1
Halley ^{a,f}	75°30'S	26°24'W	39	0.5±1.4
Lettau ^g	82°30'S	174°24'W	55	0.0±0.1
Marilyn ^g	80°0'S	165°6'E	75	0.7±0.4
Maudheim ^h	71°0.0'S	10°54'W	38	1.7±2.4
Mizuho ⁱ	70°42'S	40°18'E	2230	7.5±1.3
Neumayer ^f	70°42'S	8°24'W	50	0.7±0.2
Novolazerevskaya ^a	70°48'S	11°48'E	99	33.7±15.1
Patrick ^g	89°54'S	45°0.0'E	2835	0.3±1.3
Recovery ^a	80°48'S	22°18'W	1220	6.8±7.1
Relay station ^e	74°1.2'S	43°3.0'E	3353	2.2±0.5
Sanae ^a	70°18'S	2°24'W	52	6.7±7.1
Schwertfeger ^g	79°54'S	170°0'E	60	0.1±0.1
Svea	74°35'S	11°13'W	1250	-
Syowa ^e	69°0'S	39°36'E	21	0.0±24.2
Vostok ^a	78°30'S	106°54'E	3488	1.0±0.9

Notes: The surface slope is based on a 10 by 10 km Antarctic Topography grid (data courtesy of J. Bamber, Bristol University). Slope error estimates are the standard deviations in the mean of eight points surrounding the station.

References: a, King and Turner (1997); b, Carroll (1982); c, Allison *et al.* (1993); d, Wendler and Kodama (1984); e, Takahashi *et al.* (1998); f, König-Langlo *et al.* (1998); g, Stearns and Weidner (1993); h, Weller (1980); i, Ohata (1985).

1.4 Trajectory studies

Several techniques have been used to trace moisture source regions of Antarctic snow. Petit *et al.* (1991) and Ciais *et al.* (1995) use deuterium excess as tracer in combination with idealised isotope models. These authors conclude that the Antarctic moisture has a subtropical origin. Peixoto and Oort (1992) came to the same conclusion on the basis of atmospheric water balance studies. Other studies, including $\delta^{18}\text{O}$ (Bromwich and Weaver, 1983), and GCMs (Koster *et al.*, 1992; Delaygue *et al.*, 2000; Delmotte *et al.*, 2000), suggest a more southerly origin in the mid-latitudes.

Another method to trace source regions of Antarctic moisture is to study the pathways along which air parcels transport moisture that precipitates over the Antarctic continent. These air parcel trajectories can be determined by calculating the displacement of an air parcel during a certain time step. Different types of trajectories

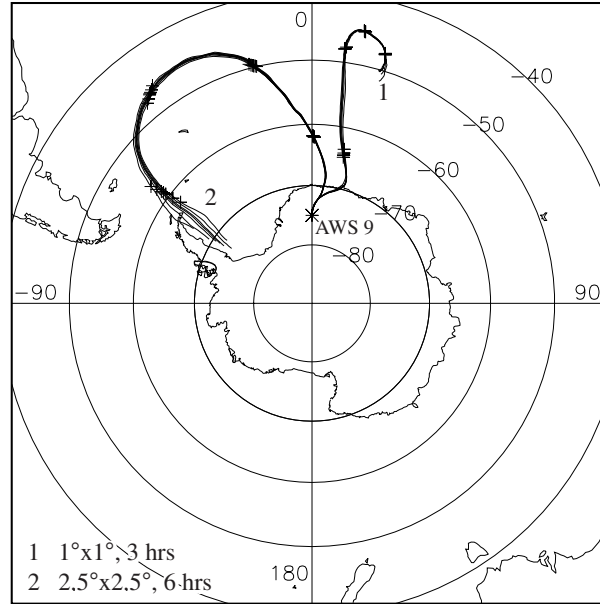


Figure 1.6. Trajectories starting at AWS 9 (DML05) at 650 hPa for 14 May 1998, 0.00 GMT, calculated five days back at two different spatial and temporal resolutions. In addition, trajectories starting at 0.1° north, east, south and west of AWS 9, and 5 hPa above and below the original trajectory are displayed. Each day back is marked with a plus sign.

can be calculated, e.g., isentropic (along surfaces of constant potential temperature), isobaric (along surfaces of constant pressure) or three-dimensional. The latter most accurately approximates the true three-dimensional transport path (Stohl *et al.*, 1995; Kottmeier and Fay, 1998).

To calculate three-dimensional air parcel trajectories, the three-dimensional displacement of an air parcel during a time step Δt is calculated using an iterative scheme:

$$\mathbf{X}_{n+1} = \mathbf{X}_0 + \frac{\Delta t}{2} [\mathbf{v}(\mathbf{X}_0, t) + \mathbf{v}(\mathbf{X}_n, t + \Delta t)]. \quad (1.1)$$

In this equation Δt is the iteration time step, \mathbf{X}_0 is the position vector of the parcel at time t , \mathbf{X}_n is the n^{th} iterative approximation of the position vector at time $t + \Delta t$ and $\mathbf{v}(\mathbf{X}, t)$ is the wind vector at position \mathbf{X} and time t . The iteration time step can be positive (forward in time) to calculate the position of an air parcel in the course of time, and negative (backward in time) to calculate the origin of an air parcel. As input for the trajectory model, three-dimensional wind fields are necessary and usually the analyses or 3 to 6 hours' forecasts of a numerical weather prediction model are used. The iteration time step is on the order of 10 minutes to 1 hour and with a temporal resolution of the three-dimensional wind fields of 3 to 6 hours, interpolation of the wind fields in time and space is necessary (Scheele *et al.*, 1996).

Figure 1.6 presents an example of a backward trajectory started at AWS 9. The

figure illustrates the sensitivity of trajectory calculations to the spatial and temporal resolution of the input wind fields and to a small change in starting point of the calculations. According to Kahl *et al.* (1989) and Stohl *et al.* (1995), uncertainties introduced by the choice of trajectory type and interpolation schemes, are on the order of 1000 km after five days calculation. Errors in the vertical wind component constitute a major source of uncertainties in the calculated trajectories. The above implies that the identified source regions after five days have an uncertainty of about nine degrees latitude. In reality, the uncertainty might be even larger because of the difference between the analysed wind fields and the real winds, and the presence of convective systems (such as fronts). In a convective system the air parcel loses its identity making it impossible to truly trace a single parcel. These important sources of errors in trajectories are difficult to assess and are not quantified in the uncertainty estimates presented here. Fortunately, precipitation in the continental polar atmosphere is generally stratiform and convective mixing is usually insignificant. Kahl *et al.* (1989) conclude that sensitivity due to differences in gridded meteorological data bases, i.e. the input wind fields, an indicator for errors in the wind fields, can be larger than the sensitivity due to different trajectory calculation methods. An additional problem is the fact that in the trajectory method not the moisture itself but an air parcel containing moisture is traced which also complicates the position-finding of the region where moisture actually enters the air parcel. Possible replacement of moisture through cycles of condensation and evaporation is not taken into account. We nevertheless think that the computed trajectories can give a reasonable estimate of the source regions of Antarctic moisture, but must be interpreted with care.

1.5 Overview

This thesis addresses the interaction between the Antarctic snow surface and the overlaying atmosphere. This interaction is studied mainly using data from the Automatic Weather Stations operated by IMAU, with additional data from the European Centre for Medium Range Weather Forecast Numerical Weather Prediction model and the Royal Netherlands Meteorological Institute (KNMI) trajectory model. Goals pursued in this thesis are:

- To study the climatological conditions in DML, to increase our understanding of the processes that influence the surface mass balance and energy budget and to aid the search for an EPICA deep drilling site in DML.
- To study the spatial and temporal variability of the surface energy budget to gain insight in the interaction between the snow surface and the atmosphere.
- To study the conditions in which snowfall generally occurs and the source regions of the moisture of the deposited snow for several deep drilling locations on the Antarctic continent.

Most chapters are based on papers (listed at the end of this thesis) and are therefore reasonably self-contained, and can be read independently of each other. This results,

however, in some overlap between the different chapters.

Chapter 2 gives a detailed description of the surface albedo of Antarctic snow and blue ice as measured in January 1998. Surface albedo is an important parameter in the surface energy budget as will be discussed in Chapters 3 and 5. This chapter discusses the effect of changing grain size and number of impurities on the albedo and presents improvements to the methods used for retrieving a surface albedo from satellite data.

Chapter 3 describes the meteorological conditions on Berkner Island over a six-year period. The meteorological data from the AWS are compared with nearby stations and used to determine the surface energy budget. The results, especially the mass balance measurements will aid in the interpretation of an ice core that BAS staff will drill close to the AWS in the near future.

Chapter 4 describes the meteorological conditions in DML and uses meteorological data from eight AWS. This makes it possible to study not only the temporal variability but also the spatial variability in the meteorological conditions.

Chapter 5 uses the meteorological data described in Chapter 4 to determine the surface energy budget in DML. The temporal and spatial variability is described and results are compared with energy balances presented in the literature for other Antarctic locations.

Chapter 6 describes moisture sources of precipitation falling at AWS 9, close to DML05, the EPICA drilling location in DML in 1998. The source regions are determined using backward air parcel trajectories and 3-dimensional wind fields and snowfall from the ECMWF Numerical Weather Prediction model. The model snowfall is compared with AWS data from AWS 8 and 9.

Chapter 7 presents the moisture source regions of precipitation at five drilling locations in Antarctica (Byrd, DML05 (AWS 9), Dome C, Dome F and Vostok). The moisture sources are determined using backward air parcel trajectories and 15-year ECMWF Re-analysis Archive (ERA-15) data to obtain a fifteen-year record. Furthermore, spatial and temporal variations in source regions are discussed.

Chapter 2

Surface albedo measurements over snow and blue ice in TM bands 2 and 4 in Dronning Maud Land, Antarctica

Summary

Ground-based observations of broadband, narrowband (in Landsat thematic mapper bands 2, 0.52 - 0.60 μm , and 4, 0.76 - 0.90 μm), and bidirectional reflectance are used to study the albedo of blue ice and snow. The measured broadband albedos for blue ice and snow are 0.60 and 0.78, respectively. The narrowband albedos in bands 2 and 4 for snow are 0.97 and 0.86, respectively, and for blue ice are 0.87 and 0.51, respectively. The measurements are point values and used to verify existing weighting functions between the broadband and narrowband albedos. Blue ice data do not comply with the existing functions. Furthermore, a new function for blue ice is derived. A simple two stream model is used to illustrate the behaviour of the snow and ice albedo as a function of reflection and absorption. The bidirectional reflectance measurements are used to derive bidirectional reflectance distribution functions (BRDFs) for snow and blue ice. The BRDF of blue ice exhibits a maximum brightening in the forward limb around a zenith angle, close to the solar zenith angle indicating specular reflectance of blue ice which is not visible for snow and glacier ice surfaces.

¹This chapter is based on: Reijmer, C.H., R. Bintanja and W. Greuell, 2001. Surface albedo measurements over snow and blue ice in thematic mapper bands 2 and 4 in Dronning Maud Land, Antarctica, *J. Geophys. Res.*, **106**(D9), 9661–9672.

2.1 Introduction

In spite of all the effort put into Antarctic meteorological and glaciological research in recent years, surprisingly little is known about the spatial and temporal distribution of the surface energy balance. This constitutes a significant gap in our understanding of the Antarctic climate. The surface energy balance is of great importance for the near-surface climate and the mass balance through, e.g., the katabatic flow, which is forced when the net radiation at the surface is negative, and surface sublimation. The calculated energy balances are usually limited to single stations (Carroll, 1982; King *et al.*, 1996; Reijmer *et al.*, 1999a), and measuring periods are usually limited (Bintanja, 2000). Satellite remote sensing has the possibility to overcome the problem of scale and remoteness of the Antarctic continent.

In recent years, satellite remote sensing has become a major contributor to our knowledge of physical properties of snow and ice, through, e.g., surface classification studies (Boresjö-Bronge and Bronge, 1999), radar altimetry measurements (Herzfeld and Matassa, 1999), brightness (surface) temperature estimations (Orheim and Lucchitta, 1988), and albedo measurements (Knap and Oerlemans, 1996; Reijmer *et al.*, 1999b). Surface temperature and albedo are two important parameters necessary to derive the surface energy balance from satellite measurements. In this study we will focus on the albedo.

The instruments on board satellites measure radiation in distinct wavelength intervals and in one specific direction. In order to calculate the surface albedo from satellite measurements one needs to correct for the intervening atmosphere and for the anisotropic reflection of the surface and have a method to convert the satellite-measured narrowband albedos to a broadband albedo over the solar spectrum. The latter two problems will be addressed in this chapter for snow and blue ice surfaces using in situ measurements of narrowband, broadband and bidirectional albedos. These measurements were carried out during a detailed glaciological and meteorological experiment in the vicinity of a blue ice area in the Heimefrontfjella, Antarctica (Figure 2.1) during the austral summer of 1997-98 (Bintanja *et al.*, 1998; Bintanja and Reijmer, 2001). The goal of this experiment was to understand more thoroughly the spatial distribution of the surface mass and energy balance and the associated processes in the atmospheric boundary layer over Antarctica.

The conversion from narrow to broadband albedo for snow and glacier ice has been addressed by several authors (Duguay and LeDrew, 1992; Knap *et al.*, 1999). Our measurements over blue ice data can possibly generalize the weighting functions developed over other types of ice and snow presented in the literature. Ice and snow do not reflect radiation isotropically, but when no knowledge is available of how the surface reflects radiation, the isotropic assumption is made. However, this assumption can cause considerable deviations of the calculated albedo compared to the actual albedo as shown by Knap and Reijmer (1998) and Greuell and de Ruyter de Wildt (1999) for glacier ice and Warren *et al.* (1998) for snow. In this chapter, measurements of bidirectional reflectance of blue ice and snow are described.

Blue ice areas are areas in Antarctica where the top ~80 m of firn has disappeared and bare ice is exposed (Bintanja, 1999). These areas appear light blue and have a

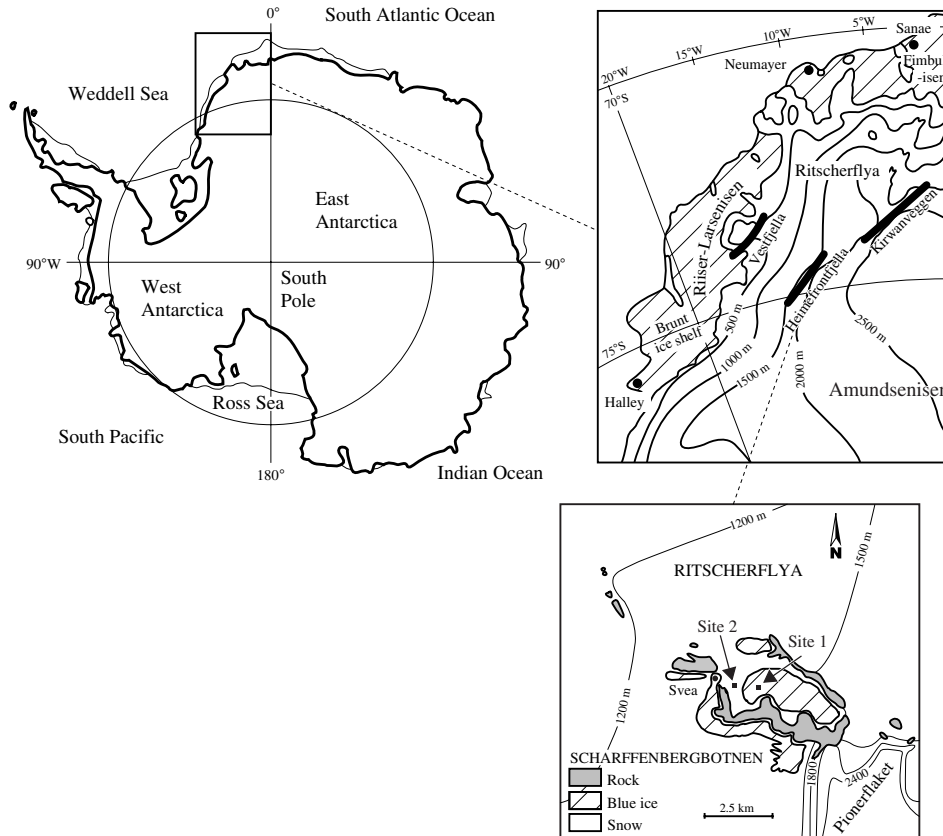


Figure 2.1. Location of the blue ice area in the Heimfrontfjella mountain range in western Dronning Maud Land, Antarctica. The locations of the two measuring sites are marked as well as the location of the Swedish research station Svea (Site 1, blue ice; Site 2, snow).

very smooth, often rippled surface. The mass balance is negative because ablation through sublimation and possibly wind scouring (melt seldom occurs) exceeds accumulation by precipitation and snowdrift deposition. Glacier ice areas also have a negative mass balance, but in contrast to blue ice areas, melt prevails. The surface of glacier ice does not appear blue and is generally not as smooth.

In Section 2.2 the experimental setup and the meteorological conditions during the experiment are described. Section 2.3 describes the measurements of the narrow-band and broadband albedo, and an attempt is made to understand the differences found between snow, blue ice, and glacier ice in terms of absorption and reflection using a simple two-stream model. Section 2.4 describes the bidirectional albedo measurements, which are further used to calculate the bidirectional reflection distribution functions (BRDFs).

2.2 Experimental setup and meteorological conditions

The narrowband, broadband, and bidirectional albedo measurements were carried out using Kipp & Zonen pyranometers and pyrhemometers. The spectral range of the four narrowband pyranometers and two narrowband pyrhemometers used in this study corresponds to bands 2 (0.52 - 0.60 μm , visible radiation) and 4 (0.76 - 0.90 μm , near-infrared radiation) of the Landsat thematic mapper (TM). Channels 2 and 4 were chosen because knowledge of the albedo in these bands allows a fairly accurate estimate of the spectrally integrated albedo, as shown by Knap *et al.* (1999). The narrowband pyranometers measure incoming and reflected irradiance. The mean cosine error of these instruments is $< 2\%$ for solar zenith angles $\theta_s < 60^\circ$. The two broadband pyranometers (CM14) measure the incoming and reflected radiation in the spectral interval 0.31 - 2.8 μm . The cosine error of the CM14 is $< 1\%$ for $\theta_s < 60^\circ$. These instruments were mounted horizontally on a bar at ~ 1.25 m above the surface and data were sampled every 2 minutes. The experimental setup was similar to that used by Knap *et al.* (1999). The instruments were placed over a uniform stretch of blue ice for 23 days (January 1 to 23, 1998) and over a flat snowfield for 13 days (January 23 to February 4, 1998). Figure 2.1 shows the location of the measurements.

The two narrowband pyrhemometers measure reflected radiance in the spectral range corresponding to the spectral range of the narrowband pyranometers. The full opening angle of the pyrhemometers is $5 \pm 0.2^\circ$. To derive the bidirectional reflectance of blue ice and snow the reflected radiance was measured near the pyranometer sites on January 21 and 24, respectively. The two instruments were rigidly connected to each other and were pointed manually toward the surface. The distance between the measured surface and the instruments was ~ 1.5 m and was kept fixed by connecting a thin synthetic wire between a small screw driven into the ice and the pyrhemometers. This resulted in an area viewed by the pyrhemometers varying from a circle with a diameter of 0.13 m at nadir to an oval with a minor axis of 0.13 m and a major axis of 0.50 m at a view zenith angle of 75° off nadir. The surface area covered by the screw and synthetic wire is small (~ 0.0001 m²) compared to the area viewed by the pyrhemometers (~ 0.05 m² at nadir), and the effect of the screw and wire are therefore assumed to be negligible. The experimental setup was similar to that used by Knap and Reijmer (1998). The reflected radiance was measured for five different view zenith angles θ_v and six different relative azimuth angles ϕ (Figure 2.2). The measurements closest to nadir were performed at 15° off nadir and the measurements closest to the solar azimuth were performed at $\phi = 30^\circ$ because of practical reasons. The sample rate of the pyrhemometers was 1 s and each angle was measured for ~ 30 s. Because this method was time-consuming, the assumption was made that the reflectance pattern is symmetric around the solar principal plane and only one half of the reflectance pattern was measured. When the surface does not exhibit structures with distinct orientations owing to, e.g., sastrugi or ripples this assumption is reasonable, as shown by the results of Greuell and de Ruyter de Wildt (1999) for glacier ice. One measurement series took ~ 1 hour. The uncertainty in the view zenith, azimuth, and slope angles is estimated to be $< 5^\circ$, 10° , and 1° , respectively.

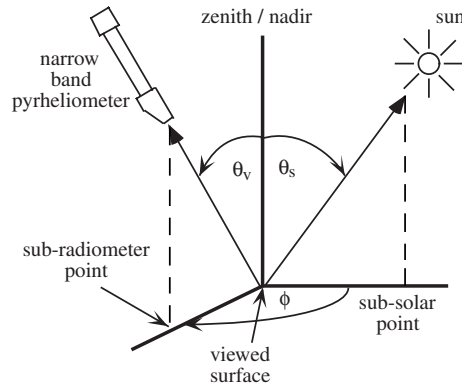


Figure 2.2. Sun surface radiometer geometry. θ_s is the solar zenith angle, θ_v is the view zenith angle, and ϕ is the relative azimuth angle.

The weather during the five-week measuring period was, in general, calm and sunny, interrupted by a few windy and overcast periods with one heavy storm around January 9. Occasionally, during overcast periods small amounts of precipitation occurred that were usually blown away within a few hours. The mean temperature near site 1 was $\sim -8^\circ\text{C}$. During two days in the beginning of January (4 and 5 January) the air temperature rose above the melting point for a few hours causing melt on the surface of the blue ice area. The bidirectional reflectance measurements were performed under clear-sky conditions. The meteorological conditions during the measuring period are described more extensively by Bintanja (2000, 2001).

2.3 Narrow and broadband albedo of blue ice and snow

In this section the narrow and broadband albedo measurements over blue ice and snow will be described. A simple two-stream model is used to explain differences in optical properties of snow, blue ice, and glacier ice. Finally, the measurements will be used to infer if the weighting functions of Duguay and LeDrew (1992), Gratton *et al.* (1993), and Knap *et al.* (1999) for snow and glacier ice are more generally valid.

2.3.1 Measurements

The narrow and broadband albedos were measured over blue ice and snow. To ensure that measuring conditions are similar to the conditions in which satellite images are acquired, periods were selected during which little to no cloud cover was present and θ_s was $< 60^\circ$. The length of these periods on individual days ranges from 0.5 to 7 hours. This resulted in ten periods over blue ice and eight periods over snow. Figure 2.3 presents narrowband albedos α_2 and α_4 (TM band 2 and 4), and broadband albedos α calculated on the basis of irradiances averaged over these periods as a function of time. It shows that the variability in the narrow and broadband albedo

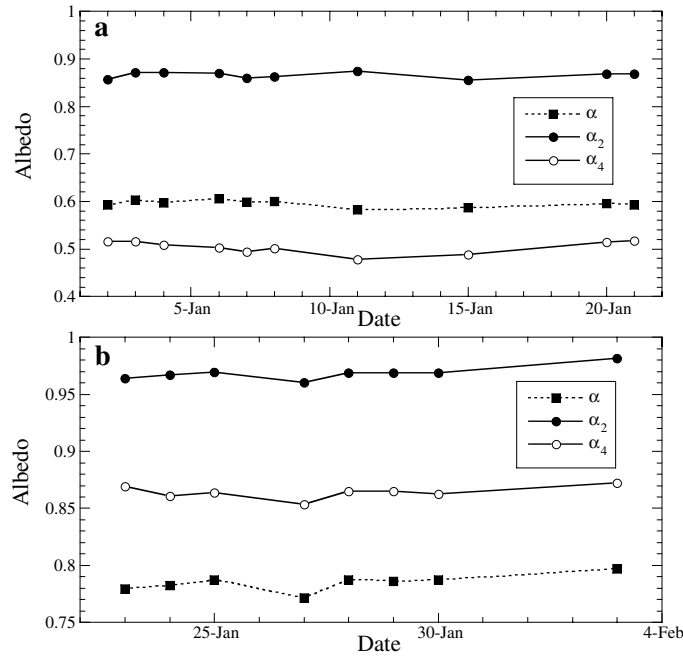


Figure 2.3. Measurements of α_2 (thematic mapper (TM) 2), α_4 (TM 4), and α (broadband) over a uniform stretch of (a) blue ice and (b) snow. Each data point refers to a period of several hours with little to no cloud cover and a solar zenith angle $< 60^\circ$.

of blue ice and snow is small. The observed variability is explained by small changes in surface texture (e.g., remains of snowfall events and meltwater) and small differences in solar zenith angle from one period to another.

The averaged α for blue ice is 0.60 and falls within the range (0.56 - 0.69) found by King and Turner (1997) and Bintanja (1999). The albedo of this particular blue ice area ranges from 0.54 to 0.61, measured with a hand-held albedometer. Variations in blue ice albedo are caused by differences in amount of air bubbles in the ice (Warren *et al.*, 1993). The more air bubbles there are, the more backscattering and the higher the albedo. The mean α for snow is 0.78. Bintanja (2000) found an albedo of 0.79 on a nearby snow field during the same period, and Bintanja and van den Broeke (1995) found a slightly higher albedo (0.81) in their experiment in the same area in the austral summer of 1992-93. These values fall within the usual range of snow albedos.

For snow, α_2 and α_4 are 0.97 and 0.86, respectively, and are higher than α . These values are comparable to the snow measurements of Winther (1994), Grenfell *et al.* (1994), and Knap *et al.* (1999). The lower broadband albedo compared to the narrow-band albedo is caused by the steep decline of the snow albedo in the near-infrared region (between 1.0 and 1.5 μm) (Figure 2.4). The contrast between the shorter wavelengths (among which are α_2 and α_4) and the longer wavelengths is such that for

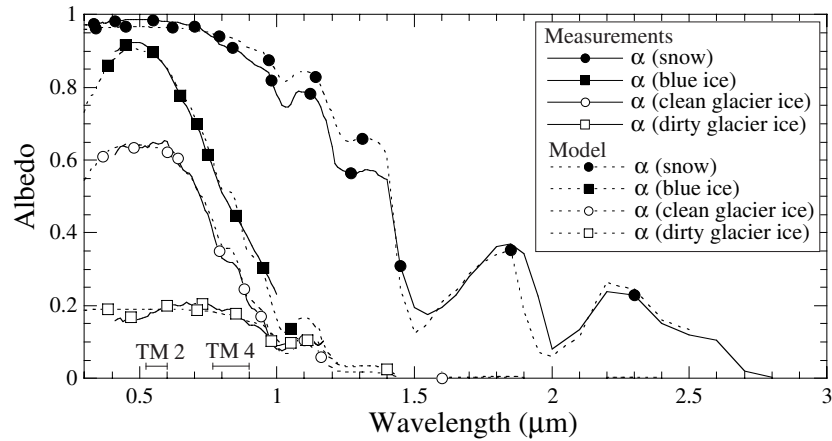


Figure 2.4. Measured spectral albedo curves of snow (Grenfell *et al.*, 1994), blue ice (Warren *et al.*, 1993) and glacier ice (Zeng *et al.*, 1984) (solid lines) and modelled spectral albedo curves of snow, blue ice, and glacier ice, using a simple two-stream model (dotted lines).

snow, $\alpha < \alpha_4 < \alpha_2$. The mean α_2 and α_4 for blue ice are 0.87 and 0.51, respectively, α_2 being higher and α_4 being lower than α . For blue ice, α_2 and α_4 are clearly lower than α_2 and α_4 for snow. These results are in agreement with spectral albedo measurements of Warren *et al.* (1993). As with snow, the albedo in the visible region is high, but toward the near-infrared the steep decline to lower values occurs at smaller wavelengths compared to snow. As a result, α_2 is representative of the shorter wavelengths and α_4 is representative of the longer wavelengths and $\alpha_4 < \alpha < \alpha_2$ for blue ice.

The spectral albedo of blue ice also differs significantly from the spectral albedo of (melting) glacier ice. Knap *et al.* (1999) present measurements of α_2 , α_4 , and α of glacier ice with different amounts of fine-grained material, debris, and meltwater on the surface measured over the Morteratsch glacier, Switzerland. In general, the broad and narrowband albedos of glacier ice are lower than those of blue ice and snow. The debris and fine-grained material increase the absorption, resulting in a lowering of the spectral albedo. This effect is smallest in the near-infrared part of the spectrum because the absorption of solar radiation in pure ice increases with wavelength (Grenfell and Perovich, 1981). Warren and Wiscombe (1980) and Warren (1982) describe this for snow, but the effect is most likely similar for ice. Thus α_2 of glacier ice decreases compared to clean ice and decreases more than α_4 , resulting in $\alpha \leq \alpha_4 < \alpha_2$, which is similar to snow. According to our measurements and those presented by Knap *et al.* (1999), α_4/α of snow and glacier ice varies between 1 and 1.2, while for blue ice, α_4/α varies between 0.8 and 0.9. Blue ice and glacier ice have comparable ratios of α_2/α , mostly varying between 1.35 and 1.5. For snow, α_2/α mostly varies between 1.1 and 1.35. These differences can be explained by the impurities in the snow and glacier ice and grain size differences as will be discussed in Section 2.3.2.

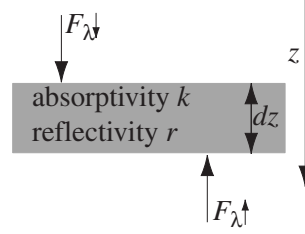


Figure 2.5. Diagram of the two-stream approximation of radiative transfer in a homogeneous, horizontally layered medium with material quantities k and r .

2.3.2 A simple two-stream model

The two-stream radiative model is a conceptually very simple model to describe radiative transfer in snow and ice (see e.g., Liljequist (1956) and Schlatter (1972)). It treats radiation as diffuse and does not explicitly compute scattering by individual particles or consider different grain sizes. This makes the model very useful in fitting albedo measurements. However, to model the spectral albedo explicitly as a function of grain sizes, water content, and/or solar elevation, a more sophisticated model is necessary, e.g., the models of Wiscombe and Warren (1980) and Warren and Wiscombe (1980). Full modelling of the surface albedo is beyond the scope of this study. Our goal is merely to illustrate the qualitative behaviour of the snow and ice albedo with changing absorption and reflection coefficient. The simple two-stream model is very suitable for this purpose.

The two-stream radiative model considers radiation to be built up of two fluxes normal to an infinitesimal thin layer of thickness dz (Figure 2.5). The upward and downward radiation streams $F_{\lambda\uparrow}$ and $F_{\lambda\downarrow}$ are a function of wavelength λ and can be expressed in terms of the absorptivity k_{λ} and reflectivity r of the medium (both have unit m^{-1}):

$$dF_{\lambda\downarrow} = -k_{\lambda} F_{\lambda\downarrow} dz - r F_{\lambda\downarrow} dz + r F_{\lambda\uparrow} dz, \quad (2.1)$$

$$dF_{\lambda\uparrow} = k_{\lambda} F_{\lambda\uparrow} dz + r F_{\lambda\uparrow} dz - r F_{\lambda\downarrow} dz. \quad (2.2)$$

When assuming a homogeneous medium in which k_{λ} and r are constant and choosing the boundary conditions $F_{\lambda\downarrow}(z_{surf}) = F_{\lambda,surf\downarrow}$ and $F_{\lambda\downarrow}(\infty) = 0$, the solutions of these equations are:

$$F_{\lambda\downarrow}(z) = F_{\lambda,surf\downarrow} e^{-\mu_{\lambda} z}, \quad (2.3)$$

$$F_{\lambda\uparrow}(z) = \alpha_{\lambda} F_{\lambda,surf\downarrow} e^{-\mu_{\lambda} z}, \quad (2.4)$$

in which μ_{λ} is the extinction coefficient, α_{λ} is the spectral surface albedo and $F_{\lambda,surf\downarrow}$ is the downward radiative flux at the surface. The extinction coefficient and the surface albedo are a function of λ and can be expressed in terms of k_{λ} and r :

$$\mu_{\lambda} = \sqrt{k_{\lambda}^2 + 2 r k_{\lambda}}, \quad (2.5)$$

$$\alpha_{\lambda} = \frac{k_{\lambda} + r - \mu_{\lambda}}{r}. \quad (2.6)$$

Table 2.1. Results of the least square method fitting of model results to measurements.

Surface	C (m^{-1})	r (m^{-1})	σ_{res}
Snow ^a	0.8	1430.	0.399
Blue ice ^b	0.0	9.5	0.074
Clean glacier ice ^c	0.4	4.5	0.059
Dirty glacier ice ^c	18.0	10.5	0.051

Notes: C , constant added to the absorption coefficient k_λ independent of wavelength; r , reflection coefficient; σ_{res} , root mean square difference between the model fit and the measurements.

References: a, Grenfell *et al.* (1994); b, Warren *et al.* (1993); c, Zeng *et al.* (1984).

The absorption coefficient k_λ of snow or ice without impurities depends strongly on wavelength and a little on the structure of the material through the density ρ_m . Impurities in the form of debris and fine-grained material are assumed to be gray absorbers and can be expressed by a constant C ($\geq 0 \text{ m}^{-1}$), independent of λ , added to k_λ : $k_\lambda = (\rho_m/\rho_i) k_{\lambda i} + C$, in which ρ_i is the density of ice and $k_{\lambda i}$ is the absorption coefficient of ice. The reflection coefficient r does not depend on wavelength but is strongly influenced by grain size and deviations from a pure crystal structure (e.g., boundaries between grains and boundaries between ice and air). It can be loosely related to an effective grain size, which means that r is large for fresh snow, decreases for older snow, and is even smaller for ice. To model μ_λ and α_λ , the measurements of k_λ of Perovich and Govoni (1991), Grenfell and Perovich (1981), and Kou *et al.* (1993) are used. They measured k_λ of bubble-free ice between wavelengths 0.25 to 0.4 μm , 0.4 to 1.4 μm and 1.4 to 2.5 μm , respectively.

Using r and C as tuning parameters, it is possible to make a reasonable approximation of the spectral albedo of snow, blue ice, and glacier ice. Figure 2.4 shows measured albedo spectra for snow (Grenfell *et al.*, 1994), blue ice (Warren *et al.*, 1993), and glacier ice (Zeng *et al.*, 1984). The best fit of the model to the measurements is evaluated using the least squares method and presented in Figure 2.4 and Table 2.1. Both show that the fits are fairly good. Under the assumption that glacier ice and blue ice have approximately the same size distribution of bubbles ($r_{glacier\ ice} \approx r_{blue\ ice}$), differences in spectral albedo are caused by morainic material. The influence of morainic material would be an increase in absorption ($C > 0 \text{ m}^{-1}$). This effect on the absorption is smallest for the longer wavelengths where ice itself becomes a great absorber (Warren and Wiscombe, 1980; Warren, 1982). For glacier ice, r is indeed of the same order of magnitude as $r_{blue\ ice}$, and C for dirty glacier ice is much larger than C for clean glacier ice and snow. Furthermore, $r_{blue\ ice}$ and $r_{glacier\ ice}$ are much smaller than r_{snow} owing to the larger grain size of ice compared to snow. This effect is largest in the near-infrared wavelengths.

Figure 2.6 presents the best fit of the model to the measurements of α_2 and α_4 as a function of r and C for blue ice, snow, and glacier ice. For glacier ice and snow the data from Knap *et al.* (1999) are used. It shows that Antarctic snow and blue ice are very clean surfaces ($C = 0 \text{ m}^{-1}$), and the differences between these surfaces

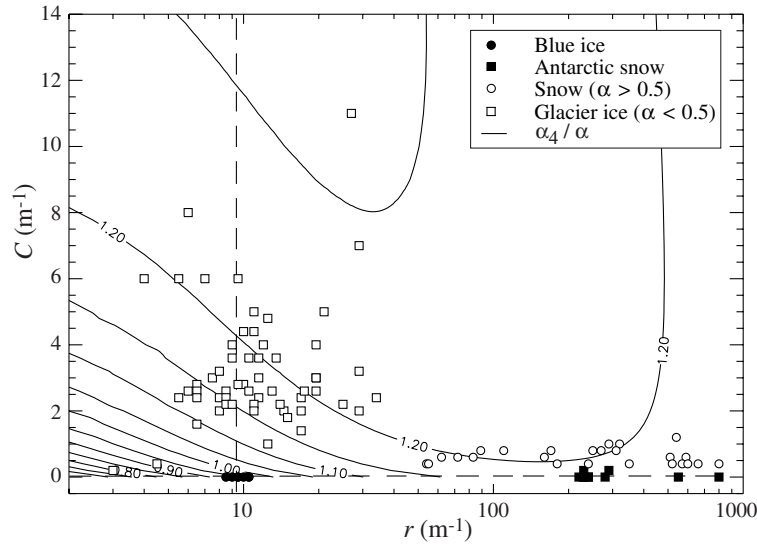


Figure 2.6. Best fit of the model to the measurements of α_2 and α_4 for snow and blue ice, and the snow and glacier ice measurements of Knap et al. (1999) measured over the Morteratsch glacier, Switzerland, in terms of the reflection coefficient r (on a logarithmic scale) and constant added to the absorption C (dots). The lines are the ratio of α_4 to α in the model as a function of r and C .

are explained by different density and grain sizes. Snow on glacier ice is not as clean as Antarctic snow, although C is still small ($C < 2 \text{ m}^{-1}$). This means that the differences in the spectral curves and thus the differences in α_2 and especially α_4 of snow and blue ice are mainly caused by density and grain size differences. For blue ice r is $\sim 10 \text{ m}^{-1}$, and for snow, r is larger than 50 m^{-1} . For glacier ice most points lie between $r = 5 - 30 \text{ m}^{-1}$ and $C = 1 - 8 \text{ m}^{-1}$. A substantial part of the differences found between blue ice and glacier ice is explained by small amounts of morainic material ($C > 0 \text{ m}^{-1}$), which affects mainly α at small λ , which explains the difference found between α_2 of glacier ice and α_2 of blue ice. The figure also shows the ratio α_4/α as a function of r and C to express the different nature of the spectral albedo curves of snow, blue ice, and glacier ice. In the measurements the ratio α_4/α is larger than 1 for glacier ice and snow and smaller than 1 for blue ice. The model is able to reproduce this difference, although the ratios in the model are larger than in the measurements owing to an underestimation of the broadband albedo in this model. The underestimation results from an underestimation of the albedo in the infrared wavelengths when a best fit is made through the two TM bands, which lie in the visible and near-infrared part of the spectrum.

2.3.3 Narrow to broadband conversion

Multispectral scanners on board satellites measure radiation in distinct wavelength intervals. To obtain a broadband albedo, a relationship between the measured nar-

Table 2.2. *Weighting functions for ice and snow presented in the literature.*

Function	Surface
$\alpha = 0.493\alpha_2 + 0.507\alpha_4$	dirty ice ^a
$\alpha = 0.493\alpha_2 + (0.203 + 0.150 \times 0.3) \alpha_4 + 0.154\alpha_7$	clean ice and snow ^a
$\alpha = (0.493 \times 1.12 + 0.203 + 0.150 \times 0.3) \alpha_4 + 0.154\alpha_7$	snow ^a
$\alpha = 0.526\alpha_2 + (0.232 + 0.130 \times 0.63) \alpha_4 + 0.112\alpha_7$	snow ^b

Notes: The indices refer to Landsat TM bands 2, 4, and 7 (2.08 μm - 2.35 μm).
References: a, Gratton *et al.* (1993); b, Duguay and LeDrew (1992)

rowband albedos and the broadband albedo is needed. In recent years several authors have derived such relationships, called weighting functions, for several types of snow and glacier ice surfaces (Duguay and LeDrew, 1992; Gratton *et al.*, 1993; Knap *et al.*, 1999).

Duguay and LeDrew (1992) and Gratton *et al.* (1993) derived weighting functions for snow and glacier ice based on discretization of generalized spectral albedo curves (Table 2.2). These functions calculate the broadband albedo as a linear combination of narrowband albedos. The coefficients in these functions are the ratio of the global irradiance in a specific wavelength band to the global broadband irradiance. When using TM bands 2 and 4, the coefficients also express how representative the TM albedos are for the broader spectral bands they represent. This limits the usefulness of a derived function, resulting in different weighting functions for different types of snow and glacier ice surfaces.

None of the weighting functions derived by Gratton *et al.* (1993) or Duguay and LeDrew (1992) gives satisfactory results for blue ice. The function for dirty glacier ice derived by Gratton *et al.* (1993) severely overestimates the albedo of blue ice. The functions of Gratton *et al.* (1993) derived for clean ice and snow and snow underestimate the albedo of blue ice as well as the albedo of snow. This could be due to the fact that these functions also use TM band 7 (α_7). However, for small grain sizes, when α_7 is largest, the term relating to α_7 is ~ 0.03 (Knap *et al.*, 1999) while the differences found between measured and calculated broadband albedo using the weighting functions are 0.05 to 0.2. The snow function of Duguay and LeDrew (1992) gives reasonable results for snow and slightly overestimates α of blue ice, but again, we neglect the term relating to α_7 .

Since it is not easy to distinguish objectively between different types of glacier ice and snow surfaces in satellite imagery, Knap *et al.* (1999) derived a weighting function valid for snow as well as glacier ice based on measurements acquired on the Morteratsch glacier, Switzerland. On the basis of a multiple linear regression the following fit was derived:

$$\alpha = 0.726 \alpha_2 - 0.322 \alpha_2^2 - 0.051 \alpha_4 + 0.581 \alpha_4^2 . \quad (2.7)$$

Figure 2.7 presents α of snow and blue ice calculated using this equation and the measurements of α_2 and α_4 versus the measured α . The measurements of Knap *et al.* (1999) are included in the figure. Figure 2.7 shows that the weighting function performs well for snow. The broadband albedo is slightly overestimated, but the

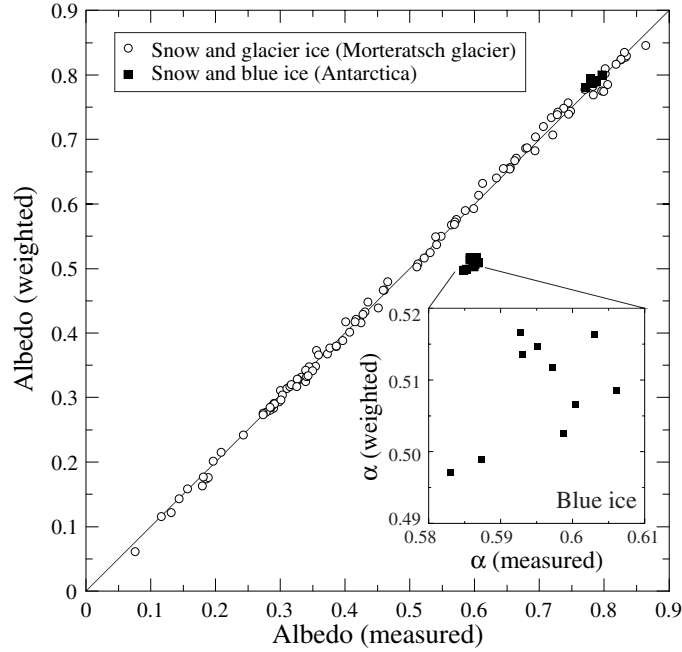


Figure 2.7. Weighted broadband albedo as a function of the measured broadband albedo for an Antarctic snow and blue ice surface (squares) and the measurements of Knap *et al.* (1999) over snow and glacier ice (circles) (Morteratsch glacier, Switzerland). The weighted albedo is calculated using equation (2.7) and the narrowband albedo measurements. The enlargement shows the details of the blue ice albedos.

residual standard deviation σ_{res} is small, $\sigma_{res} = 0.007$, $\sim 1\%$ of the snow albedo. The broadband albedo of blue ice is severely underestimated, $\sim 15\%$ of the blue ice albedo, an order of magnitude larger than for snow. Thus equation (2.7) is not a good approximation of α of blue ice.

It is possible to derive a weighting function valid for snow and blue ice simultaneously from the measurements. However, this function would, in effect, be a straight line between two clusters of points (Figure 2.7). Since it is feasible to distinguish objectively between Antarctic snow and blue ice (Boresjö-Bronge and Bronge, 1999), it is not necessary to determine such a function, but it is useful to derive a weighting function valid for blue ice alone. This function can be used together with the function of Knap *et al.* (1999) to derive broadband albedos over Antarctica where melting ice, all types of snow, and blue ice occur. However, the amount of data points is very limited (10) and the range of measured α , α_2 , and α_4 is small, which limits the usefulness of the function. On the other hand, the range of blue ice α , in general, is limited (0.56 - 0.69) (King and Turner, 1997), and no functions valid for blue ice are available. Therefore, on the basis of multiple linear regression, the following best fit was derived:

$$\alpha = 0.509 \alpha_2 + 0.309 \alpha_4 . \quad (2.8)$$

The linear correlation coefficient r^2 for this regression is high ($r^2 = 0.999$), and σ_{res} is small (0.004). Adding quadratic terms does not improve the fit significantly. Assuming that blue ice areas, in general, have approximately the same spectral signatures, this relationship should be valid for all blue ice areas. This is already indicated by the fact that our measurements are in reasonable agreement with the blue ice measurements of Warren *et al.* (1993) near Mount Howe, Antarctica.

2.4 Bidirectional reflectance of blue ice and snow

Satellites measure radiation reflected by the surface in one specific direction. However, ice and snow surfaces do not reflect radiation isotropically, i.e. in all directions the same. To calculate the albedo from satellite measurements without any knowledge of how the surface reflects radiation, the isotropic assumption is usually made. This assumption can cause considerable deviations of the calculated albedo compared to the actual albedo (Greuell and de Ruyter de Wildt, 1999). Bidirectional reflection distribution functions (BRDFs) are necessary to correct for the anisotropic reflection of the surface. Knap and Reijmer (1998) and Greuell and de Ruyter de Wildt (1999) derived these functions for glacier ice, and Warren *et al.* (1998) derived them for Antarctic snow with sastrugi. In this section, bidirectional reflectance measurements for snow and blue ice are described and used to develop parameterizations of BRDFs for Antarctic snow and blue ice.

2.4.1 Definitions and basic equations

The Sun surface radiometer geometry is defined by four angles: the solar zenith θ_s and azimuth angle ϕ_s , and the view zenith θ_v and azimuth angle ϕ_v relative to the horizontal plane (Figure 2.2). When the surface does not exhibit structures with a distinct orientation due to, e.g., sastrugi or ripples, only the relative azimuth ϕ ($\phi = \phi_s - \phi_v$) and the solar and view zenith angles are relevant. In this study, the relative azimuth angle ϕ is used and subscripts v are omitted.

The surface albedo α is defined as the ratio of the reflected irradiance F_r and incident irradiance F_i ($\alpha = F_r/F_i$). The bidirectional reflectance $\rho(\theta_s, \theta, \phi)$ (reflectance in a specific direction) is defined as:

$$\rho(\theta_s, \theta, \phi) = \frac{I(\theta_s, \theta, \phi)}{F_i}, \quad (2.9)$$

in which $I(\theta_s, \theta, \phi)$ is the reflected radiance (intensity of radiation reflected in a specific direction). For a Lambertian (isotropically reflecting) surface, I is independent of the view angles θ and ϕ , so $\alpha = \pi\rho$. For a fixed solar zenith angle a complete distribution of $\rho(\theta \in [0, \pi/2], \phi \in [0, 2\pi])$ is called a bidirectional reflectance distribution function. Deviations from isotropic reflection are expressed in the anisotropic reflection factor $R(\theta_s, \theta, \phi)$, which is defined as:

$$R(\theta_s, \theta, \phi) = \frac{\rho(\theta_s, \theta, \phi)\pi}{\alpha(\theta_s)}. \quad (2.10)$$

Table 2.3. Details of the bidirectional reflectance measurements.

Surface	α	α_2	α_4	Slope	θ_s	n	Resolution	
							$\Delta\theta$	$\Delta\phi$
Blue ice	0.60	0.87	0.51	1.0°	55° - 56°	30	15°	30°
Snow	0.78	0.97	0.86	3.2°	56° - 57°	30	15°	30°

Notes: Cloud amount was 1/8 for both measurement series but the clouds did not obscure the sun. α , broadband albedo; α_2 , narrowband albedo in TM band 2; α_4 , narrowband albedo in TM band 4; Slope, slope of the surface; θ_s , solar zenith angle; n, the number of measurements per site; $\Delta\theta$, view resolution in zenith direction; $\Delta\phi$, view resolution in azimuth direction.

For a fixed solar zenith angle, R has the property that its integral over the upper half of the hemisphere weighted by its contribution to the upward flux equals unity:

$$\pi^{-1} \int_0^{2\pi} \int_0^{\pi/2} R(\theta_s, \theta, \phi) \sin \theta \cos \theta d\theta d\phi = 1. \quad (2.11)$$

Unless stated otherwise, all these variables refer to TM bands 2 or 4.

2.4.2 Measurements

The bidirectional reflection and band albedo measurements were performed close to one another, within a range of ~ 5 m. The blue ice and snow surfaces were uniform flat, and the snow surface consisted of old wind-hardened snow. The homogeneity of both surfaces makes it possible to use α_2 and α_4 from the band measurements instead of calculating them from the bidirectional reflectance measurements. Table 2.3 presents more details of the bidirectional reflectance measurements. Since the slope of the measured surfaces was less than the uncertainty in the measurements, the horizontal polar coordinates were assumed to be equal to the surface-parallel polar coordinates.

To obtain individual BRDFs, measured reflected radiances I were converted into bidirectional reflectance ρ by means of equation (2.9) and using the simultaneous band measurements of F_i close to the BRDF measuring site. The number of radiance measurements (30) is not very large and makes it difficult to construct a complete BRDF using standard interpolation and extrapolation techniques. Therefore, following the method of Lindsay and Rothrock (1994) and Greuell and de Ruyter de Wildt (1999), a parameterization of the bidirectional reflectance of the following form was used:

$$\rho = a_0 + a_1 g_1 + a_2 g_2 + a_3 g_3, \quad (2.12)$$

where g_1 , g_2 , and g_3 are functions of the view angles θ and ϕ . The solar zenith angle was taken constant and is part of the coefficients a_i . Functions of the form $g_i = h_j p_k q_i$, with h_j and p_k equal to 1, θ , $\sin \theta$, or $\cos \theta$, and $q_1 = 1$, $q_2 = \cos \phi$, and $q_3 = \cos^2 \phi$ were tested. These forms of g_i imply symmetry around the solar principal plane and are similar to the functions tested by Greuell and de Ruyter de Wildt (1999). Owing to the specular properties of blue ice, g_3 was replaced by an exponen-

Table 2.4. Functions g_i (equation (2.12)) of the best fit and several fits from the literature.

	g_1	g_2	g_3	σ_{res}	
				TM 2	TM 4
<i>Blue ice</i>					
Best fit	$\cos \theta \sin \theta$	$\theta \sin \theta \cos \phi$	$e^{b_1 \theta^2} e^{-b_2 \psi^2}$	0.0242	0.0149
Fit a	$\cos \theta$	$\theta^2 \cos \phi$	$\theta^2 \cos^2 \phi$	0.0373	0.0279
Fit b	$(1 - \cos \theta)$	$(1 - \cos \theta)(-\cos \phi)$	$(1 - \cos \theta)(2 \cos^2 \phi - 1)$	0.0371	0.0276
Fit c	$\sin^2 \theta \sin^2 \phi$	$\sin \theta \cos \phi$	$\sin^2 \theta \cos^2 \phi$	0.0381	0.0294
<i>Snow</i>					
Best fit	θ^2	$\theta^2 \cos \phi$	$\theta^2 \cos^2 \phi$	0.0356	0.0314
Fit a	$\cos \theta$	$\theta^2 \cos \phi$	$\theta^2 \cos^2 \phi$	0.0359	0.0315
Fit b	$(1 - \cos \theta)$	$(1 - \cos \theta)(-\cos \phi)$	$(1 - \cos \theta)(2 \cos^2 \phi - 1)$	0.0359	0.0316
Fit c	$\sin^2 \theta \sin^2 \phi$	$\sin \theta \cos \phi$	$\sin^2 \theta \cos^2 \phi$	0.0445	0.0436

Notes: The performance of the fits is expressed in residual standard deviation σ_{res} for TM bands 2 and 4 for snow and blue ice.

References: Fit a, Greuell and de Ruyter de Wildt (1999); Fit b, Warren *et al.* (1998); Fit c, Lindsay and Rothrock (1994); Knap and Reijmer (1998)

tial function of the form $e^{b_1 \theta^2} e^{-b_2 \psi^2}$ (Meister *et al.*, 1998), where ψ is the relative angle to the specular direction and b_1 and b_2 are constants determining the width and intensity of the peak.

The best fit to the data was found by minimizing the residual standard deviation (σ_{res}) in ρ on the basis of multiple linear regression. Table 2.4 presents the performance of the best fit and several fits of other functions from the literature. The table shows that the best fit for blue ice is significantly better than the functions from the literature, which were used for glacier ice (Greuell and de Ruyter de Wildt, 1999; Knap and Reijmer, 1998) and snow (Warren *et al.*, 1998). The explained variance of the best fit is 79.9% and 92.1% for TM bands 2 and 4, respectively. The other fits perform 20% to 30% less. Owing to the exponential function, the best fit is the only one able to reproduce the maximum in ρ in the forward limb around $\theta = 60^\circ$. Not using the exponential function but a function with $g_3 = \cos^2 \phi$ results in 56.4% and 74.0% explained variance in TM bands 2 and 4, respectively, which is similar to the other functions. For snow the best fit and the fits presented by Greuell and de Ruyter de Wildt (1999) and Warren *et al.* (1998) do not differ significantly in performance, and the explained variance is $\sim 81\%$ and 90% for TM bands 2 and 4, respectively. The functions of Knap and Reijmer (1998) perform less well, with 10% less explained variance in both channels.

Once the functions g_i are determined, the coefficients a_i are calculated for each wavelength band and surface type (Table 2.5). The resulting four parameterizations were verified against the normalization condition (equation (2.11)). Unfortunately, the parameterized BRDFs did not satisfy this condition. The integral values varied between 1.15 and 1.27. The anisotropic reflection factors of each series were systematically adjusted so that the integral values equal unity. Knap and Reijmer (1998) experienced the same problem. They argued that the deviation from unity is caused by the different size of the areas viewed by the pyranometer and pyrliometer in

Table 2.5. Coefficients a_i multiplied by π for the best fit as presented in Table 2.4.

TM	a_0	a_1	a_2	a_3
<i>Blue ice</i>				
2	0.924	0.186	-0.050	0.00002
4	0.948	0.121	-0.100	0.00003
<i>Snow</i>				
2	0.996	-0.032	-0.082	0.075
4	0.991	-0.035	-0.113	0.095

combination with small-scale variations in reflectance. However, in this case the areas are very homogeneous, with little small-scale variation. The deviations are most probably explained by calibration problems.

Figure 2.8 presents the measured and parameterized BRDF for blue ice and snow in both wavelength bands as polar diagrams. The figure shows that although the number of measuring points is restricted, the parameterization is able to reproduce the main features of the BRDFs. It shows a strong maximum in the forward limb around $\theta = 60^\circ$ for blue ice (Figures 2.8a and 2.8b). This maximum is also found in the sunglint pattern from ocean water (Krotkov and Vasilkov, 2000). The minimum around the nadir and the maximum in the forward limb are not seen in the measurements and are a result of the parameterization and the lack of data around nadir and for $\theta > 75^\circ$. Limb brightening in all directions as seen for glacier ice (Knap and Reijmer, 1998; Greuell and de Ruyter de Wildt, 1999) is not found for blue ice or snow. The bidirectional reflectance of blue ice and snow shows limb darkening in the backward limb as seen for ocean waters (Morel *et al.*, 1995). The anisotropic reflectance factor R for blue ice ranges from 0.84 to 1.36 in TM band 2 and from 0.78 to 1.63 in TM band 4. For snow, R ranges from 0.85 to 1.3 in TM band 2 and from 0.82 to 1.41 in TM band 4.

The BRDF of snow (Figures 2.8c and 2.8d) compares reasonably well with other snow BRDFs (Suttles *et al.*, 1988; Warren *et al.*, 1998), although it does not exhibit the minimum around the zenith. This can be explained by the spatial resolution of the measurements. The pattern shows a brightening from the backward to the forward limb also seen by Suttles *et al.* (1988) and Warren *et al.* (1998). Different solar zenith angles, different wavelength bands, and different snow conditions on the various measurement sites can explain differences with respect to other measurements. A smaller solar zenith angle tends to decrease the anisotropy (Warren *et al.*, 1998). An increasing wavelength increases the anisotropic reflection as seen by Knap and Reijmer (1998) and Greuell and de Ruyter de Wildt (1999) and also visible in Figure 2.8 for both blue ice and snow. This is due to the increase of the absorption coefficient of pure ice between 0.47 and 1.03 μm (Grenfell and Perovich, 1981; Greuell and de Ruyter de Wildt, 1999). When snow gets older, the grain size increases, which increases the anisotropic reflection (Warren *et al.*, 1998).

Figure 2.9 illustrates the quality of the parameterizations. The residual standard deviation in the computed albedo (parameterization minus measurement) is plotted as a function of the view angles in a polar diagram. For blue ice, σ_{res} is small

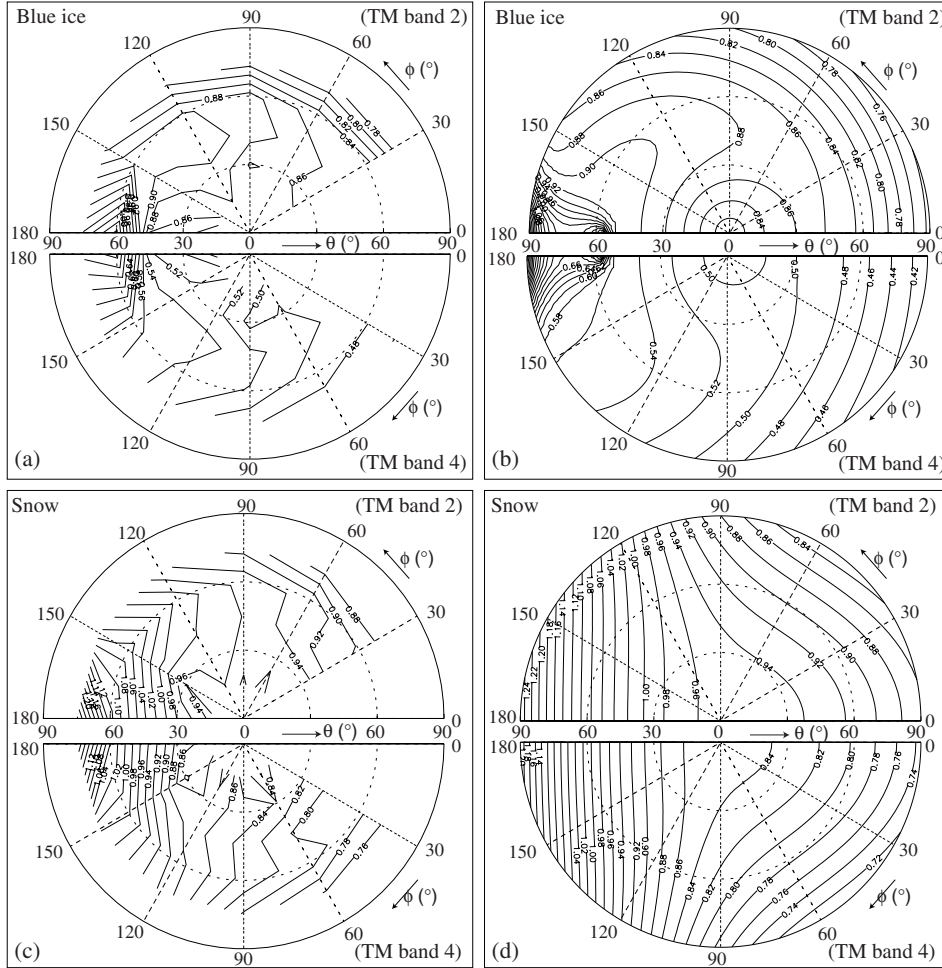


Figure 2.8. Measured bidirectional reflectance $\pi\rho$ for (a) blue ice and (c) snow and parameterized bidirectional reflectance $\pi\rho$ for (b) blue ice and (d) snow using the best fit (Table 2.4). The radial coordinate represents the view zenith angle θ , the azimuthal coordinate represents the relative Sun radiometer azimuth angle ϕ . The Sun is in $\phi = 0^\circ$. The corresponding measured band albedos are presented in Table 2.3. The solar zenith angle varied between 55° and 56° for blue ice and 56° and 57° for snow.

and varies between -0.04 and 0.05 . The maximum is slightly overestimated as well as the reflectance in the limbs. For snow, σ_{res} is larger and varies between -0.15 and 0.08 . The parameterization overestimates the reflectance in the forward limb between $\phi = 100^\circ$ and 160° and underestimates the reflectance around $\phi = 180^\circ$.

Greuell and de Ruyter de Wildt (1999) developed one parameterization for a melting glacier surface for different solar zenith angles and albedos. With two BRDFs measured over two different surfaces at approximately the same solar zenith angle,

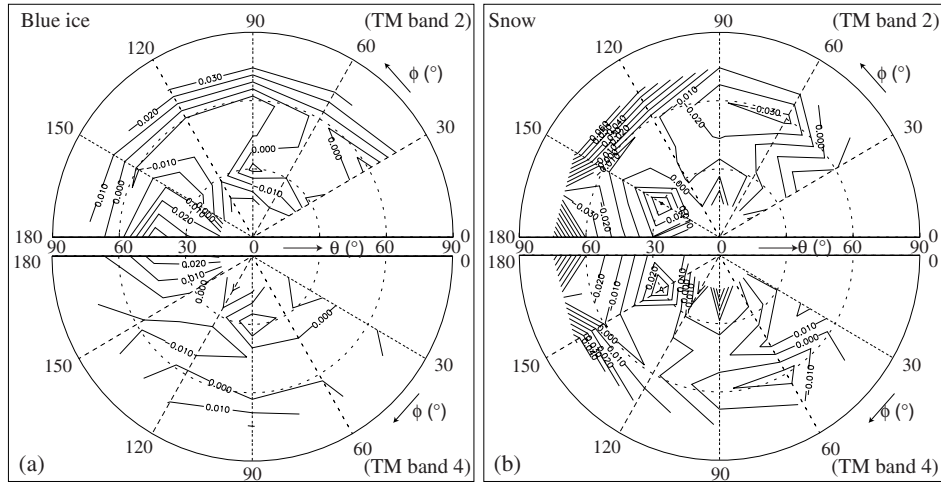


Figure 2.9. Residual standard deviation in the parameterized bidirectional reflectance $\pi\rho$ as a function of the view angles for (a) blue ice and (b) snow.

it is impossible to develop such a parameterization for our data set, as the number of measurements is too small. The above presented results also show that it is not possible to use the generalized parameterization for glacier ice presented by Greuell and de Ruyter de Wildt (1999). Our best fits have different functions and would need different coefficients owing to the different nature of the reflective patterns of snow and blue ice compared to glacier ice.

2.5 Concluding remarks

This study presents detailed albedo measurements over a snow and blue ice field in Antarctica. The mean measured broadband albedos α of snow and blue ice are 0.78 and 0.60, respectively. Narrowband albedos (α_2 and α_4) were measured in TM bands 2 and 4, resulting in mean α_2 and α_4 of 0.97 and 0.86, respectively, for snow and 0.87 and 0.51, respectively, for blue ice.

A two-stream radiative transfer model is successfully used to simulate the spectral albedos of different kinds of ice and snow surfaces by adjusting only two parameters, the reflection coefficient r and the absorption coefficient C , representing the concentration of morainic material. The values of r and C found this way for blue ice, snow, and clean and dirty glacier ice reflect some properties of the media. Blue ice and Antarctic snow contain negligible amounts of morainic material ($C = 0 \text{ m}^{-1}$). The values of r show that the number of grain boundaries, and of other deviations from a pure crystal structure, is orders of magnitude larger in snow as compared to blue ice and glacier ice.

The measurements were used to test existing weighting functions between the broad and narrowband albedos. The weighting function of Knap *et al.* (1999) works

for snow and glacier ice but not for blue ice. Other functions from the literature (Duguay and LeDrew, 1992; Gratton *et al.*, 1993) are also not able to calculate α of blue ice correctly. A new weighting function was derived to calculate the broadband albedo for blue ice. The range of measurements this function is based on is, however, limited, restricting the usefulness of the function. On the other hand, the total range of blue ice α occurring in nature is relatively small. Together with the function of Knap *et al.* (1999), this allows one to calculate the broadband albedo of the Antarctic continent where melting ice as well as all types of snow and blue ice occur.

The bidirectional reflectance measurements show that the BRDF of blue ice differs significantly from the BRDF of snow and glacier ice and does resemble the BRDF of ocean water owing to the specular properties of blue ice. An exponential function is necessary in the parameterization to represent the maximum in the forward limb. Satellite measurements from near-specular directions are therefore not representative. The measuring site for the blue ice BRDF was reasonable flat. However, in general, blue ice areas are not flat but rippled with a preferred orientation (Bintanja, 1999). In such cases the solar azimuth ϕ_s and the view azimuth ϕ_v must be taken into account and the BRDF of blue ice will change. Although for snow the parameterization functions found by Greuell and de Ruyter de Wildt (1999) for glacier perform almost as good as our best fit, it is not possible to use their generalized equation, which is a function of solar zenith angle and albedo. Their BRDF pattern is fixed by their choice of coefficients, and although our functions are the same, our pattern differs from the glacier ice pattern. To derive generalized equations valid for snow and blue ice, more measurements of BRDFs performed at different solar zenith angles and albedos are necessary. The BRDFs presented here are only useful under conditions similar to ours.

Chapter 3

The annual cycle of meteorological variables and surface energy balance on Berkner Island, Antarctica

Summary

In February 1995 an Automatic Weather Station (AWS) was placed on Thyssen Höhe, the south dome of Berkner Island, Antarctica. A fairly complete six-year meteorological data set of hourly average values was obtained, which is described in this chapter. The mean annual temperature is $\sim -24^{\circ}\text{C}$. Summer temperatures remain below 0°C all the time, so that no melt takes place. The annual mass balance is $\sim +166$ mm water equivalent. Because the AWS is located on a dome, katabatic winds are not active, the wind direction is relatively variable (directional constancy 0.42) and the wind speed relatively low (4.3 m s^{-1}). Annual average variables are compared with data of Filchner station, Recovery AWS and Halley station. The meteorological data are used to determine the surface energy fluxes for a five-year period by using a surface energy balance model. The annual average gain of energy from the sensible heat flux ($+11.2 \text{ W m}^{-2}$) is balanced largely by a negative net radiative flux (-9.8 W m^{-2}) and a small negative latent heat flux (-1.7 W m^{-2}). The annual subsurface flux is small.

¹This chapter is based on: Reijmer, C.H., W. Greuell and J. Oerlemans, 1999. The annual cycle of meteorological variables and the surface energy balance on Berkner Island, Antarctica. *Ann. Glaciol.*, **29**, 49-54. And: Reijmer, C. H., 2000. The climate of Berkner Island as observed using an Automatic Weather Station. *Filchner Ronne Ice Shelf Programme*, **13**, Alfred Wegener Inst. for Polar and Marine Res., Bremerhaven, Germany. 66-71.

3.1 Introduction

In the last two decades about 100 Automatic Weather Stations (AWS) have been deployed in Antarctica (e.g., United States Antarctica Research Program (USARP), Stearns and Weidner (1993)). Considering the vast size of the continent the amount of observations is still limited. To increase the number of surface meteorological data measurements, the use of AWS provides a relative cheap and easy way. An AWS is designed to work for long periods without being serviced and can therefore operate in remote areas and in harsh weather conditions. AWS data have been used to study meteorological processes close to the surface and climatological conditions in several regions of Antarctica (e.g., Allison *et al.* (1993); Bintanja *et al.* (1997)).

This chapter describes the annual and diurnal cycles of meteorological variables and the surface energy fluxes over Berkner Island, Filchner-Ronne ice shelf, Antarctica (Figure 3.1). Several studies have been carried out on the ice cap of Berkner Island within the framework of the Filchner Ronne Ice Shelf Programme (FRISP), a research programme of the Alfred-Wegener Institute for Polar and Marine Research (AWI), Bremerhaven. These range from short-pulse echo sounding to ice core drillings and meteorological measurements (Wagenbach *et al.*, 1994; Oerter, 1995; Gerland *et al.*, 1999). In February 1995, the Institute for Marine and Atmospheric research Utrecht (IMAU) deployed an AWS on the South Dome of the island, with the aim of providing insight into the meteorological conditions on the island, which can facilitate the interpretation of the ice-core analysis.

The station has provided a fairly complete six-year meteorological data set, which is described here and used to determine the surface energy fluxes. This study aims to show that it is feasible to derive a fairly accurate estimate of the surface energy balance from relatively simple meteorological measurements made by an AWS. The advantage of this approach is that estimates of the surface energy budgets can be made over longer periods at remote places.

Section 3.2 briefly describes the location and some technical details of the weather station. Section 3.3 describes the meteorological conditions on Berkner Island on a diurnal to annual time scale, and concludes with two case studies of snow fall events. Section 3.4 presents the energy balance model that is used to calculate the surface fluxes not measured directly by the weather station and describes the resulting surface energy budget. The chapter is concluded with a short summary of the results and some concluding remarks.

3.2 Location and experimental set-up

Berkner Island is a large island completely covered by ice and surrounded by the Filchner-Ronne ice shelf, south of the Weddell Sea, Antarctica (Figure 3.1). The AWS measurements were carried out on Thyssen Höhe, the South Dome of Berkner Island (79.57°S, 45.78°W; 886 m a.s.l.). Observations started on February 12, 1995. The station samples every 6 minutes, calculates hourly average data, transmits these data using an Argos transmitter and also stores the data locally. The AWS is designed to

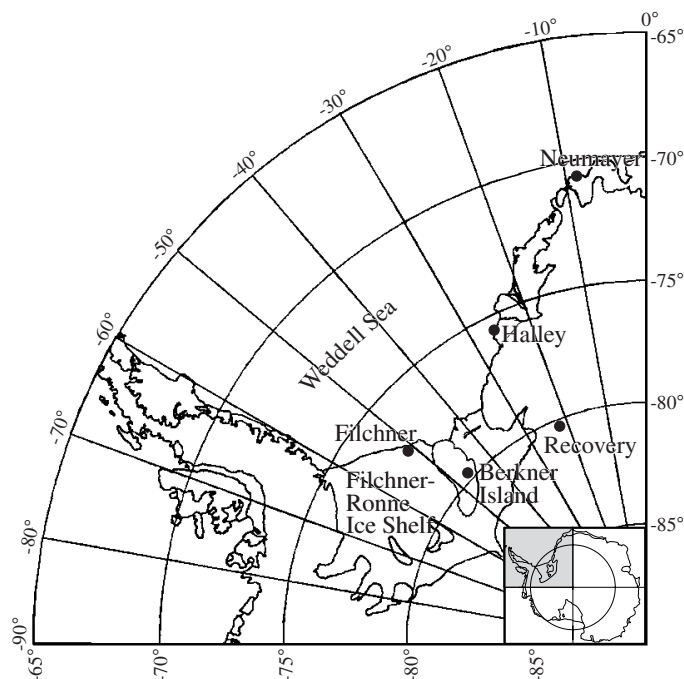


Figure 3.1. Location of the weather stations in the Filchner-Ronne ice shelf area.

work for approximately three years without being serviced. The results reported in this chapter are based on an almost six-year meteorological data set (12-2-1995 to 31-12-2000).

The station consists of a vertical mast placed on a four-legged frame. Near the top of the mast, a horizontal bar is attached on which the air temperature, wind speed, wind direction, instrument height and shortwave incoming radiation sensors are mounted (Figure 3.2). The AWS also measures snow temperature at two depths (initially 0.1 and 1.0 m) and air pressure (mounted inside the electronics box). The instrument height is a measure for the accumulation and is monitored by the station using a sonic altimeter. The AWS is situated in an accumulation zone, so the instrument height is not constant over time. The initial height was ~ 2.95 m. In February 2000 the station was visited by staff of the British Antarctic Survey. The sensors were replaced and the mast raised to obtain a sensor height of ~ 2.90 m.

The accuracy of the sensors was tested in an intercomparison experiment in the Netherlands and near the South Pole before the station was placed on Berkner Island. The sensors are not ventilated, which affects the accuracy of, particularly, the temperature sensor. Problems with the data transmission led to gaps in the data set of a few hours to a few days. About 8% of the data are lost this way. The most serious problems were caused by rime forming on the sensors. This causes the wind speed and wind direction sensors to seize, and shields the instrument height and

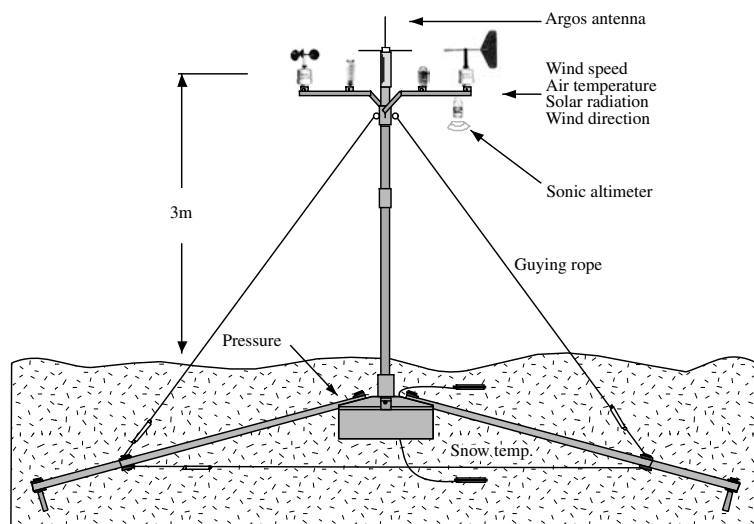


Figure 3.2. Schematic picture of the Automatic Weather Station on Berkner Island.

shortwave radiation sensor. As a result, data from these sensors are unreliable between 4 April 1995 and 30 October 1995 and for some briefer periods. A technical problem resulted in the loss of wind speed data in 2000.

We will compare the meteorological conditions on Berkner Island with the conditions at Filchner station, Halley station and Recovery Glacier AWS. Filchner station was a German summer station on the edge of the Ronne ice shelf (77.1°S, 51.2°W; 20 m a.s.l.). In 1998 a large iceberg, on which the station was located, calved from the Ronne ice shelf and the station was closed. Halley station is a permanently occupied British base on the Brunt Ice Shelf, which is located in the southeastern part of the Weddell Sea region (75.45°S, 26.4°W; 39 m a.s.l.). Meteorological measurements at this station started in 1956. Recovery Glacier AWS was placed on Recovery Glacier, situated south of the Shackleton Range, in 1994 (80.8°S, 22.3°W; 1220 m a.s.l.). For Recovery glacier and Filchner station only data for 1995 were available.

3.3 Meteorological conditions

3.3.1 The annual cycle

Figure 3.3 shows the temporal variations in the daily mean values of air temperature, wind speed, air pressure and instrument height during the six-year period. Table 3.1 shows the annual mean values and extremes (based on hourly averaged values) of the meteorological parameters for the measuring period. The results will be compared with data from Halley station, Recovery Glacier AWS and Filchner station. Table 3.2 summarises the annual mean values for Halley station (based on monthly averaged values), for Recovery Glacier AWS (based on daily averaged values) and

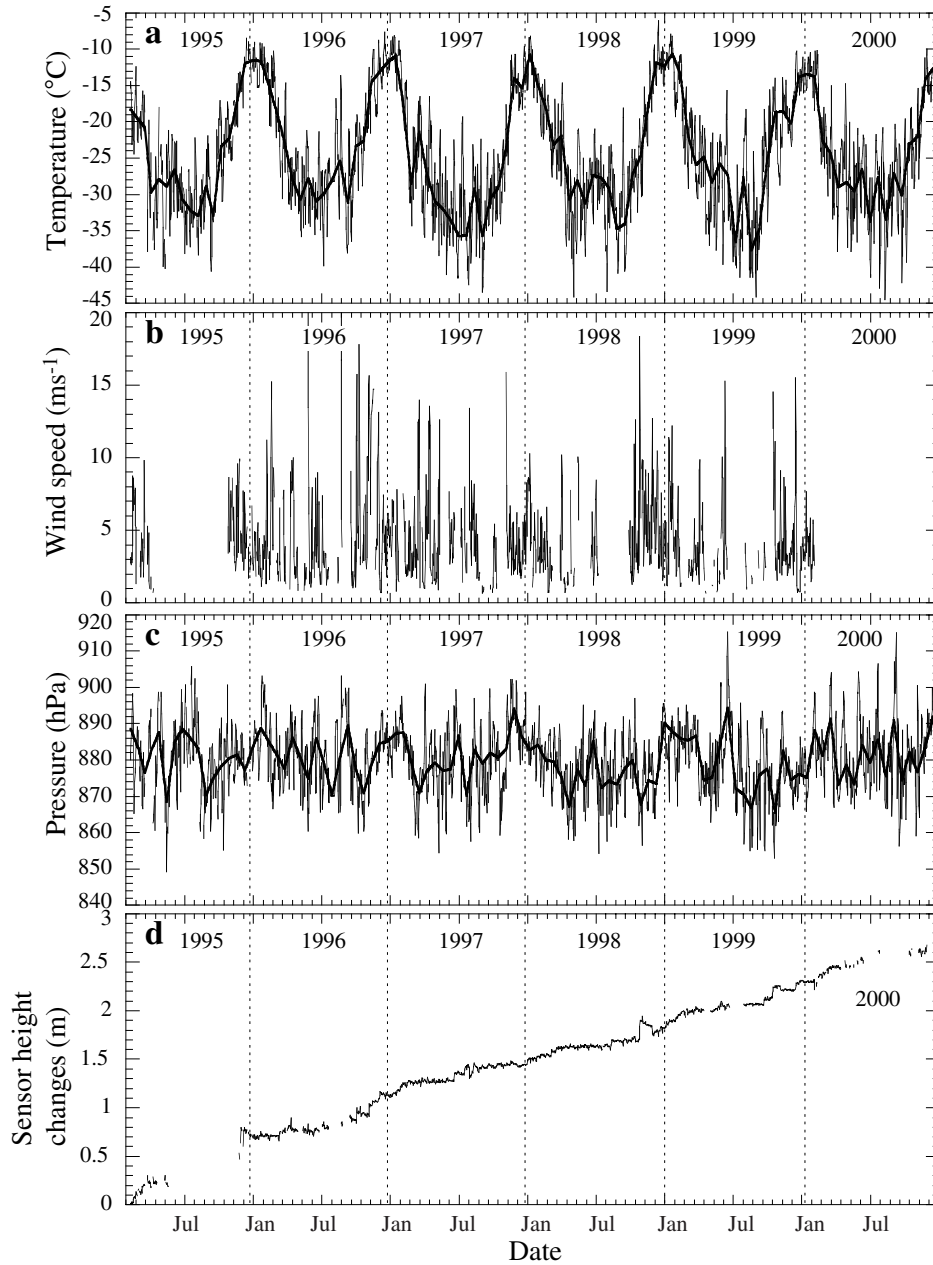


Figure 3.3. Variation in the daily mean values of (a) air temperature, (b) wind speed and (c) air pressure over the six-year measuring period, and (d) accumulation since the beginning of the measuring period. Accumulation is expressed in sensor height changes and is 0 m of snow at 12-2-1995. Thick solid lines are smoothed curves.

Table 3.1. Annual averages and extreme values for Berkner Island AWS.

		1995	1996	1997	1998	1999	2000	1995-2000
T (°C)	annual	-23.2	-22.3	-25.7	-24.3	-24.4	-24.0	-24.0±1.2
	summer	-12.6	-14.5	-15.1	-13.4	-15.5	-	-14.2±1.2
	winter	-30.3	-27.9	-32.6	-29.8	-32.4	-30.2	-30.5±1.8
T_{min} (°C)		-44.0	-45.4	-46.0	-49.7	-47.2	-46.8	-49.7
T_{max} (°C)		-3.1	-3.1	-4.4	-3.2	-3.5	-3.6	-3.1
WS (m s ⁻¹)		4.2	5.0	4.1	4.5	3.9	-	4.3±0.4
WS_{max} (m s ⁻¹)		-	45.3	32.6	34.0	34.7	-	45.3
WD (°)		36.3	359.5	13.0	2.6	355.7	-	6.3
dc		0.43	0.49	0.31	0.38	0.48	-	0.42±0.07
P (hPa)		881.4	881.2	880.8	878.2	878.7	882.3	880.4±1.6
$S \downarrow$ (W m ⁻²)		108.0	106.3	113.9	111.8	105.7	103.3	108.2±4.0
$Acc.$ (m of snow)		0.68	0.39	0.29	0.42	0.48	0.44	0.45±0.13

Notes: Averages are based on hourly values. T and WS are corrected for instrument height changes. WD is vectorially averaged. The last column are averages plus the standard deviation over six years. T , temperature; T_{min} , minimum temperature; T_{max} , maximum temperature; WS , wind speed; WS_{max} , maximum wind speed; WD , wind direction; dc , directional constancy; P , air pressure; $S \downarrow$, incoming shortwave radiation; $Acc.$, accumulation.

for Filchner station (based on three hourly averaged values). Note that for Berkner Island, January is missing for the year 1995. To obtain a mean value over a complete year, values of January 1996 are used in place of January 1995. Furthermore, 63 % of the wind speed and wind direction data was lost through rime forming in 1995. The calculated annual mean values are based on the remaining 37 %.

The AWS records show that the near-surface meteorological conditions on the south dome of Berkner Island are relatively variable compared to other stations on the Antarctic continent. Besides the seasonal variability, large variations occur on time scales of days and weeks. Because the station was placed on a dome, the near-surface climate is mainly influenced by synoptic-scale weather systems and is relatively unaffected by katabatic flow, for which a slope in the terrain would be necessary. The absence of a predominant katabatic flow is shown in the wind speed (Figure 3.3b) and wind direction as will be discussed below. Gaps in Figure 3.3b are mainly caused by freezing of the wind speed sensor, which occurs most often in winter. The wind speed is quite variable throughout the measuring period. Although large gaps are present, no significant annual variation is observed. Daily mean values vary between 0 and 20 m s⁻¹ and wind gusts (maximum of 6 min. means) can reach 40 to 50 m s⁻¹. The annual mean wind speed is ~ 4.3 m s⁻¹ (Table 3.1), which is low compared to other Antarctic stations. The long term annual mean wind speed at Halley, Recovery and Dumont d'Urville, a French station on the Adélie coast, is 6.6 m s⁻¹, 5.5 m s⁻¹ and 9.4 m s⁻¹ (King and Turner, 1997), respectively. Halley is, as Berkner Island, a station mostly affected by the large-scale flow. Recovery and especially Dumont d'Urville frequently experience severe katabatic winds. Dome C, also a station on a dome not affected by katabatic flow, observes an even lower annual mean wind speed of 2.9 m s⁻¹ (Wendler and Kodama, 1984).

Table 3.2. Annual mean values for AWS Recovery, Filchner station and Halley station.

	Recovery 1995	Filchner 1995	Halley 1995-2000
<i>T</i> (°C)	-28.0	-23.6	-18.7±1.1
<i>RH</i> (%)	-	70.7	-
<i>WS</i> (m s ⁻¹)	5.5	3.9	6.6±0.7
<i>WD</i> (°)	52.6	-	-
<i>dc</i>	0.90	-	0.59
<i>P</i> (hPa)	847.8	-	988.9±1.6
<i>CC</i> (1/10)	-	-	0.68±0.03

Notes: Averages are based on daily (Recovery AWS), three-hourly (Filchner station) and monthly averages (Halley station). For Halley station the long term (1957-2000) annual means plus standard deviation are presented (King and Turner, 1997). *T*, temperature; *RH*, relative humidity; *WS*, wind speed; *WD*, wind direction; *dc*, directional constancy; *P*, air pressure; *CC*, cloud cover.

In general, the wind direction on Berkner Island is variable, with a weak preference for directions around North. Variability of the wind direction is expressed in the directional constancy, which is the ratio of the magnitude of the vector mean wind speed to the scalar mean. A high directional constancy implies that the wind direction prefers a particular direction. The directional constancy based on hourly means for Berkner Island is 0.42 and varies between 0.31 in 1997 and 0.49 in 1996. These values can be considered low, for Antarctic conditions. Halley has a directional constancy of 0.59 and Dome C has a directional constancy of 0.60. Recovery and Dumont d'Urville both have a high directional constancy of 0.90 and 0.91, respectively, which is due to the predominant katabatic flow.

The summer on Berkner Island is short and peaked, temperatures during the summer staying below 0 °C. The maximum hourly mean temperature measured was -3.1 °C (28 January 1996) so no significant melt is expected. The lowest recorded temperature is -49.7 °C (1 August 1998). During winter, temperature fluctuations of 20 °C or more occur within a few days. The annual mean temperature for Berkner Island over the measuring period is ~-24 °C. The 10 m snow temperature, a measure for the annual mean surface temperature, is -26.4 °C (Oerter, 1995). Compared to the temperature at the German station Filchner, the temperature on Berkner Island is relatively high. Filchner station was situated on the edge of the Ronne ice shelf at sea level. This means that the temperature at Filchner station should be 5 to 7 °C higher than on the south dome of Berkner Island, based on a lapse rate of 0.006 - 0.008 K m⁻¹. This is not the case. In 1995 the annual mean temperature for Filchner was -23.6 °C compared to -23.2 °C on Berkner Island. The summer was warmer at Filchner station, -7.9 °C compared to -12.6 °C on Berkner Island and the winter was colder, -34.2 °C compared to -30.3 °C. The low temperatures at Filchner station are probably due to the presence of a strong temperature inversion which apparently does not develop at Berkner Island. The inter-annual temperature variability at Berkner Island is similar to the long term variability at Halley, ~1.1 °C.

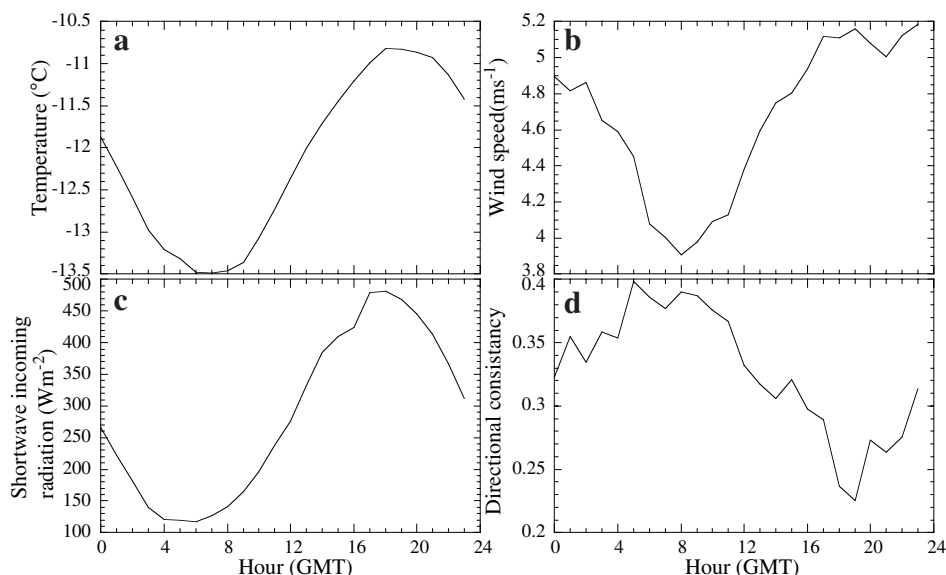


Figure 3.4. Average diurnal variations of (a) air temperature, (b) wind speed (c) shortwave incoming radiation and (d) directional constancy in January over the six-year measuring period.

The pressure record shows an annual variation (Figure 3.3c). Fourier analysis of the time series shows that $\sim 36\%$ of the annual variation is explained by the first harmonic (annual cycle) and $\sim 33\%$ by the second harmonic (semi-annual cycle). The contribution of the second harmonic to the signal is of the same order of magnitude as at Halley (39%, over 1980-96) (Van den Broeke, 1998). The lower contribution at Berkner Island is probably due to the more southern and continental location of the station.

The absence of melt implies that mass loss is caused entirely by wind erosion and/or sublimation. Figure 3.3d shows that the height of the sensor bar decreases by 2.70 m over the measuring period. Snow pit measurements 5 km from the AWS yield a mean near-surface snow density of 368.2 kg m^{-3} (Oerter, 1995; Gerland *et al.*, 1999) resulting in an annual accumulation of $\sim 166 \text{ mm}$ water equivalent per year (w.e. yr^{-1}). Results from a firn core drilled near the snow pit reveal an annual mean accumulation of $174 \text{ mm w.e. yr}^{-1}$ based on ~ 20 years of accumulation (Wagenbach *et al.*, 1994). The inter-annual variability is large (Table 3.1). There is no significant annual trend in accumulation, although the gradient in instrument height change averaged over the six-year period seems largest in the summer months. About 40% of the annual accumulation occurs in these months. In general, accumulation occurs in small events of a few centimeters. Large snow fall events in which 0.1 to 0.2 m snow accumulate occur about twice a year. In such an event a quarter to a third of the annual accumulation takes place. These snow fall events will be discussed in Section 3.3.3.

3.3.2 The diurnal cycle

Berkner Island is located south of the Antarctic polar circle where the sun remains below the horizon in winter. The lack of a diurnal varying forcing in winter results in the absence of a diurnal cycle in the meteorological parameters as temperature and wind speed. In summer, the incoming solar radiation forces a diurnal cycle in these parameters. Figure 3.4 presents the mean diurnal variations in air temperature, wind speed, shortwave incoming radiation and directional constancy in January.

Figure 3.4c shows that the maximum in shortwave radiation occurs a few hours after 12 GMT, which is due to the longitude location of the station at 45.78°W . The maximum in air temperature occurs about an hour after the maximum in shortwave radiation. In daytime, the solar radiation heats the surface resulting in more unstable conditions and (partly) destroying the surface temperature inversion. At locations where the katabatic forcing is weakly developed, this results in an increasing influence of the large scale flow expressed in the higher wind speed and a lower directional constancy during daytime. In a well developed katabatic layer the effect of a (partly) destruction of the surface temperature inversion would be a decrease in wind speed and also a decrease in directional constancy.

3.3.3 Case study of snowfall events

Near the Berkner Island AWS several shallow ice core and snow pit studies have been carried out (Wagenbach *et al.*, 1994; Oerter, 1995; Gerland *et al.*, 1999). In the near future the British Antarctic Survey plans to drill an ice core to the bedrock on the south dome of Berkner Island. In the interpretation of ice cores it is important to have knowledge of the annual amount of snow accumulation, seasonality of the accumulation and meteorological conditions during which snow fall occurs. A necessary condition for the occurrence of precipitation is the existence of a low pressure area in the vicinity of the Island. Depressions generally originate from the southern Atlantic Ocean, north of the island, and move from west to east. In the eastern sector of such a system relative warm, moist air is transported southward (Bromwich, 1988). When the depression is located to the northwest of Berkner Island, this air can bring snow to Berkner Island. When the system moves further to the east, the air has to travel over western Dronning Maud Land before arriving at Berkner Island and will have lost most of its moisture (King and Turner, 1997). There are two types of depressions bringing snow to Berkner Island.

The first type is the most common one. A depression that develops in the mid or high latitudes of the South Atlantic Ocean moving from west to east, north of Berkner Island. This type occurs frequently but seldom brings much snow. It is characterized by a decrease in pressure after the snow fall event, high wind speeds and a turning of the wind from north to east and south. At the beginning of October 1996, a depression of this type brought ~ 0.25 m of snow (Figure 3.5a to 3.5e). About half of it was blown away within a day. The pressure drops from 883 hPa to 874 hPa during the event and drops further to 857 hPa on 9 October. The wind direction changes from north to east on 9 October and south-west on 10 October. The tempera-

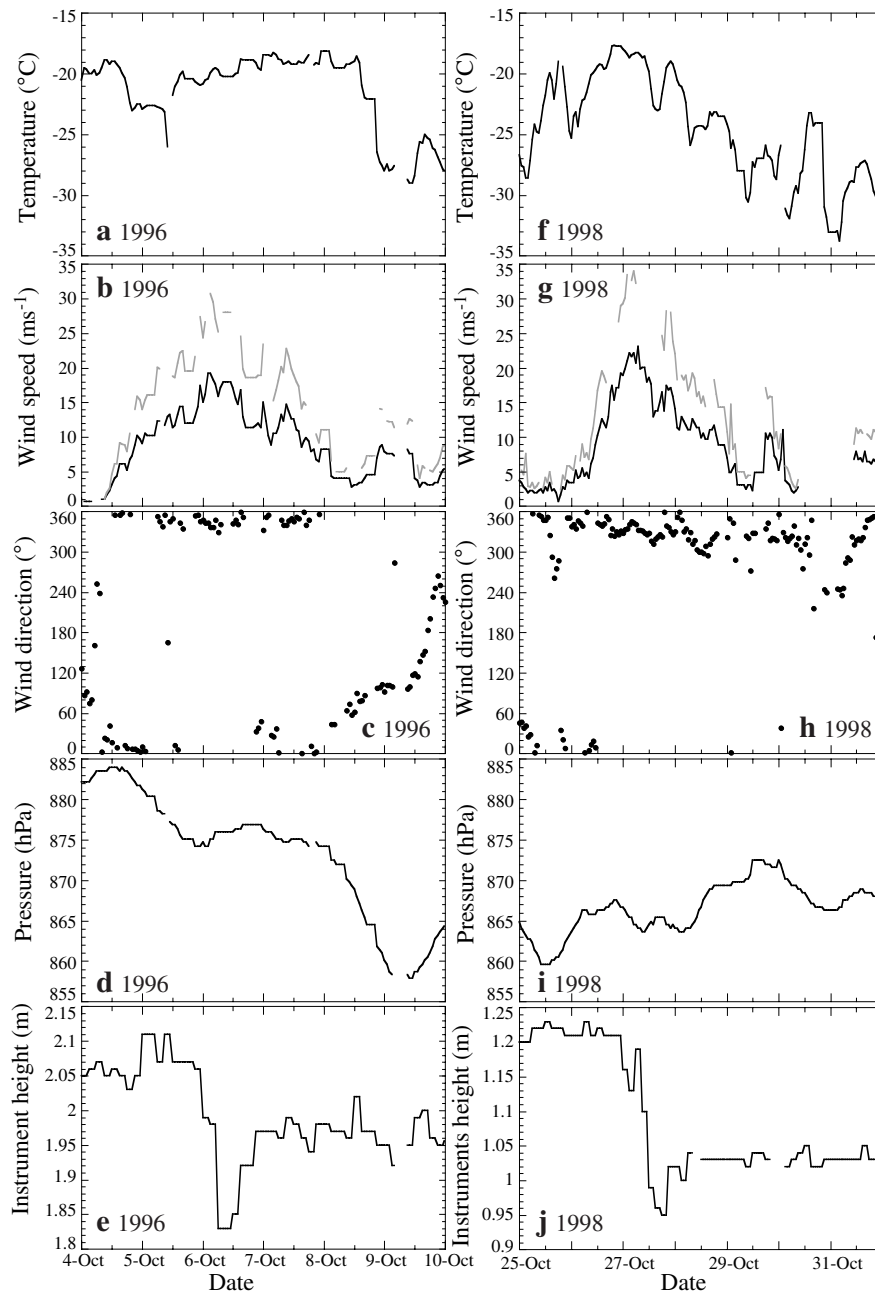


Figure 3.5. Hourly mean variation of (a,f) temperature, (b,g) wind speed, (c,h) wind direction, (d,i) air pressure and (e,j) instrument height for a snow fall event in October 1996 (left) and October 1998 (right). The upper grey line in panels (b,g) is the maximum wind speed derived from six minute means.

ture during the event is $\sim 5^\circ\text{C}$ higher than the average monthly value.

The second type is a topographically induced low. When an airstream passes a topographic barrier, like the Antarctic Peninsula, on the lee side cyclones can develop. Some of these cyclones grow into major depressions and move southward into the Weddell Sea area (King and Turner, 1997). Most of the large snow fall events are caused by this type of depression, moving from north to south close to the Peninsula and remaining to the west of Berkner Island. In this case the snow falls when the pressure is at its lowest point or already rising again. The wind speed is high and the wind direction turns from north-east to north and north-west. Figure 3.5f to 3.5j shows a snow fall event of this type at the end of October 1998. About 0.30 m of snow falls on 27 October. About 0.1 m was blown away within a day. The remaining snow settles and densifies in the month after the event (see Figure 3.3d). The pressure is already rising from 859 hPa on 25 October to 873 hPa on 30 October. The wind speed is high and the wind direction indeed turns from north on 25 October to west and south-west on 31 October. As during the first event, the temperature is relatively high, $\sim 8^\circ\text{C}$ higher than the monthly mean.

3.4 The surface energy balance

The meteorological data presented in the previous sections are used to calculate the surface energy fluxes with the aid of an energy balance model. Due to a problem with the wind speed sensor, fluxes are calculated for the period 1995-99 only. In this section the model is described and validated, after which the results are presented.

3.4.1 Model description

The model used to compute surface energy fluxes is described in Greuell and Konzelman (1994). They used the model to calculate the surface energy balance for the Swiss Federal Institute of Technology (ETH) camp location, West Greenland. We adjusted the model to suit the situation on Berkner Island. The model will be described briefly to illustrate the adjustments that were made.

The model consists of an atmospheric part and a firn part. No adjustments were made in the firn part of the model. In the firn part the model calculates the temperature and density on a grid extending vertically from the surface to 25 m depth. The distance between the grid points of the snow model changes exponentially from 10 mm at the surface to 3 m at a depth of 25 m. On this grid the thermodynamic energy equation is solved:

$$\rho c_{pi} \frac{\partial T}{\partial t} = \frac{\partial}{\partial z} \left(K \frac{\partial T}{\partial z} \right) + \frac{\partial Q_t}{\partial z} - \frac{\partial}{\partial z} (M L_M) + \frac{\partial}{\partial z} (F L_M), \quad (3.1)$$

where ρ is the density, c_p the heat capacity of ice, K is the effective conductivity, $\partial Q_t / \partial z$ the absorption of energy coming from the atmosphere, M the melt rate, F the freezing rate and L_M the latent heat of fusion. In the upper most layer of the model, Q_t is the sum of the radiative and turbulent fluxes. In the following layers

Q_t is the penetrated shortwave radiation flux. K is a function of the density and is calculated using Von Dusen's equation (Sturm *et al.*, 1997):

$$K = (2.1 \times 10^{-2}) + (4.2 \times 10^{-4} \rho) + (2.2 \times 10^{-9} \rho^3) . \quad (3.2)$$

Densification of the snow pack is possible through internal melting and/or refreezing. Furthermore, empirical relations developed by Herron and Langway (1980) describe settling and packing of the snow pack. The main result from the firn model for the surface energy balance, is the surface temperature (T_0).

In the atmospheric part of the model, the radiative and turbulent fluxes are calculated. Generally, if there is no melt, the surface energy balance is written as (fluxes towards the surface are positive):

$$S + L + H + LE + G = 0 , \quad (3.3)$$

where S is the net shortwave radiative flux (incoming minus reflected), L is the net longwave radiative flux (incoming minus emitted), H and LE the turbulent fluxes of sensible and latent heat, respectively, and G is the subsurface energy flux. The model is forced by five meteorological quantities, namely air temperature, wind speed, air pressure, incoming shortwave radiation and snow-height changes. The AWS does not measure humidity and therefore relative humidity was set to a constant value of 70% based on Filchner station measurements (Table 3.2).

The snow height changes were derived from the instrument-height measurements and influence the size and density of the uppermost grid layer. In the case presented here, the net shortwave radiation is derived from incident radiation measurements and using an albedo of dry snow of 0.8 (Bintanja and van den Broeke, 1995). The longwave incoming radiation is calculated using the parameterization of King (1996), which is derived from monthly mean values of incoming longwave radiation and temperature at four Antarctic stations:

$$L \downarrow = 0.49 + (4.70 \times 10^{-8} T_a^4) \quad (3.4)$$

where T_a is the screen level (2 m) temperature in K. The temperature measurements are corrected to give T_a . The longwave emitted radiation is calculated using the Stefan-Boltzmann law with an emissivity of 1, and the surface temperature (T_0) derived from the firn part of the model.

The fluxes of sensible and latent heat are calculated using Monin-Obukhov similarity theory. In the atmospheric surface layer the mean gradients of wind speed (u), potential temperature (θ) and specific humidity (q) are assumed to be related to the corresponding fluxes according to the flux-profile relations:

$$\frac{\kappa z}{u_*} \frac{\partial u}{\partial z} = \phi_m(\xi) \quad (3.5)$$

$$\frac{\kappa z}{\theta_*} \frac{\partial \theta}{\partial z} = \phi_h(\xi) \quad (3.6)$$

$$\frac{\kappa z}{q_*} \frac{\partial q}{\partial z} = \phi_h(\xi) , \quad (3.7)$$

where κ is the von Kármán constant (≈ 0.4), z the height above the surface, u_* the friction velocity, θ_* the turbulent temperature scale, q_* the turbulent humidity scale, ξ a non-dimensional length scale ($= z/L_{mo}$ in which L_{mo} is the Monin-Obukhov length scale) and ϕ_m and ϕ_h are the non-dimensional stability functions for momentum (m) and heat (h), respectively. The non-dimensional stability function for moisture is assumed to be equal to ϕ_h . In unstable conditions ($\xi < 0$) the expressions for ϕ of Dyer (1974) and Högström (1988) are used, while in stable conditions ($\xi > 0$) the expressions for ϕ of Duynkerke (1991) are used. Assuming a constant flux layer, the flux profile relations can be integrated analytically between two heights, i.e. the surface and the measuring height. The surface roughness length of momentum (z_0) is assumed to be 1.0×10^{-4} m and is an empirically derived value presented by King and Turner (1997). The surface roughness lengths of heat (z_h) and moisture (z_q) are calculated using the method described by Andreas (1987), so z_h and z_q are a function of z_0 and u_* . At z_0 the wind speed is zero and the specific humidity takes the ice-saturation value for T_0 . Knowing the surface roughness lengths, the humidity, the wind speed and temperature at two levels, it is possible to compute u_* , θ_* and q_* using an iterative method. The turbulent fluxes of sensible (H) and latent (LE) heat can then be calculated with:

$$H = -\rho_a c_{pa} u_* \theta_* \quad (3.8)$$

$$LE = -\rho_a L_s u_* q_* , \quad (3.9)$$

where ρ_a is the air density, c_{pa} the heat capacity of air at constant pressure and L_s the latent heat of sublimation.

3.4.2 Model validation

To validate the model output, the modelled and measured subsurface temperatures are compared. In Figure 3.6 the modelled and measured subsurface temperature at two depths are shown for the five-year period. The sensor depths were 0.1 and 1.0 m initially, which slowly increased due to accumulation. The model is able to simulate the measurements fairly well, but underestimates the temperature at both levels. During summer the differences are largest but generally remain smaller than 3.5°C . At larger depth the differences diminish. The mean difference between the modelled and measured temperature is 1.5°C at the 0.1 m level and 1.1°C at the 1.0 m level. Greuell and Konzelman (1994) also found differences of this magnitude between their modelled and measured subsurface temperature on Greenland. They attributed the differences to a thin layer of snow over an ice surface, which was not represented in the model, or to a deficiency in the simulation of internal melting. In our case, however, the snow layer is thick enough and no internal melting takes place, so this could not explain the differences found in this study.

A problem in our case is the fact that we have no direct measurements of the longwave radiation fluxes or measurements of the turbulent fluxes. This means that parameterizations are needed to calculate these fluxes. Table 3.3 shows the sensitivity of snow temperatures and fluxes to changes in the model parameters and mea-

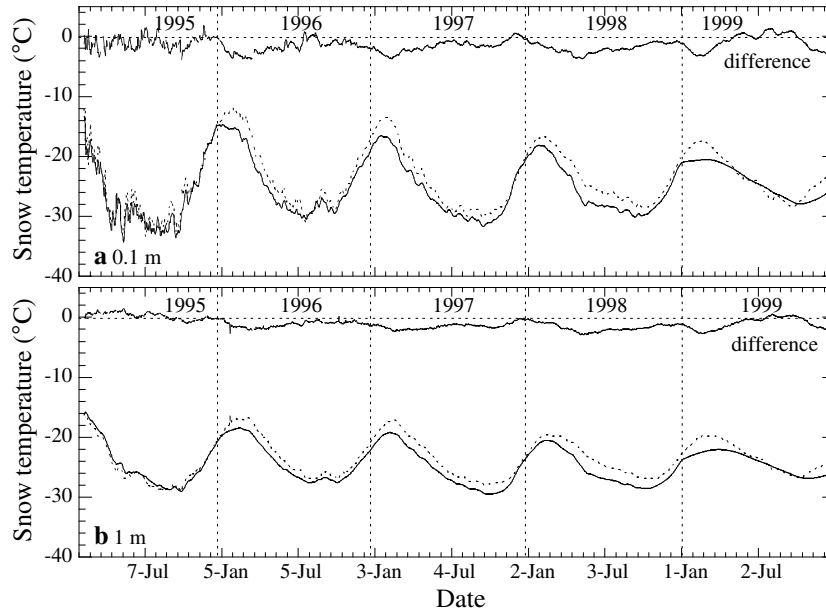


Figure 3.6. Daily mean values for the simulated (solid line) and measured (dashed line) snow temperatures at two depths over the five-year measuring period. Also shown is the difference between the measured and simulated temperatures (simulated minus measured) corrected for depth changes.

surements. The table shows that the snow temperatures and the fluxes are very sensitive to changes in the longwave incoming flux and the snow albedo. The influence of changing the longwave incoming flux on the snow temperature diminishes with increasing depth. The fluxes are less sensitive to changes in the surface roughness length and the fractional extinction coefficient of shortwave radiation penetration in snow. The snow temperatures are changed by 0.3 to 0.4 °C. Changes in the snow density, the extinction coefficient of snow and the effective conductivity do change the snow temperatures by ~ 0.2 °C but do not change the fluxes significantly. Changes in the relative humidity and the stability corrections only have a small influence on the turbulent fluxes and hardly change the snow temperatures.

The table shows that the uncertainty in the snow fluxes can be reduced by performing measurements of the surface albedo and longwave radiative fluxes. They will also change the snow temperatures significantly. More sophisticated routines calculating the extinction coefficients are available (Brandt and Warren, 1993) but require the solar radiation to be treated in small wavelength bands, which is not feasible here.

3.4.3 The annual cycle

Accepting the calculated energy fluxes in the reference run, Figure 3.7 shows the monthly mean surface energy fluxes for the complete period. To obtain estimates

Table 3.3. Sensitivity of the snow temperature and the fluxes to changes in model parameters.

Reference	Test	dT_{sn} (0.05)	dT_{sn} (0.20)	dT_{sn} (0.55)	dT_{sn} (0.80)	dS	dL	dH	dLE
$RH=70\%$	60%	-0.07	-0.03	-0.03	-0.01	0.0	0.4	0.8	-1.2
$z_0=0.1\text{ mm}$	1.0 mm	0.32	0.30	0.27	0.26	0.0	-1.0	1.3	-0.2
$\alpha=0.8$	0.75	0.61	0.72	0.66	0.63	4.9	-1.4	-2.5	-1.0
$\rho=350\text{ kg m}^{-3}$	375 kg m^{-3}	-0.10	-0.17	-0.18	-0.18	0.0	-0.1	0.0	0.0
$L\downarrow^a$	$L\downarrow^b, cc=0.7$	0.35	0.38	0.35	0.34	0.0	1.3	-1.0	-0.2
	$L\downarrow^b, cc=0.75$	0.84	0.84	0.78	0.76	0.0	3.4	-2.8	-0.6
	$L\downarrow^a+5\%$	1.23	1.20	1.12	1.08	0.0	5.3	-4.3	-0.9
$\beta=15\text{ m}^{-1}$	10 m^{-1}	0.05	0.20	0.25	0.23	0.0	0.0	0.0	0.0
$\zeta=0.36$	0.75	-0.30	-0.44	-0.41	-0.38	0.0	0.0	-0.1	0.0
ϕ^c	ϕ^d	0.07	0.08	0.08	0.06	0.0	-0.1	0.3	-0.1
$K, \text{ Von Dusen}^e$	Jansson ^e	-0.07	-0.15	-0.17	-0.17	0.0	-0.1	0.0	0.0

Notes: Between brackets the initial depth of the T_{sn} sensors in m. T_{sn} is in $^{\circ}\text{C}$ and the fluxes are in W m^{-2} . Differences are test minus reference. In each run, one parameter is changed. The mean T_{sn} in the reference run are -26.6, -26.1, -25.7 and -25.5 $^{\circ}\text{C}$, respectively, and mean fluxes are 19.6, -29.3, 11.2 and -1.7 W m^{-2} , respectively. T_{sn} , snow temperature; S , net shortwave radiation; L , net longwave radiation; H , sensible heat flux; LE , latent heat flux; RH , relative humidity; z_0 , surface roughness length; α , albedo; ρ , density snow; cc , cloud cover; β , extinction coefficient snow; ζ , fractional extinction coefficient; ϕ , stability functions; K , effective conductivity.

References: a, King (1996); b, König-Langlo and Augstein (1994); c, Högström (1988) and Duynkerke (1991); d, Dyer (1974); e, Sturm *et al.* (1997).

throughout the winter of 1995 the long-term mean wind speed is used and the sensor height is linearly interpolated. During winter the net radiative flux (R) is fully determined by the net longwave radiation flux (L). R is negative, upward directed ($\sim -20\text{ W m}^{-2}$), and almost completely balanced by a positive sensible heat flux (H) that cools the air near the surface. This is a typical feature of the surface energy balance in the Antarctic winter. The magnitude of R corresponds to values found by King *et al.* (1996). The magnitude of H corresponds to values found by Stearns and Weidner (1993) for three weather stations on the Ross Ice Shelf (Gill, Elaine and Lettau). Two other stations (Marilyn and Schwerdfeger) show larger fluxes. The latent heat flux (LE) is small during winter because of the low temperatures as was found by Stearns and Weidner (1993).

In the short Antarctic summer (November, December and January), R is positive and dominated by the net shortwave radiation flux (S), warming the surface. The warmer surface causes the emitted longwave radiation flux to increase and the conditions in the surface layer to become unstable. This is indicated by negative values of H (-5 to -10 W m^{-2}). Stearns and Weidner (1993) also found negative values for H for Gill, Elaine and Lettau AWS. LE is of the same order of magnitude as H and also negative, indicating that the snow layer loses mass by sublimation. The energy flux into the ice (G) is small. The magnitude of LE in summer is of the same order as found by Wendler *et al.* (1988) in Adélie Land (-8.7 W m^{-2}). Stearns and Weidner (1993) found slightly higher fluxes on the Ross ice shelf (-10 to -30 W m^{-2}) as did Bintanja and van den Broeke (1995) in Dronning Maud Land (-22.1 W m^{-2}). Bintanja (2000) shows however that LE found by Bintanja and van den Broeke (1995) was too

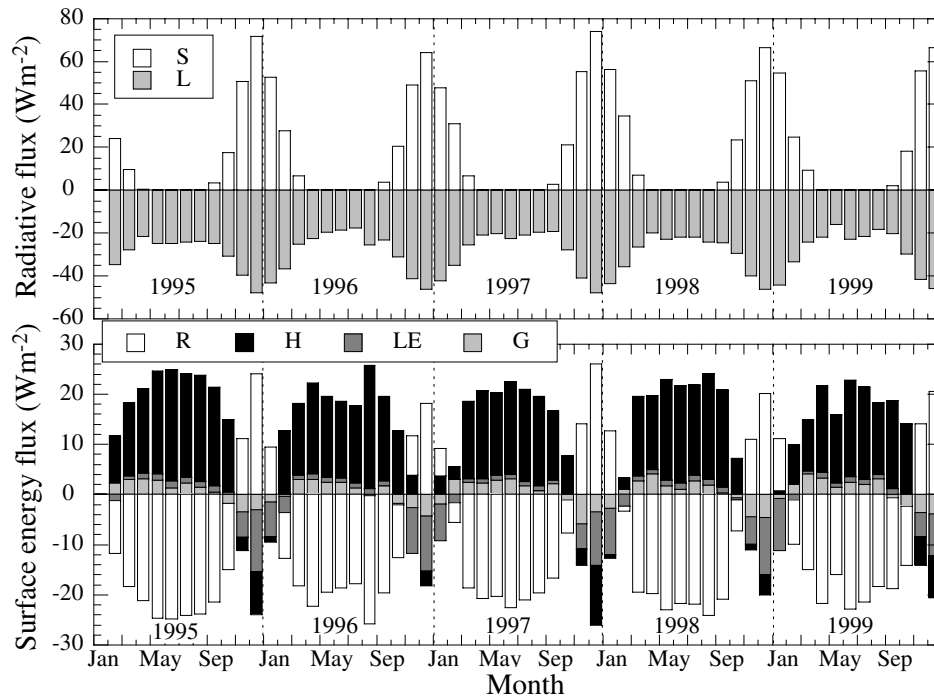


Figure 3.7. Monthly mean values for net shortwave radiation (S), net longwave radiation (L), net radiation (R), sensible heat flux (H), latent heat flux (LE) and total subsurface energy flux (G). Fluxes towards the surface are defined positive. The bars are stacked.

large due to an underestimation of the relative humidity. A recent analysis yielded a value -10.8 W m^{-2} (Bintanja, 2000). Wendler *et al.* (1988), Bintanja and van den Broeke (1995) and Bintanja (2000) find daily averaged positive values of H above snow surfaces indicating stable conditions.

Annual mean values of the surface energy fluxes are given in Table 3.4. The annual mean fluxes for 1995 are calculated using the month January of 1996 to fill in the missing values. The annual mean net radiation flux is negative and is almost equal to the value found by King *et al.* (1996) of -9.8 W m^{-2} for Halley. The negative net radiation is mainly balanced by a net downward sensible heat transport. This indicates stable conditions on the average. This balance was also found at the South Pole (Carroll, 1982) but the fluxes were twice as large ($H = 19.4 \text{ W m}^{-2}$, $R = -18.7 \text{ W m}^{-2}$). The annual mean subsurface energy flux is small. Positive values indicate cooling of the snow pack, negative values indicate warming of the snow pack. The calculated annual mean latent heat flux of -1.7 W m^{-2} corresponds to a mass loss through sublimation of $\sim 20.0 \text{ mm w.e. yr}^{-1}$. The fluxes are reasonable constant from year to year. The small turbulent fluxes in 1997 and 1999 are mainly due to the low mean wind speed in those years.

Table 3.4. Annual mean values and mean values over the 5 year period of the surface energy flux components in $W m^{-2}$.

Flux	1995	1996	1997	1998	1999	1995-1999
$S \downarrow$	98.7	93.8	99.4	100.9	96.3	97.8 ± 2.8
$S \uparrow$	-78.9	-75.0	-79.5	-80.7	-77.1	-78.2 ± 2.2
S	19.8	18.8	19.9	20.2	19.2	19.6 ± 0.6
$L \downarrow$	183.4	187.5	178.0	181.7	181.6	182.4 ± 3.4
$L \uparrow$	-214.3	-216.7	-206.6	-211.4	-209.9	-211.8 ± 3.9
L	-30.9	-29.2	-28.6	-29.7	-28.3	-29.3 ± 1.0
R	-11.1	-10.4	-8.7	-9.5	-9.1	-9.8 ± 1.0
H	12.2	12.5	9.9	11.2	10.1	11.2 ± 1.2
LE	-1.6	-2.0	-1.6	-1.8	-1.5	-1.7 ± 0.2
G	0.5	-0.1	0.4	0.1	0.5	0.3 ± 0.3

Notes: $S \downarrow$, incoming shortwave radiation; $S \uparrow$, reflected shortwave radiation; S , net shortwave radiation ($S \downarrow - S \uparrow$); $L \downarrow$, incoming longwave radiation; $L \uparrow$, emitted longwave radiation; L , net longwave radiation ($L \downarrow - L \uparrow$); R , net radiation ($S + L$); H , sensible heat flux; LE , latent heat flux; G , subsurface energy flux.

3.4.4 The diurnal cycle

Figure 3.4 shows that the important meteorological variables exhibit a marked diurnal cycle. The diurnal cycle is related to the daily variations in insolation. Figure 3.8 presents the resulting diurnal variations in the surface energy fluxes averaged over all months of January.

The diurnal cycle in S is entirely determined by the diurnal cycle in $S \downarrow$ due to the choice of a constant albedo. In reality the albedo also exhibits a diurnal variation, with a minimum at the lowest solar zenith angle, i.e. around solar noon, and is also influenced by snow sastrugi. This brings about an additional diurnal variation in $S \uparrow$. The diurnal variations in $L \downarrow$ and $L \uparrow$ are mainly determined by the variations in air and surface temperature, respectively. The maximum in the longwave radiation fluxes therefore coincide with the maximum in temperature and occur about an hour after solar noon. Because the variations in shortwave radiation are larger than the variations in longwave radiation, R is dominated by the shortwave radiation. R shows a maximum of $\sim 40 W m^{-2}$ at about solar noon (~ 15.00 GMT). During daytime, H and LE are both negative and of the same order of magnitude. Both show a minimum value of $\sim -15 W m^{-2}$ about an hour after the maximum in R . The negative H indicates unstable conditions in the boundary layer and the negative LE indicates surface sublimation. LE is negative during the entire day and indicates surface sublimation of ~ 0.2 mm w.e. per day. During night H is positive, partly balancing the negative R . The near surface air is cooled and conditions become stable.

The diurnal variations in the net radiative fluxes are comparable to the variations found by Bintanja (2000) over snow surfaces. The net longwave radiative fluxes in this study are smaller resulting in larger (less negative) net radiation fluxes at night. The net radiative fluxes found by Wendler *et al.* (1988) are considerably larger than presented here and the R presented by Bintanja (2000). This is probably due

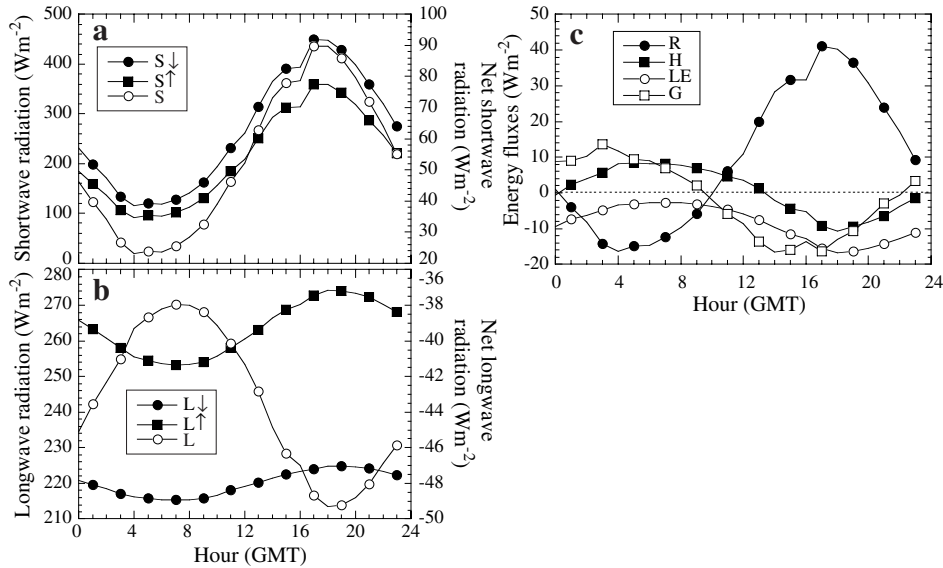


Figure 3.8. Diurnal variations in (a) shortwave radiative fluxes, (b) longwave radiative fluxes and (c) surface energy fluxes. S_{\downarrow} is incoming shortwave radiation, S_{\uparrow} reflected shortwave radiation, S_{net} net shortwave radiation, L_{\downarrow} longwave incoming radiation, L_{\uparrow} longwave outgoing radiation, L_{net} net longwave radiation, R net radiation, H sensible heat flux, LE latent heat flux and G total subsurface energy flux. Averages are calculated over all months of January.

to the more northerly location of their station resulting in larger insolation during daytime. LE in the three studies are comparable and negative the entire day. H remains positive in the study of Bintanja (2000), while in this study and the study of Wendler *et al.* (1988) H becomes negative, during unstable conditions, in daytime.

3.5 Summary and concluding remarks

The AWS on Berkner Island has provided us with a fairly complete six-year meteorological data set. The data show that the near-surface conditions on Berkner Island are largely determined by the large-scale flow; the station is located on a dome where it is unaffected by katabatic flows. The annual average air temperature is $\sim 24^{\circ}\text{C}$. In the absence of katabatic forcing, the annual mean wind speed is relatively low (4.3 m s^{-1}) and the wind direction variable (directional constancy = 0.42). The annual mean mass balance is positive and $\sim 166 \text{ mm w.e. yr}^{-1}$, which compares well with ice core studies (Wagenbach *et al.*, 1994).

Using an energy balance model we have computed the surface energy balance and subsurface temperatures. The calculated subsurface temperatures compare reasonably well with the measurements. The sensitivity analysis shows that the subsurface temperatures and surface fluxes are especially sensitive to changes in the parameterization of the incoming longwave radiation flux and the magnitude of

the extinction coefficients of penetrating shortwave radiation in snow. Nevertheless, considering the limited number of variables measured and the large number of assumptions made, the model results can be regarded as reasonably good, with mean differences between measured and modelled snow temperatures of 1.5°C at the 0.1 m level and 1.1°C at the 1 m level.

Considering the annual average values, the net shortwave radiation flux is the largest positive term (i.e., directed towards the surface) in the surface energy balance ($+19.6\text{ W m}^{-2}$). The sensible heat flux is also positive ($+11.2\text{ W m}^{-2}$). The net longwave radiation flux (-29.3 W m^{-2}) and the latent heat flux (-1.7 W m^{-2}) cool the surface on average. The annual cycle of the surface energy balance shows that in early summer the sensible heat flux is negative and heating of the snow occurs. The other months show a steady cooling of the snow pack. In the summer months the sensible heat flux becomes negative in daytime when conditions become unstable.

This study shows that using simple meteorological measurements (e.g., temperature, wind speed, pressure, incoming shortwave radiation and instrument height changes) and a surface energy balance model, it is possible to calculate the surface energy fluxes with reasonable precision, provided that model input parameters (e.g., surface roughness length and snow conductivity) and parameterizations (e.g., longwave incoming radiation and Monin-Obukhov similarity theory) used are applicable. The accuracy of the calculated fluxes can be improved by improving the parameterizations of the incoming longwave radiation for polar regions and implementing a wavelength depending extinction coefficient of shortwave radiation in snow. On the instrumental side, solving the problem of freezing of the wind speed sensor, increasing the number of observed meteorological parameters (e.g., reflected shortwave radiation, humidity and longwave radiation), and direct turbulence measurements will lead to improvements as will be shown in Chapter 5.

Chapter 4

Meteorological conditions in Dronning Maud Land, East Antarctica

Summary

We present data of eight Automatic Weather Stations (AWS) located in Dronning Maud Land (DML), East Antarctica, that have been operational since the austral summer of 1996-97. The data show the important influence of the katabatic wind on the meteorological conditions in DML. This is expressed in a maximum in potential temperature and wind speed at the sites with the steepest slope, at the edge of the Antarctic plateau. The annual mean potential temperature ranges from -18°C on the Antarctic plateau to -1°C on the slope. The annual mean wind speed ranges from $\sim 3.5\text{ m s}^{-1}$ on the plateau to $\sim 7\text{ m s}^{-1}$ on the slope. Furthermore, the wind direction is very constant at all stations and directional constancies vary between 0.67 and 0.93. On the ice shelves, the meteorological conditions are determined by the large-scale geostrophic flow. Accumulation decreases with elevation and distance from the coast from $\sim 400\text{ mm w.e. yr}^{-1}$ on the ice shelf to $\sim 30\text{ mm w.e. yr}^{-1}$ on the Antarctic plateau. Owing to the low temperatures, the specific humidity is very low. It decreases with elevation and distance from the coast, and is strongly correlated with the temperature.

4.1 Introduction

The Institute for Marine and Atmospheric Research Utrecht (IMAU), in co-operation with the Alfred Wegener Institute for Polar and Marine Research, Bremerhaven, operates nine Automatic Weather Stations (AWS) in Dronning Maud Land (DML), Antarctica (Figure 4.1). The AWS are a contribution to the European Project for Ice Coring in Antarctica (EPICA) and will provide a more thorough knowledge of the meteorological conditions in DML. This will increase our understanding of the processes influencing the surface mass balance and heat budget in DML, which will help with the interpretation of ice cores.

Several expeditions and studies focussed on DML have been carried out in recent years, to aid the search for the EPICA drill location. Relatively little was known of the climatology of DML. Data gathered during the pre-site surveys partly fills this gap and are useful in the interpretation of firn core and snow pit data. The studies of, e.g., Isaksson *et al.* (1999), Van den Broeke *et al.* (1999), Karlöf *et al.* (2000) and Oerter *et al.* (2000) focussed on the accumulation pattern in DML using snow pit and firn core measurements. King (1989) and König-Langlo *et al.* (1998) used data from coastal stations to study the climate of DML, while Jonsson (1995), Van den Broeke and Bintanja (1995) and Bintanja and Reijmer (2001) concentrated on the exceptional conditions on and near a blue ice area in DML. These studies are either limited in the amount of studied parameters, limited to only several months of measurements, usually in summer, or limited to coastal locations. The limitations are brought about by the remoteness and the harsh weather conditions of the Antarctic continent.

AWS are well suited to overcome the problems of remoteness and harsh weather conditions. Apart from the IMAU AWS, only a few AWS are operational in the DML region. South of Halley the United States Antarctica Research Program (USARP) operates two AWS (Stearns *et al.*, 1997). The Japanese Antarctic Research Expeditions (JARE) operates six AWS in cooperation with USARP, on a transect from Syowa to Dome F (Takahashi *et al.*, 1998; Enomoto *et al.*, 1998). The IMAU AWS cover the spatial gap between these two programs, the area between 15 °W - 15 °E and 72 °S - 76 °S. In the future, data could also be used to validate climate and weather prediction models currently used to study the Antarctic climate (Genthon and Braun, 1995; King and Connolley, 1997; Krinner *et al.*, 1997b; Van Lipzig *et al.*, 1999).

In this chapter we use AWS data to examine the spatial and temporal variability of the meteorological conditions in DML. Section 4.2 briefly describes the experimental set-up and location of the weather stations. In Section 4.3 the measurements are described and discussed in terms of spatial and temporal variability. The chapter is concluded with a summary and some concluding remarks.

4.2 Location and experimental set-up

The location and experimental set-up of the weather stations in DML is extensively described in Chapter 1. In this section a brief summary of the important details is given. Figure 4.1 shows the locations of the AWS in DML (see also Figure 1.4 and

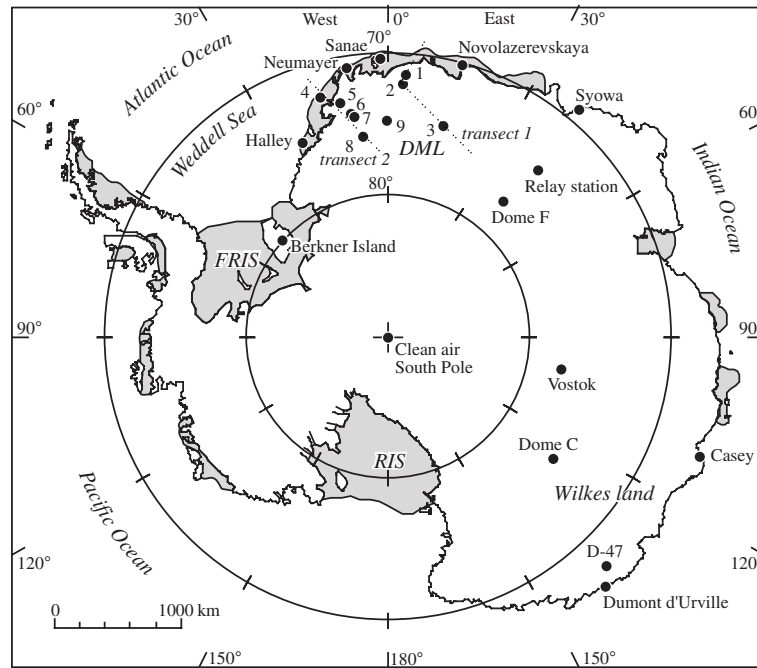


Figure 4.1. Map of Antarctica, showing the locations of the IMAU Automatic Weather Stations (AWS) and other stations mentioned in this chapter. AWS 9 is situated ~ 2 km west of the EPICA drilling site in Dronning Maud Land (DML). Shaded areas are ice shelves (FRIS, Filchner Ronne Ice Shelf; RIS, Ross Ice Shelf) and dotted lines indicate the transects presented in Figure 4.2.

Table 1.1) and other stations mentioned in this chapter. The locations of the AWS were chosen such that they cover a substantial part of western DML and represent different climate regimes. AWS 4 is located in the coastal area on an ice shelf, AWS 5 on the lower part of the ice sheet near the grounding line, AWS 1, 2, 6 and 7 close to or on the steep slope towards the Antarctic plateau and AWS 3, 8 and 9 on the Antarctic plateau. Figure 4.2 shows two elevation transects along AWS 3, 2 and 1 to the coast (transect 1) and along AWS 8, 6, 5 and 4 to the coast (transect 2). AWS 9 is located between these two transects. Nearly all stations are located on snow; AWS 7 is located on blue ice. Results from this station are presented in Bintanja and Reijmer (2001).

All stations measure air temperature, wind speed, wind direction, instrument height, air pressure and incoming shortwave radiation (Figure 1.5). Except AWS 2, all stations additionally measure firn temperatures at eight (AWS 1 and 3) or ten (AWS 4 to 9) different depths. AWS 4 to 9 additionally measure relative humidity, reflected shortwave radiation and incoming and outgoing longwave radiation. The initial height of the instruments was ~ 3 m above the surface. The accuracy of the sensors are discussed in Chapter 1.3. Hourly (AWS 1 to 3) or two-hourly (AWS 4 to 9) averages are stored locally and transmitted using Argos transmitters. Problems

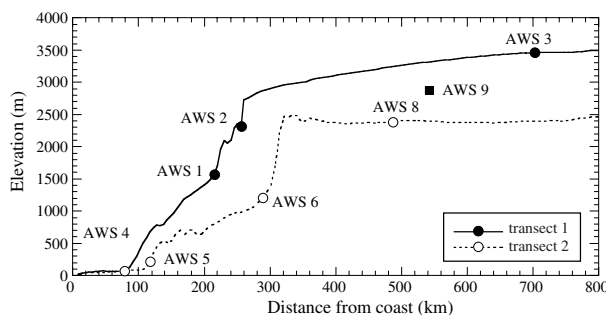


Figure 4.2. Elevation transects along AWS 3, 2 and 1 to the coast (transect 1) and along AWS 8, 6, 5 and 4 to the coast (transect 2) (see Figure 4.1). Based on data of a 10 by 10 km digital elevation model (data courtesy of J. Bamber, Bristol University).

with data transmission due to low temperatures occasionally result in gaps in the data sets of AWS 3, 8 and 9. The results presented here comprise a four-year data set for AWS 1 to 3 and a three-year data set for AWS 4 to 9.

The meteorological conditions at the AWS sites are compared with the conditions at other weather stations on the Antarctic continent (Figure 4.1 and Table 1.3). The two manned weather stations located closest to the AWS are Halley, the British research station on the Brunt Ice Shelf, and Neumayer, the German research station on the Ekström Ice Shelf. Regular meteorological measurements at Halley started in 1956 and at Neumayer in 1981. Data from these stations are presented in e.g., King (1989), König-Langlo and Herber (1996) and König-Langlo *et al.* (1998). Other (temporary) stations in the vicinity of the AWS are Relay station AWS and Dome F AWS on the Japanese transect from Syowa to Dome F. Data from these stations are presented in Takahashi *et al.* (1998).

4.3 Results

4.3.1 Prevailing synoptic conditions

The near surface climate in DML is determined by a combination of predominant katabatic winds and synoptic winds forced by transient cyclones travelling eastward parallel to the coastline. The influence of the cyclones decreases toward the interior of the continent, where the near surface climate is increasingly influenced by the katabatic wind (Parish and Bromwich, 1991, 1998). This is generally not true, but it is in DML as will be shown. The katabatic (or inversion) wind is forced by cooling of the near surface air over a sloping surface, which forces a down slope pressure gradient inducing a down slope gravitational flow.

The influence of cyclones is confined to the coastal area. The cyclones influencing DML mainly develop in the southern Atlantic Ocean or in the Weddell Sea area and travel south and eastward along the coastline (Jones and Simmonds, 1993; King and Turner, 1997). The abundance of depressions dissipating near the coast result in the

circumsolar pressure trough. Due to the location of DML south of the circumsolar trough, the mean synoptic pressure gradient forces a north-easterly flow in this area. When depressions are strong enough and travel through the southern part of the Weddell Sea area, they can enhance the katabatic flow in DML (Jonsson, 1995). A few times per year a high pressure ridge develops over DML and depressions are forced towards the continent instead of their usual path parallel to the coast line (Noone *et al.*, 1999). These depressions are responsible for most of the snow accumulation in western DML (Noone *et al.*, 1999; Reijmer and van den Broeke, 2001).

The meteorological conditions are described in terms of geographical locations of the AWS. For the purpose of clarity, DML is divided into three regions similar to the regions presented by Fortuin and Oerlemans (1990); the ice shelves, the escarpment region and the Antarctic plateau. The regions are distinguished by their climatic and topographic settings, which result in typical characteristics with respect to mean values, long-term variations and diurnal cycle of the meteorological variables.

4.3.2 Inter-annual variability

The AWS have provided us with a fairly complete three to four-year data set. In this section the inter-annual variations measured with the AWS are discussed and compared with longer time series measured at Neumayer and Halley. The records obtained so far are too short to study decadal variability in the atmospheric conditions caused by, e.g., El Nino and the Southern Oscillation (Cullather *et al.*, 1996) or the Antarctic circumsolar wave (Christoph *et al.*, 1997). Tables 4.1 and 4.2 present annual averages of the meteorological variables. Missing days in January 1997 (AWS 2) and January 1998 (AWS 5, 6 and 8) are replaced with corresponding days of the following year. This results in an addition of 1% data to AWS 2, 9% to AWS 5 and 4% to AWS 6 and 8 in the first measuring year.

Pressure The inter-annual variability in the annual mean surface pressure presented in Table 4.1 is on the order of 4 hPa. The variability over the 40-year period at Halley and the 20-year period at Neumayer is of the same order of magnitude. The annual mean surface pressure was lowest in 1998 and highest in 2000, which is also seen in the measurements at Neumayer and Halley station.

Radiation Table 4.2 presents annual mean values of the measured radiative fluxes. The radiative fluxes are more extensively described in Chapter 5. Shortwave incoming radiation ($S \downarrow$) is measured at all stations, whereas the reflected shortwave radiation ($S \uparrow$) and the longwave radiation ($L \downarrow$ and $L \uparrow$) are only measured at AWS 4 to 9. The amount of solar radiation the surface can receive ($S \downarrow$) is determined by elevation, latitude, cloud amount and cloud type, which is in DML strongly related to the distance from the coast. Figure 4.3a presents the annual $S \downarrow$ as a function of elevation. For the lower stations (AWS 1, 4, 5 and 6), $S \downarrow$ increases with elevation. $S \downarrow$ decreases with latitude when going from AWS 2 to 9 and 8, which are located at $\sim 72^\circ\text{S}$, 75°S and 76°S , respectively. The inter-annual variability in $S \downarrow$ is on the order of 5 - 10 W m^{-2} .

Table 4.1. Annual averages of the meteorological data for the IMAU AWS, Halley and Neumayer.

AWS	yr	T (°C)	θ (°C)	RH (%)	q (g kg ⁻¹)	WS (m s ⁻¹)	WD (°)	dc	P (hPa)	$acc.$ (mm w.e.)
1 (1420)	1997	-21.5	-6.6	-	-	6.8	45.1	0.72	818.6	211±8
	1998	-22.5	-7.4	-	-	6.1	53.9	0.67	815.1	130±8
	1999	-	-	-	-	6.2	55.9	0.67	817.1	133±8
	2000	-	-	-	-	5.8	59.7	0.67	818.0	33±8
2 (2400)	1997	-26.4	-1.5	-	-	6.7	108.8	0.74	714.2	111±21
	1998	-27.9	-2.6	-	-	6.3	122.0	0.77	711.0	88±15
	1999	-27.0	-2.1	-	-	6.7	118.9	0.81	713.3	13±15
3 (3453)	2000	-27.9	-3.1	-	-	6.3	121.9	0.80	713.8	114±18
	1997	-	-	-	-	-	-	-	-	3±17
	1998	-	-	-	-	-	-	-	-	62±16
4 (34)	1999	-47.8	-13.9	-	-	3.9	87.3	0.77	617.3	39±16
	2000	-48.7	-15.2	-	-	3.5	95.3	0.80	617.7	26±16
	1998	-19.2	-17.4	76.6	1.02	4.9	-	-	975.8	452±61
	1999	-19.3	-17.7	77.2	1.01	5.0	-	-	978.4	371±51
5 (363)	2000	-21.4	-20.1	81.0	0.91	4.7	-	-	981.4	324±42
	1998	-16.4	-11.7	70.8	1.02	6.6	65.8	0.93	938.6	144±28
	1999	-16.4	-11.8	71.1	1.01	6.4	65.4	0.93	941.1	270±27
6 (1160)	2000	-18.4	-14.1	75.9	0.94	6.3	64.9	0.92	943.7	158±13
	1998	-20.1	-8.2	67.1	0.77	6.6	-	-	851.7	207±23
	1999	-20.1	-8.4	68.9	0.80	6.8	-	-	854.0	333±38
8 (2399)	2000	-21.6	-10.1	75.8	0.78	6.5	67.3	0.88	855.6	311±36
	1998	-38.3	-14.8	63.9	0.23	5.4	34.4	0.89	715.6	90±7
	1999	-37.7	-14.3	64.0	0.25	5.2	31.4	0.90	717.5	62±5
9 (2892)	2000	-37.7	-14.3	64.9	0.26	4.9	30.9	0.90	718.8	28±7
	1998	-46.1	-18.8	58.5	0.13	4.6	58.5	0.89	672.3	91±8
	1999	-45.3	-18.1	59.5	0.14	4.7	54.9	0.87	674.0	84±7
N (40)	2000	-47.0	-20.1	62.1	0.12	4.1	58.8	0.88	675.3	60±8
	1997	-15.7	-14.6	-	-	9.3	102.8	0.66	986.4	-
	1998	-15.8	-14.5	-	-	9.5	99.0	0.68	982.7	-
H (39)	1999	-16.1	-15.0	-	-	9.5	102.8	0.67	985.3	-
	2000	-17.8	-17.0	-	-	8.4	109.0	0.60	988.6	-
	1997	-21.2	-20.4	-	-	5.7	-	-	989.5	-
	1998	-19.6	-18.4	-	-	6.1	-	-	984.3	-
H (39)	1999	-19.1	-18.1	-	-	6.6	-	-	986.3	-
	2000	-20.7	-20.0	-	-	5.4	-	-	990.0	-

Notes: Averages are based on hourly (AWS 1 to 3), two-hourly (AWS 4 to 9), three-hourly (Neumayer) and monthly means (Halley). To obtain averages over a complete year, missing days in January 1997 (AWS 2) and January 1998 (AWS 5, 6 and 8) are replaced with corresponding days of January 1998 and 1999, respectively. The accumulation values are based on sensor height measurements and measured density (Table 1.1). Between brackets, the elevation of the stations in m a.s.l., dashes indicate that no means could be calculated due to lack of data. T , temperature; θ , potential temperature; RH , relative humidity; q , specific humidity; WS , wind speed; WD , wind direction; dc , directional constancy; P , air pressure; $acc.$, accumulation; N, Neumayer; H, Halley.

The surface albedo α ($\alpha = S \uparrow / S \downarrow$) is higher than 0.80 at all stations. The albedo of Antarctic snow is estimated to range between 0.8 and 0.9 (King and Turner, 1997). At AWS 4 the annual mean surface albedo is highest, which is probably due to the frequent occurrence of fresh snowfall. The processes influencing the surface albedo of snow were discussed in more detail in Chapter 2.

Table 4.2. Annual average radiative fluxes and 10 m firn temperatures.

AWS	yr	$S \downarrow$ (Wm^{-2})	$S \uparrow$ (Wm^{-2})	$L \downarrow$ (Wm^{-2})	$L \uparrow$ (Wm^{-2})	R (Wm^{-2})	α	T_0 ($^{\circ}\text{C}$)	T_{10m} ($^{\circ}\text{C}$)
1 (1420)	1997	132.6	-	-	-	-	-	-	-25.5
	1998	142.4	-	-	-	-	-	-	-25.8
	1999	132.0	-	-	-	-	-	-	-25.9
	2000	132.8	-	-	-	-	-	-	-25.9
2 (2400)	1997	156.5	-	-	-	-	-	-	-
	1998	160.9	-	-	-	-	-	-	-
	1999	148.4	-	-	-	-	-	-	-
	2000	147.6	-	-	-	-	-	-	-
4 (34)	1998	120.9	-104.5	218.4	-238.4	-3.6	0.86	-18.6	-19.0
	1999	116.6	-103.0	220.5	-238.4	-4.3	0.88	-18.5	-19.0
	2000	118.6	-104.5	211.4	-230.8	-5.3	0.88	-20.6	-19.1
5 (363)	1998	122.3	-104.2	203.9	-241.1	-19.1	0.85	-17.8	-17.4
	1999	119.8	-102.8	206.5	-241.9	-18.4	0.86	-17.6	-17.5
	2000	125.3	-105.6	194.9	-234.1	-19.5	0.84	-19.7	-17.7
6 (1160)	1998	131.5	-110.1	178.7	-225.0	-24.9	0.84	-22.2	-22.3
	1999	130.0	-109.6	180.9	-225.9	-24.6	0.84	-21.9	-22.9
	2000	127.9	-108.6	175.4	-220.2	-25.5	0.85	-23.5	-22.7
8 (2399)	1998	-	-116.8	-	-	-	-	-	-38.5
	1999	129.8	-107.9	-	-	-	0.83	-	-38.6
	2000	129.4	-	-	-	-	-	-	-38.8
9 (2892)	1998	148.2	-126.8	-	-	-	0.86	-	-45.0
	1999	143.1	-124.8	-	-	-	0.87	-	-45.1
	2000	148.7	-126.3	-	-	-	0.85	-	-45.2
N (40)	1997	117.0	-105.5	223.0	-249.7	-15.2	0.90	-15.5	-
	1998	126.4	-106.4	219.9	-247.2	-7.3	0.84	-16.2	-
	1999	123.0	-104.3	219.8	-245.7	-7.2	0.85	-16.6	-

Notes: Averages are based on hourly (AWS 1 and 2), two-hourly (AWS 4 to 9) and daily means (Neumayer) and defined positive when directed towards the surface. To obtain averages over a complete year, missing days in January 1997 (AWS 2) and January 1998 (AWS 5, 6 and 8) are replaced with corresponding days of January 1998 and 1999, respectively. Between brackets, the elevation of the stations in m a.s.l., dashes indicate that no means could be calculated due to lack of data. $S \downarrow$, incoming shortwave radiation; $S \uparrow$, reflected shortwave radiation; $L \downarrow$, incoming longwave radiation; $L \uparrow$, outgoing longwave radiation; R , net radiation; α , albedo; T_0 , surface temperature; T_{10m} , 10 m firn temperature; N, Neumayer.

The amount of longwave radiation received by the surface ($L \downarrow$) is a function of temperature, humidity and cloud amount. Table 4.1 shows that these variables decrease predominantly with increasing elevation and therefore $L \downarrow$ decreases as well with increasing elevation. The outgoing longwave radiation ($L \uparrow$) is mainly determined by the surface temperature T_0 and shows a maximum at AWS 5 where also the air temperature is highest. This results in a net longwave radiative flux (L) that is negative (away from the surface) and most negative at AWS 6 (Figure 4.3b). Due to the low temperatures (below $\sim -45^{\circ}\text{C}$) the measured longwave radiative fluxes in winter are questionable at AWS 8 and 9, as are the resulting annual averages. The annual averages are therefore not presented in Table 4.2. The annual mean radiative balance ($R = S + L$, S is net shortwave radiation) is mainly determined by L and negative at all stations. Table 4.2 and Figure 4.3 also present the radiative fluxes

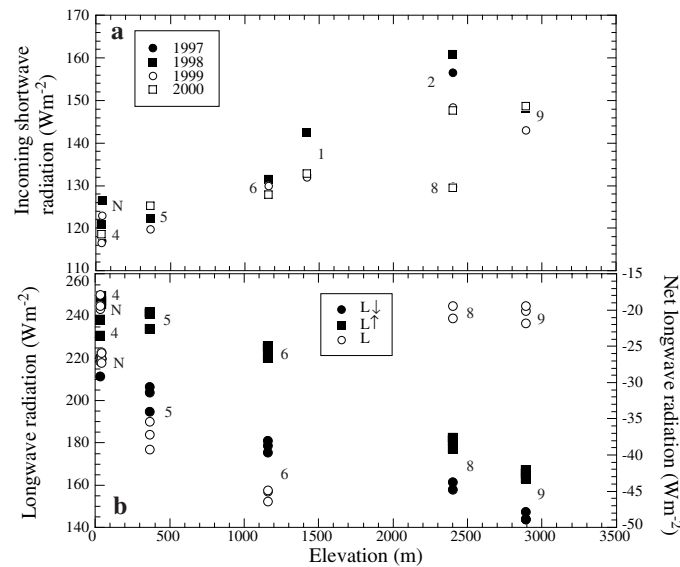


Figure 4.3. Annual mean (a) incoming shortwave radiation and (b) longwave radiation as a function of surface elevation. The numbers denote AWS sites, N is Neumayer. The values of longwave radiation measured at AWS 8 and 9 are questionable as explained in the text.

measured at Neumayer for 1997-99. Neumayer is situated on an ice shelf and the fluxes are of the same order of magnitude as at AWS 4. At both stations the resulting annual mean radiative balance is negative and on the order of -4 W m^{-2} at AWS 4 and -7 W m^{-2} at Neumayer.

Wind speed and direction The negative radiative balance is almost completely balanced by a positive (toward the surface) sensible heat flux, which results in a cooling of the near surface air, forcing a katabatic flow over sloping surfaces. Annual mean wind speeds at the AWS sites vary between $\sim 3.5 \text{ m s}^{-1}$ at AWS 3 on the plateau, $\sim 4.5 \text{ m s}^{-1}$ near the coast (AWS 4) and on the plateau at AWS 8 and 9, and $\sim 7 \text{ m s}^{-1}$ at the other stations (Table 4.1). The intensity of the katabatic flow is to a first approximation proportional to the steepness of the underlying surface (Parish and Bromwich, 1987, 1991). This results in wind speeds that are highest at the stations located close to or on the steep slope toward the Antarctic plateau. Figure 4.4 presents the annual mean wind speed in order of increasing slope. The wind speed at AWS 4 and other stations on flat ice shelves as Halley and Neumayer, is mainly determined by the large-scale geostrophic flow. Hence the higher wind speed and the larger variability in wind speed at coastal stations compared to plateau stations, which are also stations with small surface slopes but located farther from the coast and therefore less influenced by the large-scale geostrophic flow. In spite of the high surface slope at AWS 1 and 2, the annual mean wind speed is lower than at AWS 5 and 6, which is mainly due to freezing of the sensors in winter, causing an underestimation of the wind speed. The averages are based on 60 to 85% of the data

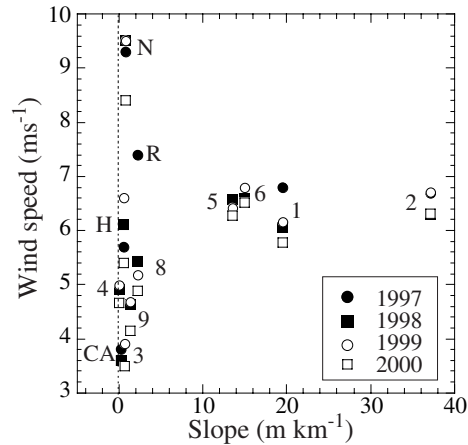


Figure 4.4. Annual mean wind speed for the AWS against slope (Table 1.1). The numbers denote the AWS sites; N, Neumayer; H, Halley; R, Relay station; CA, Clean Air station South Pole.

compared to 90 to 100 % for AWS 4 to 9. It could also be due to two-dimensional patterns in the terrain inducing confluence and divergence of the katabatic flow, which results in relatively high and low wind speeds (Parish and Bromwich, 1991), and an over-estimation of the surface slope at AWS 1 and 2. The uncertainty in the calculated slope is considerable at the stations on or near the steep slope towards the plateau (Table 1.1), due to the 10 by 10 km resolution of the digital elevation model used. Inter-annual variability in the measuring period is on the order of 1 m s^{-1} or less, which is comparable to Neumayer and Halley.

Due to the location of the stations south of the circum-polar pressure trough, the mean synoptic pressure gradient forces an easterly flow. The direction of the katabatic flow is mainly south-east at AWS 1 and 2 and more easterly at the other AWS due to the orientation of the predominant surface slope. This results in a generally easterly and very constant wind direction at almost all stations. Unfortunately, the wind direction sensor at AWS 4 has not worked properly, resulting in a lack of wind direction data for this station. However, from Neumayer data (Table 4.1) it is expected that the wind direction at AWS 4 is more variable than at the other weather stations due to its location on the ice shelf close to the coast.

The directional constancy, dc , is the ratio of the vector mean wind speed to the scalar mean. A high dc implies that the wind prefers a particular direction. All stations show high dc 's, ~ 0.70 at AWS 1, ~ 0.8 at AWS 2 and 3, and ~ 0.90 at AWS 5 to 9. The lower dc 's at AWS 1 and 2 are due to the larger difference in wind direction between the large-scale flow and the katabatic flow. Figure 4.5 shows histograms of the wind direction at AWS 1, 2, 5 and 9. At AWS 5 and 9 one maximum around 60° is visible, whereas at AWS 1 two marked tops can be seen. The first is a broad peak around 30° with two minor peaks around 20° and 40° , the general direction of the large-scale flow. The second is a sharp peak around 120° , around the direction of the surface slope, and represents the katabatic flow. At AWS 2, the top around 30° is

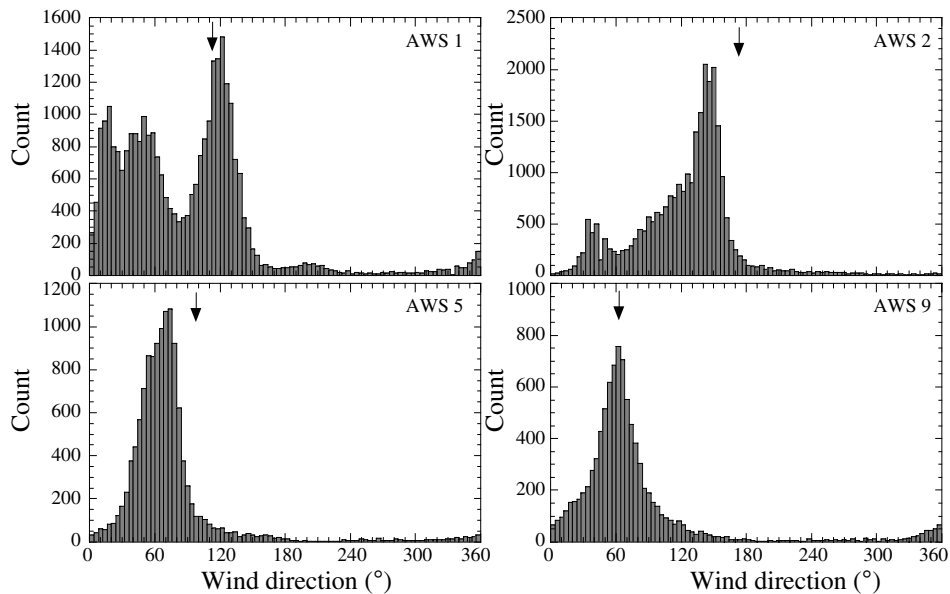


Figure 4.5. Wind direction distribution at AWS 1, 2, 5 and 9 over the entire measuring period based on hourly (AWS 1 and 2) and two-hourly (AWS 5 and 9) averages. The arrows indicate the direction of the surface slope based on a 10 by 10 km digital elevation model (data courtesy of J. Bamber, Bristol University).

much smaller than at AWS 1 while the maximum at 150° is much more pronounced and shows a larger influence of the katabatic flow at this site compared to AWS 1, although they are only ~ 30 km apart. The difference in direction of the katabatic peak is due to a difference in direction of the surface slope (arrows in Figure 4.5). The other stations show a single maximum similar to AWS 5 and 9. AWS 8 and 9 have very high dc 's compared to other stations on the Antarctic plateau. AWS 3, Dome C, Vostok and South Pole have lower dc 's, 0.80, 0.60, 0.81 and 0.79, respectively (King and Turner, 1997). This is caused by the larger surface slopes at AWS 8 and 9 compared to these stations (Table 1.1). At Relay station the surface slope is of the same magnitude as at AWS 8 as is the dc .

Temperature In general, the annual mean air temperature decreases with elevation. However, the temperature differences between the lower stations (AWS 1, 4, 5 and 6) are small or even reversed from what is expected from their elevation differences and a lapse rate of $0.006 - 0.008 \text{ K m}^{-1}$. For example, the annual mean temperature at AWS 5 is $\sim 3^\circ\text{C}$ higher than at AWS 4, while it is located ~ 300 m higher and ~ 100 km more southward. This temperature reversal was also found by Jonsson (1995), Van den Broeke *et al.* (1999) and Bintanja (2001). The potential temperature (θ) is actually increasing with elevation and has a maximum at the stations on the slope towards the plateau where also the wind speeds are highest. This is illustrated in Figure 4.6a, which presents θ at the AWS sites in order of increasing

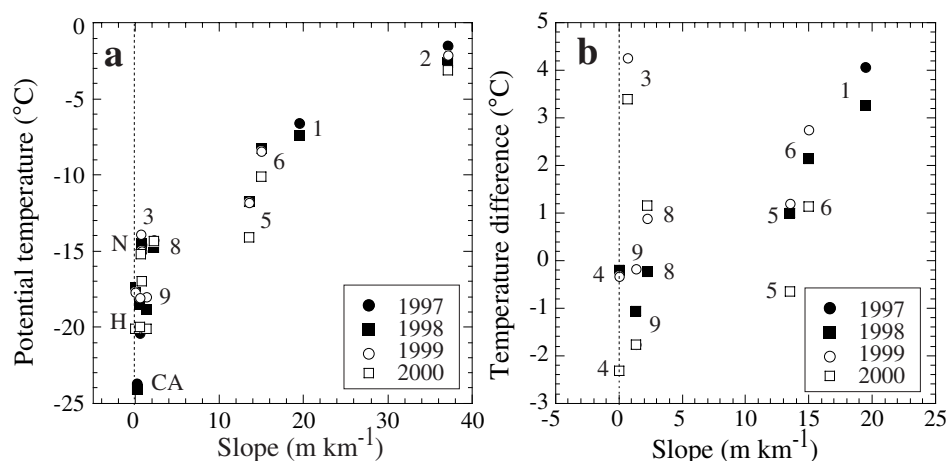


Figure 4.6. Annual mean (a) potential temperature and (b) temperature difference ($T - T_{10m}$) between the atmosphere (T) and 10 m firn (T_{10m}) for the AWS against slope (Table 1.1). The numbers denote the AWS sites: N, Neumayer; H, Halley; CA, Clean Air station South Pole.

surface slope. The increase in θ when going from the Antarctic plateau towards the coast is also found in the data presented by Allison *et al.* (1993) and Wendler *et al.* (1993, 1997). They present temperature and pressure measurements along two transects, from Dome C towards Dumont d'Urville and from Dome C towards Casey. Due to the proximity of the steep slope to the coast in Wilkes Land, no maximum is observed but an increase in θ towards the coast.

The maximum in θ in DML and the increase in θ in other regions of East Antarctica, can be attributed to the katabatic wind. Strong katabatic winds enhance vertical mixing and reduce the strength of the surface temperature inversion (Wendler *et al.*, 1993, 1997). This results in large sensible heat fluxes warming the surface, relatively high surface temperatures, and high potential temperatures (Ohata, 1985; Van den Broeke *et al.*, 1999). The high surface temperatures also intensify the outgoing longwave radiation so that the net longwave and net radiative flux become more negative. This phenomenon explains the small differences in air temperature between the lower stations (AWS 1, 4, 5 and 6) where not only the elevation increases with increasing distance from the coast but also the surface slope (Figure 4.2). It also explains the strong relation between the annual mean wind speed and the θ at locations with non-zero surface slopes.

The inter-annual temperature variability between the measured years is small, 1997 was $\sim 1^\circ\text{C}$ warmer than the following two years, 2000 was $\sim 1^\circ\text{C}$ colder than the previous two years. The differences between 1998 and 1999 are marginal. At Halley and Neumayer the variability in this period was similar. Over longer periods, the annual temperature is more variable, at Halley the annual mean temperature over the last 40 years varies between -21 and -16.5°C .

At all stations, except AWS 2, snow temperatures are measured. The snow temperature at ~ 10 m depth is often used as a measure for the long term annual mean

Table 4.3. Accumulation averages presented in the literature.

Site	Latitude	Longitude	Period	<i>acc.</i> (mm w.e. yr ⁻¹)	
				lit.	AWS
(1) Site A	71° 54.0'S	3° 05.0'E	1965-97	135±10	127±55
(2) Site C	72° 15.1'S	2° 53.5'E	1965-97	123±9	82±47
(3) Site M	75° 00.0'S	15° 00.1'E	1965-97	45±4	33±24
(4) C	72° 45.7'S	14° 35.4'W	1976-89	415	382±65
(5) D	73° 27.4'S	12° 33.5'W	1974-89	343	191±69
(6) H	74° 21.1'S	11° 43.3'W	1973-89	318	284±67
(8) CV	76° 00.0'S	8° 03.0'W	1965-97	68	60±31
(9) DML05	75° 00.2'S	0° 00.4'E	1801-97	62±21	78±16

Notes: Between brackets, the AWS closest to the location of the firn core or snow pit. *acc.*, accumulation; lit., from the literature and derived from snow pit and shallow firn core measurements; AWS, measured by the weather stations, uncertainty is the standard deviation in the annual mean.

References: Sites A, C, M, Isaksson *et al.* (1999); Van den Broeke *et al.* (1999); C, D, H, Isaksson and Karlén (1994); CV, Karlöf *et al.* (2000); DML05, Oerter *et al.* (2000).

surface temperature. At this depth the amplitude of the annual temperature wave is less than 5% of the surface value (Patterson, 1994). Table 4.2 presents the firn temperature at a depth close to 10 m (T_{10m}). At AWS 1 the initial depth was ~ 13 m, at the other stations ~ 10 m. Due to accumulation the depth of the sensors increases. T_{10m} is lower than the annual mean air temperature T and shows the same features, a decreases with elevation and relatively high values close to or on the steep slope towards the Antarctic plateau. At all sites, T_{10m} decreases ~ 0.1 °C per year. The difference in T and T_{10m} shows that the year 2000 was cold with respect to the long term annual mean and is largest at AWS 3. At the other sites the temperature difference displays a dependency on the surface slope (Figure 4.6b). The higher the surface slope the larger the difference, T_{10m} being lower than the air temperature. This is contrary to what is expected. A larger difference suggests a larger near surface temperature inversion while at the sites with a large surface slope this temperature inversion is partly destroyed by the high wind speeds. The surface temperature (T_0) is calculated from the outgoing longwave radiation assuming the snow to be a black body radiator with an emissivity of 1. At all AWS, T_0 and T_{10m} are of the same order of magnitude. However, the uncertainty in the longwave radiative fluxes (see Chapter 1) results in an uncertainty in the calculated surface temperatures of ~ 5 °C.

Accumulation The AWS measure the changes in instrument height, which is a measure for accumulation and includes processes such as snowfall, snowdrift, sublimation, deposition and densification of the snow pack. It is difficult to assess how much and when the accumulation is snowfall or snowdrift, since accumulation mostly occurs at strong winds. Table 4.1 presents annual mean accumulation values based on instrument height changes and mean snow densities as presented in Table 1.1. The given uncertainty is based on the uncertainty in the determined snow accumulation and firn density. Table 4.1 shows the expected decrease of the accumulation with altitude and distance from the coast, although the accumulation

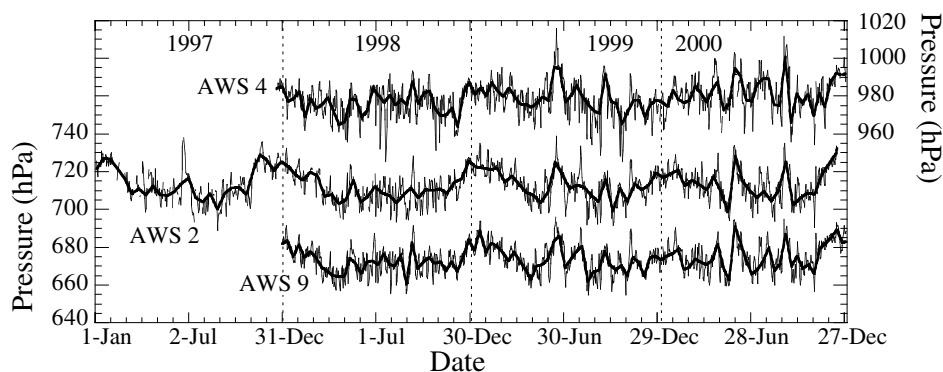


Figure 4.7. Daily averaged surface air pressure measured at AWS 4 (right axis), AWS 2 and AWS 9 (left axis). The thick lines represent smoothed curves.

is higher at AWS 6 than at AWS 5. This is not seen in ice core and snow pit studies (Table 4.3). Although located at approximately the same elevation, the accumulation at AWS 2 is higher than at AWS 8. This difference is due to the location of AWS 2 closer to the coast and on the slope towards the plateau, while AWS 8 is located further away from the coast and on the Antarctic plateau. Table 4.1 shows a large variability in the annual net accumulation. The accumulation exhibits no trend.

Table 4.3 presents accumulation values from the literature based on firn core and snow pit measurements in DML, close to or at the AWS locations. The AWS derived accumulation values are in reasonable agreement with the mean values derived from firn core and snow pit studies. Differences are explained by spatial variability in accumulation and differences in measuring period. At all AWS, except AWS 9, the average AWS measured accumulation is lower than the measurements presented in the literature but the year to year variability is considerable.

4.3.3 Seasonal cycle

As the inter-annual variations, the seasonal variations and the differences in seasonal variations between the stations depend on their geographical locations. In the figures, AWS 4 represents the coastal area and ice shelves, AWS 2 escarpment region, and AWS 9 the stations on the Antarctic plateau.

Pressure The pressure signal is variable on time scales of days to months. Figure 4.7 presents daily mean values of air pressure for AWS 4, 2 and 9, for January 1997 until December 2000. The other AWS show similar records. The variations on a daily scale are mainly due to meso-scale pressure systems (Parish, 1982; Jonsson, 1995). The more pronounced variations are seen in the records of all stations plus surrounding stations, such as Clean air (South Pole) and Relay station, almost simultaneously. This results in high correlations of the pressure signals. The correlations are highest when the stations are located reasonably close to each other.

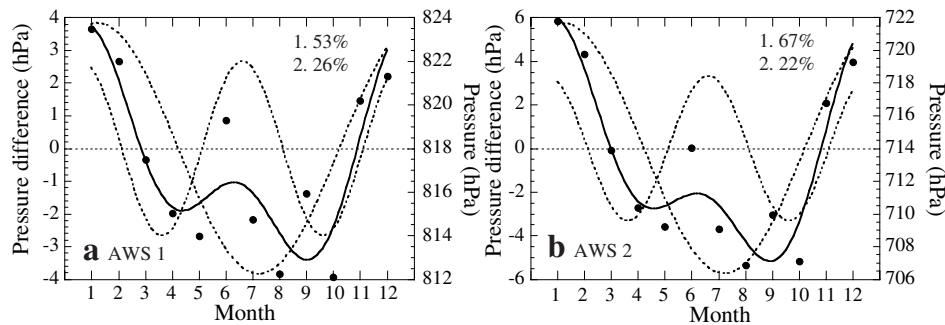


Figure 4.8. Monthly averaged pressure at (a) AWS 1 and (b) AWS 2, over the measuring period (right axis, dots). The dotted lines are the first and second harmonics and the solid line is the sum of the them (left axis). The numbers denote the amount of variance explained by the two harmonics.

Variations on larger time scales are due to phenomena like the (semi-)annual oscillation (SAO) in the pressure signal (Van Loon, 1972). The SAO consists of a twice-yearly expansion and contraction of the circumsolar pressure trough. In conjunction with the pressure changes, the circulation pattern around Antarctica changes, altering the transport strength of air from lower latitudes to Antarctica and influencing the Antarctic surface temperature (Van den Broeke, 2000a). Figure 4.8 presents two examples of SAO in the AWS data. The percentage of the variance in the signal explained by the (semi-)annual oscillation are calculated using Fourier analysis. The influence of the semi-annual signal increases from $\sim 25\%$ variance explained by the second harmonic at AWS 1 and 2, $\sim 30\%$ at AWS 4 to 8, to $\sim 40\%$ at AWS 3 and 9. These values are lower than the percentages presented by Van den Broeke (1998) for Sanae and Novolazarevskaya, 43% and 42%, respectively, over the period 1980-96. Differences can be explained by the different locations of the stations with respect to the average location of the circumsolar pressure trough and the different time periods used.

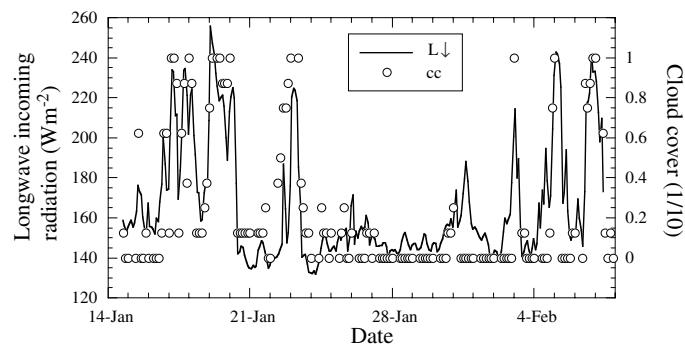


Figure 4.9. Two-hourly mean longwave incoming radiation ($L \downarrow$) measured at AWS 6 in January 1998 (left axis, solid line). The dots are the sum of the observed low and middle high cloud cover (cc).

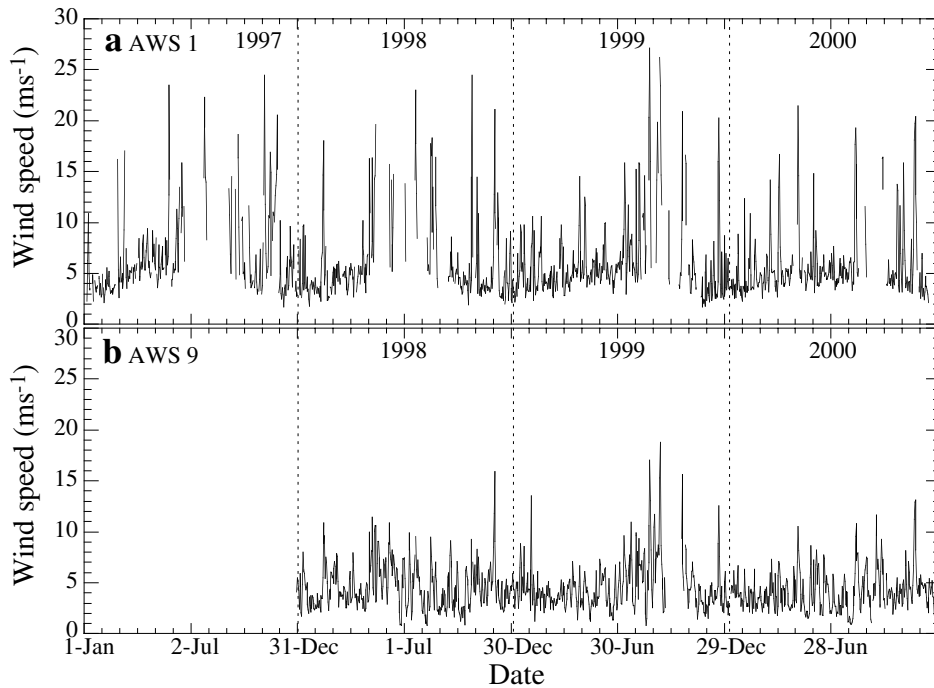


Figure 4.10. Daily mean wind speed at (a) AWS 1 and (b) AWS 9. Gaps in the data set are due to freezing of the wind sensor.

Radiation Although the annual average radiative balance R is determined by L and is negative, R is positive in summer when S dominates R . The annual variation in longwave radiation mainly follows the annual temperature wave. The short term variability on this curve is mainly determined by the sum of clouds at low and middle levels. Figure 4.9 presents the longwave incoming radiation at AWS 6 for a 3-week period in January 1998 during which cloud observations were made as part of the detailed glaciological and meteorological experiment in this area (Bintanja *et al.*, 1998; Bintanja and Reijmer, 2001). This figure shows the strong relation between $L \downarrow$ and cloud cover.

Wind speed and direction Because the katabatic flow is mainly forced by a negative net radiative flux which is balanced by a positive sensible heat flux cooling the near surface air, the wind speed and wind direction show an annual cycle related to the annual cycle in R . The annual cycle in the wind speed is largest for the stations with the highest surface slope. Figure 4.10 presents the daily averaged wind speed at AWS 1 and 9, the stations with respectively the largest and smallest amplitude in the annual wind speed curve. The amplitude is also small at AWS 3, 4 and 8. AWS 4 is located close to the coast and mainly influenced by large-scale weather conditions, while at AWS 3, 8 and 9 the surface slope is small so that the katabatic flow is not always well developed. AWS 3, 8 and 9 are only marginally influenced by the

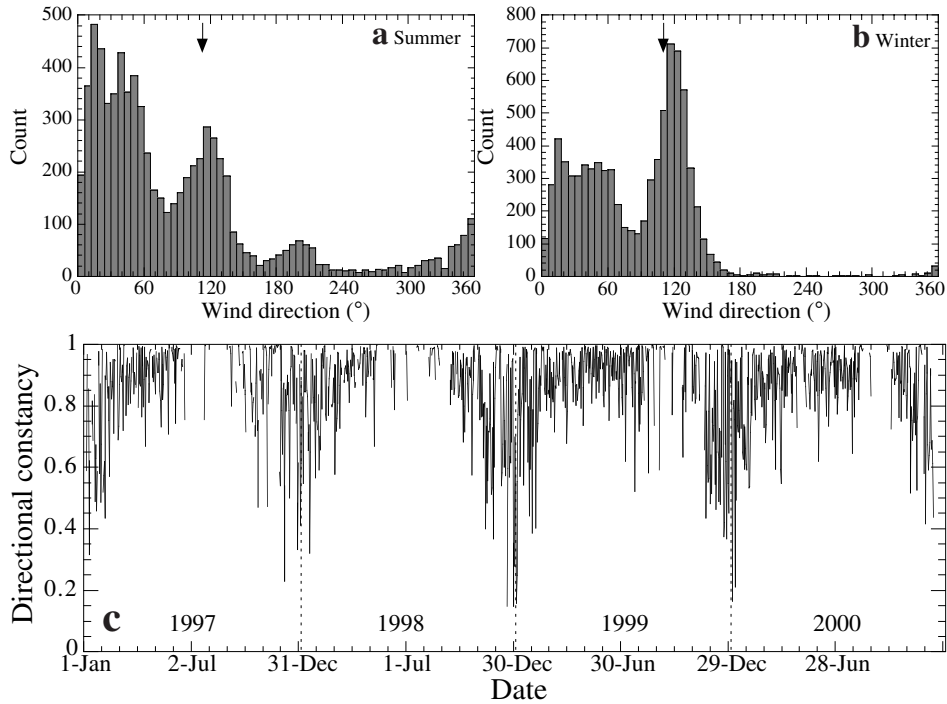


Figure 4.11. Wind direction distribution at AWS 1 over (a) all summer months (December, January, February) and (b) all winter months (June, July, August) based on hourly averages. The arrow indicates the direction of the surface slope based on a 10 by 10 km digital elevation model (data courtesy of J. Bamber, Bristol University). (c) Time series of daily mean directional constancy at AWS 1. Gaps in the data set are due to freezing of the wind sensors.

large-scale flow as seen in the high dc 's measured at these stations (Table 4.1). Figure 4.10 shows that the wind speed is very variable and can be very high. Maximum (two-)hourly mean wind speeds can reach 25 to 30 m s^{-1} and at AWS 1 a maximum 6 minute wind speed of 47 m s^{-1} was measured. The observed strong increases in wind speeds are often accompanied by a decrease in air pressure, a turning of the wind to more northerly directions by the geostrophic forcing, a strong increase in temperature and humidity, and sometimes snowfall (see Chapter 6), and are caused by passing low pressure systems.

The annual variability in wind direction is presented for AWS 1 in Figures 4.11a and b as wind direction distributions over all summer months and all winter months, respectively. In winter the peak around 120°, associated with the katabatic wind is much more pronounced than in summer. The wind direction not only has a more northern component in summer, but is also more variable. Figure 4.11c shows the daily mean directional constancy, which is smaller in summer than in winter.

Temperature and humidity The air temperature in DML is very variable, especially in winter when the meridional and vertical temperature gradients are largest.

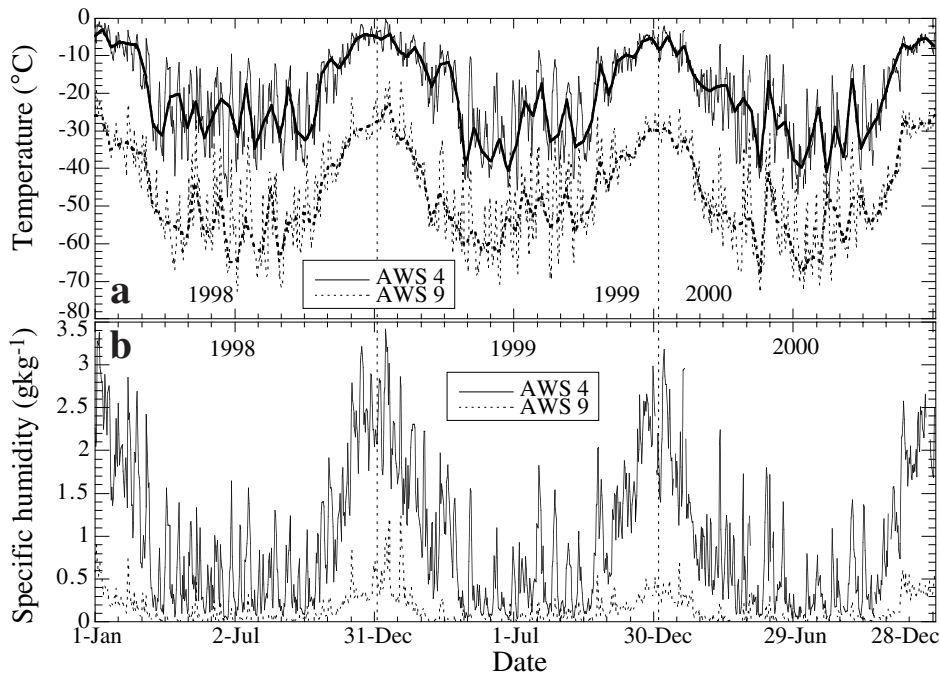


Figure 4.12. Daily mean (a) temperature and (b) specific humidity at AWS 4 (solid line) and 9 (dotted line). Thick lines are smoothed curves.

Variations of 20 to 30 °C within a few days are not uncommon and often measured at several stations almost simultaneously (Figure 4.12). These large changes in temperature often coincide with changes in wind speed and direction, and are due to passing low pressure systems advecting relative warm and moist maritime air to the south. The continental air advected under katabatic flow conditions is cold and dry. The lowest stations (AWS 4, 5 and 6) occasionally experience temperatures above 0 °C in summer, resulting in some melt. The lowest temperature measured is -78 °C at AWS 3.

The specific humidity is extremely low over Antarctica due to the low moisture holding capacity of the cold air. The relative humidity is on average low due to the mainly descending air over the continent. The decrease in temperature with increase in elevation and distance from the coast results in a decrease in specific humidity. The short term variability in humidity is large and shows a strong correlation with temperature (Figure 4.12b).

Accumulation The precipitation in coastal areas of Antarctica is often orographic induced (Bromwich, 1988). Most of the precipitation in western DML is associated with the development of an amplified wave pattern in the upper troposphere with a low pressure area over the Weddell Sea region and a high-pressure ridge over eastern DML (Noone *et al.*, 1999). This amplified wave pattern enhances northerly advection

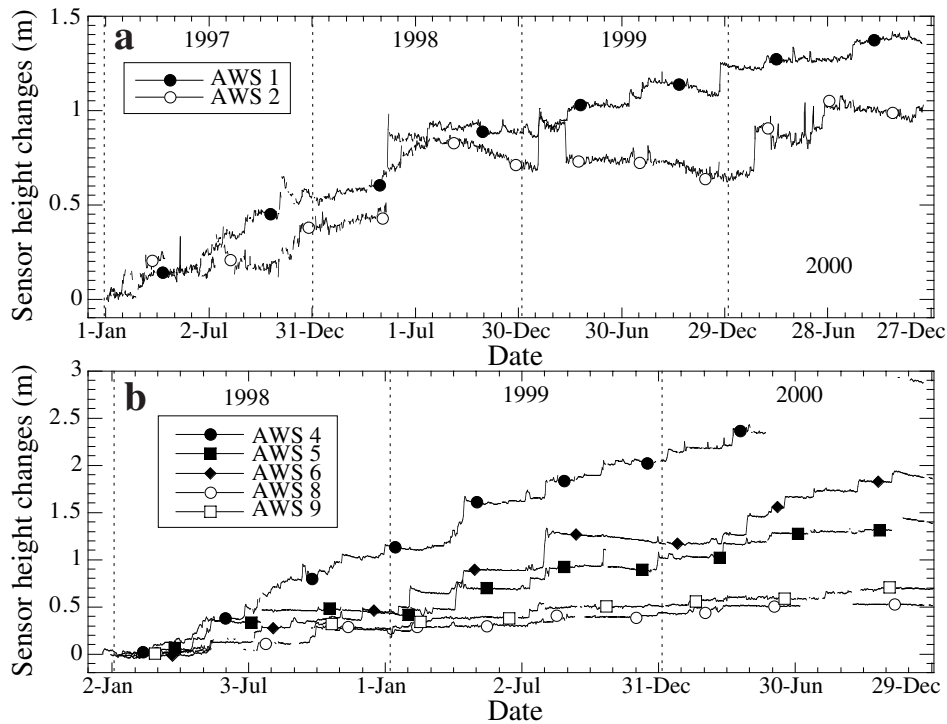


Figure 4.13. Daily averaged changes in sensor height (in m of snow). At the first measuring day the change is 0 m.

over the shelf area and in combination with the steep orography of DML the air is forced to rise and snowfall is generated. The development of this type of flow pattern occurs only a few times per year. The result is an accumulation pattern that consists of a few major events seemingly randomly distributed over the year. Figure 4.13 presents daily averaged changes in sensor height. The sudden jumps in the records are the major accumulation events, which occur 4 to 5 times per year and often bring snow over large areas. The events contribute $\sim 80\%$ of the total accumulation. The largest events produce accumulation at all weather stations. The number of major events and the amount of precipitation per event decrease with distance from the coast and elevation as can be seen in Figure 4.13.

Locally, not all precipitation results in a net accumulation. For example, in February 1999 ~ 0.3 m snow accumulated at AWS 2 in one event, but almost everything was blown away at the end of March 1999, resulting in an almost zero net accumulation in 1999. Figure 4.13 also shows the occurrence of densification and sublimation of the snow pack after a major event. See for example the increase in sensor height at AWS 6 after the event in February 1999. The increase in sensor height over periods of months as seen for AWS 6 and also at AWS 2, is mainly due to settling of the snow pack and a little sublimation. It also shows an increase in settling and sublimation

during the summer months.

Due to the nature of the accumulation events, three or four years of accumulation measurements is not sufficient to determine seasonality in the accumulation. GCM results show that at least 5 to 10 years accumulation are necessary to obtain a significant annual cycle in the accumulation. The fact that most of the accumulation occurs in a few major events per year, not confined to a particular season has serious implications for the analysis of for example the $\delta^{18}\text{O}$ in ice cores (Schlosser, 1999). The absence of net accumulation in a certain year as observed at AWS 1 in 2000, and 2 in 1999, hampers the interpretation even more.

4.3.4 Daily cycle

The AWS in DML are all located south of the Antarctic polar circle, which means that the sun is below the horizon several months per year. The lack of a diurnal varying forcing in winter results in an absence of a diurnal cycle in the meteorological parameters in this time of the year. In the summer months the diurnal variations in mainly incoming solar radiation $S \downarrow$ and albedo α cause a diurnal varying positive (towards the surface) net shortwave radiative flux, which forces variations in other meteorological parameters. Figure 4.14 presents the diurnal cycle in $S \downarrow$, α , temperature, relative humidity, specific humidity, wind speed, wind direction and directional constancy at AWS 2, 4 and 9 averaged over all months of January.

Figures 4.14a and b present the diurnal variations in $S \downarrow$ and α . The amplitude of the diurnal variations in $S \downarrow$ is largest for the most northern stations (compare AWS 2 and 9). Cloud amount decreases with increasing distance from the coast and therefore $S \downarrow$ is lower closer to the coast (compare AWS 4 and AWS 9). The albedo exhibits a minimum at the lowest solar zenith angles, i.e., around solar noon. The diurnal cycle in temperature is most pronounced at AWS 9 on the plateau. Near the coast, the oceans are ice free in January and have a moderating effect on the temperature at AWS 4. Furthermore, the heat conductivity and capacity of snow decreases for drier and lower density (inland) snow resulting in an amplification of the extremes at more inland locations. At AWS 2 the mean wind speed is highest. At this location (and other slope locations), the stronger mixing does not allow for the diurnal buildup of the boundary layer to the same extent as in flatter areas resulting in a smaller temperature amplitude at the slope stations. Although the specific humidity shows a maximum in the afternoon, the relative humidity exhibits a minimum during day-time owing to the variations in temperature, varying the maximum possible amount of moisture in the air.

The net radiation warms the surface and (partly) destroys the surface temperature inversion. A decrease in strength of the temperature inversion results in an increased vertical transport of horizontal impuls. In areas where the katabatic winds are weakly developed (non-sloping areas), this results in an increase in wind speed in day-time while in areas where the katabatic wind is well developed (sloping areas with a maximum wind speed close to the surface) the wind speed decreases. Figure 4.14d shows both regimes. At AWS 4 and 9 the wind speed increases during day as seen at Dome C by Wendler and Kodama (1984), while at AWS 2 the wind

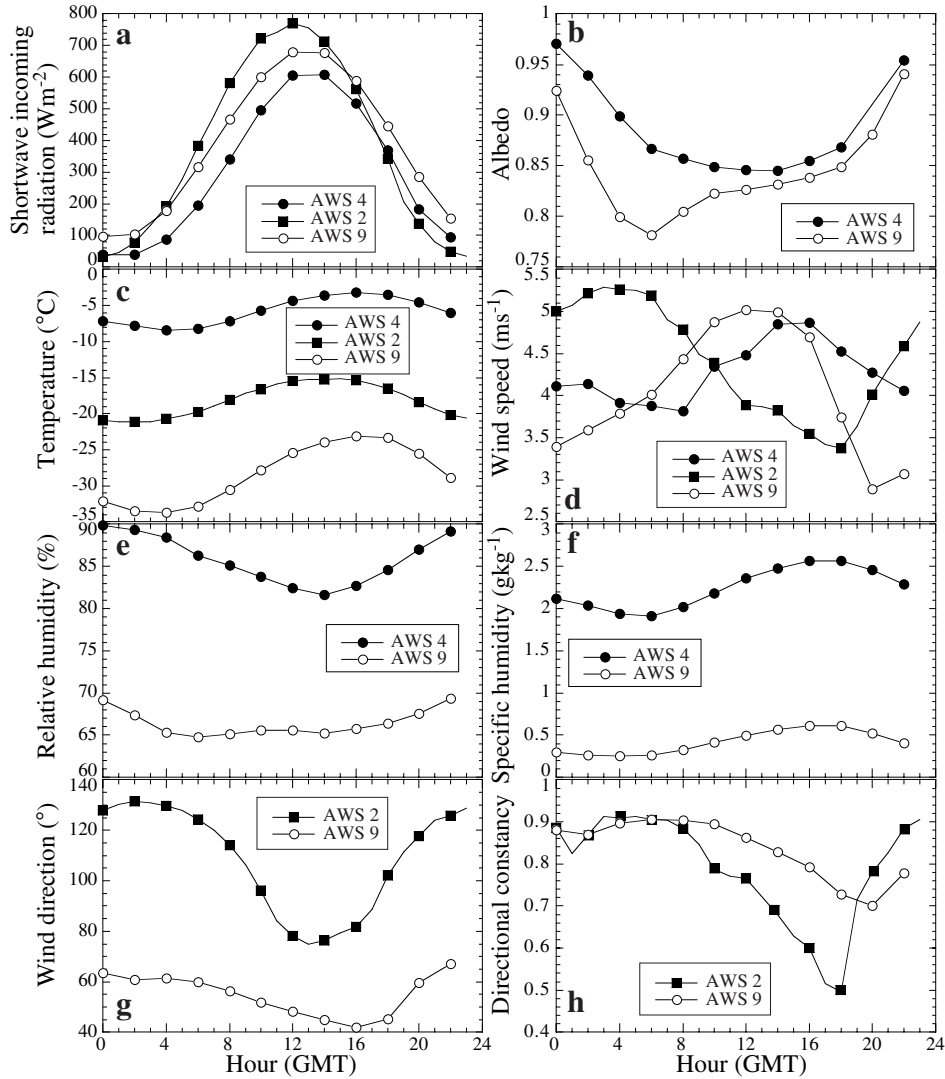


Figure 4.14. Average diurnal variations of (a) shortwave incoming radiation, (b) albedo, (c) air temperature, (d) wind speed, (e) relative humidity, (f) specific humidity, (g) wind direction and (h) directional constancy in January over the three or four-year measuring period at AWS 4, 2 and 9.

speed decreases, as seen at D-47, a station on the slope of the continent in Wilkes Land (Figure 4.1) (Wendler *et al.*, 1988). The time lag between the minimum in wind speed and the maximum in temperature is ~ 4 hours (Wendler *et al.*, 1988), the time the katabatic wind needs to adjust to changes in the forcing. The decrease in inversion strength also affects the wind direction and the directional constancy. Due to the weakened katabatic forcing, the variability in wind direction increases and the

directional constancy decreases. The wind direction turns anti-clockwise to more northerly and easterly directions, the direction of the large-scale geostrophic flow. Figure 4.14g also shows that the difference in wind direction between the large-scale flow and the katabatic flow is larger at AWS 2 than at AWS 9.

4.4 Summary and concluding remarks

The data of eight Automatic Weather Stations located in Dronning Maud Land, Antarctica, are presented. The stations have provided us with a fairly complete three to four-year data set. DML is divided into three regions similar to the regions defined by Fortuin and Oerlemans (1990); the ice shelves, the escarpment region and the Antarctic plateau. The regions are distinguished by their climatic and topographic settings, which results in typical characteristics with respect to mean values, and annual and diurnal cycles of the meteorological variables.

Near the coast, on the ice shelves the surface is flat, resulting in a weak katabatic flow, and conditions are mainly determined by the large-scale geostrophic flow. The wind direction is variable, and directional constancies reasonably low (~ 0.60) compared to other Antarctic locations. The wind speed does not show an annual cycle, and shows a maximum during day-time in the diurnal cycle, which is typical for stations not affected by a strong katabatic flow. At AWS 4 annual mean temperature is $\sim -20^\circ\text{C}$ and annual mean wind speed is $\sim 4.5\text{ m s}^{-1}$.

In the escarpment region and on the Antarctic plateau the data show the important influence of the katabatic wind on the meteorological conditions. The wind speed shows a maximum on the slope towards the plateau where the katabatic forcing is largest. Annual mean wind speed ranges from $\sim 3.5\text{ m s}^{-1}$ at AWS 3 on the plateau to $\sim 7\text{ m s}^{-1}$ on the slope (AWS 1, 2, 5 and 6). The strong katabatic winds enhance vertical mixing and reduce the strength of the surface temperature inversion (Wendler *et al.*, 1993). This results in large sensible heat fluxes warming the surface, visible in a maximum in potential temperature at the locations with the highest wind speed. The annual mean potential temperature varies between -18°C on the plateau and -1°C on the slope at AWS 2. At the slope stations a clear annual cycle in the wind speed is observed, higher wind speed in winter compared to summer, owing to the stronger cooling. In summer, diurnal variations in katabatic forcing result in diurnal variations in wind speed. The wind direction is constant and mainly determined by the down slope katabatic wind. The directional constancy varies between 0.67 at AWS 1 to 0.93 at AWS 5. The accumulation is highest near the coast and decreases with increasing distance from the coast, from $\sim 400\text{ mm w.e.yr}^{-1}$ at AWS 4 to $\sim 30\text{ mm w.e.yr}^{-1}$ at AWS 3.

Chapter 5

The temporal and spatial variability of the surface energy balance in Dronning Maud Land, East Antarctica

Summary

The data of seven Automatic Weather Stations (AWS) presented in the previous chapter are used together with a model based on Monin-Obukhov similarity theory, to calculate the surface energy budget for a two and three-year period. The surface conditions are determined largely by a katabatic flow resulting in a maximum in potential temperature and wind speed at the sites with the steepest slope. The annual average energy gain at the surface from the downward sensible heat flux varies between $\sim 3 \text{ W m}^{-2}$ and 25 W m^{-2} , with the highest values at the sites with the highest wind speeds and potential temperatures. The negative net radiative flux largely balances the sensible heat flux and ranges from $\sim 2 \text{ W m}^{-2}$ to $\sim 28 \text{ W m}^{-2}$; maxima are related to the maxima in surface slope and wind speed and suggest a strong connection between the heat budget and the katabatic flow in DML. The average latent heat flux is generally small and negative ($\sim -1 \text{ W m}^{-2}$) indicating mass loss through sublimation.

¹This chapter is based on: Reijmer, C.H. and J. Oerlemans, 2000. Temporal and spatial variability of the surface energy balance in Dronning Maud Land, East Antarctica. *J. Geophys. Res.*. Submitted.

5.1 Introduction

Surprisingly little is known about the spatial and temporal distribution of the surface energy budget over Antarctica, although much effort has been put into Antarctic meteorological and glaciological research in recent years. This constitutes a significant gap in our understanding of the Antarctic climate. The surface energy balance consists of five main components and can be expressed as:

$$S + L + H + LE + G = 0, \quad (5.1)$$

in which S and L are the net shortwave and net longwave radiative flux, respectively. H and LE are the turbulent fluxes of sensible and latent heat, respectively, and G is the subsurface energy flux including melt. The surface energy budget is of great importance for the near surface climate and mass balance through, e.g., the katabatic flow, which is forced when net radiation at the surface is negative and the near surface air is cooled, and surface sublimation. In the literature presented energy budgets are usually limited to single stations (Carroll, 1982; King *et al.*, 1996; Reijmer *et al.*, 1999a), measuring periods are usually limited to the summer months (Ohata, 1985; Bintanja, 2000) and often not all budget terms are calculated (Stearns and Weidner, 1993). In this chapter we present the complete energy balance for several locations in Antarctica and over a period of several years.

At present, the Institute for Marine and Atmospheric Research Utrecht (IMAU) operates nine Automatic Weather Stations (AWS) in Dronning Maud Land (DML), Antarctica (Figure 5.1) with the main objective to extend our knowledge of the near surface climate and heat budget of Antarctica. Data from the AWS is presented in the previous chapter and gives us insight into the meteorological conditions in DML over a period of several years following up on the studies of Jonsson (1995), König-Langlo *et al.* (1998) and Bintanja and Reijmer (2001). The data could also be used to validate climate and weather prediction models currently used to study the Antarctic climate (Genthon and Braun, 1995; King and Connolley, 1997; Krinner *et al.*, 1997b; Van Lipzig *et al.*, 1999).

The weather stations are a contribution to the European Project for Ice Coring in Antarctica (EPICA). The broad objective of EPICA is to reconstruct the Antarctic climate record with high resolution. To achieve this objective, two deep ice cores will be drilled, of which one lies in DML. The purpose of the AWS within this project is to increase our knowledge about the mass balance in DML and to study the energy exchange between atmosphere and snow surface, and therefore help with the interpretation of ice cores.

In this study we examine the spatial and temporal variability of the surface energy budget in DML. The surface energy budget is determined using measurements and model calculations. Section 5.2 briefly describes the experimental set-up and location of the weather stations. The experimental set-up is more extensively described in Chapter 1. The experimental description is followed by a general description of the meteorological conditions in DML, which are more extensively described in Chapter 4. Section 5.4 gives a brief description of the energy balance model and

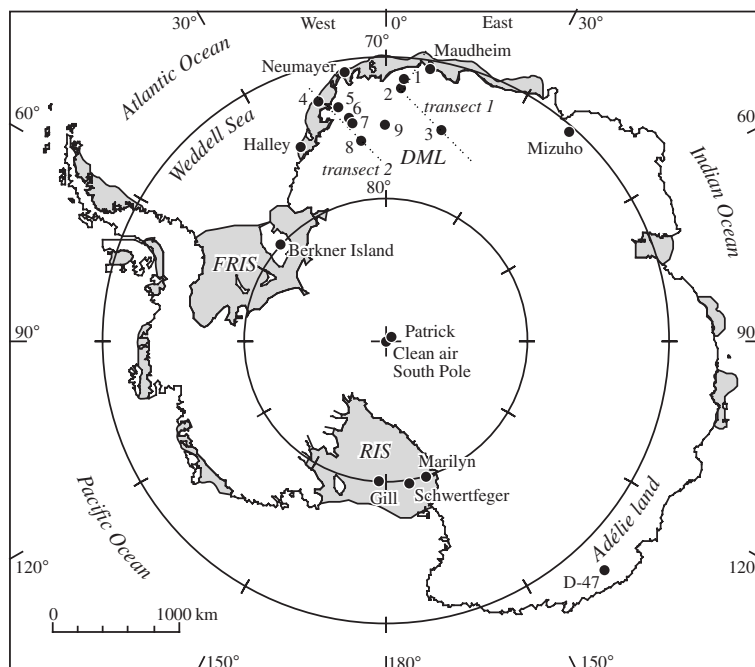


Figure 5.1. Map of Antarctica, showing the locations of the Automatic Weather Stations (AWS) and other stations mentioned in this chapter. AWS 9 is located ~ 2 km west of the EPICA drilling site in Dronning Maud Land (DML). Shaded areas are ice shelves (FRIS, Filchner Ronne Ice Shelf; RIS, Ross Ice Shelf) and dotted lines indicate the transects presented in Figure 5.2.

a verification of the model. The results of the budget calculations are described in Section 5.5 and discussed in Section 5.6.

5.2 Location and experimental set-up

The location and experimental set-up of the weather stations in DML is extensively described in Chapter 1. In this section a brief summary of the important details is given. Figure 5.1 shows the locations of the nine AWS in DML (see also Figure 1.4) and other stations mentioned in this chapter (see Table 1.1 for more details). The locations of the AWS were chosen such that they cover a substantial part of western DML and represent different climate regimes. AWS 4 is located in the coastal area on an ice shelf, AWS 5 on the lower part of the ice sheet near the grounding line, AWS 1, 2, 6 and 7 close to or on the steep slope towards the Antarctic plateau and AWS 3, 8 and 9 on the Antarctic plateau. Figure 5.2 shows two elevation transects along AWS 3, 2 and 1 to the coast (transect 1) and along AWS 8, 6, 5 and 4 to the coast (transect 2). AWS 9 is located between these two transects.

All stations measure air temperature, wind speed, wind direction, instrument height, air pressure and incoming shortwave radiation (Figure 1.5). Except AWS 2,

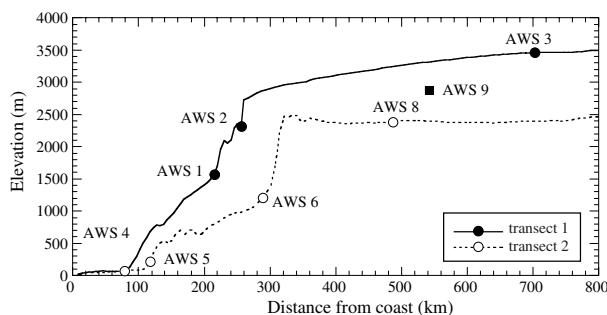


Figure 5.2. Elevation transects along AWS 3, 2 and 1 to the coast (transect 1) and along AWS 8, 6, 5 and 4 to the coast (transect 2) (see Figure 4.1). Based on data of a 10 by 10 km digital elevation model (data courtesy of J. Bamber, Bristol University).

all stations additionally measure firn temperatures at eight (AWS 1 and 3) or ten (AWS 4 to 9) different depths. AWS 4 to 9 additionally measure relative humidity, reflected shortwave radiation and incoming and outgoing longwave radiation. The initial height of the instruments was ~ 3 m above the surface (Table 1.1). The accuracy of the sensors is discussed in Chapter 1. Hourly (AWS 1 to 3) or two-hourly (AWS 4 to 9) averages are stored locally and transmitted using Argos transmitters. Problems with data transmission occasionally result in gaps in the data set. AWS 3, 8 and 9 stop transmitting in winter due to low temperatures. The results presented here comprise a three-year data set for AWS 1 to 3 and a two-year data set for AWS 4 to 9.

5.3 Prevailing meteorological conditions

The meteorological conditions are more extensively described in Chapter 4. Here, we give a short description. The climate in DML is mainly influenced by transient cyclones travelling eastward along the coast. The influence of the cyclones decreases towards the interior of DML, where the near surface climate is increasingly dominated by the katabatic flow (Parish and Bromwich, 1991, 1998). The results of the energy balance calculations in the next sections are presented in terms of the geographical locations of the AWS. For the purpose of clarity, DML is divided into three regions similar to the regions presented by Fortuin and Oerlemans (1990); the ice shelves, the escarpment region and the Antarctic plateau. The regions are distinguished by their climatic and topographic settings, which results in typical characteristics with respect to mean values, long-term variations and diurnal cycle of the meteorological variables. To illustrate the general near-surface conditions in DML, Figure 5.3 presents monthly mean air temperature, specific humidity, wind speed and daily mean accumulation for AWS 4, 6 and 9. AWS 4 represents the ice shelves region, AWS 6 the escarpment region and AWS 9 the plateau region. Table 5.1 presents annual averages of temperature, wind speed and humidity for all stations.

The air temperature in DML is highly variable, especially in winter when the north-south and vertical temperature gradients are largest. Fluctuations of 20 to

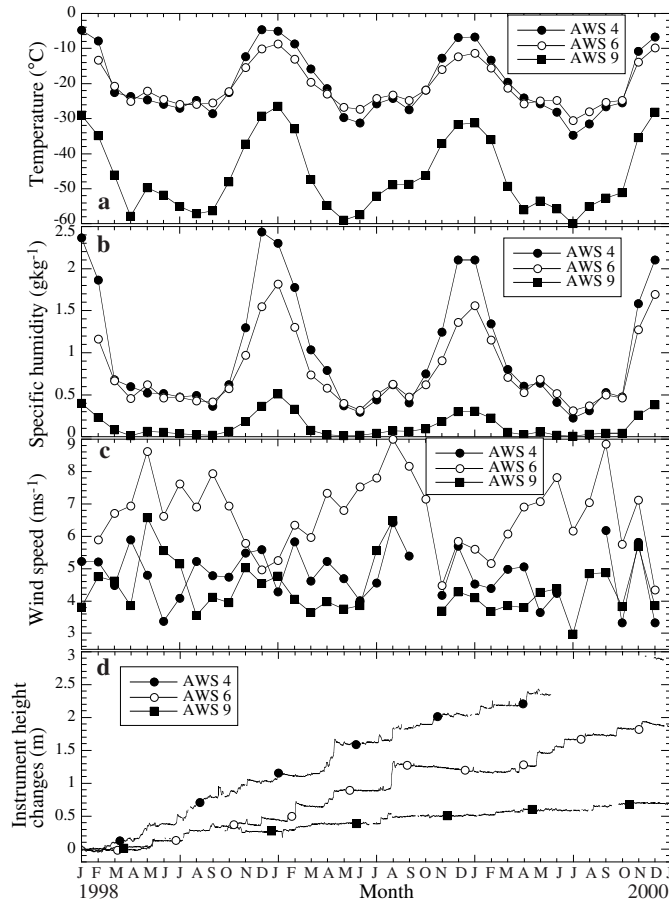


Figure 5.3. Monthly mean (a) air temperature, (b) specific humidity and (c) wind speed, and (d) daily mean instrument height changes of AWS 4, 6 and 9 for the period January 1998 until December 1999.

30 °C within a few days are not uncommon and are often measured at several stations almost simultaneously (not shown). In summer, the lowest stations (AWS 4, 5 and 6) occasionally experience temperatures above 0 °C. The annual and monthly mean temperature differences between the lowest stations (AWS 1, 4, 5 and 6) are small or even reversed from what is expected from their elevation differences (Figure 5.3a, AWS 4 and 6). For example, the annual mean temperature at AWS 5 is ~ 3 °C higher than at AWS 4, while located ~ 300 m higher and ~ 100 km more southward. This temperature reversal is attributed to the increase in katabatic wind speed with increasing surface slope and was also found by Jonsson (1995) and Van den Broeke *et al.* (1999). The measured inter-annual variability is small. The relative as well as the specific humidity decreases with distance from the coast and increasing elevation (Figure 5.3b and Table 5.1). The specific humidity is extremely low, especially in winter with values of 0.5 g kg^{-1} near the coast to 0.05 g kg^{-1} on the plateau. The

Table 5.1. Annual averages of the meteorological data for the AWS.

AWS	yr	T (°C)	θ (°C)	RH (%)	q (g kg ⁻¹)	WS (m s ⁻¹)	α	$acc.$ (mm w.e.)
1 (1420)	1997	-21.5	-6.6	-	-	6.8	-	211±8
	1998	-22.7	-7.4	-	-	6.1	-	130±8
	1999	-	-	-	-	6.2	-	133±8
2 (2400)	1997	-26.3	-1.5	-	-	6.7	-	111±21
	1998	-27.9	-2.6	-	-	6.3	-	88±15
	1999	-27.6	-2.1	-	-	6.7	-	13±15
3 (3453)	1999	-47.8	-13.9	-	-	3.9	-	39±16
4 (34)	1998	-19.2	-17.4	76.6	1.02	4.9	0.86	452±61
	1999	-19.3	-17.7	77.2	1.01	5.0	0.88	371±51
5 (363)	1998	-16.4	-11.7	70.8	1.02	6.6	0.83	144±28
	1999	-16.4	-11.8	71.1	1.01	6.4	0.84	270±27
6 (1160)	1998	-20.1	-8.2	67.1	0.77	6.6	0.81	207±23
	1999	-20.1	-8.4	68.9	0.80	6.8	0.83	333±38
8 (2399)	1998	-38.3	-14.8	63.9	0.23	5.4	-	90±7
	1999	-37.7	-14.3	64.0	0.25	5.2	0.80	62±5
9 (2892)	1998	-46.1	-18.8	58.5	0.13	4.6	0.83	91±8
	1999	-45.3	-18.1	59.5	0.14	4.7	0.84	84±7

Notes: Averages are based on hourly (AWS 1 to 3) or two-hourly means (AWS 4 to 9). To obtain averages over a complete year, missing days in January 1997 (AWS 2) and January 1998 (AWS 5, 6 and 8) are replaced with corresponding days of January 1998 and 1999, respectively. The accumulation values are based on sensor height measurements and measured density (Table 1.1). Between brackets the elevation of the stations in m a.s.l, dashes indicate that no means could be calculated due to lack of data. T , temperature; θ , potential temperature; RH , relative humidity; q , specific humidity; WS , wind speed; α , albedo; $acc.$, accumulation.

short-term variability in relative as well as specific humidity is large and shows a strong correlation with temperature. At all stations except AWS 4 and 9, a clear annual cycle in wind speed is observed (Figure 5.3c). The wind speed is higher in winter due to the stronger katabatic forcing. Maximum (two-)hourly mean wind speeds can reach 25 to 30 m s⁻¹. Annual mean wind speeds vary between ~4 m s⁻¹ at AWS 3 on the plateau, ~5 near the coast (AWS 4) and near AWS 8 and 9, to ~7 m s⁻¹ at the other stations. The wind speed at AWS 1 and 2 is probably under-estimated, due to freezing of the sensors in winter. Accumulation is derived from sensor height measurements and decreases with distance to the coast and increasing elevation. Accumulation occurs mainly in a few major events per year contributing ~80% to the total annual accumulation (Figure 5.3d). The annual variability is large, especially at the high accumulation sites close to the coast. If we assume mean densities of 390 g kg⁻¹ at AWS 4 (data courtesy of L. Karlöf, 1999) and 335 g kg⁻¹ at AWS 9 (data courtesy of H. Oerter, 2000), then the annual accumulation amounts to 452 ± 80 mm w.e. yr⁻¹ near the coast (AWS 4) and 91 ± 11 mm w.e. yr⁻¹ on the plateau (AWS 9) in 1998. This is a bit higher than the mean values derived from shallow firn core studies. Isaksson and Karlén (1994) present an averaged value of 415 mm w.e. yr⁻¹ (1976-89) near the coast near AWS 4, and Karlöf *et al.* (2000) and Oerter *et al.* (2000) present average values of 68 mm w.e. yr⁻¹ (1965-97) and 62 mm w.e. yr⁻¹ (1801-97) for the Antarctic plateau near AWS 8 and 9, respectively.

5.4 Model description and validation

The surface energy fluxes presented in Section 5.5 are partly based on measurements and partly based on model calculations. The model we use to calculate the turbulent fluxes and subsurface temperatures is extensively described in Chapter 3 and by Greuell and Konzelman (1994) and Reijmer *et al.* (1999a). Here, we give a short description.

Equation 5.1 presents the surface energy balance. Fluxes towards the surface are taken positive. S can be expressed as $(1 - \alpha)S_g$ where α is the surface albedo and S_g the global radiation at the surface. S_g and α are derived from measurements or, when measurements are not available, α is taken constant (AWS 1 and 2, $\alpha = 0.82$). L equals the incoming minus the emitted longwave flux ($L \downarrow - L \uparrow$). $L \downarrow$ is directly measured (AWS 4 to 9) or parameterised as a function of screen-level (2 m) temperature (T_a , in K) (AWS 1, 2, and 8):

$$L \downarrow = 27.17 + 3.3616 * 10^{-8} T_a^4 . \quad (5.2)$$

The parameterization is based on two-hourly mean measurements of $L \downarrow$ and T_a at AWS 6 and 9. T_a is calculated from the measured temperatures using the flux-profile relations presented in Chapter 3. No dependency on humidity or cloud cover could be included because the stations do not measure these variables. Since $L \downarrow$ is strongly dependent on humidity and cloud cover (see Chapter 4), this introduces a significant error in the calculated $L \downarrow$. Figure 5.4 illustrates the performance of equation 5.2 and a parameterisation presented by King (1996) (see equation 3.4). Both parameterisations under-estimate the variability in $L \downarrow$ due to the omission of humidity and cloud cover in the parameterisations. Equation 5.2 explains $\sim 34\%$ of the total variance, the parameterisation of King (1996) $\sim 19\%$. The annual mean $L \downarrow$ is under-estimated by $\sim 8\%$ when using equation 5.2 and over-estimated by $\sim 8\%$ when using King (1996) (Equation 3.4). $L \uparrow$ is calculated using the Stefan-Boltzmann law for black body radiation, $L \uparrow = \sigma T_0^4$, with surface temperature T_0 , Stefan-Boltzmann constant σ and an emissivity of 1.

The surface temperature T_0 is calculated using a firn model. In the firn model the subsurface temperatures are calculated on a vertical grid extending 25 m into the firn. This model includes shortwave radiation penetration, melting, refreezing and densification of the snow pack. The surface temperature is a linear extrapolation of the firn temperature of the upper two grid layers. The initial profiles of temperature are based on snow temperature measurements and the initial profiles of density are based on firn core measurements (data courtesy of M.R. van den Broeke, 1999, L. Karlöf, 1999 and H. Oerter, 2000).

The turbulent fluxes are calculated from the vertical gradients in wind speed, temperature and specific humidity between sensor height and the surface using Monin-Obukhov similarity theory. In unstable conditions the stability functions presented by Högström (1988) are used, in stable conditions the functions presented by Duynkerke (1991). The surface roughness length of momentum is assumed to be 0.1 mm (King and Turner, 1997) and empirically determined. The surface roughness lengths of heat and moisture are calculated using the method described by Andreas

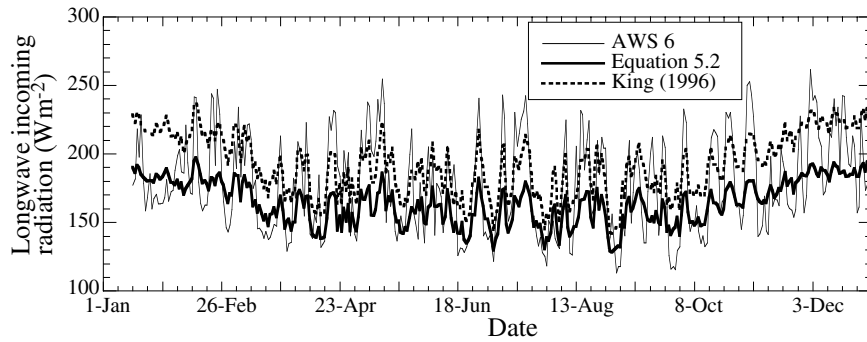


Figure 5.4. Longwave incoming radiation measured at AWS 6 for 1998 (thin solid line), parameterised using equation 5.2 (bold solid line) and parameterised using equation 4 of King (1996) (Equation 3.4) (bold dashed line).

(1987). T_0 is taken from the firn model. The specific humidity at the surface is the ice-saturation value for T_0 . The screen-level temperatures and specific humidities are calculated from temperature and relative humidity measurements corrected for changes in measurement height. For AWS 1 and 2 the relative humidity was not measured and therefore taken constant ($RH = 65\%$, which is $\sim 2\%$ lower than the average RH measured at AWS 6 and 8, stations located at slightly lower elevation than AWS 1 and 2). The subsurface energy flux is the residual of the other terms and is subdivided into a conductive heat flux, a penetrating part of the shortwave radiative flux, melting and refreezing.

The only measurements available to tune the model with, are $L \uparrow$ and the subsurface temperatures. The model is fine-tuned using the extinction coefficients for solar radiation to minimise the difference in simulated and measured $L \uparrow$ (when available), else by minimizing the temperature difference between simulated snow temperatures and measurements of the highest snow sensor. This method can be used for all sites except AWS 2. The resulting differences are presented in Table 5.2 and Figure 5.5. Figure 5.5a presents the simulated and measured $L \uparrow$ and the difference between the two for January 1998 at AWS 4 after tuning. Other stations show similar results. During the short peaked summer $L \uparrow$ is slightly over-estimated and in winter slightly under-estimated. On average, simulated $L \uparrow$ is under-estimated, which implies that the simulated T_0 is also on average under-estimated by $\sim 0.4^\circ\text{C}$ at AWS 4, 5 and 6, $\sim 1.6^\circ\text{C}$ at AWS 8 and $\sim 3.8^\circ\text{C}$ at AWS 9 (Table 5.2). In winter, AWS 8 and 9 have problems with measuring $L \uparrow$ due to the low temperatures (Chapter 1). This could explain part of the larger differences between measured and simulated $L \uparrow$ at these sites. However, the differences found are smaller than the estimated uncertainty of 20 W m^{-2} in the longwave radiation measurements. The extreme values are larger than 20 W m^{-2} and represent surface temperature differences up to 20°C .

Figure 5.5b presents the measured and simulated snow temperature at initial depth of 0.05 m and the temperature difference for AWS 4, after tuning. Note that the depth of the snow temperature sensors slowly increased due to accumulation. In

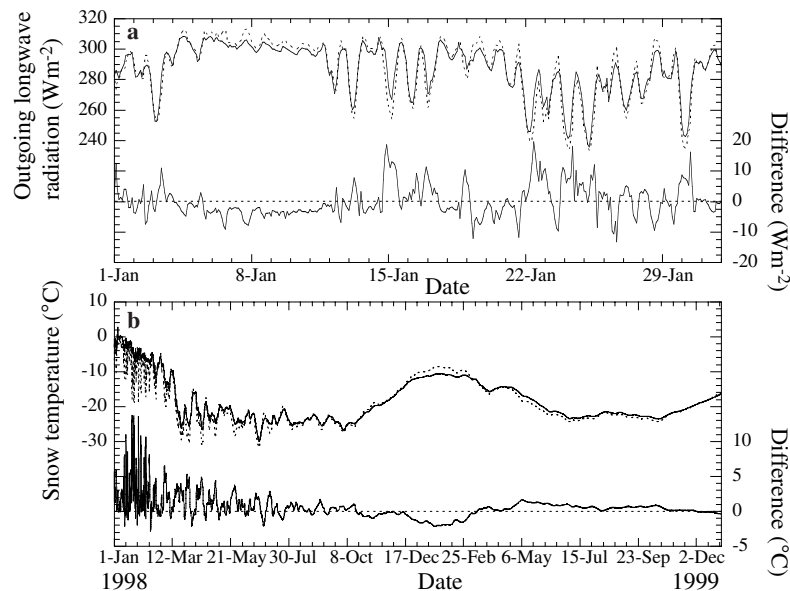


Figure 5.5. (a) Measured (solid line) and simulated (dotted line) outgoing longwave radiation and the difference between the two (measured minus simulated) for January 1998 for AWS 4. (b) Measured and simulated snow temperature at initial dept of 0.05 m and the difference between the two (measured minus simulated) for AWS 4, for 1998 and 1999.

the first summer, when the sensor is still reasonably close to the surface, the snow temperature is most variable and differences are largest and show large variations. When snow depth increases the variability on time scales of days decreases and differences in simulated and measured temperature diminish. The simulated temperatures are too low in summer and too high in winter. The amplitude of the simulated annual temperature cycle is too small, the average temperatures are too high and the snow pack slowly warms at all stations.

AWS 6 is located at the same location as site 3 of Bintanja (2000). Bintanja (2000) presents the energy balance over a period of 37 days in the austral summer of 1997-98, which has an overlap of ~ 20 days with our measuring period. He uses direct turbulence measurements with a sonic anemometer and a Lyman- α hydrometer to validate the turbulent fluxes. The results of our model can be validated independently by comparing the results of AWS 6 with results of his site 3 (Figure 5.6). The figure shows that the temporal variations agree reasonably well. On average, R at AWS 6 is lower than at site 3 at night, which is mainly due to an under-estimation of S . The average difference in R is -9.4 W m^{-2} . The variability in H and LE shows a reasonable agreement, but H is $\sim 3.6 \text{ W m}^{-2}$ and LE is $\sim 4.1 \text{ W m}^{-2}$ higher at AWS 6 compared to site 3, averaged over the 20 days period. The differences in H and LE can partly be explained by the different methods used to determine the fluxes, simulated using Monin-Obukhov similarity theory opposite of direct measurements using a sonic-anemometer and a Lyman- α hydrometer.

Table 5.2. Quantities related to the differences in simulated and measured $L \uparrow$ and T_{snow} .

	D_{mean}	D_{min}	D_{max}	σ_{diff}
		$L \uparrow$ ($W m^{-2}$)		
AWS 4	1.7	-25.7	34.6	4.9
AWS 5	1.4	-60.1	35.7	5.4
AWS 6	2.6	-18.8	38.5	4.8
AWS 8	5.4	-28.2	65.1	11.8
AWS 9	10.7	-31.1	54.9	6.6
		T_{snow} ($^{\circ}C$)		
AWS 1	-0.16	-6.2	11.3	1.7
AWS 4	0.51	-2.8	13.7	1.5
AWS 5	0.67	-7.2	10.1	1.7
AWS 6	0.24	-4.6	5.2	0.8
AWS 8	0.72	-6.4	13.0	2.3
AWS 9	0.66	-6.6	9.4	1.9

Notes: Values are based on (two-)hourly means and averaged over 1997-98 for AWS 1 and 1998-99 for AWS 4 to 9. At the temperatures prevailing at AWS 4 to 9, $1 W m^{-2}$ change in $L \uparrow$ represents $\sim 0.27^{\circ}C$ to $0.35^{\circ}C$ temperature change. $L \uparrow$, outgoing longwave radiation; T_{snow} , snow temperature at initial depth of 0.05 m; D_{mean} , mean absolute difference (measured minus simulated); D_{min} , minimum difference; D_{max} maximum difference; σ_{diff} standard deviation of the difference.

The sensitivity of the calculated heat budget was tested by varying different model parameters. The results suggest that the subsurface temperatures are very sensitive to changes in the amount of shortwave radiation penetrating the snow pack, i.e., sensitive to the snow density, the albedo and the extinction coefficients of snow. For example, decreasing the density of the snowfall from $350 kg m^{-3}$ to $300 kg m^{-3}$ increases the mean temperature of the snowpack by $\sim 0.4^{\circ}C$, and decreasing the fractional extinction coefficient of penetrating shortwave radiation from 0.88 to 0.30 increases the subsurface temperature by $\sim 0.2^{\circ}C$. However, the surface temperatures and thereby the turbulent fluxes are not very sensitive to changes in shortwave radiation penetration. The turbulent fluxes are more sensitive to changes in, e.g., roughness length and $L \downarrow$ parameterisation. An increase in roughness length for momentum from 0.1 mm to 1.0 mm decreases the subsurface temperatures by $\sim 0.3^{\circ}C$ and decreases the sensible heat flux by $\sim 1.3 W m^{-2}$, which is due to a decrease in the friction velocity. An increase in incoming longwave radiation of $\sim 5\%$ decreases the surface temperatures by $\sim 1^{\circ}C$, increases the sensible heat flux by $\sim 4 W m^{-2}$ and the latent heat flux by $\sim 1 W m^{-2}$. These results are in accordance with sensitivity experiments performed with similar models (Reijmer *et al.*, 1999a; Bintanja, 2000).

The uncertainties resulting from the uncertainties in the measurements, the use of parameterisations and model output brings about a considerable uncertainty in the determined heat budget terms. The uncertainty in the measured radiative fluxes (Chapter 1) results in an uncertainty in the estimated net radiation ($R = S + L$) of the same order of magnitude as the flux itself. Because R is small compared to the individual radiative fluxes, the uncertainty in R is mainly determined by the size of

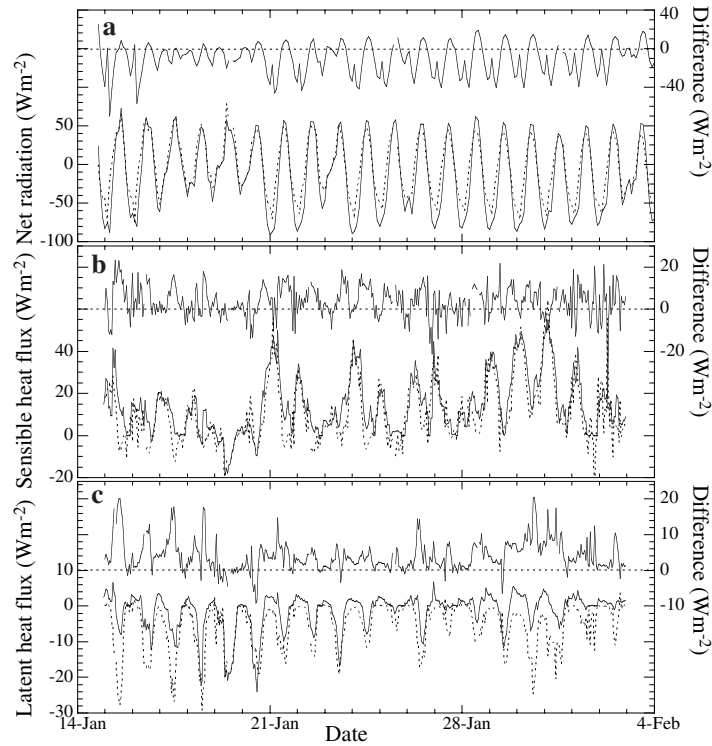


Figure 5.6. Fluxes of (a) net radiation, (b) sensible heat and (c) latent heat measured at AWS 6 (solid line) and site 3 of Bintanja (2000) (dotted line) and the difference between the two (AWS 6 minus site 3, top solid line) for about 20 days in January 1998. The turbulent fluxes at site 3 of Bintanja (2000) are direct turbulence measurements with a sonic anemometer and a Lyman- α hydrometer.

the flux and does not improve significantly by using measurements of $L \downarrow$ instead of using a parameterization. However, knowledge of $L \uparrow$ does improve the estimated turbulent fluxes owing to an improvement in knowledge of T_0 . This results in an uncertainty of $\sim 20\%$ when $L \uparrow$ is not measured and $\sim 10\%$ when it is measured, based solely on uncertainties in the measurements used to calculate the fluxes. Uncertainties brought about by the method used to calculate the fluxes are difficult to assess. Based on the difference between our results and the directly measured fluxes of Bintanja (2000), the uncertainty in the turbulent fluxes could be as large as 50%.

5.5 Results

5.5.1 Annual mean surface energy balance

The surface energy balance was calculated for all AWS, except 3 and 7, over the periods 1997-99 (AWS 1 and 2) and 1998-99 (AWS 4 to 9). Table 5.3 presents the

Table 5.3. Annual mean energy balances.

AWS	yr	$S \downarrow$	$S \uparrow$	S	$L \downarrow$	$L \uparrow$	L	R	H	LE	G
1 (1420)	1997	139.2	-114.2	25.0	163.0	-215.2	-52.2	-27.2	27.1	0.0	0.1
	1998	143.0	-117.3	25.7	160.3	-210.6	-50.3	-24.6	24.5	0.1	0.0
2 (2400)	1997	154.8	-126.9	27.9	152.4	-200.0	-47.6	-19.7	20.7	-0.5	-0.5
	1998	156.0	-127.9	28.1	149.3	-195.2	-45.9	-17.8	18.4	-0.5	-0.1
	1999	151.5	-124.2	27.3	149.8	-196.0	-46.2	-18.9	19.9	-0.3	-0.7
4 (34)	1998	117.5	-101.0	16.5	218.4	-236.8	-18.4	-1.9	2.9	-0.8	-0.2
	1999	113.4	-98.4	15.0	220.5	-236.5	-16.0	-1.0	1.7	-0.8	0.1
5 (363)	1998	117.1	-96.6	20.5	203.9	-239.9	-36.0	-15.5	17.5	-1.5	-0.5
	1999	115.4	-95.5	19.9	206.5	-240.5	-34.0	-14.1	16.1	-1.5	-0.5
6 (1160)	1998	127.0	-103.9	23.1	178.7	-223.2	-44.5	-21.4	22.3	-0.2	-0.7
	1999	125.7	-103.6	22.1	180.9	-223.4	-42.5	-20.4	20.8	0.1	-0.5
8 (2399)	1998	140.0	-111.8	28.2	137.9	-171.4	-33.5	-5.3	6.2	-1.0	0.1
	1999	130.9	-104.6	26.3	139.1	-171.4	-32.3	-6.0	7.0	-0.8	-0.2
9 (2892)	1998	141.5	-117.3	24.2	126.6	-152.4	-25.8	-1.6	2.3	-0.7	0.0
	1999	137.5	-114.4	23.1	130.4	-154.6	-24.2	-1.1	2.0	-0.7	-0.2

Notes: Fluxes are in W m^{-2} and positive directed towards the surface. Averages are based on hourly means. To obtain averages over a complete year, missing days in January 1997 (AWS 2) and January 1998 (AWS 5, 6 and 8) are substituted with corresponding days of January 1998 and 1999, respectively. Between brackets the elevation of the stations in m a.s.l.. For AWS 1, 1999 is missing due to a broken temperature sensor. $S \downarrow$, incoming shortwave radiation; $S \uparrow$, reflected shortwave radiation; S , net shortwave radiation ($S \downarrow - S \uparrow$); $L \downarrow$, incoming longwave radiation; $L \uparrow$, outgoing longwave radiation; L , net longwave radiation ($L \downarrow - L \uparrow$); R , net radiation ($S + L$); H , sensible heat flux; LE , latent heat flux; G , sub-surface energy flux.

annual average energy balance for these stations. The annual averaged energy balance on Antarctica is dominated by a negative radiative flux R ($R = S + L$). R is mainly determined by the net longwave radiation L which varies between -16 and -52 W m^{-2} (Table 5.3). S varies between 15 and 28 W m^{-2} . R is almost completely balanced by a positive sensible heat flux H , ranging from 2 W m^{-2} at AWS 4 to 28 W m^{-2} at AWS 1. Positive H indicates that the near-surface atmosphere is on average stable and the near surface air is cooled. This is the main forcing of the persistent katabatic flow on Antarctica. The low moisture content of the air results in small and negative latent heat fluxes LE at almost all stations, varying between -1.5 W m^{-2} at AWS 5 and 0.1 W m^{-2} at AWS 6. A negative LE of $\sim -1 \text{ W m}^{-2}$ implies $\sim 11 \text{ mm w.e. yr}^{-1}$ sublimation of the snow surface, ~ 0 to 10% of the annual accumulation per site. The subsurface energy flux G is small and varies in sign from year to year.

5.5.2 Seasonal cycle

Figure 5.7 presents the monthly mean surface heat budget of AWS 4, 6 and 9 where AWS 4 represents the ice shelves, AWS 6 the escarpment region and AWS 9 the plateau region. Due to the low temperatures on the Antarctic continent melt seldomly occurs so the snow is generally dry and α high, 0.80 - 0.85 (Table 5.1). S , albeit small, dominates the radiative budget in summer, which results in positive values of

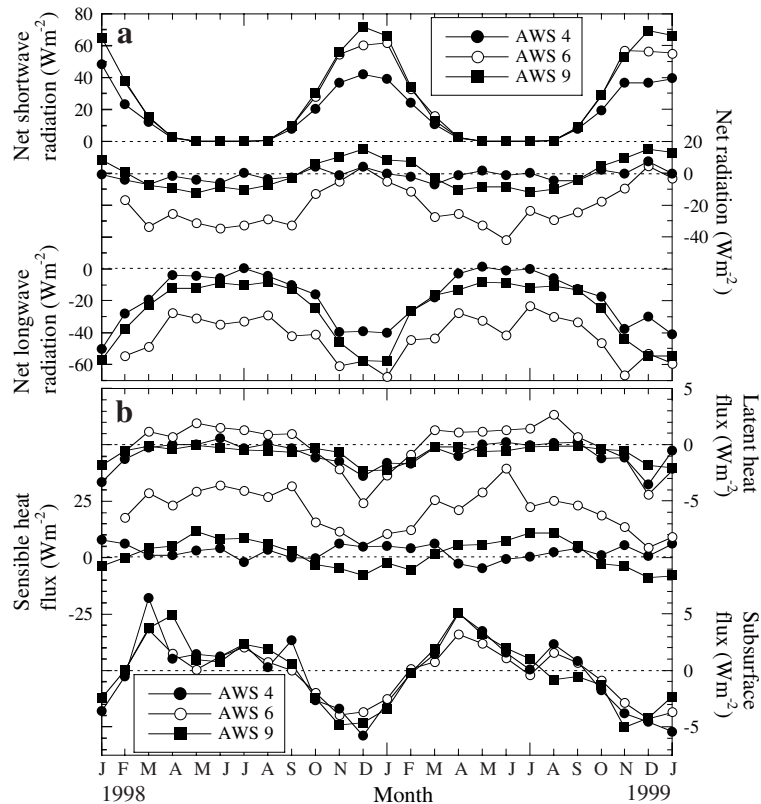


Figure 5.7. Monthly mean energy balance for AWS 4, 6 and 9 for 1998 and 1999. (a) Presents the radiative fluxes, (b) the turbulent and subsurface fluxes. Dotted lines indicate 0 W m^{-2} . Note the different scales on the vertical axis.

R (Figure 5.7a). In winter, in the absence of solar radiation, L determines the radiative budget and R is negative. The amount of time R is positive in summer increases with increasing distance from the coast, disregarding AWS 4 where R is $\sim 0 \text{ W m}^{-2}$ during the entire year. At AWS 1, R remains negative, also during summer, which is unusual for summer conditions. Bintanja (2000) also found negative R in summer for three sites on the slope towards the Antarctic plateau. This phenomenon will be discussed more extensively in the next section. At AWS 4, R occasionally becomes positive between October and February. At AWS 5 and 6, R is positive in December and at AWS 2 R is positive from November until January. At the highest sites R is positive from October to February.

Because R is largely balanced by H , H is in general positive in winter and negative in summer, especially at the higher stations, AWS 2, 8 and 9 (Figure 5.7b). At AWS 1, 5, and 6, H becomes very small in summer but remains positive. This indicates, on average, stable or near neutral conditions in the surface layer. Unstable conditions in the surface layer in summer at the higher stations are due to the de-

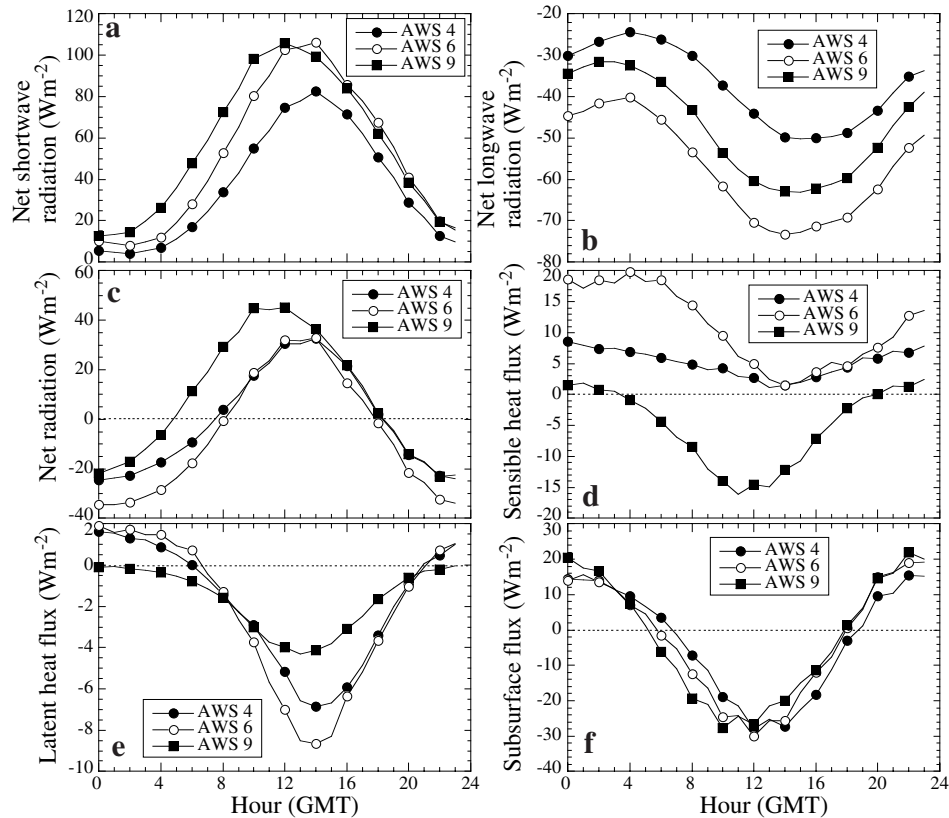


Figure 5.8. Diurnal cycle of the surface energy budget in summer (December, January, February) for AWS 4, 6 and 9. (a) Net shortwave radiation, (b) net longwave radiation, (c) net radiation, (d) sensible heat flux, (e) latent heat flux and (f) subsurface energy flux. Dotted lines indicate $0 Wm^{-2}$.

crease in wind speed and the more vigorous warming of the surface by the sun due to lower amount of clouds at larger distance from the coast. LE is very small and positive (condensation) in winter and negative (sublimation) in the short summer. The subsurface energy flux is small all year round, varying between -5 and $5 Wm^{-2}$ and shows warming of the snow pack in summer and cooling in winter. In summer, surface temperatures occasionally can reach $0^{\circ}C$ for 1 or 2 hours at AWS 4, 5 and 6 and melt occurs. The melt water does not runoff but percolates into deeper layers and refreezes, forming ice lenses as observed at AWS 4.

5.5.3 Daily cycle

The diurnal cycle in the surface energy budget is mainly due to changes in insolation and therefore most pronounced in summer. S heats the surface and destroys (in part) the surface temperature inversion, weakening the katabatic flow. Figure 5.8 presents

the diurnal cycle of the heat budget in summer (December, January and February) at AWS 4, 6 and 9. The diurnal cycle in S is much larger than in L , $80 - 110 \text{ W m}^{-2}$ and $25 - 35 \text{ W m}^{-2}$, respectively. This results in an R that is dominated by S and positive in day-time for ~ 10 hours at the lower sites (AWS 1 to 6) to ~ 13 hours at the sites on the plateau (Figure 5.8a). The diurnal cycle of $L \downarrow$ is small, so the diurnal cycle in L is mainly caused by variations in $L \uparrow$. Therefore, energy losses due to L are largest when the surface temperature is highest, which is about an hour after solar noon. The phase difference between the stations is due to the longitudinal location of the stations.

H is mainly determined by the temperature difference between air and surface, and wind speed. During daytime the conditions are neutral or only marginally unstable at the lower sites (AWS 1, 4, 5 and 6) while at the higher sites (AWS 2, 8 and 9) unstable conditions prevail, resulting in warming of the lower boundary layer (Figure 5.8b). At night, H is positive and largest for the stations with the highest wind speed. LE is small at all stations and shows condensation at night and sublimation during day. G shows a marked diurnal cycle which is closely related to the solar heating of the snow pack.

5.6 Discussion

5.6.1 The katabatic wind regime

The results presented in the previous sections suggest that the katabatic flow is of great importance to the meteorological conditions and thereby the surface energy balance in DML. The intensity of the katabatic flow is, to a first approximation, proportional to the steepness of the underlying surface (Parish and Bromwich, 1987, 1991). Figure 5.9a presents the annual mean wind speed as a function of the surface slope. The surface slope is calculated using a $10 \times 10 \text{ km}$ Antarctica surface topography and is based on linear interpolation of the elevation difference between the four points surrounding the AWS location, giving a reasonable estimate of the surface slope that affects the katabatic flow (Table 1.1).

Figure 5.9a shows that the wind speed is highest at the sites with the highest surface slope, which is on the steep slope towards the plateau. The stronger winds enhance vertical mixing and reduce the strength of the surface temperature inversion, which results in high potential temperatures (θ) and sensible heat fluxes (Ohata, 1985; Wendler *et al.*, 1993; Van den Broeke *et al.*, 1999). The control of the strength of the katabatic wind on the boundary-layer processes is referred to as katabatic wind regime and explains the small differences in air temperature between the lower stations (AWS 4 to 6) where not only the elevation increases with increasing distance from the coast but also the surface slope. θ actually increases with elevation, resulting in a maximum at the stations on the slope towards the plateau (Figure 5.9b). A similar maximum was found by Van den Broeke *et al.* (1999), and attributed to the katabatic wind regime. The katabatic wind regime also explains the absence of a clear annual cycle of the wind speed at sites 4 and 9, where the surface slope is very

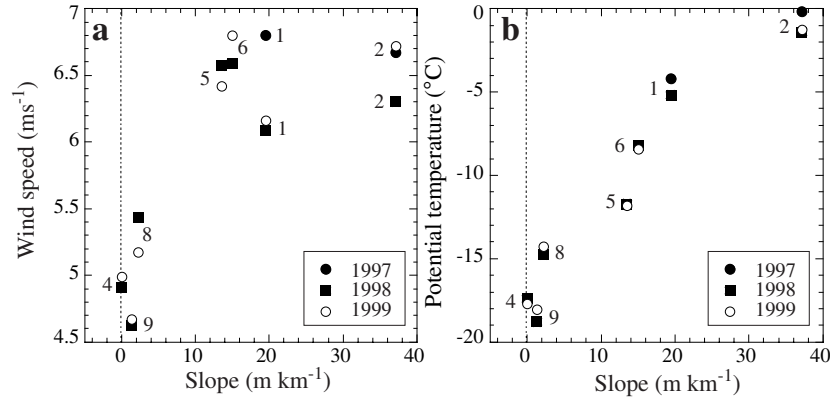


Figure 5.9. Annual mean (a) wind speed and (b) potential temperature as a function of surface slope (Table 1.1). The numbers denote the AWS sites.

small. In spite of the high surface slope and θ at AWS 1 and 2, the annual mean wind speed is lower than at AWS 5 and 6, which is partly explained by the underestimation of the wind speed due to freezing of the sensors in winter and partly by two-dimensional effects of the terrain causing confluence and divergence of the flow and resulting in relatively high and low wind speeds, respectively. Due to uncertainties in determining the surface slope and freezing of the wind speed sensors, θ is probably a better measure of the influence of the katabatic wind on the surface fluxes than the actual measured wind speed and will be used in the remaining sections.

5.6.2 The surface energy balance

The spatial variations in the surface energy balance presented in Section 5.5 suggest a dependency on the strength of the katabatic flow but also on the location of the site with respect to the distance from the coast, latitude and elevation. Figure 5.10 shows the annual mean energy balance at the AWS sites (Table 5.3), as a function of θ (Table 5.1).

The apparent dependency of the net shortwave radiation S on θ results from the increase in elevation and distance from the coast at AWS 1 to 6 that coincides with the increase in surface slope. Variations in S depend mainly on the surface albedo, the elevation and latitude of the site, and cloud amount. S increases as a function of elevation and distance from the coast, hence the high S at AWS 8 and 9, and is due to a decrease in cloud cover with increasing distance from the coast. At Neumayer the cloud amount was ~ 0.66 (König-Langlo and Herber, 1996), compared to ~ 0.35 near AWS 6 (Bintanja and van den Broeke, 1995) in January 1993. On the plateau, S mainly depends on latitude. Note that at AWS 1 and 2 α is not measured and the estimated value is kept constant.

Net longwave radiation L is negative and decreases with increasing θ . This maximum in L at the sites with the highest θ coincides with a maximum in wind speed and surface slope (Figure 5.9). The relatively high surface temperatures increase L \uparrow ,

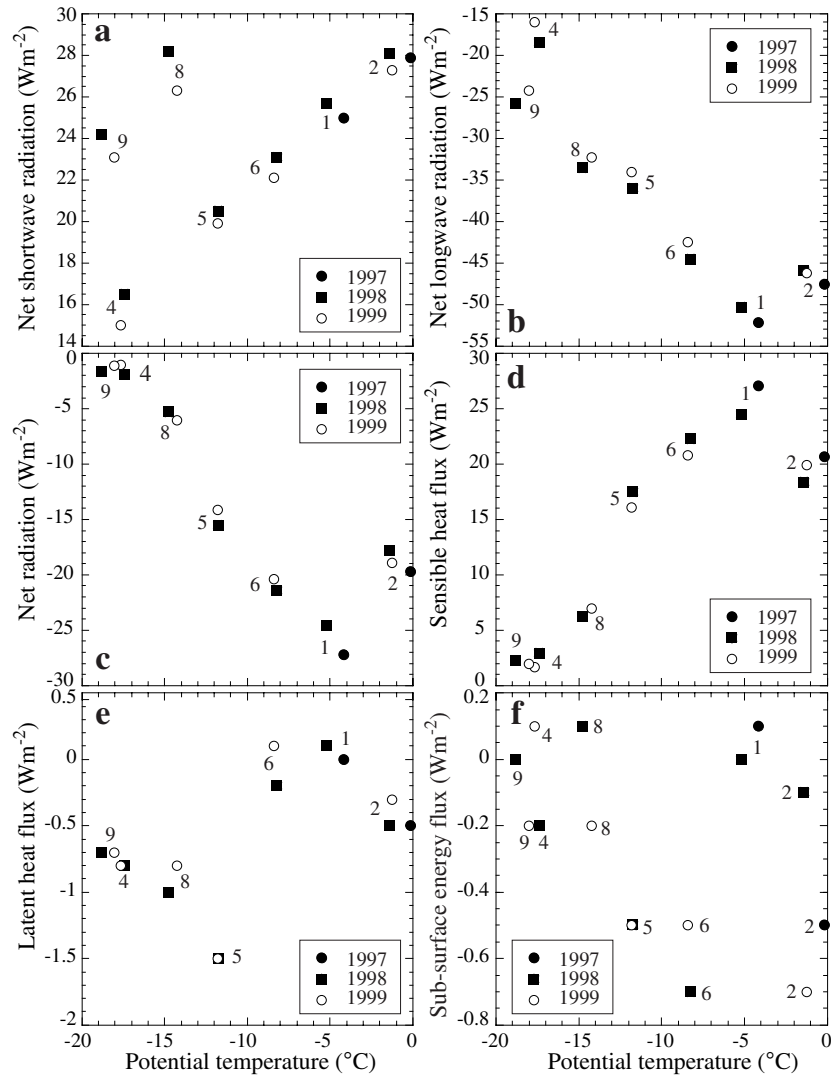


Figure 5.10. Annual averaged surface energy balance components of (a) net shortwave radiation, (b) net longwave radiation, (c) net radiation, (d) sensible heat flux, (e) latent heat flux and (f) subsurface energy flux as a function of potential temperature (Table 5.1). The numbers denote the AWS sites.

which brings about the maximum in L . Because L dominates the radiation balance, R also shows a maximum on the edge of the plateau where θ is highest. R is balanced almost completely by a positive H , which also shows a maximum at the site with the highest θ . H and R at AWS 2 deviate from this tendency. Both fluxes are smaller than is expected from the measured θ . This is probably due to the under-estimation of the wind speed due to freezing of the sensor.

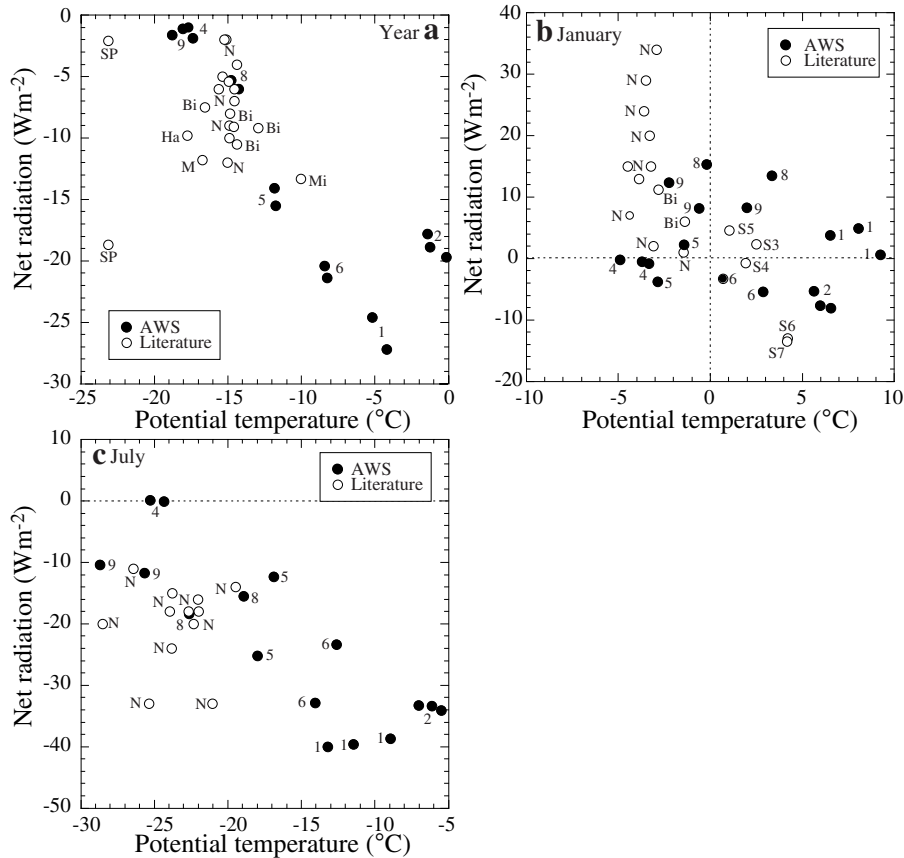


Figure 5.11. (a) Annual mean and monthly mean net radiative flux as a function of potential temperature for (b) January and (c) July. Closed circles with numbers denote the AWS sites. Open circles denote measurements presented in the literature: N, Neumayer (Schmidt and König-Langlo, 1994; König-Langlo and Herber, 1996); Ha, Halley; SP, South Pole; M, Maudheim (King and Turner, 1997); Mi, Mizuho (King and Connolly, 1997); Bi, Berkner Island (Reijmer et al., 1999a); S5, site 5 (Bintanja and van den Broeke, 1995); S3, site 3; S4, site 4; S6, site 6; S7, site 7 (Bintanja, 2000).

The dependency of the surface energy balance on θ and thereby wind speed and surface slope, is mainly determined by the winter balance (Figure 5.11) due to the very short and peaked summer on Antarctica. In summer, heating of the surface by solar radiation reduces the sensible heat flux and thereby the cooling of the near surface air, weakening the katabatic flow and increasing the influence of the large scale flow, resulting in the diurnal cycles in the energy budget terms. The unusual negative R in summer at the sites on the slope towards the plateau is explained by the southern location of the escarpment region in DML compared to the rest of East Antarctica and was also found by Bintanja (2000). The large surface slope results in relatively high wind speeds and sensible heat fluxes at elevations where at other

locations the slopes are less steep and the wind speeds less severe. This could also explain the difference in diurnal variations in H between the sites on the Antarctic plateau (AWS 2, 8 and 9) and on or near the slope (AWS 1, 4, 5 and 6) (Figure 5.8), conditions being stable at the escarpment stations and unstable at the plateau stations. In winter, R decreases with increasing θ .

The relative contribution of H and LE to the heat budget at the various sites also exhibits an annual cycle (Figure 5.12) (Bintanja *et al.*, 1997). In winter, the contribution of LE to the turbulent fluxes is small due to the low temperatures. The Bowen ratio ($B = H/LE$) is positive at all stations except AWS 9 and is on the order of 20. In summer, the fluxes are smaller and the contribution of LE increases resulting in B varying between -5 and 5. B is positive for AWS 8 and 9 and negative for all other stations.

5.6.3 Comparison with other studies

The results presented in the previous sections can be compared to calculations presented in the literature.

Bintanja and van den Broeke (1995) and Bintanja (2000) present the energy balance for the austral summer of 1992-93 and 1997-98 for two stations located at exactly the same location as AWS 6, named site 5 and site 3, respectively. Their results are summarised in Table 7 of Bintanja (2000). He showed that the constant relative humidity assumed by Bintanja and van den Broeke (1995) was too low, which resulted in an exceptionally large LE of -22.1 W m^{-2} . Comparing January 1999 and 2000 with the results of Bintanja (2000) shows that our S and L are smaller. This results in a negative R at AWS 6, -5.3 and -3.2 W m^{-2} , respectively, while R at site 3 is small and positive, 2.3 W m^{-2} . H is of the same order of magnitude, $\sim 10 \text{ W m}^{-2}$ and LE is smaller in our results, -2.6 and -2.0 W m^{-2} compared to -10.8 W m^{-2} . The differences can partly be explained by annual variability but also by the different methods used to calculate the turbulent fluxes (see Section 5.2).

The mean diurnal cycle derived at AWS 6 is also in reasonable agreement with results from Bintanja (2000). H shows near neutral conditions in day-time averaged over two years, which agrees with Bintanja (2000). The diurnal cycle of LE shows positive values at night while in Bintanja (2000) LE remains negative 24 hours per day. Wendler *et al.* (1988) present the diurnal cycle for a weather station (D-47) on the intermediate plateau in Adélie Land, East Antarctica. Their results are generally comparable to our results from AWS 1, 2 and 6. However, at D-47, S is higher during daytime, probably due to the more northerly location of the station compared to the AWS used here, and R is positive during day-time. H is higher during night, which is probably due to higher wind speed at D-47 (annual average $\sim 12.8 \text{ m s}^{-1}$). The sublimation is also larger at D-47 and LE becomes positive during night.

Almost all estimates of the annual surface heat budgets found in literature are from stations near the coast (King *et al.*, 1996; König-Langlo and Herber, 1996; Reijmer *et al.*, 1999a) or the South Pole (Carroll, 1982; King and Turner, 1997). To examine to what extent the results presented in previous sections for DML can be extended to the entire continent, Figure 5.11a presents annual mean R as a function of θ . Be-

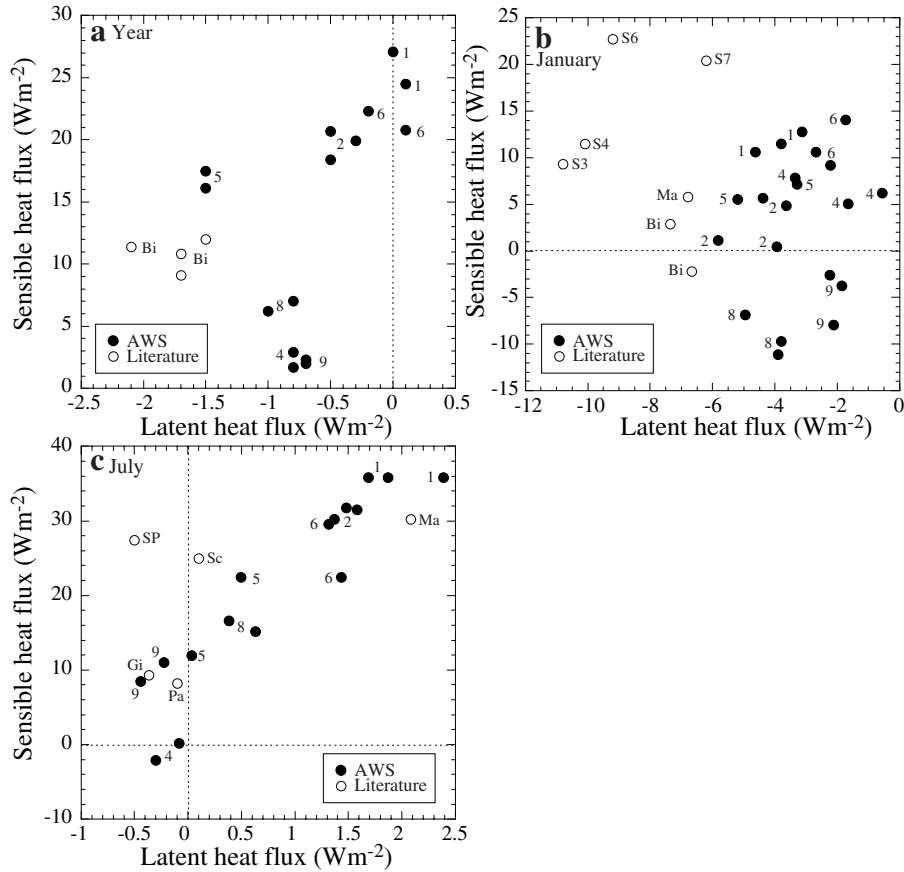


Figure 5.12. (a) Annual mean and monthly averaged values of sensible heat as a function of latent heat for (b) January and (c) July. Closed circles with numbers denote the AWS sites. Open circles are measurements presented in the literature: SP, South Pole; Pa, Patrick; Ma, Marilyn; Sc, Schwertfeger; Gi, Gill (Stearns and Weidner, 1993); Bi, Berkner Island (Reijmer et al., 1999a); S3, site 3; S4, site 4; S6, site 6; S7, site 7 (Bintanja, 2000).

cause R is almost completely balanced by $H + LE$, $H + LE$ as a function of θ shows similar results. The spread in R is considerable, especially at the sites with low θ , which are the sites on the plateau and on ice shelves where the surface slope and thereby wind speeds are reasonably low. On plateau stations like South Pole but also Berkner Island, R seems to have no dependence on slope but more on latitudinal position (not shown). The difference between AWS 8 and 9 and South Pole is an order of magnitude in R as well as in $H + LE$.

Stations on ice shelves, close to the coast are largely influenced by the synoptic weather systems and less by katabatic flow. Fluxes of R and $H + LE$ at AWS 4 seem exceptionally small compared to their value at other coastal stations in this area. At Halley, Maudheim and Neumayer, annual mean R are $-9.8 W m^{-2}$, $-11.8 W m^{-2}$ and

-7 W m^{-2} (Schmidt and König-Langlo, 1994; König-Langlo and Herber, 1996; King and Turner, 1997), respectively, compared to $\sim -1.5 \text{ W m}^{-2}$ at AWS 4. This can partly be explained by the under-estimation of the surface temperature in the model, which results in $L \uparrow$ that is on average $\sim 1.7 \text{ W m}^{-2}$ too low (Table 5.2).

Most of the measurements presented in the literature are carried out in the summer months December and January (Ohata, 1985; Wendler *et al.*, 1988; Bintanja and van den Broeke, 1995; Bintanja, 2000). Figure 5.11b presents R as function of θ for January. The figure shows no dependency on θ at all. There is only a tendency for the stations on the ice shelves to have a negative θ while stations close to the edge of the plateau have positive θ . The spread is fairly large and can partly be explained by inter-annual variability in the average monthly weather conditions and the different length of the measuring periods at the presented stations. For stations on ice shelves the size of the ice shelf and the location of the station on the ice shelf, e.g., close to up-wind mountains or close to the edge also plays a role. The summer balance is mainly determined by the net shortwave radiation. The winter balance does exhibit a relation with θ , although the spread, especially in the results from Neumayer station, is fairly large.

5.7 Concluding remarks

The weather stations have provided us with a fairly complete three to four year data set for seven locations in Dronning Maud Land, East Antarctica. Meteorological conditions at these stations are mainly determined by the large scale flow on the ice shelf and by the katabatic wind regime at the other sites. Wind directions are generally very constant and wind speed and potential temperature increase with increasing surface slope.

Surface energy balance calculations at the seven locations indicate that the energy balance in DML is strongly connected to the potential temperature and hence surface slope and wind speed. Stronger winds enhance vertical mixing and reduce the strength of the surface temperature inversion, which results in high potential temperatures, sensible heat fluxes (Ohata, 1985; Wendler *et al.*, 1993; Van den Broeke *et al.*, 1999) and relatively high surface temperatures. The result is a maximum in H and $L \uparrow$, and therefore L , at the steeper slopes where θ is highest. Because L dominates the radiation balance, R also shows a maximum at these sites. S depends on distance from the coast probably due to a decrease in cloud amount. LE is small at all sites, but indicates that still ~ 0 to 10% of the annual accumulation sublimates.

The energy balances calculated here are generally comparable to energy balance estimations for stations at similar locations presented in the literature. Differences found are explained by the different geographical positions of the sites, especially the larger distance from the coast of the escarpment region in DML compared to other regions of East Antarctica, the different time periods the budget was calculated for and the different methods used to calculate the budget.

The energy balance results are presented in terms of the geographical position of the stations categorised in three regions; the ice shelves, the escarpment region

and the Antarctic plateau. The regions are distinguished by their climatic and topographic settings, which results in typical characteristics with respect to mean values, long-term variations and diurnal cycle of meteorological variables and energy balance. The ice shelves, especially the smaller ones, are mainly influenced by synoptic weather conditions due to their location at the coast and their flat surface. The energy balance in the escarpment region is mainly determined by the strength of the katabatic flow and strongly depends on surface slope and wind speed. On the Antarctic plateau the influence of the large-scale flow is limited, cloud amounts are low and due to the flat surface, katabatic flows are weakly developed. Here, climate and heat budgets are mainly determined by the elevation, through temperature, of the site and the latitude through shortwave radiation. Note however, that this results mainly from the stations in DML where the steep slope towards the Antarctic plateau is at reasonable distance from the coast. At most other locations the slope is closer to the coast. The influence of large-scale flow will probably be larger at these sites.

The amount of surface energy balance data is still limited and owing to the vast size of the continent it is not likely that the spatial and temporal coverage of these type of measurements will considerably improve in the near future. Hopefully our results are useful in validating output from climate and weather prediction models currently used to study the Antarctic climate (Genthon and Braun, 1995; King and Connolley, 1997; Van Lipzig *et al.*, 1999). The weather station data constitute an independent data set not used in the analysis procedure of climate and weather prediction models. Furthermore, two stations are located on the plateau where errors in model elevation are smallest and the interpretation of differences found between model and measurements is not as difficult as in the coastal and escarpment area where the errors in model elevation are substantial.

Chapter 6

Moisture sources of precipitation in Western Dronning Maud Land, Antarctica

Summary

Moisture sources for snow falling in Dronning Maud Land (DML), Antarctica, are calculated for 1998 using three dimensional five-days backward air parcel trajectories. The drilling site of the European Project for Ice Coring in Antarctica in DML is chosen as the main arrival point (75.0°S, 0.01°E). A distinction is made between trajectories with and without snowfall at arrival. Of the snowfall trajectories, 40 - 80 % are located in the Atlantic Ocean within 4 days before arrival. Evaporation along these trajectories is largest 3 to 4 days before arrival. The air parcels are then located between 40 and 60°S in the Atlantic Ocean where surface temperatures range between 0 and 20°C. A case study for May 1998 shows that when snow falls exceptionally high temperatures and wind speeds prevail in the atmospheric boundary layer. The position of the trajectories in the boundary layer suggests a source region for this event between 40 and 50°S and 20 and 60°W in the Atlantic Ocean, where sea surface temperatures vary between 5 and 15°C.

¹This chapter is based on: Reijmer, C.H. and M.R. van den Broeke, 2000. Moisture sources of precipitation in Western Dronning Maud Land, Antarctica. *Antarctic Science*, **13**(2), 210–220.

6.1 Introduction

Many deep ice cores have been drilled in the Antarctic and Greenland ice sheet, e.g., Vostok and Byrd (Antarctica), Greenland Ice Core Project (GRIP and North GRIP) and Greenland Ice Sheet Project (GISPII) (Greenland Ice-core Project (GRIP) Members, 1993; Petit *et al.*, 1999). The European Project for Ice Coring in Antarctica (EPICA) aims to drill a further two cores. The main objective of EPICA is to construct a high resolution climate record for the Antarctic and compare the results with other Antarctic and Greenland records. The Atlantic Ocean is considered an important link between Antarctic and Greenland climate records (Stocker, 1999). One of the EPICA cores will therefore be drilled in Dronning Maud Land (DML), an area of Antarctica bordering the Atlantic Ocean (Figure 6.1). The relatively high accumulation rate at the selected drilling site, ~ 62 mm water equivalent per year (w.e. yr^{-1}) (Oerter *et al.*, 2000), makes it possible to obtain a detailed record of the last glacial-interglacial cycle.

The climate recorded in ice cores is mainly determined by the conditions in which snowfall occurs. This need not be representative for the mean conditions at that point (Noone and Simmonds, 1998; Noone *et al.*, 1999). Several factors such as seasonality of snowfall and changes in moisture source regions may bias the ice core record (Jouzel *et al.*, 1997). The ratio of oxygen isotopes ($\delta^{18}\text{O}$) in the snow is often used to reconstruct temperature records from ice cores (Petit *et al.*, 1999). However, $\delta^{18}\text{O}$ in Antarctic snow represents a complex history of the moist parcel. It depends on the temperature of the ocean from which the moisture evaporated, the subsequent cycles of condensation and evaporation and the temperature at which the moisture finally condenses to form precipitation. This hampers the interpretation of the $\delta^{18}\text{O}$ record. A change in $\delta^{18}\text{O}$ could indeed reflect a realistic temperature change but could also be caused by a change in moisture source region or seasonality of the precipitation.

Several techniques have been used to trace moisture source regions of Antarctic snow. Petit *et al.* (1991) and Ciais *et al.* (1995) use deuterium excess as tracer in combination with idealized isotope models. They conclude that the Antarctic moisture has a subtropical origin, 30 - 40 °S and 20 - 40 °S, respectively. Peixoto and Oort (1992) came to the same conclusion on the basis of atmospheric water balance studies (8 - 40 °S). Other studies including $\delta^{18}\text{O}$ (Bromwich and Weaver, 1983) and General Circulation Model (GCM) studies (Delaygue *et al.*, 2000; Delmotte *et al.*, 2000) suggest a more southern origin, 55 - 60 °S and 30 - 60 °S, respectively. Differences in source regions could be due to the differences in methods used, and do not necessarily contradict each other.

In this study we use a combination of techniques to assess moisture sources for DML. To identify precipitation events we use data from nine Automatic Weather Stations (AWS) and we use a trajectory model to trace the moisture sources of the precipitation events. Using the trajectory method enables us to describe specific transport pathways in contrast with the GCM approach (Delaygue *et al.*, 2000; Delmotte *et al.*, 2000), which only gives the location of the source region without an indication of the transport path or the air mass age. The approach in this study is similar to the study of Noone *et al.* (1999), who use European Centre for Medium Range Weather

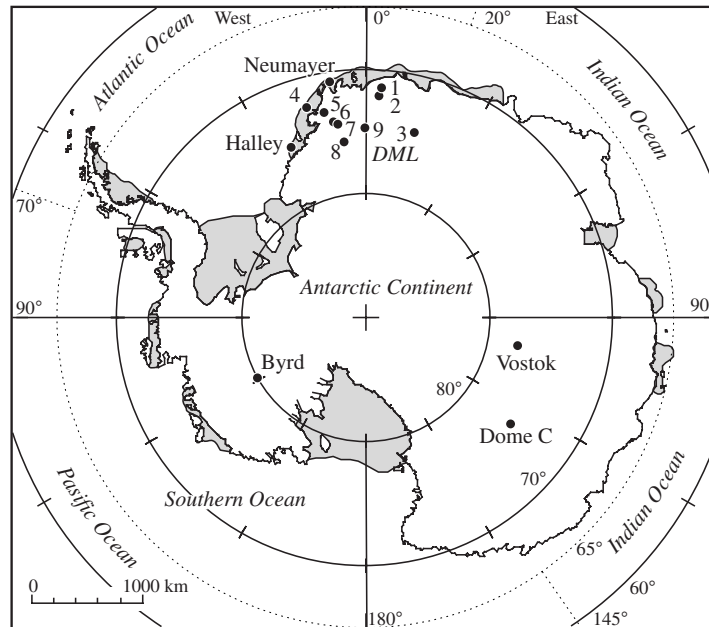


Figure 6.1. Map of Antarctica showing the locations of the Automatic Weather Stations. AWS 9 is situated ~ 2 km west of the EPICA drilling site in Dronning Maud Land (DML). Shaded areas are ice shelves, dotted lines are boundaries of areas defined in the text.

Forecasts (ECMWF) reanalysis to describe the seasonal patterns and trajectories of significant snowfall in the DML region. However, Noone *et al.* (1999) concentrate on the general characteristics of major events while the focus in this study is on the source regions of the moisture.

In Section 6.2 we briefly describe the weather stations and in Section 6.3 the trajectory model. In Section 6.4, a one-year record of AWS accumulation is analysed and compared with ECMWF modelled snowfall. Using the wind fields of the ECMWF model, backward air parcel trajectories are computed and described in Section 6.5 to assess moisture source regions of the snow in 1998. A high accumulation event in May 1998 is described in more detail in Section 6.6.

6.2 The Automatic Weather Stations

The Institute for Marine and Atmospheric Research Utrecht (IMAU) operates nine AWS in Dronning Maud Land, Antarctica (Figure 6.1). AWS 1 to 3 were installed in January 1997 along a traverse line connecting the Norwegian research station Troll to the Antarctic plateau (Winther *et al.*, 1997). AWS 4 to 8 were installed in the austral summer of 1997-98 on a transect ranging from the coast along the Swedish research stations Wasa and Svea to the plateau (Holmlund *et al.*, 2000). AWS 9 was placed in

December 1997 ~ 2 km west of the EPICA drilling site in DML.

The AWS measure air temperature, air pressure, wind speed and direction, instrument height, firn temperature (except AWS 2) and downward directed short-wave radiation. AWS 4 to 9 additionally measure relative humidity, upward directed shortwave radiation and upward and downward directed longwave radiation (Figure 1.5). The sampling rate is six (AWS 1 to 3) and five (AWS 4 to 9) minutes. Hourly (AWS 1 to 3) and two-hourly (AWS 4 to 9) averages are stored and transmitted via Argos satellites. The instrument height is measured using a sonic height sensor. The changes in instrument height are a measure for the amount of accumulation in m snow. The initial height of the instruments was ~ 3 m above the surface (Table 1.1). In this study we focus on AWS 8 and 9. The weather stations are more extensively described in Chapter 1.

6.3 The trajectory model

We use the trajectory model developed by the Royal Netherlands Meteorological Institute (KNMI) to calculate air parcel backward trajectories (Scheele *et al.*, 1996). This model computes the three-dimensional displacement of an air parcel during a time step Δt using an iterative scheme:

$$\mathbf{X}_{n+1} = \mathbf{X}_0 + \frac{\Delta t}{2} [\mathbf{v}(\mathbf{X}_0, t) + \mathbf{v}(\mathbf{X}_n, t + \Delta t)]. \quad (6.1)$$

In this equation Δt is the iteration time step, \mathbf{X}_0 is the position vector of the parcel at time t , \mathbf{X}_n is the n^{th} iterative approximation of the position vector at time $t + \Delta t$ and $\mathbf{v}(\mathbf{X}, t)$ is the wind vector at position \mathbf{X} and time t . The iteration time step is -10 minutes. The iteration stops when the horizontal distance between \mathbf{X}_n and \mathbf{X}_{n+1} is less than 300 m and the relative vertical (pressure) difference, defined as $\frac{P_{n+1} - P}{P_{n+1}}$, is less than 0.0001. The model is able to compute different types of trajectories, e.g., isentropic, isobaric or three-dimensional. The latter is used because it most accurately approximates the true three-dimensional transport path (Stohl *et al.*, 1995; Kottmeier and Fay, 1998).

We use the output from the ECMWF operational Numerical Weather Prediction (NWP) model as input for the trajectory model. The wind fields are first guess fields, not analyses, to ensure physical balance in the meteorological fields, which assures accurate representation of the vertical wind speed component. Note that in April 1998 the orography in the ECMWF model was improved and the resolution changed from T213 ($\sim 0.8^\circ$) to T319 ($\sim 0.6^\circ$). For the trajectory model, the resolution of the input data is kept constant at 1.5° in the horizontal plane, 31 levels in the vertical and 6 hours in time. This makes interpolation in time and space necessary. The spatial interpolation is bi-linear in the horizontal and linear with $\log(\text{pressure})$ in the vertical. The time interpolation is quadratic.

Uncertainties that are introduced by the choice of trajectory type and interpolation schemes are on the order of 1000 km after 5 days calculation (Kahl *et al.*, 1989;

Stohl *et al.*, 1995). Errors in the vertical wind component are a major source of uncertainties in the calculated trajectories. This implies that the usefulness of identifying source regions after 5 days is limited to areas with horizontal dimensions on the order of 1000 km, ~ 9 degrees latitude. In reality, the uncertainty might be larger because of the difference between the first guess wind fields and the real winds, and the presence of convective systems (e.g., fronts). In a convective system the air parcel loses its identity making it impossible to trace a single parcel deterministically. This important source of errors in trajectories is difficult to assess and is not quantified in the uncertainty estimate. Fortunately, precipitation in the polar atmosphere is generally stratiform and convective mixing will be small. Kahl *et al.* (1989) conclude that sensitivity due to differences in gridded meteorological data bases, an indicator for errors in wind fields, can be larger than the sensitivity due to different trajectory calculation methods. So, computed trajectories must be interpreted with care.

6.4 Model and measurement comparison

In the following analysis a distinction is made between trajectories with and without snowfall on arrival at the AWS sites. To investigate the ability of the ECMWF model to correctly analyse meteorological parameters at the AWS sites, measurements from two stations on the higher plateau, AWS 8 and 9, are compared with the ECMWF data at the grid points of the AWS. The other stations are either too close to large orographic gradients and therefore subject to large uncertainties in the first guess fields or suffer from lack of data. As such, they are not included in this analysis. Model snowfall is based on the cumulative snowfall in the first 12 forecast hours and suffers from model spin-up. Snowfall from the 0 to 12 hours forecast is $\sim 9\%$ less than the amount from the 12 to 24 hours forecast (Turner *et al.*, 1999).

In general, the meteorological parameters such as air pressure, air temperature, wind speed and wind direction are reasonably well reproduced by the ECMWF model, especially after the resolution and orographic improvements. The AWS measurements show that most accumulation occurs in ~ 4 major events per year contributing $\sim 80\%$ to the total annual accumulation (Figure 6.2). It is difficult to quantitatively verify the snowfall in the ECMWF model using AWS observations as they are very different types of data. The AWS measures instrument height, which includes processes such as snowfall, snowdrift, sublimation, deposition and densification of the snow pack. In case of accumulation, it is difficult to assess how much and when the accumulation is snowfall or snowdrift. Furthermore, the model precipitation represents the mean precipitation rate over the area of a grid cell rather than one location within the cell.

If we assume mean densities of 345 g kg^{-1} (L. Karlöf, personal communication 1999) and 335 g kg^{-1} (H. Oerter, personal communication 2000) at AWS 8 and 9, respectively, then an annual accumulation results of $\sim 90 \text{ mm w.e. yr}^{-1}$ at AWS 8 and $\sim 91 \text{ mm w.e. yr}^{-1}$ at AWS 9. The ECMWF snowfall in 1998 was $\sim 55 \text{ mm w.e. yr}^{-1}$ at both sites. The ECMWF accumulation is lower compared to both AWS values. Noone *et al.* (1999) compared cumulative accumulation measured by a thermistor

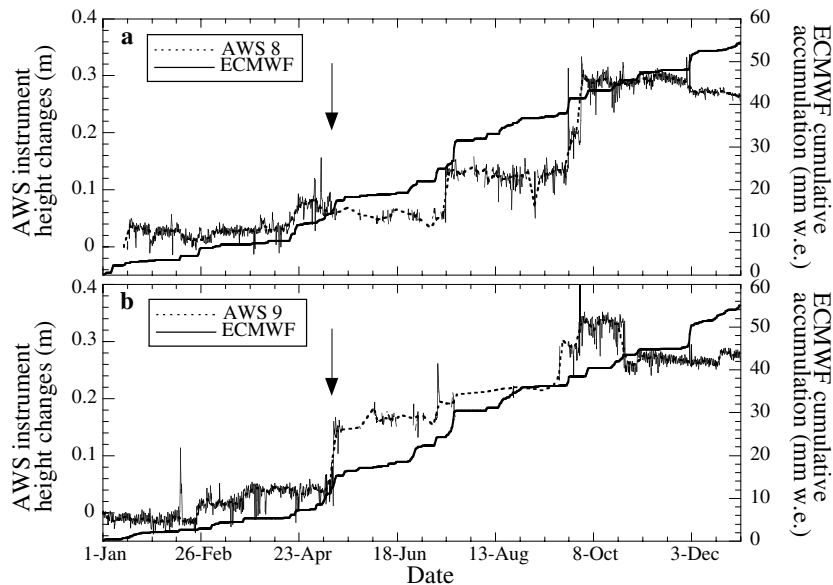


Figure 6.2. Accumulation record at (a) AWS 8 and (b) AWS 9 for 1998. Left axis, cumulative instrument height changes in m snow measured at the AWS sites. Right axis, ECMWF cumulative snowfall in mm w.e. at the AWS grid points. Arrows indicate the snowfall event in May 1998.

(77°S, 10°W) with ECMWF model precipitation, and found an overestimation of the accumulation in the model. Precipitation in the coastal areas of Antarctica is often orographic induced (Bromwich, 1988). Errors in the model orography could therefore have great influence on the amount and location of model snowfall. Genton and Braun (1995) show that the ECMWF orography (improved in April 1998) was ~ 1000 m too high in DML resulting in too little precipitation on the Antarctic plateau in this area (Turner *et al.*, 1999). This explains part of the found difference at AWS 8 and 9 but does not explain the overestimation found by Noone *et al.* (1999). Differences are also explained by the difficulty to distinguish snowfall from snowdrift in the AWS data and the fact that the model snowfall represents the mean of a grid cell rather than one location within the cell. The difference suggest that the precipitation is not uniformly distributed in a model grid cell.

From medium deep ice cores and snow pits the mean accumulation near AWS 8 was estimated to be ~ 68 mm w.e. yr⁻¹ over the last 182 years (Karlöf *et al.*, 2000) and ~ 62 mm w.e. yr⁻¹ over the last 200 years at AWS 9 (Oerter *et al.*, 2000). The ECMWF snowfall in 1998 (55 mm w.e. yr⁻¹) is similar to these estimates. The model seems to reflect better the mean conditions at a site rather than actually capturing a high accumulation year. In 1999 the annual accumulation at AWS 8 and 9 was lower, 62 mm w.e. yr⁻¹ and 84 mm w.e. yr⁻¹, respectively. The high accumulation values in 1998 can be explained by the fact that in 1997-98 a strong El Nino was observed. Jones and Simmonds (1993) showed for the 1982-83 and 1986-87 El Nino events that winter cyclones are more intense. This results in a greater than normal advection of heat

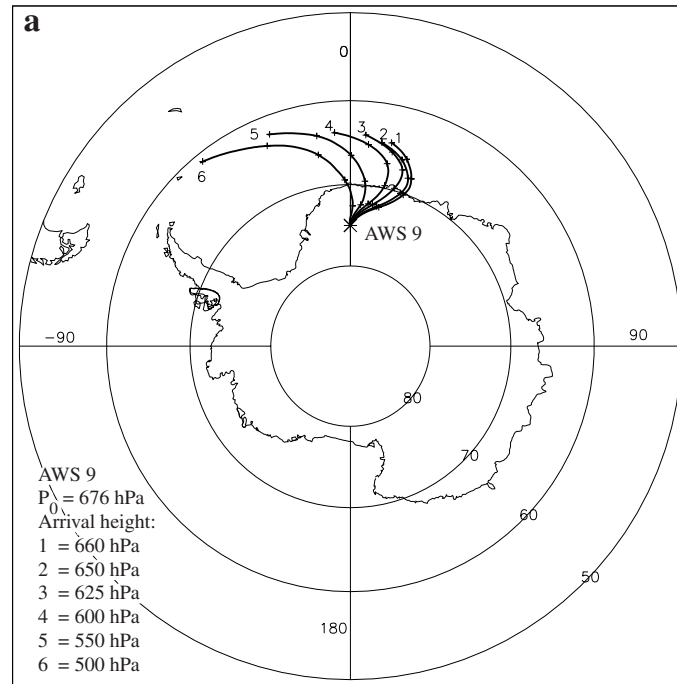


Figure 6.3. (a) Mean five-days backward trajectories arriving at AWS 9, starting at six different pressure levels above the surface. Each day back is marked with a plus sign. The cross is the location of AWS 9.

and moisture in DML and possible higher accumulation. However, measurements at Halley, the British research station on the Brunt ice shelf, and at Neumayer, the German research station on the Ekström ice shelf, show that the temperature and wind speed in 1998 were about average. The mean pressure was lower than average, which can indicate larger than average depression activity in 1998.

Figure 6.2 compares AWS instrument height measurements at AWS 8 and 9 with ECMWF snowfall at those locations for 1998. The individual events are not well correlated. For example, in May 1998 a major snowfall event was recorded at AWS 9 and not at AWS 8. The ECMWF model shows snowfall at both stations for that event. The discrepancies are due to model limitations. The model gives regional scale results, not local. Note that there is no apparent seasonality in the timing of the snowfall events.

6.5 Trajectories in 1998

Trajectory calculations are initiated (and air parcels arrive) every 12 hours (0.00 GMT and 12.00 GMT) at six different pressure levels above the surface with starting point 75.0°S, 0.01°E (AWS 9). Trajectories that intersect the surface are omitted from the

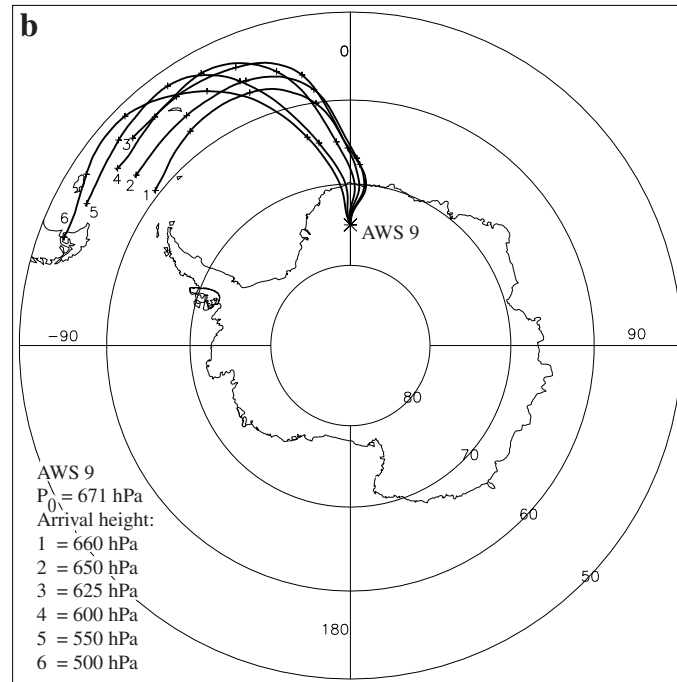


Figure 6.3. Continued. (b) As (a) but only trajectories with snowfall at arrival are taken into account.

analysis ($\sim 9\%$ of the trajectories). We make distinction between cases with and without snowfall at arrival, based on ECMWF snowfall. To mark a trajectory as a snowfall trajectory, at least 0.5 mm w.e. of snow must have accumulated in the 12 hours preceding the parcel arrival. For 1998, this resulted in 23 events at AWS 9, which represents $\sim 37\%$ of the total ECMWF model accumulation.

Figure 6.3a presents the mean of all trajectories and Figure 6.3b the mean of snowfall trajectories, arriving at AWS 9 at different altitudes. Both show a cyclonic curvature reflecting the substantial influence of cyclones on the air parcel paths in Antarctic coastal regions. Due to the higher wind speeds at higher altitudes, the distance travelled by air parcels arriving at higher altitudes is larger and their origin is further to the west. There is no clear seasonal shift in curve or direction of the trajectories due to, e.g., the semi-annual oscillation (SAO). In 1998, the SAO is weakly developed in this area. SAO and the influence of SAO on the Antarctic climate are more extensively described in, e.g., Van Loon (1972) and Van den Broeke (2000b). Trajectories for AWS 8 (not shown) are similar but shifted towards the west. Noone *et al.* (1999) examine the mean poleward moisture flux in the sector 10°W to 15°E to study the general approach direction of the moisture. In agreement with our results they find that the moisture approaches from the northeast.

Figures 6.4a and b present the pressure level of the mean trajectories and mean snowfall trajectories, respectively, arriving at 650 hPa at AWS 9, $\sim 20 \text{ hPa}$ above the

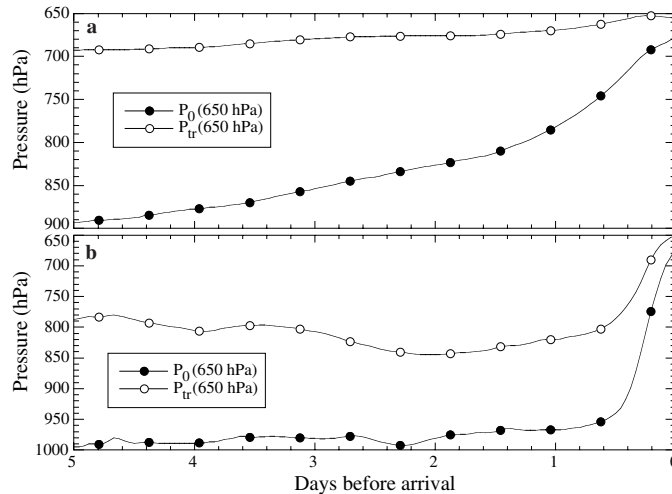


Figure 6.4. (a) Mean vertical displacement in pressure of all trajectories arriving at 650 hPa. (b) As (a) but only trajectories with snowfall at arrival at AWS 9 are taken into account. P_0 , mean surface pressure; P_{tr} , mean trajectory pressure.

surface within the maximum in the poleward moisture transport found by Noone *et al.* (1999). On average, snowfall trajectories are situated at higher pressure levels and have higher surface pressures along their path because they travel closer to sea level. The non-snowfall trajectories remain longer over the continent, which is reflected in the lower surface and trajectory pressure. Figures 6.3 and 6.4 show that snowfall and non-snowfall trajectories are quite different in character. Because only snowfall trajectories will contribute to the accumulation and therefore be reflected in an ice core, care must be taken only to consider those trajectories that contribute to the accumulation to obtain an unbiased assessment of the recorded climate signal.

The maritime nature of snowfall trajectories is also illustrated in Figure 6.5, which shows the percentage of trajectories located in a certain region. To define these regions, the Southern Hemisphere is divided into 5 regions: the Atlantic Ocean ($70^\circ\text{W} - 20^\circ\text{E}$), the Indian Ocean ($20^\circ\text{E} - 145^\circ\text{E}$), the Pacific Ocean ($145^\circ\text{E} - 70^\circ\text{W}$), the Southern Ocean (between the Antarctic continental boundaries and 65°S) and the Antarctic continent (Figure 6.1). The trajectories in Figure 6.4 have their arrival height within the boundary layer at 650 hPa, ~ 20 hPa above the surface at AWS 9. Figure 6.5d shows that 1 day before arrival most snowfall parcels (60%) are in the Southern (Atlantic) Ocean or in the Atlantic Ocean (25%). In days 2 to 4 before arrival, 70 to 80% of the parcels are in the Atlantic Ocean. Five days before arrival, 30% of the parcels are in the Pacific Ocean. Delaygue *et al.* (2000) suggested a larger contribution from the Indian Ocean, 5 - 15% compared to 0 - 5% in our results. This is partly due to the size of their grid box ($10^\circ \times 2^\circ$) and the displacement of their DML grid box towards the south and east of our point ($75 - 77^\circ\text{S}$, $0 - 10^\circ\text{E}$). The contribution of the Southern Ocean calculated by Delaygue *et al.* (2000) is of the same order of magnitude ($\sim 15\%$), but the contribution of the Pacific Ocean is much larger,

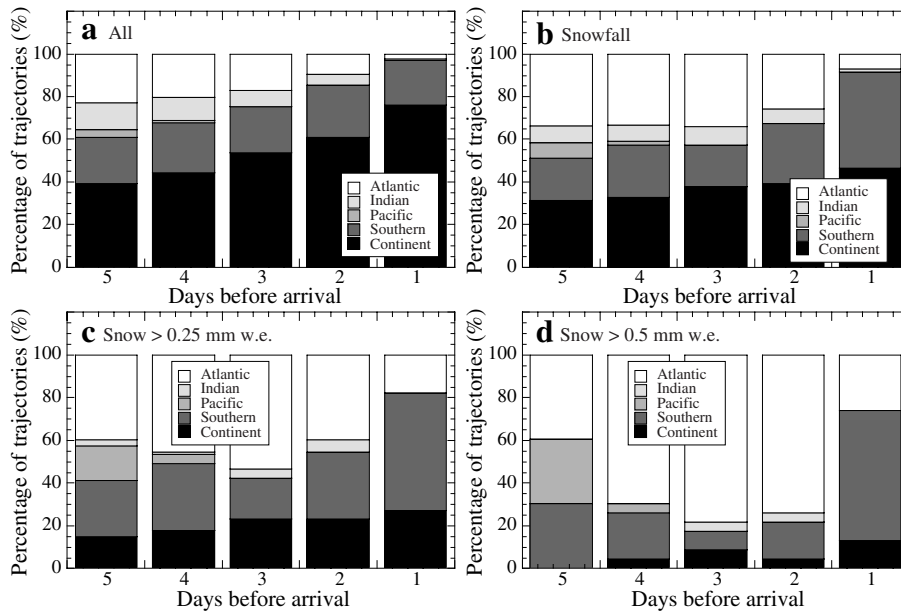


Figure 6.5. Percentage of the backward trajectories, started at AWS 9, with their source region in one of the five regions defined in the text and Figure 6.1. (a) All trajectories are taken into account, (b) all trajectories with snowfall, (c) all trajectories with more than 0.25 mm w.e. snowfall and (d) with more than 0.5 mm w.e. snowfall in the 12 hours preceding arrival at AWS 9 are taken into account.

20 - 30% compared to 0 - 5% in Figure 6.5. The contribution of the Atlantic Ocean is the most important in both studies, but the amounts differ, 35 - 60% compared to 40 - 80% in our results. In this analysis the assumption is made that all moisture in the air parcel originates from somewhere along the five-days trajectories. Taking the moisture already in the parcel into account, the contribution of the Pacific Ocean will probably increase due to the mean westerly flow, and the contribution from the Atlantic Ocean decrease. The results would then better resemble the results of Delaygue *et al.* (2000).

When the snowfall criterion is changed to 0.25 mm w.e. of snow in the 12 hours preceding the parcel arrival (Figure 6.5c), 73 events (68.7% of the accumulation) are taken into account. The contribution of the Atlantic Ocean decreases to 40 - 50%, 2 to 5 days before arrival. The contributions of the Southern Ocean and the Continent, trajectories remaining close to or on the continent, increase with ~10% on each day before arrival. Taking all snowfall events into account (223 events, Figure 6.5b) decreases the contribution of the Atlantic Ocean even further to 30 - 40% and increases the percentage of trajectories remaining over the continent to ~40%. When all trajectories are taken into account results are completely different (Figure 6.5a). The majority of the parcels now originate from the continent, ~20% remains fairly close to the continent in the Southern Ocean, 10 to 20% comes from the Atlantic Ocean and the rest from the Indian Ocean. Almost none originates from the Pacific Ocean.

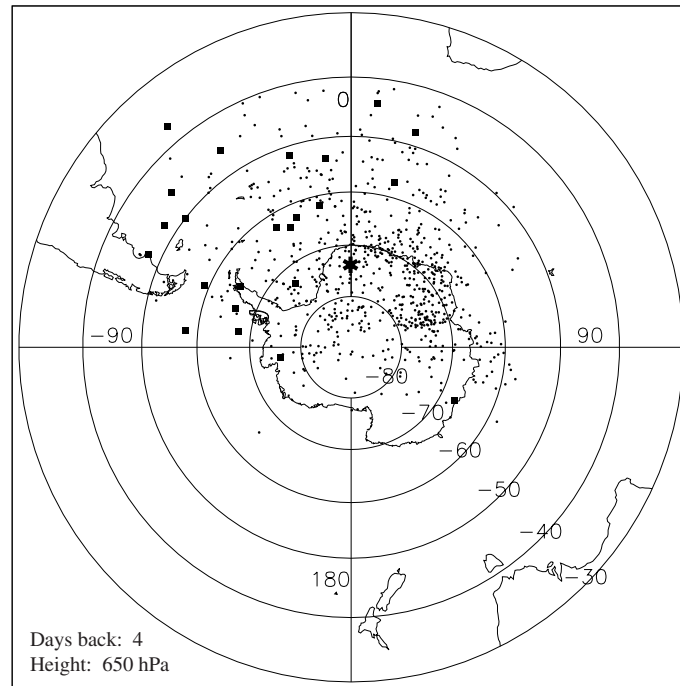


Figure 6.6. Locations of all trajectories 4 days before arrival at AWS 9 at 650 hPa for 1998. The asterisk indicates the location of AWS 9, the squares are the positions of trajectories with more than 0.5 mm w.e. snowfall at arrival.

Figure 6.6 shows the position of all trajectories 4 days before arrival at AWS 9 at 650 hPa, in which the squares represent the positions of trajectories with more than 0.5 mm w.e. snowfall at arrival. The variability in both snowfall and non-snowfall points is significant and becomes larger when going further back in time and when the arrival height is higher. Almost all trajectories remain south of 40°S within the five days of trajectory calculation and none reaches farther north than 30°S.

Assuming the origin of the moisture to be distributed along the five-day snowfall trajectories, the source region of the moisture in DML is most likely the Atlantic Ocean (Figure 6.5). To be able to specify the source region more precisely the specific humidity along the snowfall trajectories, the surface latent heat flux (LE) and the surface temperature underneath the snowfall trajectories are determined. Figure 6.7 displays the temperature difference between trajectory level and surface, LE and the specific humidity. LE shows a maximum ~4 days before arrival and increases (less evaporation) when going towards the Antarctic. The specific humidity slightly increases between 5 and 2.5 days before arrival. The mean trajectory height is ~200 hPa above the surface and the mean difference in surface temperature and potential trajectory temperature is negative indicating stable conditions. When the temperature difference is negative and large in magnitude, vertical mixing is less likely and the air parcel is not likely to interact with the surface. It is therefore difficult to assess

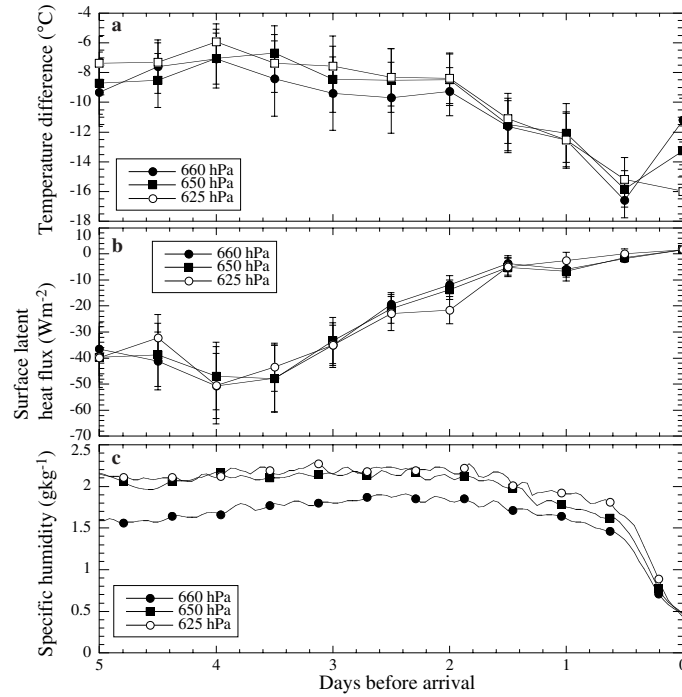


Figure 6.7. (a) Mean temperature difference (surface temperature minus potential temperature) along the snowfall trajectories. (b) Surface latent heat flux (defined negative when directed away from the surface) averaged over all snowfall trajectories and (c) mean specific humidity at trajectory level. In (a) and (b), error bars indicate 1 standard deviation from the mean.

whether the parcels are in the boundary layer and able to interact with the surface. The temperature difference is smallest ~ 4 days before arrival which coincides with the strongest evaporation (Figure 6.7a) and a small increase in specific humidity. The largest snowfall events (with more than 1.0 mm w.e. in the 12 hours preceding arrival) have their four-day origin between 40° and 50°S .

From our results it follows that the most likely source region of snow in DML is the Atlantic Ocean between ~ 40 and 60°S . This is at the southern edge of source regions defined by Petit *et al.* (1991) ($30 - 40^\circ\text{S}$) and Ciais *et al.* (1995) ($20 - 40^\circ\text{S}$) using deuterium excess as an indicator and Peixoto and Oort (1992) based on atmospheric water balance studies ($8 - 40^\circ\text{S}$). Our results are more in agreement with GCM studies which define source regions between 30 and 60°S (Delaygue *et al.*, 2000; Delmotte *et al.*, 2000). Our source region is to the north and over warmer seas compared to oxygen isotope studies which define source regions between 55 and 60°S with sea surface temperatures between 0 and 1°C (Bromwich and Weaver, 1983). Our source region has a wider meridional extend and sea surface temperatures may vary between 0 and 20°C .

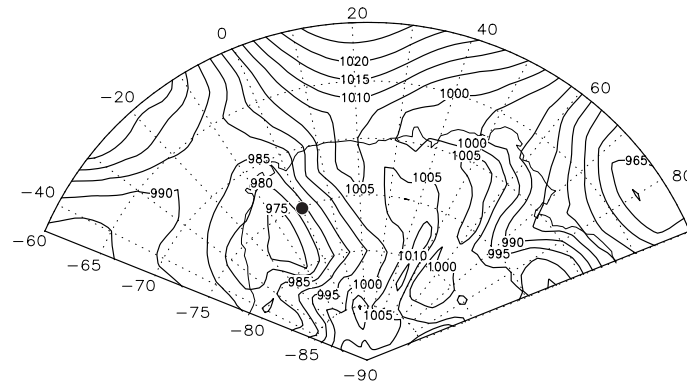


Figure 6.8. Sea level pressure for 12 May 1998, 0.00 GMT. The dot indicates the location of AWS 9.

6.6 Case study: a major snowfall event in May 1998

In 1998, ~ 4 major snowfall events took place (Figure 6.2), that contributed $\sim 80\%$ of the total annual accumulation. The event in May 1998 was the most pronounced event, with accumulation at all AWS except 7 and 8, and also in the ECMWF analysis. In general, snowfall in western DML is associated with the development of a cyclone in the Weddell Sea area and a high-pressure ridge over eastern DML. The strong north-easterly flow connected to this ridge in combination with the steep orography of DML forces the air to rise and snowfall is generated. The event described here is similar to the events described by Noone *et al.* (1999).

In May 1998, a significant amount of snow accumulated in DML varying from ~ 20 mm w.e. at AWS 1 and 4 to ~ 160 mm w.e. at AWS 2. The event started on the 11th when a high pressure ridge extended sufficiently south to force depressions towards the continent and away from their climatological track, parallel to the coast-line (Figure 6.8). From the 11th to the 14th the northerly flow advects two depressions with warm and moist air south towards the continent. After the 14th the ridge moves east and breaks down rapidly.

Figure 6.9 shows the temperature, specific humidity, wind speed, wind direction, pressure and accumulation measured at AWS 9 for 10 days in May containing the event. The mean temperature in May is $\sim -50^\circ\text{C}$. The temperature during this event rapidly increases from -60°C on 10 May to -24°C on 13 May, which is exceptionally high. Simultaneously, the specific humidity increases from almost 0 to 0.8 g kg^{-1} . The wind speed is also high, exceeding 15 m s^{-1} compared to a monthly mean of 6.6 m s^{-1} . The wind direction changes from north-east (50°), the direction of the katabatic flow, to north (0°), in the direction of the large scale geostrophic flow. The pressure increases to a maximum of 685 hPa showing the development of the high pressure ridge. The temporary dips in pressure at 11 and 13 May are caused by depressions. The surface height, a measure for accumulation, increases ~ 0.10 m at 12 May. Figure 6.9 additionally shows the ECMWF records at the AWS location. There is a good agreement between the records.

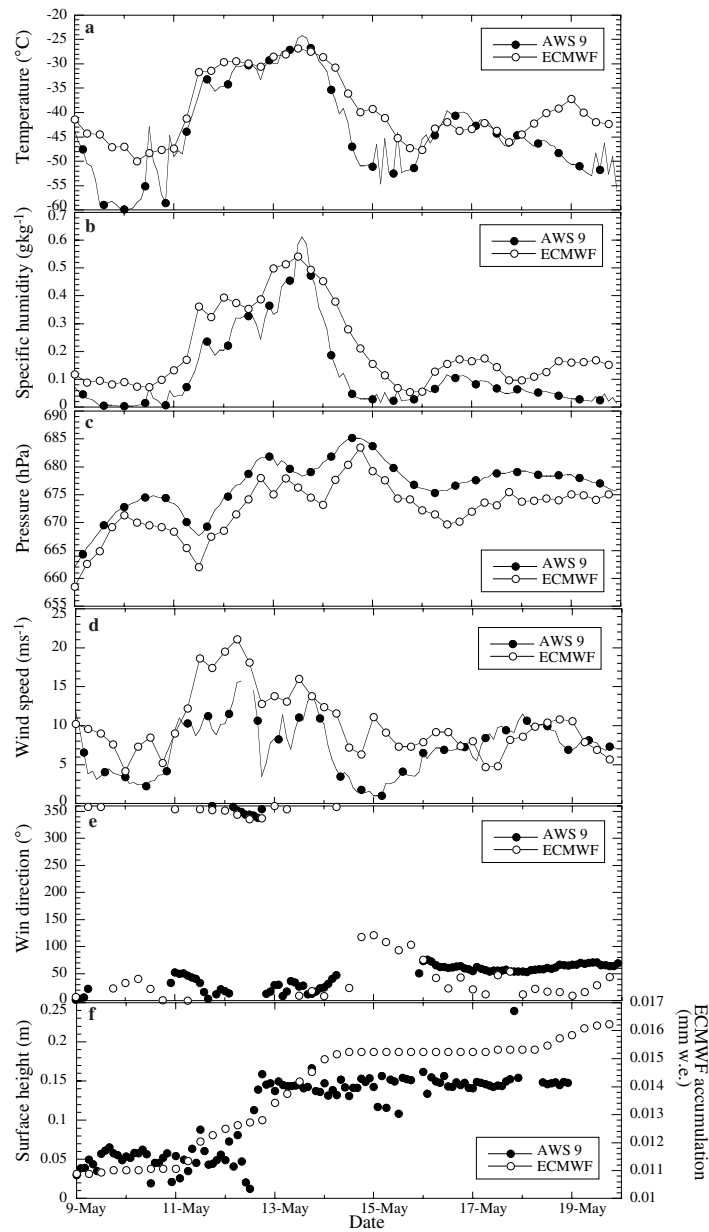


Figure 6.9. Hourly mean (AWS) and 6 hourly variation (ECMWF) of (a) temperature, (b) specific humidity, (c) air pressure (d) wind speed, (e) wind direction and (f) accumulation at AWS 9 for the snowfall event in May 1998. Closed circles present AWS data, open circles ECMWF surface values. In (f) the surface height is 0 m and the ECMWF accumulation 0 mm w.e. at 1 January 1998.

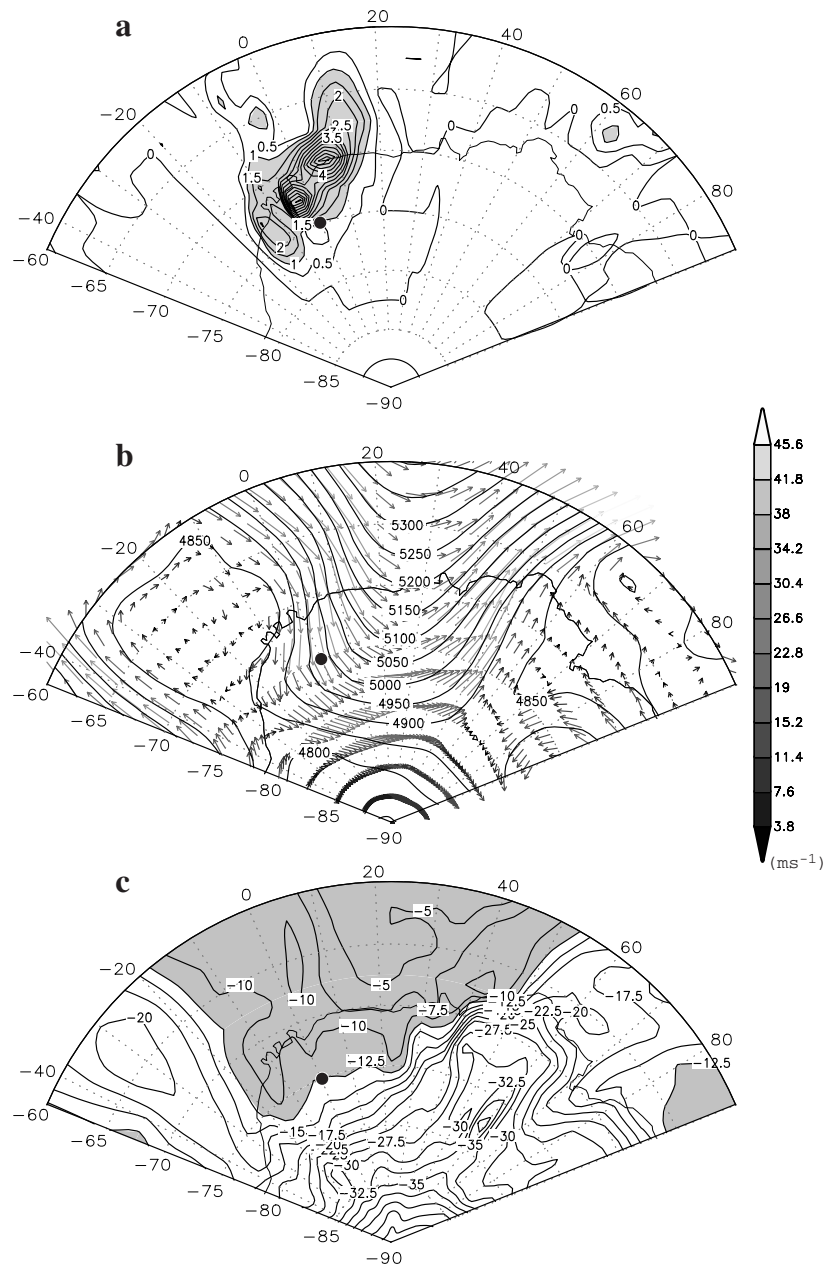


Figure 6.10. ECMWF fields for 13 May 1998, 12.00 GMT. (a) Forecast snowfall in the previous 6 hours in mm w.e. (b) Height of the 500 hPa level in m plus the wind field in m s^{-1} at the same height. (c) The temperature at 850 hPa, shaded values exceed -12.5°C . The dot indicates the location of AWS 9. (a) Is a forecast field, (b) and (c) are analyses fields.

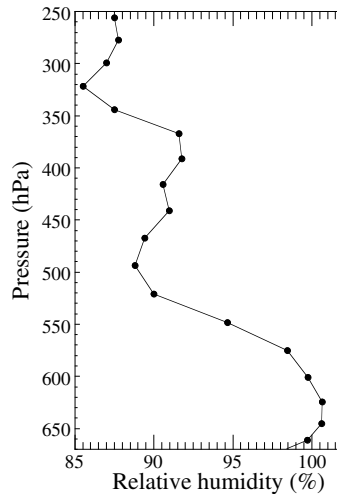


Figure 6.11. Mean vertical relative humidity profile at AWS 9 for the period 11 to 14 May 1998 from the ECMWF model.

Figure 6.10 is an example of the ECMWF fields of the snowfall event at 13 May 1998, 12.00 GMT. Figure 6.10a shows that the snowfall is concentrated in an area along the coast from 20°W to 20°E , parallel to the orography. All AWS are located in the area with snowfall except AWS 3. Figure 6.10b shows the height of the 500 hPa level and the wind vectors at that same level illustrating the large scale flow. Clearly visible is the blocking high pressure ridge with its axis at 30°E and the strong northerly flow over western DML and the strong southerly flow over eastern DML. The warm air mass advected southwards can be identified in Figure 6.10c as a tongue of high temperatures spreading southwards along the coast. In eastern DML, where the flow is from the south, cold and dry continental air is advected northwards.

From 11 until 14 May the air at AWS 9 was saturated from the surface up to ~ 600 hPa suggesting condensation in this area (Figure 6.11). Backward trajectories were calculated for this event with the lowest three starting levels falling within this layer. Figure 6.12 shows trajectories arriving at 13 May 12.00 GMT at AWS 9. It shows that, independent of the arrival height at the AWS site, the transport pathway is the Atlantic Ocean. The difference between the surface temperature and potential temperature of the trajectory is smallest 4 days before arrival (9 May at 12.00) for the lowest three trajectories (Figure 6.13a). At this day, the boundary layer is ~ 100 hPa high topped by a saturated layer reaching the 750 hPa level. The air parcels are in the saturated layer and probably able to interact with the surface. Surface evaporation along the lowest three trajectories is strongest 3 to 4 days before arrival (9 to 10 May). The specific humidity of the air parcels gradually increases during these days from ~ 0.5 to 3.5 g kg^{-1} . The last two days before arrival the surface latent heat flux is positive (condensation/deposition) and the specific humidity of the air parcels decreases. This suggests that the moisture source region for this event is likely to be

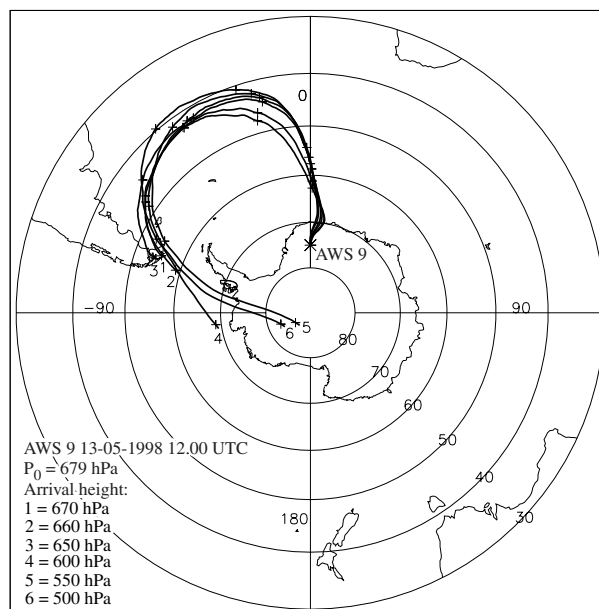


Figure 6.12. Five-day backward trajectories starting at AWS 9 for 13 May 1998, 12.00 GMT at 6 different levels.

dominated by the area between 40 and 50 °S and 20 and 60 °W, in the Atlantic Ocean. The sea surface temperature in this area is between 5 and 15 °C. The specific humidity record suggests that ~50 % of the moisture arriving at AWS 9 originates from this region.

6.7 Summary and conclusions

In this chapter we combined AWS data and trajectories to assess moisture sources for the snow accumulated on the plateau in Western Dronning Maud Land, Antarctica, in 1998. A distinction between snowfall and non-snowfall trajectories was made.

Substantial differences are found between accumulation measured at the AWS sites and ECMWF precipitation estimates. These differences are probably caused by the difficulty to distinguish precipitation from other processes in the measurements, errors in ECMWF model orography and the fact that model snowfall represents the mean of a grid cell rather than one location within the cell. The accumulation measurements did not show any seasonality. The record is at present too short and the number of events with substantial snowfall is too small (~4) to make any firm conclusions. However, the fact that the snowfall is not uniform or continuous over the year has significant implications for identifying annual layers in data from ice cores.

A case study of a snowfall event in May 1998 shows that snow falls during extreme weather conditions, which was also found by Noone *et al.* (1999). Trajectories

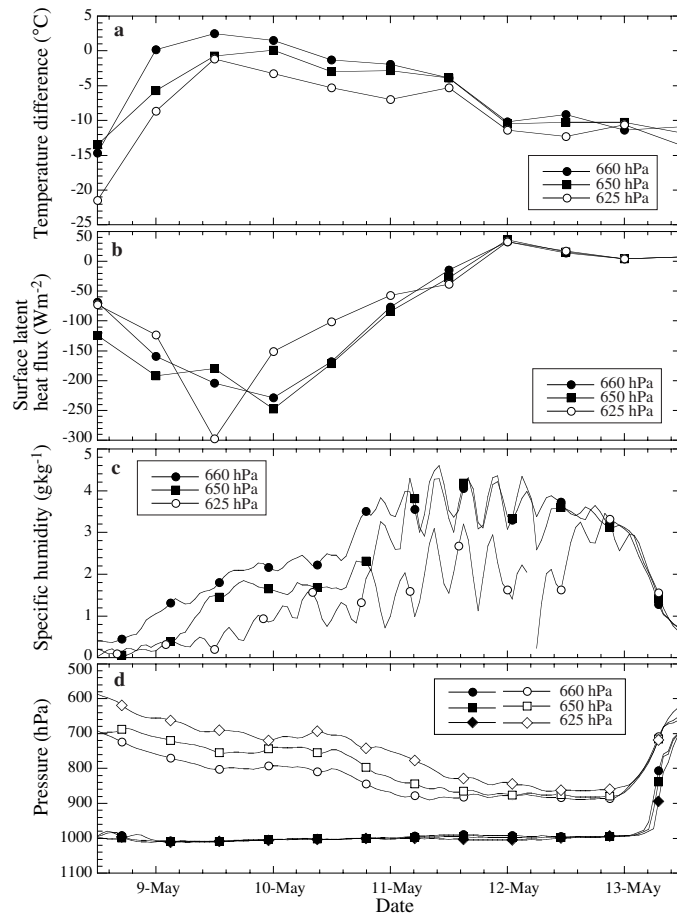


Figure 6.13. (a) Temperature difference (surface temperature minus potential temperature) along the trajectories starting at AWS 9 for 13 May 1998, 12.00 GMT at 3 different levels 5 days back. (b) Surface latent heat flux averaged over all snowfall trajectories and (c) mean specific humidity at trajectory level. (d) Mean vertical displacement in pressure of the snowfall trajectories, closed symbols are surface pressure, open symbols trajectory pressure.

calculated for this event show a source region of the moisture dominated by the western part of the Atlantic Ocean between 40 and 50 °S and 20 and 60 °W.

Considering all the trajectories shows that ~40 - 80% of the snow that falls at AWS 9 in 1998 originates from the Atlantic Ocean, ~10% from the Pacific Ocean and almost none from the Indian Ocean. Based on trajectory height, temperature difference, the surface latent heat flux and the specific humidity, the origin of the moisture is most likely between 40 and 60 °S in the Atlantic Ocean where sea surface temperatures vary between 0 and 20 °C. This is in agreement with results from GCM studies (Delaygue *et al.*, 2000; Delmotte *et al.*, 2000).

Differences in source regions resulting from different studies do not necessarily

contradict each other but could be the result of the different methods used. The advantage of GCMs is that moisture parcels are directly traced from evaporation point to precipitation point and simulations of other climates than the present are possible. A disadvantage is the use of climatologies and the coarse resolution (order of 10°) to enable long time integrations and the loss of information about the transport pathways. Deuterium excess and $\delta^{18}\text{O}$ studies have the advantage to use the actual composition of the snow. However, the idealized models used to determine the source regions, are not able to account for the complexity of atmospheric processes. Atmospheric water balance studies are the least suitable to determine source regions for Antarctic snow. They merely show large regions with a net evaporation or condensation surplus.

Air parcel trajectories have the advantage of using wind fields forced by observations with a fairly good resolution and air parcels are directly traced. A problem is that not the moisture itself but an air parcel containing moisture is followed: possible replacement of moisture through cycles of condensation and evaporation along the trajectory is not taken into account. The uncertainty in the trajectory calculations contributes significantly to the uncertainty in the identified moisture source region. The error estimates given in literature introduced by choice of trajectory type and interpolation schemes are on the order of 1000 km or 9° (Kahl *et al.*, 1989; Stohl *et al.*, 1995) when calculating 5 days back. The actual uncertainty is even larger due to errors in the analysed wind fields and the presence of convective systems (e.g., fronts). In a convective system the air parcel loses its identity making it impossible to trace a single parcel deterministically. Calculation of an ensemble of trajectories can give an impression of the sensitivity of the trajectories to convective systems and changes in flow pattern. Because the different atmospheric conditions that lead to precipitation in DML are quite similar, the one year record of snowfall trajectories presented here can be considered to give an estimate of the variability one might expect over a longer period.

Chapter 7

Air parcel trajectories to five deep drilling locations on Antarctica, based on the ERA-15 data set

Summary

We define moisture sources of snow falling at five Antarctic deep drilling locations: Byrd, DML05, Dome C, Dome F and Vostok. Five-day backward air parcel trajectories are used, based on European Centre for Medium Range Weather Forecasts Re-analysis data, ERA-15 (1979-93). A distinction is made between cases with and without snowfall at the point of arrival based on model precipitation. ERA-15 precipitation is in reasonable agreement with measured accumulation at Byrd, but seriously underestimates the amount of precipitation on the East Antarctic ice sheet. The trajectories show that the oceans closest to the site contribute most moisture. The latitude band contributing most ($\sim 30\%$ of the total annual precipitation) is $50 - 60^\circ\text{S}$, i.e., the area just north of the sea ice edge. The calculated trajectories show seasonal dependency, resulting in a seasonal cycle in the moisture sources, which is further enhanced by a seasonal cycle in the amount of precipitation. The inter-annual variability of the source regions is on the order of 3 latitude degrees. At DML05, a significant northward moving moisture source region is detected, while at Dome C a significant southward movement is observed.

¹This chapter is based on: Reijmer, C.H., M.R. van den Broeke and M.P. Scheele, 2001. Air parcel trajectories to five deep drilling locations on Antarctica, based on the ERA-15 data set. *J. Climate*, Submitted.

7.1 Introduction

Deep ice cores have been drilled at several locations in the Antarctic and Greenland ice sheet, e.g., Vostok, Byrd and Dome F (Antarctica), Greenland Ice Core Project (GRIP and North GRIP) and Greenland Ice Sheet Project (GISPII) (Greenland Ice-core Project (GRIP) Members, 1993; Dome-F Ice Core Research Group, 1998a,b; Petit *et al.*, 1999). The main objective of the European Project for Ice Coring in Antarctica (EPICA) is to construct a high resolution climate record for the Antarctic by drilling two additional cores and compare the results with other Antarctic and Greenland records. The EPICA cores are drilled at Dome C (Wolff *et al.*, 1999) and DML05 (Oerter *et al.*, 2000) (Figure 7.1). The low accumulation rate at Dome C, ~ 36 mm water equivalent per year (w.e. yr^{-1}) (Petit *et al.*, 1982), hopefully produces a record of several glacial-interglacial cycles, while the relatively high accumulation rate at DML05, ~ 62 mm w.e. yr^{-1} (Oerter *et al.*, 2000), enables one to obtain a detailed record of the last glacial-interglacial cycle. Furthermore, DML05 is located in Dronning Maud Land (DML), an area which is considered to be an important link between Antarctic and Greenland ice core records.

The climate recorded in ice cores is determined by the conditions that prevail when snowfall occurs. These need not be representative for the mean climate conditions at that point (Noone *et al.*, 1999). Factors such as seasonality of snowfall and changes in moisture source region may bias the ice core record in a systematic way (Jouzel *et al.*, 1997; Schlosser, 1999). Several techniques have been used to trace moisture source regions of Antarctic snow. Petit *et al.* (1991) and Ciais *et al.* (1995) use deuterium excess as tracer in combination with idealized isotope models. They conclude that the Antarctic moisture has a subtropical origin, 30 - 40 °S and 20 - 40 °S, respectively. Peixoto and Oort (1992) came to the same conclusion on the basis of atmospheric water balance studies (8 - 40 °S). Other studies including $\delta^{18}\text{O}$ (Bromwich and Weaver, 1983), General Circulation Models (GCM) (Delaygue *et al.*, 2000; Delmotte *et al.*, 2000), and trajectory studies (Reijmer and van den Broeke, 2001), suggest a more southerly origin, 55 - 60 °S, 30 - 60 °S and 40 - 60 °S, respectively.

In this study we use a trajectory model and European Centre for Medium Range Weather Forecasts (ECMWF) Re-analysis (ERA-15) data to trace moisture sources of five Antarctic locations. The locations chosen are the two EPICA drilling sites (DML05 and Dome C) and three sites on the polar plateau where deep drillings have been carried out in the past, namely Byrd, Dome F and Vostok (Herron, 1982; Legrand and Delmas, 1987; Dome-F Ice Core Research Group, 1998b) (Figure 7.1, Table 7.1). The approach in this study is similar to that of Reijmer and van den Broeke (2001), who described trajectories to DML05 for 1998. Noone *et al.* (1999) also used ERA-15 data to describe seasonal patterns and trajectories of significant snowfall in the DML region.

In Section 7.2 the trajectory model and ERA-15 are briefly described. Section 7.3 describes the characteristics of the model snowfall compared to measurements. In Section 7.4 the calculated trajectories are described. The chapter is concluded with a summary and discussion of the results.

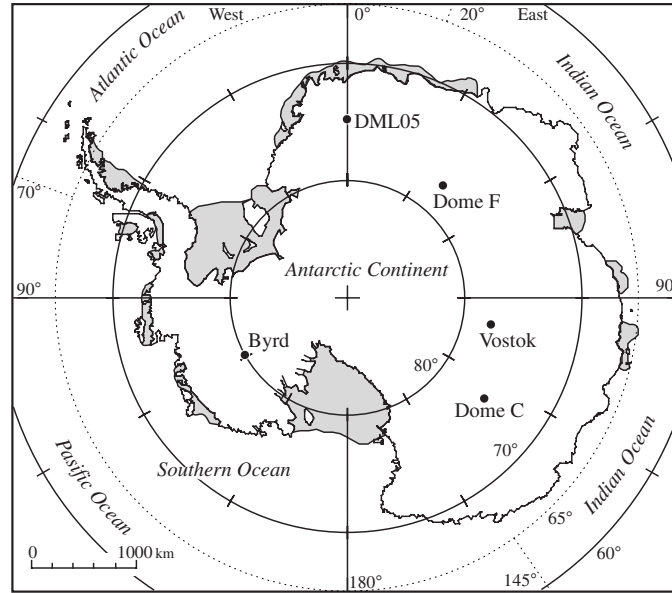


Figure 7.1. Map of Antarctica showing the main arrival locations of the trajectories. Dotted lines are boundaries of ocean regions defined in the text.

7.2 The trajectory model

To calculate air parcel trajectories we use the trajectory model developed by the Royal Netherlands Meteorological Institute (KNMI) (Scheele *et al.*, 1996). This model computes the three-dimensional displacement of an air parcel during a time step Δt using an iterative scheme:

$$\mathbf{X}_{n+1} = \mathbf{X}_0 + \frac{\Delta t}{2} [\mathbf{v}(\mathbf{X}_0, t) + \mathbf{v}(\mathbf{X}_n, t + \Delta t)]. \quad (7.1)$$

In this equation Δt is the iteration time step, \mathbf{X}_0 is the position vector of the parcel at time t , \mathbf{X}_n is the n^{th} iterative approximation of the position vector at time $t + \Delta t$ and $\mathbf{v}(\mathbf{X}, t)$ is the wind vector at position \mathbf{X} and time t . The iteration time step is -10 minutes. The iteration stops when the horizontal distance between \mathbf{X}_n and \mathbf{X}_{n+1} is less than 300 m and the relative vertical pressure difference, defined as $\frac{P_{n+1} - P}{P_{n+1}}$, is less than 0.0001. The model is able to compute different types of trajectories, e.g., isentropic, isobaric or three-dimensional. The latter is used because it most accurately approximates the true three-dimensional transport path (Stohl *et al.*, 1995; Kottmeier and Fay, 1998).

As input for the trajectory model we use ERA-15 data (1979-93) (Gibson *et al.*, 1997). The wind fields are the 6 hours forecasted fields, not analyses, to ensure physical balance in the meteorological fields, giving the most accurate representation of the vertical wind speed component. ERA-15 data have a horizontal spectral resolu-

Table 7.1. Characteristics of the five starting points for trajectory calculations.

Station	Latitude	Longitude	Elevation (m a.s.l.)	Slope (m km ⁻¹)	Distance (km)	<i>P</i> (mm w.e. yr ⁻¹)	<i>Acc.</i>
Byrd	80° 0'S	119° 24'W	1530 (1605)	3.5	689.5	159±53	160 ^a
DML05	75° 00.2'S	0° 00.4'E	2892 (2769)	1.3	602.0	29±6	62±21 ^b
Dome C	74° 30'S	123° 0'E	3280 (3042)	0.3	945.4	16±9	36±5 ^c
Dome F	77° 19'S	39° 42.2'E	3810 (3283)	0.0	927.8	7±3	30 ^d
Vostok	78° 30'S	106° 54'E	3488 (3409)	1.0	1362.5	6±2	22.5 ^e

Notes: The surface slope and distance from the coast are based on a 10 by 10 km Antarctic Topography (data courtesy of J. Bamber, Bristol University). The error estimate in the model precipitation is the standard deviation in the annual means over the 15-year period. Elevation, measured elevation; between brackets, ERA-15 model elevation; *P*, model precipitation; *Acc.*, measured accumulation.

References: a, Herron (1982); b, Oerter *et al.* (2000); c, Petit *et al.* (1982); d, Dome-F Ice Core Research Group (1998b); e, Legrand and Delmas (1987).

tion of T106 ($\sim 1.7^\circ$) and 31 σ -levels in the vertical. For the trajectory model, the resolution of the input data is kept constant at 1.5° in the horizontal plane, 31 levels in the vertical and 6 hours in time. This makes interpolation in time and space necessary: spatial interpolation is bi-linear in the horizontal and linear in the logarithmic value of the air pressure in the vertical, time interpolation is quadratic (Scheele *et al.*, 1996).

Uncertainties that are introduced by the choice of trajectory type and interpolation schemes, are on the order of 1000 km after 5 days calculation (Kahl *et al.*, 1989; Stohl *et al.*, 1995). Errors in the vertical wind component constitute a major source of uncertainties in the calculated trajectories. The above implies that the identified source regions after 5 days have an uncertainty of ~ 9 degrees latitude. In reality, the uncertainty might be even larger because of the difference between the forecasted wind fields and the real winds, and the presence of convective systems (such as fronts). In a convective system the air parcel loses its identity making it impossible to truly trace a single parcel. These important sources of errors in trajectories are difficult to assess and are not quantified in the uncertainty estimates presented here. Fortunately, precipitation in the continental polar atmosphere is generally stratiform and convective mixing is usually insignificant. Furthermore, Cullather *et al.* (1997) showed that the analyses, and therefore probably also the forecast fields, in ERA-15 are superior to analyses of the National Centers for Environmental Prediction for large-scale circulation features and moisture budget of the high southern latitudes. Kahl *et al.* (1989) conclude that sensitivity due to differences in gridded meteorological data bases, i.e. the input wind fields, an indicator for errors in the wind fields, can be larger than the sensitivity due to different trajectory calculation methods. An additional problem is the fact that in the trajectory method not the moisture itself but an air parcel containing moisture is traced, which also complicates the position-finding of the region where moisture actually enters the air parcel. Possible replacement of moisture through cycles of condensation and evaporation is not taken into account. We nevertheless think that the computed trajectories can give a reasonable estimate of the source regions of Antarctic moisture, but must be interpreted with care.

Table 7.2. Starting pressure levels for the air parcel backward trajectory calculations, and mean surface pressure (P_0) in hPa.

level	Byrd	DML05	Dome C	Dome F	Vostok
P_0	805.9	685.6	661.3	639.7	630.9
1	800	680	650	630	620
2	790	670	640	620	610
3	780	660	630	610	600
4	750	625	600	575	575
5	700	575	550	525	525
6	625	500	475	450	450

Trajectories are calculated 5 days back in time and calculations are initiated (and air parcels arrive) every 12 hours (0.00 GMT and 12.00 GMT) at six different pressure levels above the surface. Table 7.2 presents the six levels and the mean model surface pressure at the five locations. Trajectories that intersect with the surface are omitted from the analysis; this represents $\sim 10\%$ of the trajectories starting at the lowest level.

In the following a distinction is made between trajectories with and without snowfall on arrival (based on ERA-15 snowfall). ERA-15 snowfall is based on the cumulative snowfall in the first 12 forecast hours and suffers from model spin-up, and is $\sim 9\%$ less than the amount from the 12 to 24 hours forecast (Turner *et al.*, 1999). To mark a trajectory as a snowfall trajectory, unless stated otherwise, at least 1.0, 0.35, 0.25, 0.20 and 0.15 mm w.e. of snow must have accumulated in the 12 hours preceding the parcel arrival at Byrd, DML05, Dome C, Dome F and Vostok, respectively. This ensures that $\sim 50\%$ of the total precipitation is represented in the snowfall trajectories. Unless stated otherwise, all events refer to amount of precipitation in 12 hours time.

7.3 Precipitation

The main mechanisms leading to precipitation in the coastal regions and on the East Antarctic plateau are described by Bromwich (1988), King and Turner (1997) and Cullather *et al.* (1998). Precipitation in the coastal areas of Antarctica is often orographic induced. The cyclones associated with the snowfall in the coastal regions seldom penetrate far inland and precipitation over the higher parts of the Antarctic plateau, where Dome C, Dome F and Vostok are located, may also be associated with radiative cooling of the air, instead of orographic lifting (Bromwich, 1988). The precipitation amounts on the plateau are usually small.

Owing to the orographic nature of most Antarctic precipitation, errors in the model orography can have great influence on the amount and location of model snowfall. This complicates the comparison between measured and modelled accumulation and will have the largest effect on the amount of precipitation at the stations reasonably close to the coast, Byrd and DML05. Genthon and Braun (1995) show that the ERA-15 orography is up to 1000 m too high in western DML resulting in too little precipitation on the Antarctic plateau in this area (Turner *et al.*, 1999), and

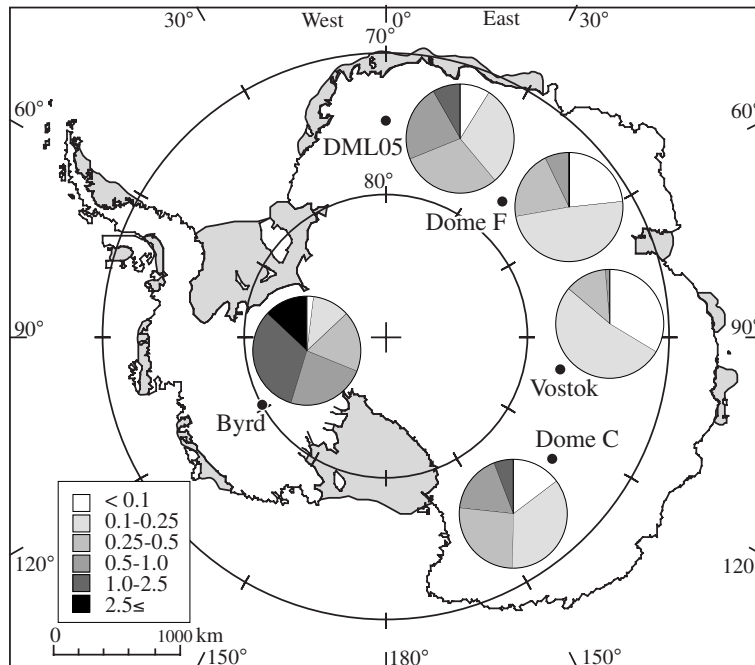


Figure 7.2. Percentage of the total 15-year precipitation grouped by 12 hourly totals bound by <0.1, 0.25, 0.5, 1.0, 2.5 and ≥ 2.5 mm w.e. per 12 hours at the five sites.

up to 1000 m too low in eastern DML where Dome F is located. Table 7.1 shows that at all stations, except Byrd, the model orography is too low, from 79 m at Vostok to 527 m at Dome F. Another factor complicating the comparison between measured and model accumulation, is the model resolution. Furthermore, accumulation is the result of precipitation, snowdrift erosion and deposition, sublimation and condensation. The later processes are disregarded in the analysis, although they are probably locally not negligible (Bromwich, 1988; Van den Broeke, 1997; Cullather *et al.*, 1998).

Table 7.1 additionally presents the annual mean precipitation in ERA-15 at the 5 drilling locations. The precipitation decreases with increasing elevation and is exceptionally low over the Antarctic plateau. The precipitation at Byrd is high compared to other locations. The accumulation map presented by Vaughan *et al.* (1999) shows that the accumulation on the West Antarctic plateau is considerably higher than in East Antarctica. Except at Byrd, the modelled precipitation is lower than the measured accumulation presented in the literature, the difference being largest for Dome F and Vostok. The differences found here agree with Turner *et al.* (1999). In that paper a comparison is made between annual mean accumulation (precipitation minus evaporation) in ERA-15 and an accumulation distribution compiled from measurements, presented by Giovinetto and Bentley (1985). In West Antarctica, ERA-15 accumulation resembles the measured accumulation better than in East Antarctica where the model consistently underestimates precipitation (Turner *et al.*, 1999). This underesti-

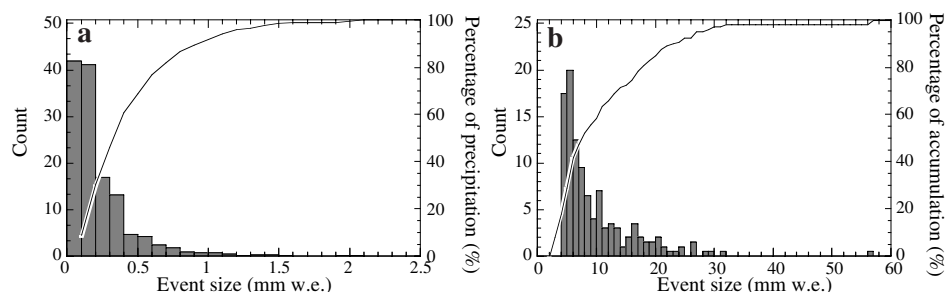


Figure 7.3. Distribution of mean annual number of events (left axis, bars) and cumulative percentage of annual mean precipitation, (right axis, line) at DML05 in (a) ERA-15 and (b) measurements (Chapter 4).

mation is also found in other climate models (Bromwich *et al.*, 1998; Cullather *et al.*, 1998) and can be partly attributed to the coarse resolution of these models, unable to represent the spatial variations in moisture transports (Cullather *et al.*, 1998).

Figure 7.2 presents the distribution of precipitation events based on 12 hourly totals at DML05. As expected from the described precipitation mechanisms and annual mean temperatures, the contribution of smaller events increases with increasing elevation and distance from the coast. At Vostok and Dome F, all events are smaller than 1 mm w.e., while at Byrd 45% of the total precipitation is caused by events larger than 1 mm w.e. Dome C is slightly more continental than DML05, given the fact that at Dome C $\sim 50\%$ of the precipitation is derived from events smaller than 2.5 mm w.e. compared to $\sim 38\%$ at DML05. Vostok is the most continental station, with 86% of the total precipitation caused by events smaller than 0.25 mm w.e. Annual distributions (not shown) are similar to the 15-year distribution (Figure 7.2). The largest events do not occur each year and contribute significantly to the inter-annual variability in precipitation. The smallest events (<0.1 mm w.e. per 12 hours) contribute an equal amount at all stations each year (~ 2.5 mm w.e. yr^{-1}).

In the model, the precipitation is mainly defined by a large number of small events, while in reality the precipitation is dominated by several major events. Measurements with a sonic altimeter at DML05 (Figure 7.3b) show that $\sim 40\%$ of the annual accumulation was deposited in ~ 20 events of 10 mm w.e. of snow in 12 hours (~ 0.03 m snow) per year. Events in which ~ 17 mm w.e. accumulates in 12 hours, occur ~ 6 times per year and contribute $\sim 20\%$ to the total accumulation. The occurrence of several large events instead of many small events in the measurements suggests that not all small events in the model are realistic and is the reason to take only the larger events into account in the trajectory analysis.

Figure 7.4 presents total annual and monthly precipitation at DML05 and Dome C for the 15-year ERA period. The variability, presented as the standard deviation in the 15-year annual mean (Table 7.1), is considerable. At Dome C the inter-annual variability is on the order of 50% of the annual mean precipitation. The annual time series are not well correlated. Except for the correlation between Dome C and Vostok, which is 0.75, the correlation coefficients are smaller than 0.45 and not significant

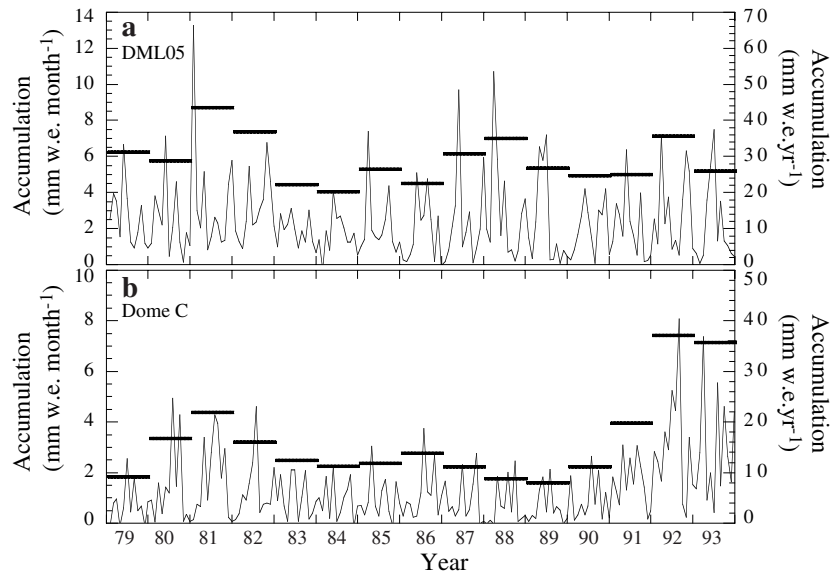


Figure 7.4. Monthly (thin lines, left axis) and annual (thick lines, right axis) accumulation at (a) DML05 and (b) Dome C over the 15-year ERA period.

at the 5% level. On shorter time scales, the records are not well correlated either. Correlation between separate events is only significant between Dome C and Vostok. The precipitation at Vostok appears to lag 0 to 12 hours behind Dome C, with a maximum correlation of 0.35 at 0 hours time shift. The lack of correlation between any of the other stations is probably caused by the considerable distance between the stations, >1000 km compared to ~600 km between Dome C and Vostok.

Figure 7.5 presents the mean annual cycle in model precipitation for DML05 and Dome C. All stations show an increase in precipitation in the winter months. This was also found in measurements (Bromwich, 1988), and model results (Cullather

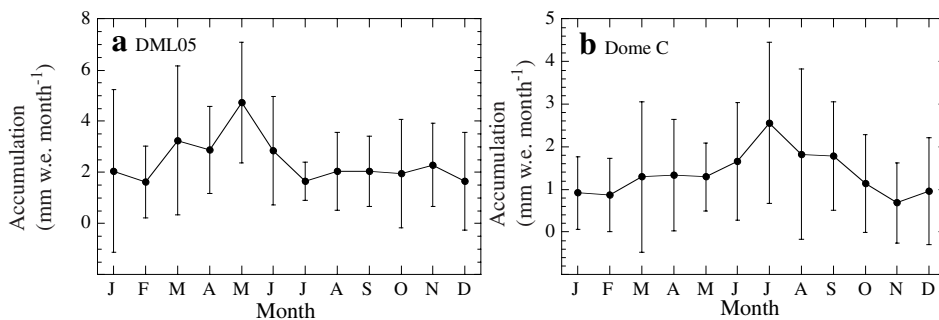


Figure 7.5. Annual cycle in model precipitation based on monthly averages for (a) DML05 and (b) Dome C. The error bars denote the standard deviation in the 15-year mean.

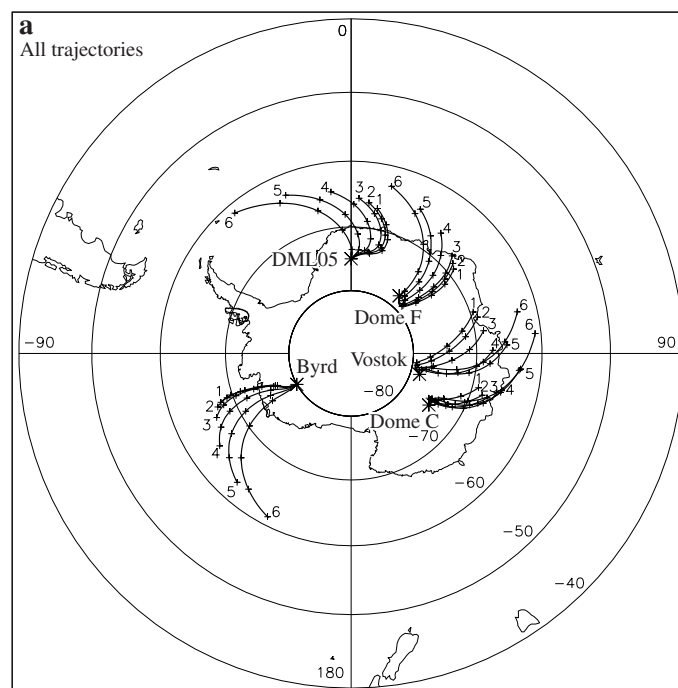


Figure 7.6. Mean five-day backward trajectories starting at six different pressure levels above the surface (Table 7.2, 6: highest level). Each day back is marked with a plus sign, the asterisks denote the arrival locations. (a) Shows the mean of all trajectories.

et al., 1998; Delaygue *et al.*, 2000). The seasonal cycles at Dome F and Dome C are very similar and show a maximum in July. At DML05 and Byrd a maximum is found in May. Seasonally averaged, most precipitation at DML05 occurs in autumn (37%) and at Dome C and Dome F in winter (37% and 35%, respectively). At Vostok, most precipitation occurs in the summer months (30%) and at Byrd, precipitation is highest in autumn and winter (33% and 30%, respectively).

7.4 Results of trajectory calculations

7.4.1 Mean trajectories

Figure 7.6a presents the mean of all trajectories and Figure 7.6b the mean of the snowfall trajectories, averaged over the 15-year ERA period, at six different pressure levels (Table 7.2). All trajectories show a cyclonic curvature reflecting the substantial influence of cyclones on the air parcel paths over Antarctica. The radius of curvature is smallest for the stations closest to the coast, Byrd and DML05, where cyclonic influences are largest. The radius of curvature increases with increasing arrival altitude due to the increase in advection speed. The lower trajectories arriving at Dome

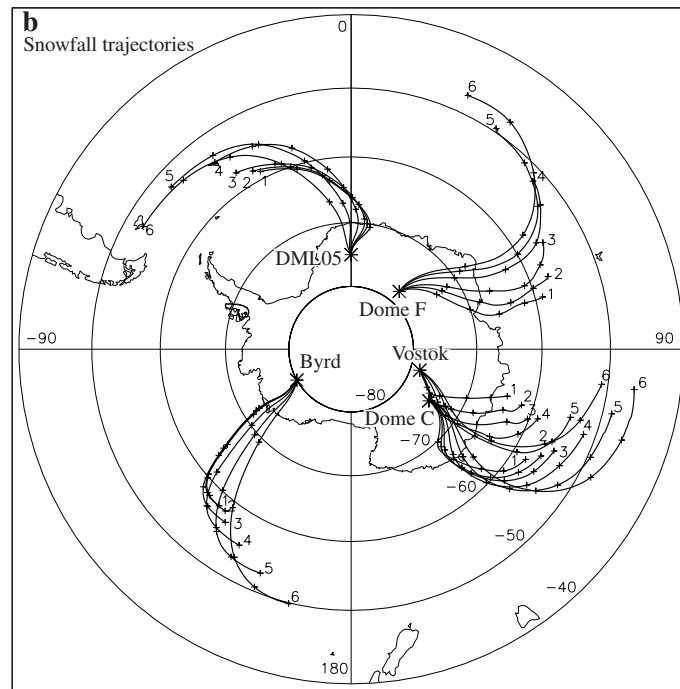


Figure 7.6. Continued. (b) As (a), but the mean of snowfall trajectories.

C, Dome F and Vostok, mostly remain over the continent, while at Byrd and DML05 most air parcels partly travel over the ocean. Due to the higher wind speeds at higher altitudes, the distance travelled by air parcels arriving at higher altitudes is larger, at level 6 about twice as large as at level 1, and their origin is further north and west. At Vostok and Dome C, the lower levels have more western pathways compared to the higher levels, while at the other stations the pathways are more western with increasing altitude. Especially the pathways of the lower trajectories are influenced by the surface, which results in an abrupt anti-cyclonic turn in the last day before arrival. The arrival directions are mainly from the northeast at DML05 and Byrd, and south to southwest at Dome F, Dome C and Vostok. This corresponds to the dominant wind direction near the surface at these locations, which is determined by the direction of the katabatic flow.

The snowfall trajectories presented in Figure 7.6b are clearly different and originate from locations farther north. The mean distance travelled by an air parcel is about twice as large compared to non-snowfall air parcels (3000-4000 km versus 1500-2000 km). At Byrd and DML05, the trajectories also originate from farther west. At Dome C, Dome F and Vostok, the trajectories are shifted to the east when compared to the mean of all trajectories. The resulting trajectories arriving at Vostok show that the air parcels travelled over Dome C within 12 hours before arrival and originate from about the same region. This could partly explain the correlation be-

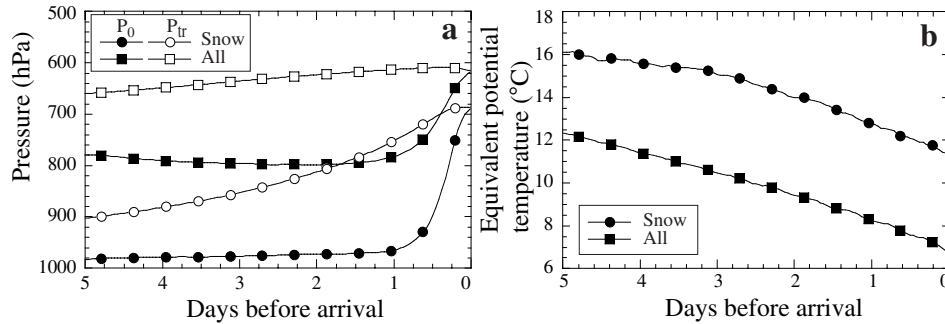


Figure 7.7. Mean (a) pressure, (b) equivalent potential temperature of snowfall and all trajectories arriving at DML05 at 625 hPa. P_0 , surface pressure; P_{tr} , trajectory pressure.

tween precipitation at Dome C and Vostok.

The different nature of the snowfall trajectories is further illustrated in Figure 7.7, which presents pressure and equivalent potential temperature (θ_e) along trajectories arriving at DML05, at 625 hPa. Results for the other locations are similar. Figure 7.7 shows that on average, snowfall trajectories are situated at higher pressure levels and have higher surface pressure along their path, because they travel closer to sea level. Therefore, air parcels in snowfall trajectories are more likely to interact with the surface and exchange moisture. θ_e is the temperature a parcel would have when brought adiabatically to 1000 hPa with all its moisture condensed and the resulting latent heat used to warm the parcel. θ_e is higher for snowfall trajectories owing to the larger moisture content and higher temperature when compared to all trajectories. The temperature at trajectory level (not shown) is 10 to 15 °C higher for snowfall trajectories and remains fairly constant until the continent is reached, ~1 day before arrival. The specific humidity for the snowfall trajectories (not shown) shows a small maximum ~4 days before arrival. The mean specific humidity for all trajectories is much lower owing to the lower temperature, and decreases in a linear fashion. In the remaining of this chapter only the snowfall trajectories will be described.

Judging from the general cyclonic curvature of the trajectories, the air parcel paths are likely to be influenced by the seasonality in strength and location of cyclones. However, Reijmer and van den Broeke (2001) did not find a clear annual cycle for 1998. This could be due to the short time period, while 5 to 10 years of precipitation data are necessary to obtain a significant seasonal cycle in precipitation. Figure 7.8 shows seasonally averaged snowfall trajectories. In summer (DJF), when cyclones are less intense and travel at further distance from the continent, the cyclonic curvature of the trajectory is small and the air parcels have their most southern and eastern origin. In the autumn (MAM) and spring (SON), when the surface pressure shows a minimum, and cyclones are probably most intense and travel closest to the continent, the trajectories show their most western origin, and air parcels travel the largest distances. Winter (JJA) trajectories are similar to autumn and spring, but have a slightly more northern origin. The seasonal shift is smallest at Byrd and largest at Vostok. Here, the cyclonic curvature is entirely absent in summer.

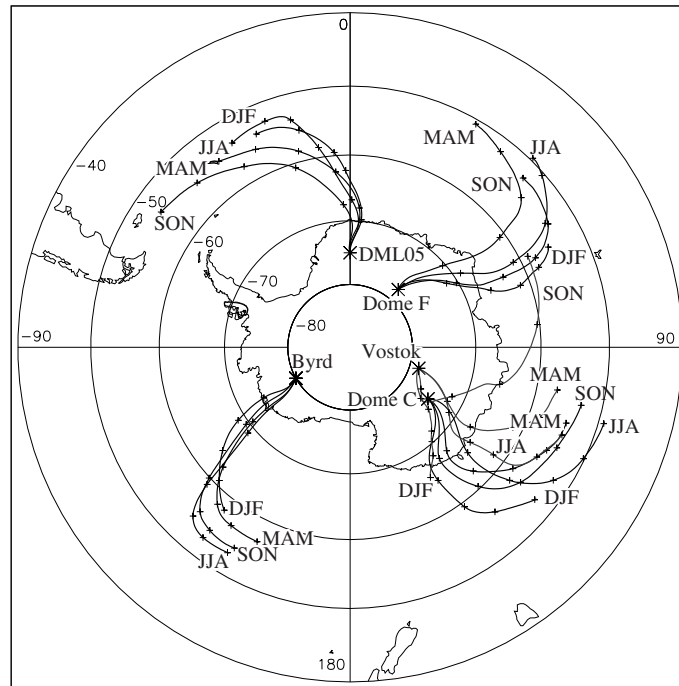


Figure 7.8. Mean five-day backward trajectories arriving at level 4 above the surface (Table 7.2). Asterisks mark the drilling sites, each day back is marked with a plus sign. Trajectories arriving at Vostok are grey to distinguish them from trajectories arriving at Dome C. DJF, summer; MAM, autumn; JJA, winter; SON, spring.

The variation in the individual trajectories is considerable, as shown in Figure 7.9. It increases with increasing altitude and increasing number of days before arrival. Assuming that the moisture source of Antarctic precipitation lies somewhere along the five-day mean snowfall trajectory, we speculate that the moisture sources for the precipitation is located between 50°S and 60°S for all five locations. At DML05 the moisture originates probably from the western part of the Southern Atlantic Ocean in agreement with Reijmer and van den Broeke (2001). At Dome F, Vostok and Dome C, the Indian Ocean provides the moisture. The source region of Vostok and Dome C precipitation is at almost the same location, in the eastern part of the Indian Ocean. Precipitation at Byrd comes from the Pacific Ocean.

Noone *et al.* (1999) show that the largest moisture transport to DML05 occurs at ~600 hPa, ~60 hPa above the surface, which is best represented by level 4. In the further analyses of the trajectories the air parcels arriving at level 4 are taken to represent the largest moisture transport. Calculated from individual snowfall trajectories, ~5% of the moisture precipitating at the drilling locations originates more than 5 days before arrival. Therefore, the assumption is made that the main moisture source of Antarctic precipitation is distributed along the five-day mean snowfall trajectories. Furthermore, Reijmer and van den Broeke (2001) show that ~50% of the moisture

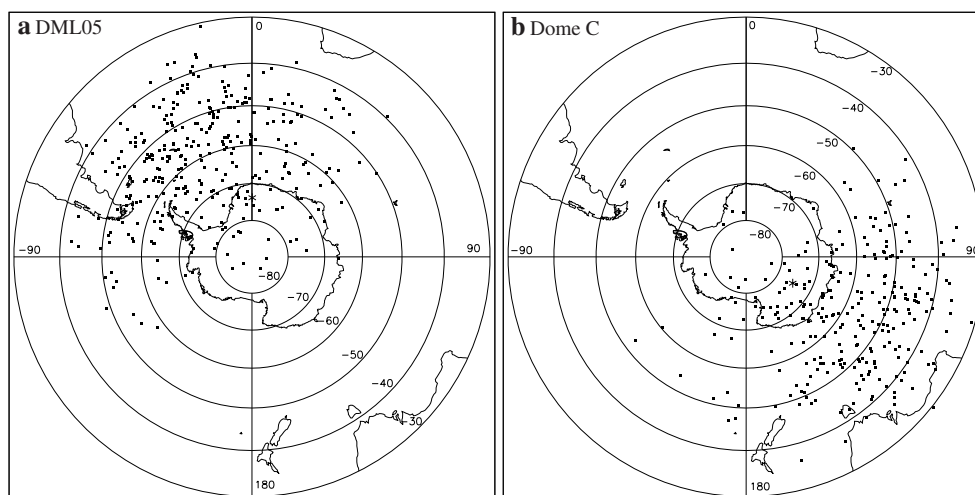


Figure 7.9. Locations of snowfall trajectories 4 days before arrival at (a) DML05 (625 hPa) and (b) Dome C (600 hPa). The asterisks denote the location of the stations.

arriving at DML05 originates 3 to 5 days before arrival. Here, the specific humidity shows a maximum ~ 4 days before arrival. Seasonally (not shown) the maximum in specific humidity varies between 3 days before arrival in summer to 5 days in autumn. The location of the air parcels 4 days before arrival will therefore be taken as representative for the main source region for moisture.

7.4.2 Moisture source regions

To get a better insight in the actual contribution of the various oceans and latitude bands to the precipitation at the five drilling sites, the southern hemisphere is divided into five regions similar to the regions presented by Reijmer and van den Broeke (2001): the Southern Atlantic Ocean ($70^\circ\text{W} - 20^\circ\text{E}$), the Southern Indian Ocean ($20^\circ\text{E} - 145^\circ\text{E}$), the Southern Pacific Ocean ($145^\circ\text{E} - 70^\circ\text{W}$), the Southern Ocean (between the Antarctic continental boundaries and 65°S) and the Antarctic continent (Figure 7.1). Furthermore, the southern hemisphere is divided into six latitude bands bound by 40°S , 50°S , 60°S , 70°S , 80°S and 90°S . Figure 7.10 presents the percentage of the snowfall trajectories distributed over the five ocean regions, 1 and 4 days before arrival. The air parcels arrive at level 4 (Table 7.2).

Figure 7.10 shows that one day before arrival at Dome C, Dome F and Vostok, most air parcels (45 - 85%) are above the Antarctic continent. At Byrd and DML05, which are located closer to the coast, more than 50% of the snowfall trajectories are still over the Southern Ocean. From days 2 to 5, the contribution of the continent and Southern Ocean decreases and the contribution of the ocean closest to the station increases. The larger the distance from the coast, the larger the amount of trajectories that remain over the Southern Ocean or continent. The main moisture source for

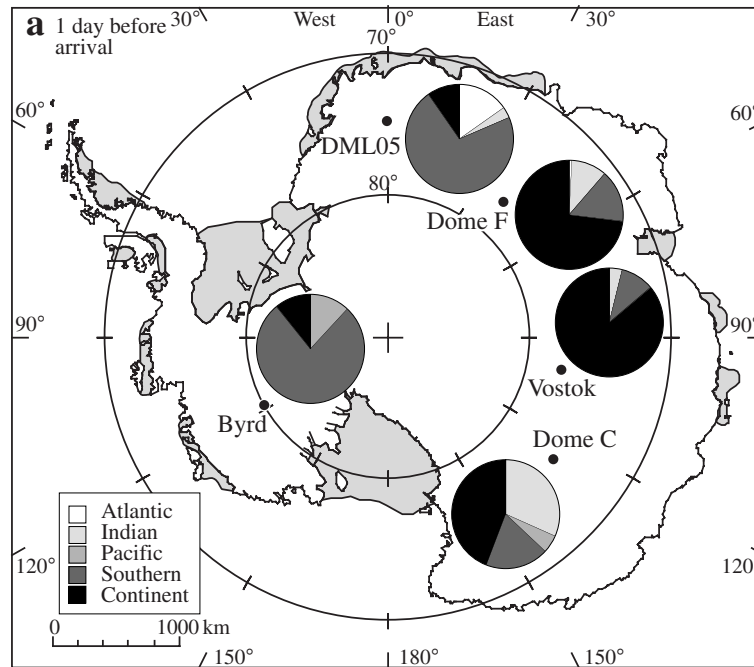


Figure 7.10. Distribution of source regions for snowfall trajectories arriving at level 4 (Table 7.2). (a) One day before arrival. Source regions are defined in the text and in Figure 7.1

DML05 is the Atlantic Ocean, with $\sim 60\%$ of the trajectories located there 3 to 5 days before arrival. Due to the cyclonic curvature of the trajectories the contribution of the Pacific Ocean increases with increasing time before arrival at DML05, to 10% at day 5. The contribution of the Indian Ocean is on the order of 7% . These results are similar to the results presented by Reijmer and van den Broeke (2001) for 1998, and to the present day climate simulation of Delaygue *et al.* (2000), although the contribution of the Pacific Ocean is larger in the latter and smaller in the former. At Dome F, the contribution of the Indian Ocean dominates, and varies between 45% and 65% . The contribution of the Atlantic Ocean is $\sim 25\%$. The contribution of the Pacific Ocean on Dome F is negligible. At Vostok, the contribution of the Atlantic Ocean is $\sim 7\%$, and is of the same magnitude as the contribution of the Pacific Ocean. The main contributor of moisture to the snowfall at Vostok is the Indian Ocean ($30 - 45\%$), and the contribution of the continent remains larger than 25% . In comparison, Delaygue *et al.* (2000) show a contribution of the continent of less than 10% to the precipitation at Vostok. In their study the Indian Ocean is also the main contributor, but the contribution of the Indian Ocean as well as the Atlantic and Pacific Ocean is higher. At Dome C, the contribution of the Atlantic Ocean is negligible. About $60 - 75\%$ of the snowfall originates from the Indian Ocean. Although located reasonably close to the Pacific Ocean, the contribution of the Pacific Ocean is only $8 - 15\%$, due to the cyclonic curvature of the trajectories. The main moisture source for Byrd is the

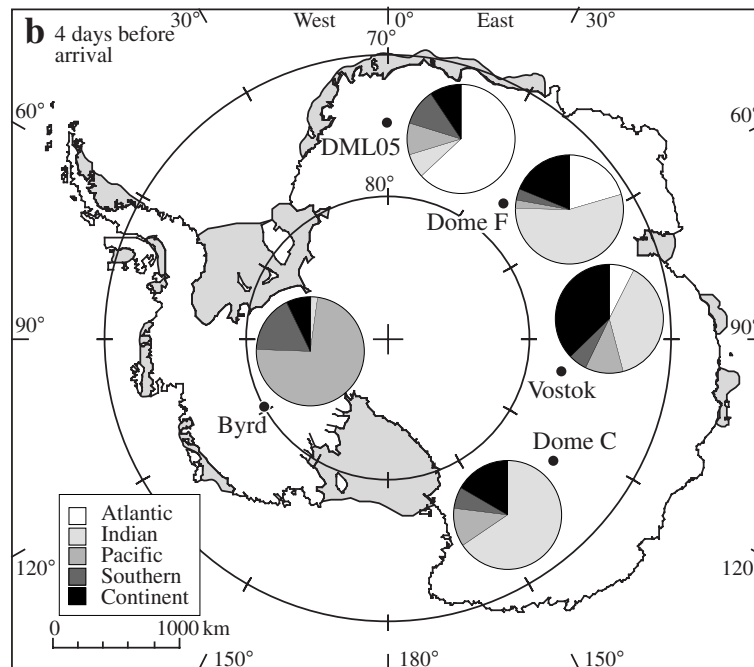


Figure 7.10. Continued. (b) As (a), four days before arrival.

Pacific Ocean (65 - 75%). The contribution of the Indian Ocean to the precipitation at Byrd is surprisingly small, ~5%. The contribution of the Atlantic Ocean is negligible. The small influence of the Indian Ocean on Byrd is caused by the small curvature in the mean snowfall trajectories.

Figure 7.11 presents the percentage of precipitation of which the air parcels are located in six different latitude bands, 4 days before arrival. The air parcels arrive at level 4 (Table 7.2). The contribution of different latitude bands to the precipitation is very similar for all stations. A maximum contribution of ~30% is found between 50 and 60°S. About 75% is contributed by the latitude band between 40 and 70°S. Less than 10% originates from north of 40°S. At Vostok and to a lesser extent at Byrd, the maximum is located closer to the continent, between 70 and 80°S for Vostok and 60 and 70°S for Byrd. This suggests a considerable contribution of the Southern Ocean to the precipitation at Vostok.

We briefly looked at seasonal cycles in the ocean and latitudinal distribution. Figure 7.12 presents the distribution of source regions per season for DML05 and Dome C. In winter, the trajectories have their most northern origin, which is reflected in the largest contribution of the ocean closest to the stations in this season (Figure 7.12a and b). The radius of curvature is smallest in the equinoctial seasons at all stations, which results in the largest contribution of the ocean west of the closest ocean in these seasons, e.g., Pacific Ocean at DML05 and Atlantic Ocean at Dome F. At Dome C, the contribution of the Indian Ocean is smallest and that of the Pacific Ocean

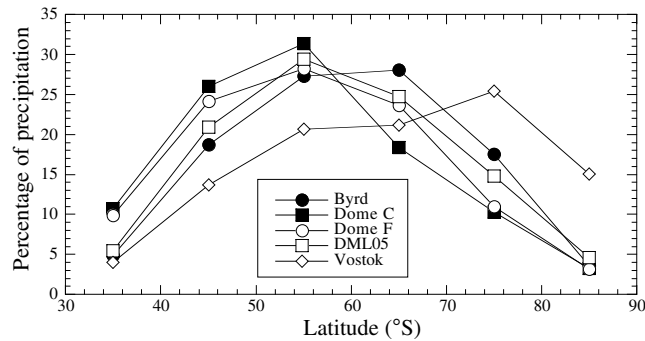


Figure 7.11. Percentage of precipitation of which the trajectories are located in six different latitude bands, bound by 40°S , 50°S , 60°S , 70°S , 80°S and 90°S , 4 days before arrival, at level 4 (Table 7.2).

is largest in summer. At Vostok the contribution of the Indian and Pacific Ocean are similar in summer, while in the other months the Indian Ocean dominates (not shown). At Byrd, the east-west differences are small and seasonality is most pronounced in the latitude distribution.

Figures 7.12c and d show the percentage of the total precipitation per season and latitude band, 4 days before arriving at DML05 and Dome C, at level 4. At DML05, there is no significant seasonality in the latitude distribution of the moisture sources. The maximum is always between 50 and 60°S . The magnitude of the maximum is largest in autumn when most precipitation occurs. The contribution to the total precipitation of this season and latitude band is $\sim 12\%$. At Dome F, the maximum is located most northerly in autumn and winter, and moves south in spring and summer. Because most snow at Dome F falls in winter, this maximum at low latitudes in summer, has only a small effect on the annual distribution (Figure 7.11). The distribution at Vostok is similar to Dome F. In winter and spring most moisture originates from $50 - 60^{\circ}\text{S}$, in summer from south of 70°S . Because the precipitation is fairly evenly distributed over the seasons at Vostok the shift south of the moisture origin is clearly visible in the annual distribution (Figure 7.11). The distribution at Dome C is similar to Dome F and Vostok, although the maximum shift south occurs in autumn. Almost half of the annual 55% from band $40 - 60^{\circ}\text{S}$ at Dome C is contributed in winter. At Byrd, the location of the source region is most south in summer and most north in winter. The maximum contribution occurs in autumn and winter from latitude band $50 - 70^{\circ}\text{S}$.

7.4.3 Inter-annual variability

Figure 7.13 presents the annual mean latitude of the air parcels 4 days before arrival at level 4, for DML05 and Dome C. The average location is at $\sim 60^{\circ}\text{S}$ for all stations, except Vostok. The inter-annual variability expressed in the standard deviation in the 15-year mean increases with increasing distance from the coast of the arrival location from 2.0 at DML05 to 4.9 at Vostok. For individual years, temporal variability

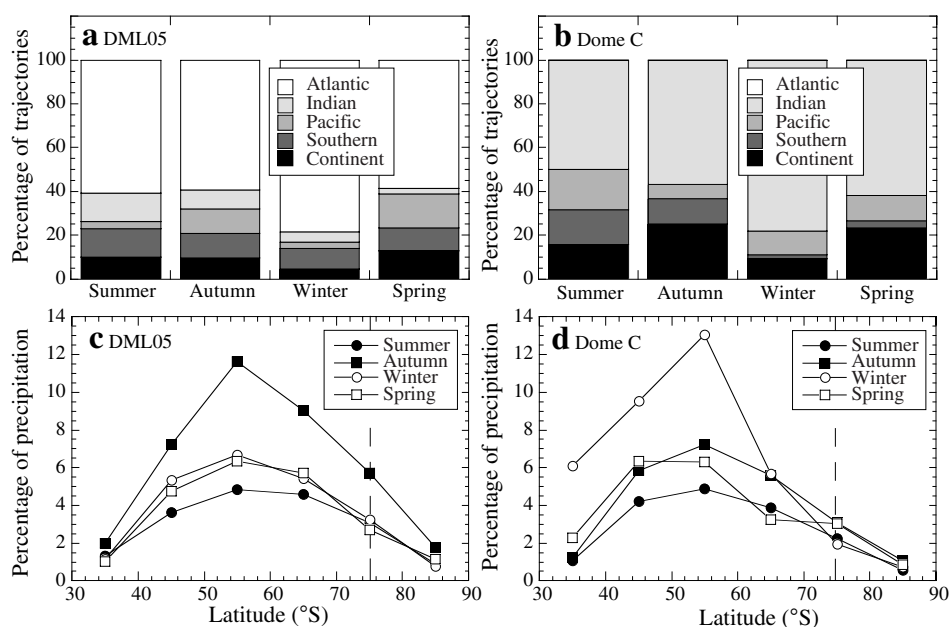


Figure 7.12. Distribution of source regions for snowfall trajectories per season. Source regions are defined in the text and in Figure 7.1. (a) and (b) present ocean regions and (c) and (d) latitude bands. The location is taken 4 days before arrival, at level 4 (Table 7.2), at DML05 (a, c) and Dome C (b, d). Dashed lines indicate the latitude location of the stations.

is larger when the source region is located more to the south. For example, the standard deviation in the annual mean increases in a linear fashion from 2.0 to 3.0 when the source region for DML05 moves from 58°S to 66°S. In the 15-year ERA period there is a trend northward of the source region for all stations except Dome C. The trend is however, only significant at the 5% level at DML05. At Dome C there is a significant trend southward. There is no clear explanation for this trend.

Except at Vostok, a southward migration of the source regions goes together with an eastward migration. The inter-annual variability in longitude location is considerable (Figure 7.13c and d) and is of the same order of magnitude as the seasonal variability. The standard deviation in the 15-year mean is 9.9 at DML05 and 4.9 at Dome C. There is no significant trend at any of the stations. The large variability can result in a shift in main ocean contribution. At Vostok the shift is largest and varies from the Atlantic Ocean in 1982 to the Pacific Ocean in 1987 and 1991 (not shown).

The source location is an intricate function of the strength and pathways of cyclones and is through that related to the annual mean precipitation, temperature, and pressure. In general, at DML05, Dome C and Dome F, the moisture source regions are located more south in years with high annual mean temperature, high surface pressure and high precipitation, while at Byrd and Vostok the source regions are located more south in years with less precipitation and lower surface pressure and temperature.

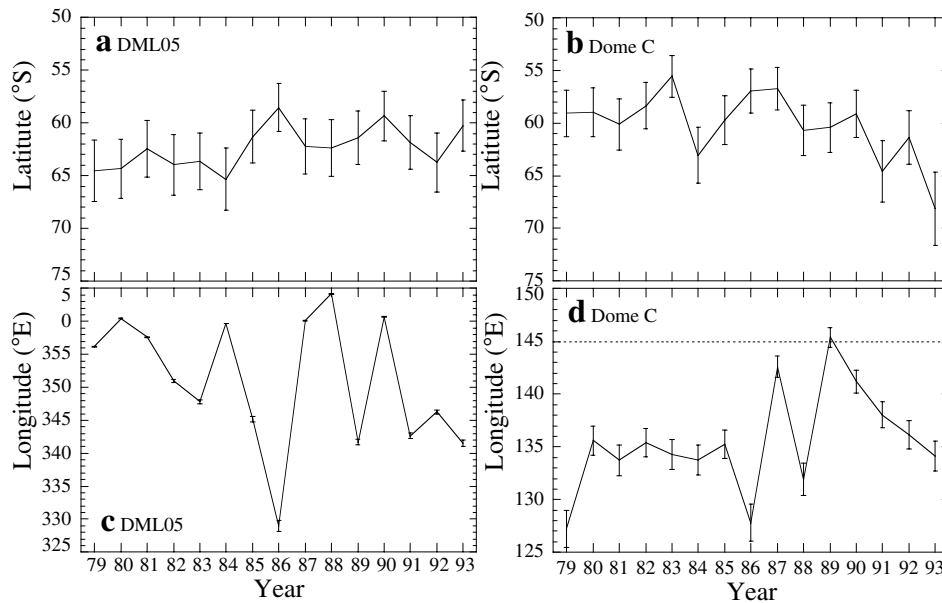


Figure 7.13. Annual mean (a,b) latitude and (c,d) longitude position at day 4 before arrival at level 4, at DML05 and Dome C. The error bars denote 1 standard deviation from the mean.

7.5 Summary

Moisture sources for snow falling at five locations on Antarctica were determined using five-day backward air parcel trajectories based on the European Centre for Medium Range Weather Forecasts 15-year Re-analysis data (ERA-15). Five ice core drilling sites (Byrd, DML05, Dome C, Dome F, Vostok) were chosen as arrival points. A distinction is made between trajectories with and without snowfall at arrival, based on model precipitation. Trajectories were marked as snowfall trajectories when at least 1.0, 0.35, 0.25, 0.20 and 0.15 mm w.e. of snow accumulated in the 12 hours preceding the parcel arrival at Byrd, DML05, Dome C, Dome F and Vostok, respectively, ensuring that ~50% of the total annual precipitation is represented in the snowfall trajectories.

The model precipitation at Byrd is in reasonable agreement with measured accumulation, but on the East Antarctic ice sheet, where the other sites are located, the model seriously underestimates precipitation, probably due to the inadequate spatial resolution of the model (Cullather *et al.*, 1997). Averaged over the 15-year period, the model precipitation shows a seasonal cycle. Peaks are found at Byrd and DML05 in autumn, at Dome C and Dome F in winter and at Vostok in summer. However, the temporal variability is considerable.

The mean trajectories show a cyclonic curvature reflecting the substantial influence of cyclones on air parcel pathways over Antarctica. Snowfall trajectories are about twice as long as non-snowfall trajectories and originate generally from far-

ther north and west. There is a seasonal shift in the mean snowfall trajectories. In summer, the air parcels originate on average more from the south and east, while in winter mostly from the north, and in autumn and spring mostly from the west. The annual variations in moisture source region are a function of variations in strength and pathways of cyclones, in sea ice extent, in altitude of the parcels and stability of the atmosphere. When defining the location of the air parcels 4 days before arrival as an indicator of the main source region, trends in this location will represent a trend in source region. The temporal variability in moisture source region is on the order of 3 degrees latitude. During the period under consideration (1979-93), a significant trend northward in moisture source region is found for DML05, and a significant trend southward for Dome C.

If the assumption is made that the spread in air parcel locations 4 days before arrival at level 4, is representative for the source region distribution, we conclude that moisture sources for precipitation are generally located between 50 and 60 °S in the ocean closest to the arrival point. This region contributes ~30% to the total annual precipitation. The latitude band 40 - 70 °S, which is the band just north of the sea ice edge, contributes ~75%. The sea surface temperatures in this latitude band ranges between 0 and 20 °C. This results in a main contribution of the Atlantic Ocean for precipitation at DML05 (55 - 65%), the Indian Ocean at Dome F (45 - 65%), Vostok (30 - 45%) and Dome C (60 - 75%), and the Pacific Ocean at Byrd (65 - 75%). The trajectories show seasonal dependency, resulting in a seasonal cycle in the moisture sources. The seasonal cycle is enhanced by that in the precipitation.

The snowfall trajectories arriving at Vostok pass over Dome C, 12 hours before arrival. This partly explains the correlation between precipitation at Dome C and Vostok. The source region for precipitation at Vostok is south of the source region of Dome C, although some overlap is present. Therefore, the ice core records are also likely to show similarities, assuming that the general circulation patterns and resulting snowfall trajectories remained reasonably constant over time. Note that the results presented here are based on the present day climate. No attempt has yet been made to extend the results to past climates.

Bibliography

- Allison, I., G. Wendler and U. Radok, 1993. A climatology of the East Antarctic ice sheet (100°e to 140°e) derived from automatic weather stations. *J. Geophys. Res.*, **98**(D5), 8815–8823.
- Anderson, P. S., 1994. A method for rescaling humidity sensors at temperatures well below freezing. *Journal of Atmospheric and Oceanic Technology*, **11**, 1388–1391.
- Andreas, E. L., 1987. A theory for the scalar roughness and the scalar transfer coefficients over snow and sea ice. *Boundary-Layer Meteorol.*, **38**(1-2), 159–184.
- Bintanja, R., 1999. On the glaciological, meteorological and climatological significance of Antarctic blue ice areas. *Rev. Geophys.*, **37**(3), 337–359.
- Bintanja, R., 2000. Surface heat budget of Antarctic snow and blue ice: Interpretation of spatial and temporal variability. *J. Geophys. Res.*, **105**(D19), 24,387–24,407.
- Bintanja, R., 2001. Mesoscale meteorological conditions in Dronning Maud Land, Antarctica, during summer: A qualitative analysis of forcing mechanisms. *J. Appl. Meteorol.*, **39**(12), 2348–2370.
- Bintanja, R. and C. H. Reijmer, 2001. Meteorological conditions over Antarctic blue ice areas and their influence on the local surface mass balance. *J. Glaciol.*, **47**(156), 37–50.
- Bintanja, R. and M. R. van den Broeke, 1995. The surface energy balance of Antarctic snow and blue ice. *J. Appl. Meteorol.*, **34**(4), 902–926.
- Bintanja, R., S. Jonsson and W. H. Knap, 1997. The annual cycle of the surface energy balance of Antarctic blue ice. *J. Geophys. Res.*, **102**(D2), 1867–1881.
- Bintanja, R., C. H. Reijmer, H. Snellen and M. P. A. Thomassen, 1998. Meteorological and glaciological investigations on a blue ice area in the Heimefrontfjella, Dronning Maud Land, Antarctica: The follow-up of the 92-93 experiment. 1997-98 field report, Inst. for Mar. and Atmos. Res., Utrecht Univ., Utrecht, Netherlands. 43 pp.
- Boresjö-Bronge, L. and C. Bronge, 1999. Ice and snow-type classification in the Vestfold Hills, East Antarctica, using Landsat-TM data and ground radiometer measurements. *Int. J. Remote Sens.*, **20**(2), 225–240.
- Brandt, R. E. and S. G. Warren, 1993. Solar-heating and temperature profiles in Antarctic snow and ice. *J. Glaciol.*, **39**(131), 99–110.
- Bromwich, D. H., 1988. Snowfall in high southern latitudes. *Rev. Geophys.*, **26**(1), 149–168.
- Bromwich, D. H. and C. J. Weaver, 1983. Latitudinal displacement from main mois-

- ture source controls $\delta^{18}\text{O}$ of snow in coastal Antarctica. *Nature*, **301**, 145–147.
- Bromwich, D. H., R. I. Cullather and M. L. van Woert, 1998. Antarctic precipitation and its contribution to the global sea-level budget. *Ann. Glaciol.*, **27**, 220–226.
- Carroll, J. J., 1982. Long-term means and short-term variability of the surface energy balance components at the South Pole. *J. Geophys. Res.*, **87**(C6), 4277–4286.
- Christoph, M., T. Barnett and E. Roeckner, 1997. The Antarctic circumpolar wave in a coupled ocean-atmosphere GCM. Report no. 235, Max-Planck-Institut für Meteorology. 28 pp.
- Ciais, P., J. W. C. White, J. Jouzel and J. R. Petit, 1995. The origin of present-day Antarctic precipitation from surface deuterium excess data. *J. Geophys. Res.*, **100**(D9), 18,917–18,927.
- Cullather, R., D. Bromwich and M. van Woert, 1996. Interannual variations in Antarctic precipitation related to El Niño-Southern Oscillation. *J. Geophys. Res.*, **101**(D14), 19,109–19,118.
- Cullather, R., D. Bromwich and R. Grumbine, 1997. Validation of operational numerical analyses in Antarctic latitudes. *J. Geophys. Res.*, **102**(D12), 13,761–13,784.
- Cullather, R., D. Bromwich and M. van Woert, 1998. Spatial and temporal variability of Antarctic precipitation from atmospheric methods. *J. Climate*, **11**, 334–367.
- Dansgaard, W., S. J. Johnsen, H. B. Clausen, D. Dahl-Jensen, N. S. Gundestrup, C. U. Hammer, C. S. Hvidberg, J. P. Steffensen, A. E. Sveinbjrnsdottir, J. Jouzel and G. Bond, 1993. Evidence for general instability of past climate from a 250-kyr ice-core record. *Nature*, **364**, 218–220.
- Delaygue, G., V. Masson, J. Jouzel, R. D. Koster and R. J. Healy, 2000. The origin of Antarctic precipitation: a modelling approach. *Tellus*, **52B**, 19–36.
- Delmotte, M., V. Masson and J. Jouzel, 2000. A seasonal deuterium excess signal at Law Dome, coastal eastern Antarctica: A southern ocean signature. *J. Geophys. Res.*, **105**(D6), 7187–7197.
- Dome-F Ice Core Research Group, 1998a. Deep ice-core drilling at Dome Fuji and glaciological studies in East Dronning Maud Land, Antarctica. *Ann. Glaciol.*, **27**, 333–337.
- Dome-F Ice Core Research Group, 1998b. Preliminary investigation of palaeoclimate signals recorded in the ice core from Dome Fuji station, East Dronning Maud Land, Antarctica. *Ann. Glaciol.*, **27**, 338–342.
- Duguay, C. R. and E. F. LeDrew, 1992. Estimating surface reflectance and albedo from Landsat-5 Thematic Mapper over rugged terrain. *Photogramm. Eng. Remote Sens.*, **58**(5), 551–558.
- Duynkerke, P. G., 1991. Radiation fog: a comparison of model simulation with detailed observations. *Monthly Weather Review*, **119**(2), 324–341.
- Dyer, A. J., 1974. A review of flux-profile relationships. *Boundary-Layer Meteorol.*, **7**, 363–372.
- Enomoto, H., H. Motoyama, T. Shiraiwa, T. Saito, T. Kameda, T. Furukawa, S. Takahashi, Y. Kodama and O. Watanabe, 1998. Winter warming over Dome Fuji, Eastern Antarctica and semiannual oscillation in the atmospheric circulation. *J. Geophys. Res.*, **103**(D18), 23,103–23,111.
- Fortuin, J. P. F. and J. Oerlemans, 1990. Parameterisations of the annual surface tem-

- perature and mass balance of Antarctica. *Ann. Glaciol.*, **14**, 78–84.
- Genthon, C. and A. Braun, 1995. ECMWF analysis and predictions of the surface climate of Greenland and Antarctica. *J. Climate*, **8**, 2324–2332.
- Gerland, S., H. Oerter, J. Kipfstuhl, F. Wilhelms, H. Miller and W. Miners, 1999. Density log of a 181 m long ice core from Berkner Island, Antarctica. *Ann. Glaciol.*, **29**, 215–219.
- Gibson, J. K., P. Källberg, S. Uppala, A. Hernandez, A. Nomura and E. Serrano, 1997. ERA-15 description. ECMWF Re-analysis project report series 1, European Centre for Medium-Range Weather Forecasts, Reading, England. 72 pp.
- Giovinetto, M. B. and C. R. Bentley, 1985. Surface balance in ice drainage systems of Antarctica. *Antarc. J. U.S.*, **20**(4), 6–13.
- Gratton, D. J., P. J. Howart and D. J. Marceau, 1993. Using Landsat-5 Thematic Mapper and digital elevation data to determine the net radiation field of a mountain glacier. *Remote Sens. Environ.*, **43**, 315–331.
- Greenland Ice-core Project (GRIP) Members, 1993. Climate instability during the last interglacial period recorded in the GRIP ice core. *Nature*, **364**, 203–207.
- Grenfell, T. C. and D. K. Perovich, 1981. Radiation absorption coefficients of polycrystalline ice from 400–1400 nm. *J. Geophys. Res.*, **86**(C8), 7447–7450.
- Grenfell, T. C., S. G. Warren and P. C. Mullen, 1994. Reflection of solar radiation by the Antarctic snow surface at ultraviolet, visible, and near-infrared wavelengths. *J. Geophys. Res.*, **99**(D9), 18,669–18,684.
- Greuell, W. and M. de Ruyter de Wildt, 1999. Anisotropic reflection by melting glacier ice: Measurements and parameterizations in Landsat TM bands 2 and 4. *Remote Sens. Environ.*, **70**, 265–277.
- Greuell, W. and T. Konzelman, 1994. Numerical modelling of the energy balance and the englacial temperature of the Greenland ice sheet. Calculations for the ETH-camp location (West Greenland, 1155 m a.s.l.). *Global and Planetary Change*, **9**, 91–114.
- Herron, M. M., 1982. Impurity sources of F^- , Cl^- , NO_3^- and SO_4^{2-} in Greenland and Antarctic precipitation. *J. Geophys. Res.*, **87**(C4), 3052–3060.
- Herron, M. M. and C. C. Langway, 1980. Firn densification: an empirical model. *J. Glaciol.*, **25**(93), 373–385.
- Herzfeld, U. C. and M. S. Matassa, 1999. An atlas of Antarctica north of 72.1°S from GEOSAT radar altimeter data. *Int. J. Remote Sens.*, **20**(2), 241–258.
- Högström, U., 1988. Non-dimensional wind and temperature profiles in the atmospheric surface layer: a re-evaluation. *Boundary-Layer Meteorol.*, **42**, 55–78.
- Holmlund, P., K. Gjerde, N. Gundestrup, M. Hansson, E. Isaksson, L. Karlöf, M. Nyman, R. Pettersson, F. Pinglot, C. H. Reijmer, M. Stenberg, M. Thomassen, R. van de Wal, C. van der Veen, F. Wilhelms and J.-G. Winther, 2000. Spatial gradients in snow layering and 10 m temperatures at two EPICA-Dronning Maud Land (Antarctica) pre-site-survey drill sites. *Ann. Glaciol.*, **30**, 13–19.
- IPCC, 1995. Climate change 1995: The science of climate change. In: Houghton, J. T., L. G. M. Filho, B. A. Callander, N. Harris, A. Kattenberg and K. Maskell, editors, *Contribution of Working Group I to the Second Assessment Report of the Intergovernmental Panel on Climate Change*. Cambridge University Press, Cambridge, UK.

- Isaksson, E. and W. Karlén, 1994. Spatial and temporal patterns in snow accumulation, western Dronning Maud Land, Antarctica. *J. Glaciol.*, **40**(135), 399–409.
- Isaksson, E., M. R. van den Broeke, J.-G. Winther, L. Karlöf, J. F. Pinglot and N. Gundestrup, 1999. Accumulation and proxy-temperature variability in Dronning Maud Land, Antarctica, determined from shallow firn cores. *Ann. Glaciol.*, **29**, 17–22.
- Jones, D. A. and I. Simmonds, 1993. A climatology of southern hemisphere extratropical cyclones. *Climate Dynamics*, **9**, 131–145.
- Jonsson, S., 1995. Synoptic forcing of wind and temperature in a large cirque 300 km from the coast of East Antarctica. *Antarctic Science*, **7**(4), 409–420.
- Jouzel, J., 1999. Calibrating the isotope paleothermometer. *Science*, **286**, 910–911.
- Jouzel, J., R. B. Alley, M. Cuffey, W. Dansgaard, P. Grootes, G. Hoffmann, S. J. Johnsen, R. D. Koster, D. Peel, C. A. Shuman, M. Stievenard, M. Stuiver and J. White, 1997. Validity of the temperature reconstruction from water isotopes in ice cores. *J. Geophys. Res.*, **102**(C12), 26,471–26,487.
- Kahl, J. D., J. M. Harris and G. A. Herbert, 1989. Intercomparison of three long-range trajectory models applied to Arctic haze. *Tellus*, **41B**, 524–536.
- Karlöf, L., J.-G. Winther, E. Isaksson, J. Kohler, J. F. Pinglot, F. Wilhelms, M. Hansson, P. Holmlund, M. Nyman, R. Pettersson, M. Stenberg, M. P. A. Thomassen, C. van der Veen and R. S. W. van de Wal, 2000. A 1500 year record of accumulation at Amundsenisen western Dronning Maud Land, Antarctica, derived from electrical and radioactive measurements on a 120 m ice core. *J. Geophys. Res.*, **105**(D10), 12,471–12,483.
- King, J. C., 1989. Low-level wind profiles at an Antarctic coastal station. *Antarctic Science*, **1**(2), 169–178.
- King, J. C., 1996. Longwave atmospheric radiation over Antarctica. *Antarctic Science*, **8**(1), 105–109.
- King, J. C. and W. M. Connolley, 1997. Validation of the surface energy balance over the Antarctic ice sheets in the U.K. Meteorological Office Unified Climate Model. *J. Climate*, **10**, 1273–1287.
- King, J. C. and J. Turner, 1997. *Antarctic Meteorology and Climatology*. Cambridge Univ. Press, New York. 409 pp.
- King, J. C., P. S. Anderson, M. C. Smith and S. D. Mobbs, 1996. The surface energy and mass balance at Halley, Antarctica during winter. *J. Geophys. Res.*, **101**(D14), 19,119–19,128.
- Knap, W. H. and J. Oerlemans, 1996. The surface albedo of the Greenland ice sheet: Satellite-derived and in situ measurements in the Søndre Strømfjord area during the 1991 melt season. *J. Glaciol.*, **42**(141), 364–374.
- Knap, W. H. and C. H. Reijmer, 1998. Anisotropy of the reflected radiation field over melting glacier ice: Measurements in Landsat TM bands 2 and 4. *Remote Sens. Environ.*, **65**, 93–104.
- Knap, W. H., C. H. Reijmer and J. Oerlemans, 1999. Narrowband to broadband conversion of Landsat-TM glacier albedos. *Int. J. Remote Sens.*, **20**(10), 2091–2110.
- König-Langlo, G. C. and E. Augstein, 1994. Parameterization of the downward long-wave radiation at the Earth's surface in polar regions. *Meteorologisch Zeitschrift*, **3**,

- 343–347.
- König-Langlo, G. C. and A. Herber, 1996. The meteorological data of the Neumayer station (Antarctica) for 1992, 1993 and 1994. Technical report, Alfred Wegener Institute for Polar and Marine Research, Bremerhaven. 101 pp.
- König-Langlo, G. C., J. C. King and P. Pettre, 1998. Climatology of the three coastal Antarctic stations Dumont d'Urville, Neumayer, and Halley. *J. Geophys. Res.*, **103**(D9), 10,935–10,946.
- Koster, R. D., J. Jouzel, R. J. Suozzo and G. L. Russell, 1992. Origin of July Antarctic precipitation and its influence on deuterium content: A GCM analysis. *Climate Dynamics*, **7**, 195–203.
- Kottmeier, C. and B. Fay, 1998. Trajectories in the Antarctic lower troposphere. *J. Geophys. Res.*, **103**(D9), 10,947–10,959.
- Kou, L., D. Labrie and P. Chylek, 1993. Refractive indices of water and ice in the 0.65- to 2.5 μm spectral range. *Appl. Opt.*, **32**(19), 3531–3540.
- Krinner, G., C. Genthon and J. Jouzel, 1997a. GCM analysis of local influences on ice core delta signals. *Geophys. Res. Lett.*, **24**(22), 2825–2828.
- Krinner, G., C. Genthon, Z.-X. Li and P. Van, 1997b. Studies of the Antarctic climate with a stretched-grid general circulation model. *J. Geophys. Res.*, **102**(D12), 13,731–13,745.
- Krotkov, N. A. and A. P. Vasilkov, 2000. Reduction of skylight reflection effects in the above-water measurement of diffuse marine reflectance: Comment. *Appl. Opt.*, **39**(9), 1379–1381.
- Legrand, M. and R. J. Delmas, 1987. A 220-year continuous record of volcanic H_2SO_4 in the Antarctic ice sheet. *Nature*, **327**, 671–676.
- Liljequist, G. H., 1956. Energy exchange of an Antarctic snowfield, short-wave radiation (Maudheim 70°03' S, 10°56' W). V. Penetration of solar radiation into the snow. In: *Norwegian-British-Swedish Antarctic Expedition, 1949-1952, Scientific Results*, volume 2, part. 1A, pages 93–103. Norsk Polarinst., Oslo.
- Lindsay, R. W. and D. A. Rothrock, 1994. Arctic sea ice albedo from AVHRR. *J. Climate*, **7**, 1737–1749.
- Meister, G., S. Sandmeier and W. Ni, 1998. Analyzing hyperspectral BRDF data of a grass lawn and watercress surface using an empirical model. In: *Proc. of IGARSS'98*, pages 1246–1248. Seattle, Wash.
- Morel, A., K. J. Voss and B. Gentili, 1995. Bidirectional reflectance of oceanic waters: A comparison of modeled and measured upward radiance fields. *J. Geophys. Res.*, **100**(C7), 12,143–12,150.
- Mulvaney, R., R. Röthlisberger, E. W. Wolff, S. Sommer, J. Schwander, M. A. Hutterli and J. Jouzel, 2000. The transition from the glacial period in inland and near-coastal Antarctica. *Geophys. Res. Lett.*, **27**(17), 2673–2676.
- Noone, D. and I. Simmonds, 1998. Implications for the interpretation of ice-core isotope data from analysis of modelled Antarctic precipitation. *Ann. Glaciol.*, **27**, 398–402.
- Noone, D., J. Turner and R. Mulvaney, 1999. Atmospheric signals and characteristics of accumulation in Dronning Maud Land, Antarctica. *J. Geophys. Res.*, **104**(D16), 19,191–19,212.

- Oerlemans, J. and R. Bintanja, 1995. Snow and ice cover and climate sensitivity. In: *The Role of Water and the Hydrological Cycle in Global Change*, volume I 31 of NATO ASI Series, pages 189–198.
- Oerter, H., 1995. The German Filchner V campaign in 1995: an overview and preliminary results from Berkner Island. In: Oerter, H., editor, *Filchner-Ronne Ice Shelf Programme. Report 9*, pages 91–96. Alfred Wegener Institute for Polar and Marine Research, Bremerhaven.
- Oerter, H., F. Wilhelms, F. Jung-Rothenhäusler, F. Göktas, H. Miller, W. Graf and S. Sommer, 2000. Accumulation rates in Dronning Maud Land, Antarctica, as revealed by dielectric-profiling measurements at shallow firn cores. *Ann. Glaciol.*, **30**, 27–34.
- Ohata, T., 1985. Heat balance at the snow surface in a katabatic wind zone, east Antarctica. *Ann. Glaciol.*, **6**, 174–177.
- Orheim, O. and B. K. Lucchitta, 1988. Numerical analysis of Landsat Thematic Mapper images of Antarctica: Surface temperatures and physical properties. *Ann. Glaciol.*, **11**, 109–120.
- Parish, T. R., 1982. Surface airflow over East Antarctica. *Monthly Weather Review*, **100**, 84–90.
- Parish, T. R. and D. H. Bromwich, 1987. The surface windfield over the Antarctic ice sheets. *Nature*, **328**, 51–54.
- Parish, T. R. and D. H. Bromwich, 1991. Continental-scale simulation of the Antarctic katabatic wind regime. *J. Climate*, **4**, 135–146.
- Parish, T. R. and D. H. Bromwich, 1998. A case study of Antarctic katabatic wind interaction with large-scale forcing. *Monthly Weather Review*, **126**, 199–209.
- Patterson, W., 1994. *The Physics of Glaciers*. Pergamon. 480 pp.
- Peixoto, J. P. and A. H. Oort, 1992. *Physics of Climate*. American Institute of Physics, New York. 520 pp.
- Perovich, D. K. and J. W. Govoni, 1991. Absorption coefficients of ice from 250 to 400 nm. *Geophys. Res. Lett.*, **18**(7), 1233–1235.
- Petit, J. R., J. Jouzel, M. Pourchet and L. Merlivat, 1982. A detailed study of snow accumulation and stable isotope content in Dome C (Antarctica). *J. Geophys. Res.*, **87**(C6), 4301–4308.
- Petit, J. R., J. W. C. White, N. W. Young, J. Jouzel and Y. S. Korotkevich, 1991. Deuterium excess in recent Antarctic snow. *J. Geophys. Res.*, **96**(D3), 5113–5122.
- Petit, J. R., J. J. D. Raynaud, N. I. Barkov, J. M. Barnola, I. Basile, M. Benders, J. Chappellaz, M. Davis, G. Delaygue, M. Delmotte, V. M. Kotlyakov, M. Legrand, V. Y. Lipenkov, C. Lorius, L. Pepin, C. Ritz, E. Saltzman and M. Stievenard, 1999. Climate and atmospheric history of the past 420,000 years from the Vostok ice core, Antarctica. *Nature*, **399**, 429–436.
- Reijmer, C. H. and M. R. van den Broeke, 2001. Moisture sources of precipitation in Western Dronning Maud Land, Antarctica. *Antarc. Sci.*, **13**(2), 210–220.
- Reijmer, C. H., W. Greuell and J. Oerlemans, 1999a. The annual cycle of meteorological variables and the surface energy balance on Berkner Island, Antarctica. *Ann. Glaciol.*, **29**, 49–54.
- Reijmer, C. H., W. H. Knap and J. Oerlemans, 1999b. The surface albedo of the Vat-

- najökull ice cap, Iceland: A comparison between satellite-derived and ground-based measurements. *Boundary-Layer Meteorol.*, **92**(1), 125–144.
- Röthlisberger, R., E. W. Wolff, R. Mulvaney, M. A. Hutterli and S. Sommer, 2000. Factors controlling nitrate in ice cores: Evidence from the Dome C deep ice core. *J. Geophys. Res.*, **105**(D16), 20565–20573.
- Scheele, M. P., P. C. Siegmund and P. F. J. van Velthoven, 1996. Sensitivity of trajectories to data resolution and its dependence on the starting point: In or outside a tropopause fold. *Meteorol. Appl.*, **3**, 267–273.
- Schlatter, T. W., 1972. The local surface energy balance and subsurface temperature regime in Antarctica. *J. Appl. Meteorol.*, **11**, 1048–1062.
- Schlosser, E., 1999. Effects of seasonal variability of accumulation on yearly mean $\delta^{18}\text{O}$ values in Antarctic snow. *J. Glaciol.*, **45**(151), 463–468.
- Schmidt, T. and G. C. König-Langlo, 1994. Radiation measurements at the German station Neumayer 1982 - 1992. Technical report, Alfred Wegener Institute for Polar and Marine Research, Bremerhaven. 66 pp.
- Stearns, C. R. and G. A. Weidner, 1993. Sensible and latent heat flux estimates in Antarctica. In: Bromwich, D. H. and C. R. Stearns, editors, *Antarctic Meteorology and Climatology: Studies on Automatic Weather Stations.*, volume 61 of *Antarctic Research Series*, pages 109–138, Washington, DC. American Geophysical Union.
- Stearns, C. R., R. E. Holmes and G. A. Weidner, 1997. Antarctic automatic weather stations: 1996-1997. *Antarct. J. U.S.*, **32**(5), 174–178.
- Steinhage, D., U. Nixdorf, U. Meyer and H. Miller, 1999. New maps of the ice thickness subglacial topography in Dronning Maud Land, Antarctica, determined by means of airborne radio echo sounding. *Ann. Glaciol.*, **29**, 267–272.
- Stenberg, M., M. Hansson, P. Holmlund and L. Karlöf, 1999. Variability in snow layering and snow chemistry in the vicinity of two drill sites in western Dronning Maud Land, Antarctica. *Ann. Glaciol.*, **29**, 33–37.
- Stocker, T. F., 1999. Past and future reorganizations in the climate system. *Quaternary Science Reviews*, **19**(1-5), 301–319.
- Stohl, A., G. Wotawa, P. Siebert and H. Kromp-Kolb, 1995. Interpolation errors in wind fields as a function of spatial and temporal resolution and their impact on different types of kinematic trajectories. *J. Appl. Meteorol.*, **34**, 2149–2165.
- Sturm, M., J. Holmgren, M. König and K. Morris, 1997. The thermal conductivity of seasonal snow. *J. Glaciol.*, **43**(143), 26–41.
- Suttles, J. T., R. N. Green, P. Minnis, G. L. Smith, W. F. Stayler, B. A. Wielicki, I. J. Walker, D. F. Young, V. R. Taylor and L. L. Stone, 1988. Angular radiation models for Earth-atmosphere system. vol. 1: Shortwave radiation. In: *NASA Ref. Publ.*, 1184. NASA, Wash., DC.
- Tabacco, I. E., A. Passerini, F. Corbelli and M. Gorman, 1998. Determination of the surface and bed topography at Dome C, East Antarctica. *J. Glaciol.*, **44**(146), 185–191.
- Takahashi, S., T. Kameda, H. Enomoto, T. Shiraiwa, Y. Kodama, S. Fujita, H. Motoyama, O. Watanabe, G. Weidner and C. Stearns, 1998. Automatic weather station program during Dome Fuji Project by JARE in East Dronning Maud Land, Antarctica. *Ann. Glaciol.*, **27**, 528–534.

- Taylor, K., G. Lamorey, G. Doyle, R. Alley, P. Grootes, P. Mayewski, J. White and L. Barlow, 1993. The flickering switch of late pleistocene climate change. *Nature*, **361**, 432–435.
- Turner, J., W. M. Connelley, S. Leonard, G. J. Marshall and D. G. Vaughan, 1999. Spatial and temporal variability of net snow accumulation over the Antarctic from ECMWF re-analysis project data. *Int. J. Climatol.*, **19**, 697–724.
- Van den Broeke, M. R., 1997. Spatial and temporal variation of sublimation on Antarctica: Results of a high-resolution general circulation model. *J. Geophys. Res.*, **102**(D25), 29,765–29,777.
- Van den Broeke, M. R., 1998. The semi-annual oscillation and Antarctic climate. Part 2: Recent changes. *Antarc. Sci.*, **10**(2), 184–191.
- Van den Broeke, M. R., 2000a. On the interpretation of Antarctic temperature trends. *J. Climate*, **31**, 3885–3889.
- Van den Broeke, M. R., 2000b. The semi-annual oscillation and Antarctic climate. Part 5: impact on the annual temperature cycle as derived from NCEP/NCAR re-analysis. *Climate Dynamics*, **16**, 369–377.
- Van den Broeke, M. R. and R. Bintanja, 1995. The interaction of katabatic winds and the formation of blue-ice areas in East Antarctica. *J. Glaciol.*, **41**(138), 395–407.
- Van den Broeke, M. R., J.-G. Winther, E. Isaksson, J. F. Pinglot, L. Karlöf, T. Eiken and L. Conrads, 1999. Climate variables along a traverse line in Dronning Maud Land, East Antarctica. *J. Glaciol.*, **45**(150), 295–302.
- Van Lipzig, N., E. van Meijgaard and J. Oerlemans, 1999. Evaluation of a regional atmospheric model using measurements of surface heat exchange processes from a site in Antarctica. *Monthly Weather Review*, **127**, 11,994–12,011.
- Van Loon, H., 1972. Pressure in the southern hemisphere. *American Meteorological Society, Meteorological Monographs*, **13**(35), 59–86.
- Vaughan, D. G., J. L. Bamber, M. Giovinetto, J. Russel and A. P. R. Cooper, 1999. Reassessment of net surface mass balance in Antarctica. *J. Climate*, **12**(4), 933–946.
- Wagenbach, D., W. Graf, A. Minikin, U. Trefzer, J. Kipfstuhl, H. Oerter and N. Blindow, 1994. Reconnaissance of chemical and isotopic firn properties on top of Berkner Island. *J. Glaciol.*, **20**, 307–312.
- Warren, S. G., 1982. Optical properties of snow. *Rev. Geophys.*, **20**(1), 67–89.
- Warren, S. G. and W. J. Wiscombe, 1980. A model for the spectral albedo of snow. II: Snow containing atmospheric aerosols. *J. Atmos. Sci.*, **37**, 2734–2745.
- Warren, S. G., R. E. Brandt and R. D. Boime, 1993. Blue ice and green ice. *Antarc. J. U.S.*, **28**(5), 255–256.
- Warren, S. G., R. E. Brandt and P. O. Hinton, 1998. Effect of surface roughness on bidirectional reflectance of Antarctic snow. *J. Geophys. Res.*, **103**(E11), 25,789–25,807.
- Weller, G., 1980. Spatial and temporal variations in the south polar surface energy balance. *Monthly Weather Review*, **108**, 2006–2014.
- Wendler, G. and Y. Kodama, 1984. On the climate of Dome C, Antarctica, in relation to its geographical setting. *J. Climatol.*, **4**, 495–508.
- Wendler, G., N. Ishikawa and Y. Kodama, 1988. The heat balance of the icy slope of Adelie Land, Eastern Antarctica. *J. Appl. Meteorol.*, **27**, 52–65.
- Wendler, G., J. Andre, P. Pettre, J. Gosink and T. Parish, 1993. Katabatic winds in

- Adélie coast. In: Bromwich, D. H. and C. R. Stearns, editors, *Antarctic Meteorology and Climatology: Studies on Automatic Weather Stations.*, volume 61 of *Antarctic Research Series*, pages 23–46, Washington, DC. American Geophysical Union.
- Wendler, G., C. Stearns, G. Weidner, G. Dargaud and T. Parish, 1997. On the extraordinary katabatic winds of Adélie Land. *J. Geophys. Res.*, **102**(D4), 4463–4474.
- Werner, M., U. Mikolajewicz, M. Heimann and G. Hoffmann, 2000. Borehole versus isotope temperatures on Greenland: Seasonality does matter. *Geophys. Res. Lett.*, **27**(5), 723–726.
- Winther, J.-G., 1994. Spectral bi-directional reflectance of snow and glacier ice measured in Dronning Maud Land, Antarctica. *Ann. Glaciol.*, **20**, 1–5.
- Winther, J.-G., M. R. van den Broeke, L. Conrads, T. Eiken, R. Hurlen, G. Johnsrud, L. Karlöf, S. Onarheim, C. Richardson and R. Schorno, 1997. EPICA Dronning Maud Land pre site survey 1996/97. 1996-97 field report, Norwegian Polar Inst., Tromsø, Norway. 22 pp.
- Wiscombe, W. J. and S. G. Warren, 1980. A model for the spectral albedo of snow. I: Pure snow. *J. Atmos. Sci.*, **37**, 2712–2733.
- Wolff, E., I. Basile, J. Petit and J. Schwander, 1999. Comparison of Holocene electrical records from Dome C and Vostok, Antarctica. *Ann. Glaciol.*, **29**, 89–93.
- Zeng, Q., M. Cao, X. Feng, F. Liang, X. Chen and W. Sheng, 1984. A study of spectral reflection characteristics for snow, ice and water in the north of China. In: Goodison, B., editor, *Hydrological Applications of Remote Sensing and Remote Data Transmission*, pages 451–462. International Association of Hydrological Sciences. Publication No. 145.

Samenvatting

Het klimaat op aarde kent in de geschiedenis van zijn bestaan een aantal aanzienlijke fluctuaties. De klimaatvariaties worden over het algemeen veroorzaakt door natuurlijke variaties in factoren, zoals de sterkte van zonne-instraling, oceaanstromingen en atmosferische samenstelling door bijvoorbeeld vulkaanuitbarstingen. In de afgelopen ~ 100 jaar wordt het klimaat bovendien beïnvloed door antropogene bronnen, zoals CO_2 - en methaanemissies uit het verbranden van fossiele brandstoffen. De gevoeligheid van het klimaat voor veranderingen in, b.v., zonne-instraling of atmosferische samenstelling, verschilt per regio op aarde. Klimaatstudies hebben aangetoond dat de polaire gebieden veel gevoeliger zijn voor klimaatveranderingen dan andere gebieden, door de albedo-terugkoppeling. De albedo-terugkoppeling is de extra verandering van het klimaat (b.v. een temperatuur verandering) die optreedt door veranderingen in de hoeveelheid zonlicht die door de aarde wordt gereflecteerd door, b.v., het groeien of verdwijnen van gletschers en ijskappen bij een initiële klimaatverandering. In dit licht gezien zijn de Groenlandse en Antarctische ijskappen interessante gebieden om te bestuderen, ook om hun mogelijke bijdrage aan zeespiegelstijging. Het smelten van de Groenlandse ijskap zal de zeespiegel met ~ 7 m laten stijgen terwijl het compleet afsmelten van de Antarctische ijskap de zeespiegel met ~ 60 m zou laten stijgen. Ter vergelijking, het water dat bewaard wordt in gletsjers en kleine ijskappen vertegenwoordigt een potentiële bijdrage aan de zeespiegelstijging van ~ 0.5 m. Een zeespiegelstijging van ~ 60 m zou tot gevolg hebben dat van Nederland alleen de top van de Veluwe en Zuid Limburg nog boven het water uitsteken.

Niet alleen de (veranderende) oppervlakte-omstandigheden op de Groenlandse en Antarctische ijskap bevatten waardevolle klimaatinformatie, het ijs zelf is ook een belangrijke bron van historische klimaatinformatie. Data betrekking hebbend op de historische toestand van de atmosfeer, zoals temperatuur, chemische samenstelling en atmosferische circulatie, zijn opgeslagen in het ijs. Doordat het ijs behoorlijk dik is (3 tot 4 km) en de accumulatie snelheden laag zijn, zijn de tijdreeksen die uit het ijs gehaald kunnen worden 150 tot 500 kjaar lang en omvatten enkele glaciaal-interglaciaal cycli. Om toegang tot deze informatie te krijgen zijn in de afgelopen jaren verschillende ijskernen in de Groenlandse en Antarctische ijskap geboord, bijvoorbeeld de Vostok, Byrd, Dome F en Taylor Dome ijskernen op Antarctica en de GRIP, North GRIP en GISPII ijskernen op Groenland. Deze ijskernen hebben ons

inzicht gegeven in het klimaat over de laatste 150 tot 400 kjaar op deze locaties door de isotopensamenstelling van het ijs zelf, de aanwezigheid van andere elementen in het ijs, en de samenstelling van de luchtbelletjes ingevangen in het ijs. Figuur 1.1 toont een voorbeeld van een tijdreeks verkregen uit de Vostok-ijskern op Antarctica.

De interpretatie van de verkregen tijdreeksen is echter niet eenvoudig. Een klimaatreeks is van weinig waarde zolang de leeftijd van het ijs als functie van de diepte onbekend is. Het tellen van jaarlagen is de meest nauwkeurige methode om de leeftijd van het ijs te bepalen. Wanneer de lagen echter te dun worden en de jaartallen bij vulkanische aslagen onbekend zijn of vulkanische aslagen ontbreken, dan zal er afgegaan moeten worden op andere gedateerde klimaatreeksen en ijsstroommodellen. Dit introduceert extra onzekerheden en kan resulteren in compleet verschillende interpretaties van tijdreeksen uit ijskernen. De volgende stap is het relateren van de verkregen tijdreeksen van isotopen (b.v. waterstof en zuurstof) en gasinhoud (zoals CO₂ en methaan) aan de toestand van de atmosfeer op een bepaald tijdstip. Het klimaat dat opgeslagen wordt in ijskernen wordt grotendeels bepaald door de omstandigheden waaronder sneeuwval optreedt. Dit hoeft niet representatief te zijn voor de gemiddelde omstandigheden op die locatie. Verschillende factoren kunnen daardoor de interpretatie van ijskernen beïnvloeden, zoals het veranderen van de seizoensafhankelijkheid van de neerslag en veranderingen in brongebieden van het vocht.

De stabiele isotoopverhoudingen van waterstof (δD) en zuurstof ($\delta^{18}O$) in het ijs worden vaak gebruikt als een proxy voor temperatuur en zijn voorbeelden van hoe tijdreeksen uit ijskernen worden gerelateerd aan klimaatreeksen. In Antarctische ijskernen wordt de temperatuur vaak gerelateerd aan deuteriumexcess d , wat een lineaire combinatie is van δD en $\delta^{18}O$. Om een temperatuurtijdreeks te verkrijgen uit d of $\delta^{18}O$ wordt verondersteld dat de relatie tussen d of $\delta^{18}O$ en de jaargemiddelde temperatuur lineair is en constant in tijd en ruimte. De temperatuurreeksen die zo verkregen worden tonen veel overeenkomsten tussen Groenland en Antarctica over de laatste 150 kjaar, al komen niet alle temperatuurvariaties die op Groenland worden gevonden overeen met variaties op Antarctica (figuur 1.2).

De aanname dat er een lineaire relatie bestaat tussen de temperatuur en d of $\delta^{18}O$ is redelijk goed. Maar de relaties zijn gebaseerd op de huidige atmosferische condities en de aanname dat deze constant blijven in de tijd is twijfelachtig. Boorgattemperaturen en verschillende isotopen in het Groenlandse ijs suggereren dat het temperatuurverschil tussen het laatste glaciële maximum (LGM) ongeveer twee keer zo groot is als geschat met behulp van $\delta^{18}O$, wat aangeeft dat de coëfficiënten van de lineaire relaties niet constant zijn in de tijd. $\delta^{18}O$ en d in Groenlandse en Antarctische sneeuw vertegenwoordigen een verscheidenheid aan complexe processen. Ze hangen af van de temperatuur van het oceaانwater waaruit het vocht verdampt, de daaropvolgende cycli van condensatie en verdamping, en de temperatuur waarop het vocht pakketje uiteindelijk condenseert om neerslag te vormen. De relatie tussen temperatuur en $\delta^{18}O$ of d zal daarom afhangen van het brongebied van het vocht, lokale omstandigheden en seizoensvariaties in sneeuwval. Dit belemmert de interpretatie van $\delta^{18}O$ en d .

Ondanks de problemen die de interpretatie van ijskernen met zich meebrengt

hebben de $\delta^{18}\text{O}$ en d reeksen en reeksen van andere isotopen en gasinhoud van het ijs waardevolle informatie opgeleverd over het klimaat van de afgelopen 150 tot 400 kjaar. Ze hebben echter niet alle vragen die men had kunnen beantwoorden en nieuwe vragen opgeworpen. Hoe zijn klimaatveranderingen gekoppeld tussen het Noordelijk en Zuidelijk Halfrond? Blijven de snelle klimaatvariaties, die gevonden zijn op Groenland, beperkt tot het Noordelijk Halfrond of zijn het mondiale fenomenen? Om deze en andere vragen te kunnen beantwoorden zullen de Antarctische en Groenlandse ijskernen vergeleken moeten worden met andere tijdreeksen zoals verkregen uit boomringen, meersedimenten en diepzeeboringen. Automatische weerstations hebben een toegevoegde waarde doordat ze inzicht verschaffen in de lokale omstandigheden waaronder sneeuwval optreedt en de interactie tussen de atmosfeer en het sneeuwoppervlak. Verder kan het gebruik van *General Circulation Models*, klimaatmodellen en numerieke weersverwachtingsmodellen, informatie geven over de toestand van de atmosfeer in het heden en verleden en over de brongebieden van de neerslag.

Dit proefschrift behandelt a) het gebruik van weerstations bij het bepalen van het klimaat nabij het oppervlak en de oppervlaktebudgetten van Antarctica, en b) het bepalen van de brongebieden van Antarctisch vocht met behulp van een trajectoriënmodel en een atmosferisch model. De belangrijkste motivatie tot deze studie is de boring van twee ijskernen op Antarctica in het kader van het *European Project for Ice Coring in Antarctica* (EPICA).

EPICA is een wetenschappelijk project waarin tien Europese landen¹ samenwerken om twee diepe ijskernen op Antarctica te boren en te analyseren. Het belangrijkste doel van het project is om een klimaatreeks met hoge tijdsresolutie te construeren voor Antarctica en deze te vergelijken met reeksen verkregen op andere locaties op Antarctica en Groenland. De EPICA-kernen worden geboord op Dome C en DML05 (figuur 1.3). De locatie van Dome C is gekozen vanwege zijn ligging op een lokale ijskap top, waardoor verstoringen in de gelaagdheid van het ijs door ijsstroming minimaal zullen zijn. Daarnaast is het ijs op die locatie ruim 3000 m dik en is de accumulatiesnelheid laag (~ 36 mm waterequivalent per jaar (w.e. yr^{-1})) waardoor het mogelijk wordt een tijdreeks met een lengte van ~ 500 kjaar te verkrijgen die enkele glacialen en interglacialen omvat. Het boren op Dome C is gestart in de zomer op het Zuidelijk Halfrond van 1997-98.

De Atlantische Oceaan wordt beschouwd als een belangrijke schakel tussen de klimaatreeksen van Antarctica en Groenland. Daarom wordt de tweede EPICA-ijskern geboord in Dronning Maud Land (DML), een gebied van Antarctica dat grenst aan de Atlantische Oceaan. De relatief hoge accumulatie op de gekozen locatie (~ 62 mm w.e. yr^{-1}) maakt het mogelijk om een gedetailleerde tijdreeks te verkrijgen over het laatste glaciaal en interglaciaal. Het boren op DML05 is gestart in de zomer op het Zuidelijk Halfrond van 2000-01. Daaraan voorafgaand zijn uitgebreide expedities naar DML geweest om de optimale locatie voor de boring te bepalen. De verkenningen zijn in 1995-96 gestart en omvatten onder andere het in kaart brengen van het ijsoppervlak en het gesteente onder het ijs, het boren van

¹België, Denemarken, Duitsland, Frankrijk, Groot Brittannië, Italië, Nederland, Noorwegen, Zweden en Zwitserland

ondiepe ijskernen om de accumulatie in DML te bepalen en het bestuderen van de meteorologie van DML met behulp van automatische weerstations en atmosferische modellen. Het doel van het gebruik van weerstations en atmosferische modellen binnen EPICA is om een beter begrip van de massabalans van DML te krijgen en om de interactie tussen de atmosfeer en het sneeuwoppervlak te bestuderen. Dit alles om de interpretatie van ijskernen te verbeteren.

In de laatste 20 à 30 jaar zijn ongeveer 100 weerstations op Antarctica geplaatst ter bestudering van de meteorologische processen dicht bij het oppervlak. Gezien de uitgestrektheid van het Antarctische continent is het aantal meetlocaties nog steeds beperkt. Verder zijn de stations niet gelijkmatig over het continent verdeeld en staat geen van deze stations in DML. De weerstations zijn ontworpen om lange periodes te kunnen werken zonder onderhoud en bieden de mogelijkheid om meteorologische metingen te verrichten op afgelegen locaties in extreme weersomstandigheden. Het Instituut voor Marien en Atmosferisch onderzoek Utrecht (IMAU) heeft 10 weerstations op Antarctica geplaatst waarvan 9 in DML, in het kader van EPICA. DML was een van de minst onderzochte gebieden van Antarctica. Het gebied is rond 1920 door Noorse walvisvaarders waarschijnlijk als eerste bezocht. De eerste significante wetenschappelijke expeditie die het gebied bezochten waren de Duitse Schwabenland expeditie in 1938-39 en de Noors-Brits-Zweedse expeditie in 1949-52. Permanente bewoning en onafgebroken meteorologische observaties begonnen in begin 1950 vooruitlopend op het Internationaal Geofysisch jaar 1957-58 op Halley, een Britse bases op de Brunt Ice Shelf. In de daaropvolgende jaren zijn verschillende stations in het gebied gesticht. Sanae, een Zuid Afrikaanse basis gesticht in 1961 en Neumayer, een Duitse basis gesticht in 1981, zijn de enige permanente bases in de buurt. Deze stations staan echter allen aan de kust. Het permanent meten van meteorologische variabelen in het binnenland is pas begonnen met de IMAU automatische weerstations. Figuur 1.4 toont de locaties van de weerstations in DML en figuur 1.5 laat zien hoe de stations eruit zien.

Dit proefschrift beschrijft de interactie tussen het sneeuwoppervlak en de atmosfeer, ter ondersteuning van de interpretatie van ijskernen. Deze interactie wordt voornamelijk bestudeerd met behulp van data komende van automatische weerstations met aanvullende data van het *European Centre for Medium Range Weather Forecast* (ECMWF) numerieke weersverwachtingsmodel en het Koninklijk Nederlands Meteorologisch Instituut trajectoriënmodel. Doelen nagestreefd in dit proefschrift zijn:

- Het bestuderen van de klimatologische condities in DML om meer begrip te krijgen voor de processen die de oppervlaktemassabalans en het energiebudget beïnvloeden en ter ondersteuning van de keuze van de EPICA-boorlocatie in DML.
- Het bestuderen van de variabiliteit in tijd en ruimte van de oppervlakte-energiebalans om inzicht te krijgen in de interactie tussen het sneeuwoppervlak en de atmosfeer.
- Het bestuderen van de condities waaronder sneeuwval optreedt en het vaststellen

van de brongebieden van het vocht dat als sneeuw valt op een aantal Antarctische boorlocaties.

In Hoofdstuk 2 worden metingen van breed-band, smalle-band en bi-directionele reflectie gebruikt ter bestudering van de albedo van blauw ijs en sneeuw. Gedurende de zomer speelt de oppervlaktealbedo een belangrijke rol in de warmte uitwisseling tussen het oppervlak en de atmosfeer. Het doel was om methodes, die gebruikt worden om de oppervlakte albedo uit satelliet metingen te bepalen, te verbeteren en meer begrip te krijgen voor de processen die de waarde van de albedo beïnvloeden.

In de hoofdstukken 3, 4 en 5 wordt de data van de tien weerstations op Antarctica beschreven en gebruikt om de oppervlakte-energiebalans te bepalen. Eén weerstation staat op Berkner Island, een eiland in de Filchner-Ronne ice shelf, de rest is geplaatst in DML op twee lijnen loodrecht op de kust. Zoals verwacht zijn de sterkte van de katabatische stroming in combinatie met de geostrofe stroming de bepalende factoren voor de omstandigheden nabij het oppervlak op deze locaties. De katabatische stroming varieert in kracht afhankelijk van de helling van het oppervlak en de sterkte van de temperatuurinversie, en is niet aanwezig op het Berkner Island station dat op een ijskap top staat. In DML varieert de katabatische stroming in sterkte wat resulteert in een maximum windsnelheid en potentiële temperatuur op de stations met de grootste helling van het oppervlak, aan de rand van het Antarctische plateau. De jaargemiddelde windsnelheid varieert tussen de 4 m s^{-1} aan de kust en op het plateau, tot 7 m s^{-1} op de helling naar het plateau. De jaargemiddelde potentiële temperatuur varieert tussen $-18 \text{ }^\circ\text{C}$ and $-1 \text{ }^\circ\text{C}$. De jaargemiddelde temperatuur varieert tussen de $-16 \text{ }^\circ\text{C}$ in het kustgebied waar ook temperaturen boven $0 \text{ }^\circ\text{C}$ kunnen voorkomen, en $-46 \text{ }^\circ\text{C}$ op het Antarctische plateau. Doordat de temperaturen zo laag zijn, is de specifieke vochtigheid erg laag. De meeste accumulatie treedt op nabij de kust en de hoeveelheid neemt af met toenemende hoogte boven zeeniveau en toenemende afstand tot de kust, van $\sim 400 \text{ mm w.e. yr}^{-1}$ tot $\sim 30 \text{ mm w.e. yr}^{-1}$.

De weerstationdata zijn verder gebruikt, samen met een model gebaseerd op Monin-Obukhov gelijkvormigheidstheorie, om het oppervlakte-energiebudget over de meetperiode te berekenen. De sterkte van de katabatische stroming bepaalt niet alleen de meteorologische condities nabij het oppervlak maar ook het oppervlakte-energiebudget. De jaargemiddelde toename van energie van het oppervlak door de naar beneden gerichte voelbare warmteflux varieert tussen de 3 W m^{-2} en 25 W m^{-2} , met de hoogste waarden op de locaties waar ook de windsnelheid en potentiële temperatuur maximaal is. De voelbare warmteflux wordt voornamelijk in evenwicht gehouden door een negatieve netto stralingsflux die toeneemt van 2 W m^{-2} naar 28 W m^{-2} . De gemiddelde latente warmteflux is klein en negatief ($\sim -1 \text{ W m}^{-2}$) en wijst op massaverlies door sublimatie. De jaargemiddelde fluxen in de sneeuw zijn klein ($\sim -0.2 \text{ W m}^{-2}$).

In hoofdstukken 6 en 7 worden brongebieden van het vocht dat als sneeuw op vijf boorlocaties op Antarctica valt (Byrd, DML05, Dome C, Dome F en Vostok) bepaald met behulp van 5 dagen teruggerekende trajectoriën van luchtpakketjes berekend met data van het ECMWF. Een onderscheid tussen trajectoriën met en zonder neerslag bij aankomst is gemaakt op basis van modelneerslag. Van de neerslag trajec-

toriën eindigend op DML05 in 1998, bevindt zich 40 - 80% boven de Atlantische Oceaan tussen 40 en 60°ZB binnen 4 dagen voor aankomst. De verdamping aan het zeeoppervlak langs de trajectoriën is het grootst gedurende de eerste helft. Een gedetailleerde studie van een neerslaggeval in mei 1998 laat zien dat als er sneeuw valt, de luchttemperatuur en windsnelheid in de atmosferische grenslaag relatief hoog zijn. De trajectoriën berekend met de ECMWF heranalysedataset (ERA-15) omvatten een periode van 15 jaar en laten zien dat de oceanen het dichtst bij de vijf boorlocaties het meest bijdragen aan de neerslag. De breedtegraadband die het meest bijdraagt (~30% van de jaarlijkse neerslag) is 50 - 60°ZB, het gebied ten noorden van de rand van het zeeijs. De berekende trajectoriën vertonen een seizoensafhankelijkheid die resulteert in een seizoensvariatie in de brongebieden van het vocht, hetgeen nog eens versterkt wordt door een seizoensvariatie in de hoeveelheid neerslag.

Dankwoord

Zoals elk proefschrift is ook dit proefschrift niet tot stand gekomen zonder de hulp en steun van diverse mensen. Deze personen wil ik hier graag bedanken.

Allereerst wil ik mijn promotor Hans Oerlemans bedanken voor het vervullen van een langgekoesterde droom, namelijk een bezoek brengen aan Antarctica, voor zijn steun, motiverende en sportieve aanwezigheid in de kamer naast de mijne. Ik heb officieel geen co-promotor, maar Richard Bintanja, Wouter Greuell en Michiel van den Broeke hebben onofficieel en ongemerkt gezamenlijk die taak vervuld. Ik heb veel van jullie geleerd en hoop dat ik ook in de komende jaren nog kan genieten van jullie kennis en enthousiasme voor het vak Ijs en Klimaat in het algemeen en voor Antarctica in het bijzonder. Ook de andere leden van de Ijs en Klimaat groep wil ik bedanken voor hun nuttige inhoudelijke en tekstuele tips en hun gezelschap. Het is een periode geweest waar ik met veel plezier op terug kijk.

Bij een project als deze, waar veel gemeten wordt is goede technische ondersteuning onontbeerlijk. Hierbij wil ik dan ook de IMAU-technici Wim Boot, Marcel Portanger, Henk Snellen en Michel Bolder bedanken voor de technische ondersteuning, de computerondersteuning, de af en toe sterke verhalen en voor de gezelligheid, ook buiten het IMAU. Ik heb veel van jullie geleerd, bijvoorbeeld dat sneeuwscooters ook een elektrische starter kunnen hebben.

Aan het begin van mijn promotieonderzoek heb ik 3 maanden op Antarctica doorgebracht waar met name het gezelschap van Richard en Henk die periode tot een onvergetelijke tijd hebben gemaakt. I would also like to thank the other members of SWEDARP 1997-98 expedition, among which Martijn Thomassen, Lars Karlöf, Malin Stenberg, Mart Nyman and Knut Gjerde. They made Christmas, new years eve and my birthday unforgettable.

Placing and operating ten automatic weather stations was and is not only a matter of IMAU. The Berkner Island station was placed by staff of the Alfred-Wegener Institute for Polar and Marine Research (AWI), Bremerhaven, and visited several times by staff of the British Antarctic Survey (BAS). Especially Robert Mulvaney and Andrew Rankin and colleagues from BAS are thanked for their effort to dig out the Berkner Island station in February 2000; displacing $\sim 16 \text{ m}^3$ snow is not a light task. Furthermore, the members of SWEDARP 1997-98 expedition to Svea and Wasa, AWI staff, especially Hans Oerter, and the members of the Norwegian traverse team of 1996-97 and 2000-01 are thanked for their invaluable help with placing and servicing the Automatic Weather Stations in Dronning Maud Land. Natuurlijk horen

hier ook Dan Zwartz en Nicole van Lipzig genoemd te worden. Zij hebben vier weerstations bezocht waarvan er niet één maar twee uitgegraven moesten worden.

Het trajectoriënwerk was niet mogelijk geweest zonder de hulp van een aantal KNMI-mensen; Rinus Scheele, die min of meer de eigenaar is van het KNMI trajectoriënmodel, Peter Siegmund, die me de ins en outs van het werken op de ECMWFcomputers heeft bijgebracht, Erik van Meijgaard, die me in contact bracht met hiervoor genoemde personen en, samen met Nicole, met nuttige tips kwam voor de interpretatie van de trajectoriën.

In ruim vier jaar op het IMAU heb ik maar liefst vijf verschillende kamergenoten gehad. In volgorde van opkomst: Herbert Koekoek (5 maanden), Henk Schuttelaars (3 maanden), Huib de Swart (8 maanden), Bruce Denby (30 maanden) en Dirk van As (3 maanden). Ik wil met name Bruce bedanken voor zijn rustgevende aan- en afwezigheid. De toon waarop je vragen altijd begonnen met 'Carleen,..... mag ik je wat vragen?' zal me nog lang bijblijven.

Het leven bestaat gelukkig niet alleen uit werken. Alle IMAU-ers wil ik daarom bedanken voor de gezellige lunches, theepauzes (waaronder natuurlijk de WK en EK voetbaltotodiscussies), zwemuurtjes en badmintonuurtjes.

Wouter wil ik nogmaals noemen, maar nu voor al die uren op de tennisbaan en de gezellige tijd die we onder andere op IJsland en in Nice samen hebben doorgebracht.

Alle andere mensen waarmee ik de afgelopen jaren regelmatig getennist heb wil ik ook graag bedanken, waaronder de tennisteam van T.C. de Uithof en het winterbinnen-clubje waarvan Herman Prins, Saar Schuling, Henrike Hartemink en Marcel van den Berk de harde kern vormen. Onder het kopje tennis wil ik ook graag de leden van ex-team 1, nu team 2, van T.C de Uithof, waarvan ik al jaren trouw fan ben, bedanken voor al die gezellige zonnige zondagen langs de tennisbaan.

Een aantal goede vrienden wil ik verder nog bedanken voor hun interesse en de goede gesprekken die we in de loop van de jaren gehad hebben. Ten eerste zijn dat dé Mari/jons, Marion Diemel en Marjon de Hond, verder natuurlijk de part-time bewoners van ons appartement Koen de Hart en Marion van Beek voor hun gezelschap tijdens de lange Championsleague avonden. Daarnaast mogen natuurlijk Ingeborg Struijk, Jos de Laat, Mascha Giebels en Maurice Gieling niet vergeten worden.

Tenslotte wil ik natuurlijk mijn (schoon-)familie bedanken voor hun steun, interesse en vertrouwen in mij. Speciaal wil ik mijn vader en moeder bedanken voor de kans die ze me gegeven hebben om te gaan studeren maar ook voor het geduld waarmee ze mijn, vaak misschien onbegrijpelijke, uitweidingen over het Antarctische klimaat, hebben aangehoord. Saskia, bedankt voor je aanwijzingen ter verbetering van de leesbaarheid van het Nederlandstalige gedeelte van dit proefschrift en Johan bedankt voor al je sjouwwerk bij drie verhuizingen. Ik hoop dat ik ook bij de komende verhuizing op je kan rekenen.

De laatste woorden heb ik bewaard voor Sander. Zonder jouw liefde, steun en relativerende aanwezigheid waren dit vier zware jaren geworden.

Carleen Reijmer
juli, 2001.

List of publications

- Reijmer, C. H., W. Greuell and J. Oerlemans, 1999. The annual cycle of meteorological variables and the surface energy balance on Berkner Island, Antarctica. *Ann. Glaciol.*, **29**, 49–54.
- Reijmer, C. H., W. H. Knap and J. Oerlemans, 1999. The surface albedo of the Vatnajökull ice cap, Iceland: A comparison between satellite-derived and ground-based measurements. *Boundary-Layer Meteorol.*, **92**(1), 125–144.
- Reijmer, C. H., R. Bintanja and W. Greuell, 2001. Surface albedo measurements over snow and blue ice in thematic mapper bands 2 and 4 in Dronning Maud Land, Antarctica. *J. Geophys. Res.*, **106**(D9), 9661–9672.
- Reijmer, C. H. and M. R. van den Broeke, 2001. Moisture sources of precipitation in Western Dronning Maud Land, Antarctica. *Antarc. Sci.*, **13**(2), 210–220.
- Reijmer, C. H. and J. Oerlemans, 2001. Temporal and spatial variability of the surface energy balance in Dronning Maud Land, East Antarctica. *J. Geophys. Res.* Submitted.
- Reijmer, C. H., M. R. van den Broeke and M. P. Scheele, 2001. Air parcel trajectories to five deep drilling locations on Antarctica, based on the ERA-15 data set. *J. Climate*, Submitted.
- Bintanja, R., C. H. Reijmer and S. J. M. A. Hulscher, 2001. Detailed observations of the rippled surface of Antarctic blue ice areas. *J. Glaciol.*, In press.
- Bintanja, R. and C. H. Reijmer, 2001. Meteorological conditions over Antarctic blue ice areas and their influence on the local surface mass balance. *J. Glaciol.*, **47**(156), 37–50.
- Bintanja, R. and C. H. Reijmer, 2001. A simple parameterization for snowdrift sublimation over Antarctic snow surfaces. *J. Geophys. Res.*, In press.
- Greuell, W., C. H. Reijmer and J. Oerlemans, 2001. Broadband, and Landsat-TM and AVHRR narrowband albedos of snow and glacier ice: measurements from aircraft, NTB conversion and surface classification. *Remote Sens. Environ.*, Submitted.
- Holmlund, P., K. Gjerde, N. Gundestrup, M. Hansson, E. Isaksson, L. Karlöf, M. Nyman, R. Pettersson, F. Pinglot, C. H. Reijmer, M. Stenberg, M. Thomassen, R. van de Wal, C. van der Veen, F. Wilhelms and J.-G. Winther, 2000. Spatial

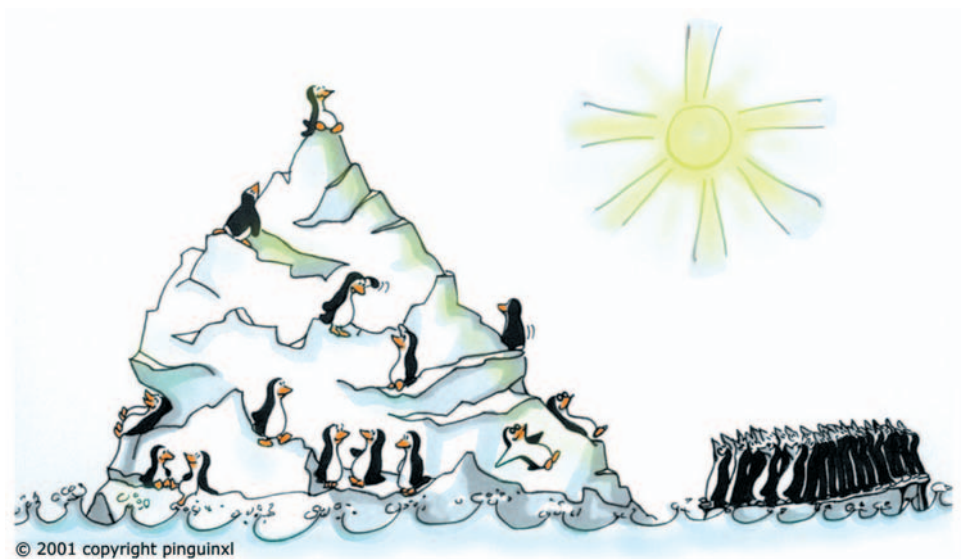
- gradients in snow layering and 10 m temperatures at two EPICA-Dronning Maud Land (Antarctica) pre-site-survey drill sites. *Ann. Glaciol.*, **30**, 13–19.
- Knap, W. H. and C. H. Reijmer, 1998. Anisotropy of the reflected radiation field over melting glacier ice: Measurements in Landsat TM bands 2 and 4. *Remote Sens. Environ.*, **65**, 93–104.
- Knap, W. H., C. H. Reijmer and J. Oerlemans, 1999. Narrowband to broadband conversion of Landsat-TM glacier albedos. *Int. J. Remote Sens.*, **20**(10), 2091–2110.

Non-reviewed publications

- Reijmer, C.H., 1997. Antarctic Automatic Weather Stations: A contribution to EPICA. *Circumpolar J.*, **12**, 3–8.
- Reijmer, C. H., 1998. Nederlandse Antarctica-expeditie, 1997-98. *De Vak-idiot*, jaargang 98-99, **1**, 10–14.
- Reijmer, C. H., 2000. The climate of Berkner Island as observed using an Automatic Weather Station. *Filchner Ronne Ice Shelf Programme*, **13**, Alfred Wegener Institute for Polar and Marine Research, Bremerhaven, Germany. 66–71.
- Reijmer, C. H., 2000. Vijf jaar meteorologische waarnemingen op Antarctica. *Meteorologica*, jaargang 9, **3**, 4–7.

Curriculum Vitae

Carleen Reijmer is geboren op 21 januari 1974 in Pannerden (Gelderland). Zij doorliep de lagere school aan de R.K. basisschool Sint Aloysius te Pannerden. In 1986 begon ze aan haar middelbare schoolopleiding aan het Liemers College te Zevenaar, waar zij het Atheneum B diploma in juni 1992 in ontvangst mocht nemen. In september 1992 is zij begonnen aan de studie Natuur- en Sterrenkunde aan de Universiteit Utrecht. Na haar propedeutisch examen in september 1993 heeft zij de bovenbouwstudie Meteorologie en Fysische Oceanografie gekozen die zij in april 1997 met goed gevolg heeft afgerond met het Doctoraal examen. Als onderdeel van haar afstudeerscriptie, dat zich richtte op het bepalen van de oppervlaktealbedo van sneeuw en ijs met behulp van satellietwaarnemingen, nam ze deel aan een meteorologische expeditie naar de Vatnajökull ijskap op IJsland. Vanaf mei 1997 tot mei 2001 werkte zij als Onderzoeker in Opleiding in dienst van NWO aan het Instituut voor Marien en Atmosferisch onderzoek Utrecht (IMAU) aan haar promotieonderzoek dat als onderwerp het Antarctische klimaat heeft. Als onderdeel van dit werk nam ze deel aan een meteorologische expeditie naar Antarctica (SWEDARP 97/98). Vier jaar promotieonderzoek hebben geleid tot het proefschrift dat u nu in handen heeft.



© 2001 copyright pinguinxl